Longitudinal Λ and $\overline{\Lambda}$ polarization at the COMPASS Experiment

Donghee Kang

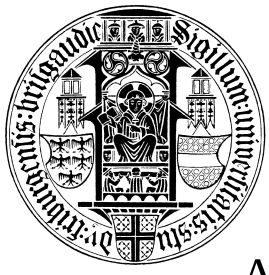

FAKULTÄT FÜR MATHEMATIK UND PHYSIK
ALBERT-LUDWIGS-UNIVERSITÄT FREIBURG

Longitudinal Λ and $\overline{\Lambda}$ polarization at the COMPASS Experiment

Inaugural-Dissertation
zur
Erlangung des Doktorgrades
der
Fakultät für Physik
der
Albert-Ludwigs-Universität Freiburg im Breisgau

vorgelegt
von
Donghee Kang
aus Korea

September 2007

Dekan:	**Prof. Dr. Jörg Flum**
Leiter der Arbeit:	**Prof. Dr. Kay Königsmann**
Referent:	**Prof. Dr. Kay Königsmann**
Koreferent:	**Prof. Dr. Ulrich Landgraf**
Tag der Verkündung des Prüfungsergebnisses:	**29. Oktober 2007**

Contents

Chapter 1

Introduction

In the beginning of the twentieth century Rutherford [1] concluded that atoms consist of a very small nucleus with a cloud of electrons around. More than 50 years after Rutherford's discovery, experiments at SLAC [2] showed a scaling invariance property of the $ep \to e'X$, where is essentially independence of the momentum transfer between the electron and the proton. The result might give evidence of a substructure in the proton and was immediately interpreted by R. P. Feynman. In his initial parton theory [3], now called the Quark Parton Model (QPM), he assumed that the proton was composed of point-like partons as an explanation both of scaling and of the no momentum transfer dependence for structure functions. The partons were later identified with the quarks postulated in 1964 independently by M. Gell-Mann [4] and G. Zweig [5]. In our present understanding all hadrons are composed of constituent quarks and are bound together with gluons by the strong color force. A theory of the strong interactions among quarks and gluons, Quantum Chromo Dynamic (QCD) explains why quarks combine in certain configurations to form the observed patterns of particles.

Despite having been intensively studied by the investigation of the spin structure of hadrons both theoretically and experimentally during the past several years, the spin structure of hadrons is still not understood at a fundamental level in QCD. The first puzzling result for the spin structure of the nucleon was reported by the European Muon Collaboration (EMC) [6], and later confirmed by the Spin Muon Collaboration (SMC) [7]: Quarks and antiquarks carry only 30% of the total contribution of spin to the nucleon. This surprising discrepancy comes from the point of view of the relativistic QPM, which expected the result amounts to about 60% of the contribution to the nucleon's spin [8]. This astonishing result leads to the so-called *nucleon spin crisis*.

Complementary information on the polarization of strange quarks and antiquarks in the nucleon can be accessed by measuring the longitudinal polarization of Λ and $\overline{\Lambda}$ hyperon in $lN \to l'\Lambda(\overline{\Lambda})X$. Λ particles are unique among light hadrons in that their polarization can be

easily reconstructed due to their parity-violating weak decay. Since the Λ contains a strange quark, it has been proposed that Λ and $\overline{\Lambda}$ polarization is potentially a powerful way of probing the polarized s and $\bar{s}$ quark. Additionally, the Λ polarization can also be used for other interesting measurements of polarized fragmentation functions in Deep Inelastic Scattering (DIS). The knowledge of the hadronization mechanism is playing a very important role in the interpretation of semi-inclusive DIS, but the description of the fragmentation process is currently not predicted in the QCD framework.

When a longitudinally polarized lepton beam is scattered off an unpolarized nucleon target, only quarks of a particular spin orientation participate in this interaction. The outgoing struck quark is thus polarized and Λ produced from its fragmentation may remember its spin orientation. Formally such a correlation of longitudinal spin transfer from the quark q to the Λ hyperon may be expressed in terms of a polarized fragmentation function. Consequently, a measurement of the longitudinal polarization of the Λ hyperon is believed to provide information on the spin structure of the Λ hyperon in a certain kinematic limit. There exists a highly non-trivial spin structure of the nucleon, and by the same token, it is also interesting to consider the spin structure of Λ hyperon. This work exploits an ansatz in order to contribute an important piece towards solving the spin puzzle of the nucleon and baryon by utilizing the Λ polarization.

The COMPASS (**CO**mmon **M**uon and **P**roton **A**pparatus for **S**tructure and **S**pectroscopy) experiment at CERN (Conseil Europeen de Rescherche Nucleaire) in Geneva was designed to explore and disentangle the contribution from the different quark flavors and from gluons to the nucleon's spin in DIS [9]. Chapter 2 supplies the theoretical framework needed to interpret the results of a DIS experiment. The discussion is extended to perturbative QCD, which clarifies the important role of the spin structure function of the baryons. The physics topic of this work, the longitudinal Λ polarization, will be introduced in Chapter 3. This Chapter will give insight on the longitudinal spin transfer $q \rightarrow \Lambda$ via a measurement of the Λ polarization. Chapter 4 gives a brief overview of the experimental apparatus at COMPASS. Chapter 5 is dedicated to explain a strategy for tagging the Λ and $\overline{\Lambda}$ events. The selection scheme is applied to the COMPASS data collected during the years 2002 to 2004 with a longitudinally polarized target. Subsequently, an extraction method of the Λ polarization from the acceptance corrected angular distribution of the decay products will be presented. In the last Chapter all obtained results of the spin transfer of Λ and $\overline{\Lambda}$ will be discussed and compared with theoretical predictions.

Chapter 2

The Spin Structure of Baryons

2.1 Polarized Deep Inelastic Scattering

It is believed that the nucleon spin is distributed among valence quarks, sea quarks, gluons, and their orbital momenta. The nucleon spin S_N can be decomposed into contributions from different constituents and is given in unit of $\hbar$ by [8]

$$S_N = \frac{1}{2} = \frac{1}{2}\Delta\Sigma + \Delta G + L_q + L_g, \tag{2.1}$$

where $\Delta\Sigma$ is the sum of the spin contributions from quarks and antiquarks, ΔG the spin contribution from gluons, while L_q and L_g stand for the contribution from the orbital angular momentum of quarks and gluons, respectively. In order to find the different contributions to S_N, a wide variety of experimental approaches has been applied to investigate the nucleon spin structure.

Polarized Deep Inelastic Scattering has been the key tool for probing the internal structure of the nucleon. In DIS experiments charged leptons l are scattered inelastically with a large momentum transfer off a nucleon N:

$$l + N \rightarrow l' + X. \tag{2.2}$$

To investigate the spin structure of hadrons longitudinally polarized leptons are scattered off targets with longitudinally or transversely polarized nucleons. It implies the exchange of a virtual vector boson between the lepton and one of the partons inside the target nucleon exchanging a high four-momentum that breaks up the nucleon and forms a final hadronic state X. In the case of $\mu^{\pm}$-nucleon or $e^{\pm}$-nucleon scattering, a neutral vector boson, γ or Z^0, is exchanged, while a charged vector boson $W^{\pm}$ is exchanged in a neutrino-nucleon reaction.

2.1.1 Kinematics

The illustration for a muon-nucleon DIS process is shown in Fig. 2.1. In DIS, the cross section can be expressed as a function of two variables, namely the negative squared 4-momentum transfer Q^2 and energy loss ν of the scattered particle. The lepton four-momentum is given by k for the incoming muon and k' for the scattered muon. The angle between incoming and outgoing lepton in the laboratory system is θ. The four-momentum squared of the virtual photon is given by

$$q^2 = (k - k')^2 . \tag{2.3}$$

By neglecting the lepton rest mass,

$$-q^2 = Q^2 \simeq 4EE' sin^2 \frac{\theta}{2}, \tag{2.4}$$

where E, E' are the energy of the incoming and the scattered lepton, respectively. Q^2 is positive and a resolving power of the photon $\lambda \approx \frac{1}{Q}$. The energy transfer from the virtual photon to the nucleon is defined by

$$\nu = \frac{P \cdot q}{M} = E - E' , \tag{2.5}$$

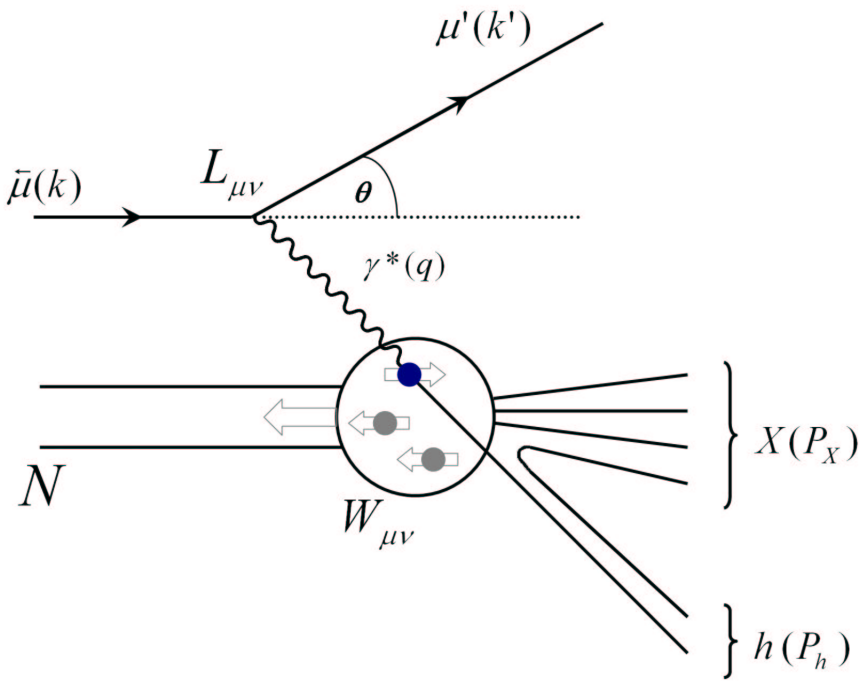

Figure 2.1: Illustration of the deep inelastic muon nucleon scattering process together with kinematic quantities as defined in the text.

At COMPASS, the target nucleon with mass M is at rest in the laboratory frame and therefore the four-momentum of the target nucleon is given by $P = (M, \vec{0})$. Defining P and q, the invariant mass squared of the hadronic final state W^2 can be expressed as

$$W^2 = (P+q)^2 = M^2 + 2M\nu - Q^2 \,. \tag{2.6}$$

The DIS is considered as a process in which $1/Q$ is smaller than the size of the nucleon such that the leptons scatter off a single parton. Furthermore, W^2 has to be larger than 4 $(\mathrm{GeV/c^2})^2$ to ensure the complete break-up of the nucleon instead of forming hadronic resonances [10, 11].

One can describe the DIS process introducing two more dimensionless scaling variables

$$\begin{aligned} x &= \tfrac{Q^2}{2P\cdot q} &&= \frac{Q^2}{2M\nu}\,, \\ y &= \tfrac{P\cdot q}{P\cdot k} &&= \frac{\nu}{E}\,. \end{aligned} \tag{2.7}$$

Here, x can be identified for large values of Q^2 with the fractional momentum of the target nucleon carried by the struck quark, and y with the energy fraction of the projectile transferred from the incoming lepton to the nucleon. x is a measure of the inelasticity of the scattering process. In an elastic scattering process, the target remains intact, and consequently $W^2 = M^2$, which implies $x = 1$. DIS is formally defined as the lepton-nucleon scattering for Q^2, $\nu \to \infty$ at fixed x. The kinematic quantities used as characterization are summarized in Table 2.1. In semi-inclusive scattering processes, additional kinematic variables z and x_F are required for each detected hadron, which will be discussed in the context of semi-inclusive Λ production in Section 3.2.1 and Section 3.3.1.

2.1.2 Cross Sections

In general, the cross section of lepton-nucleon scattering can be calculated by contracting the leptonic tensor $L_{\mu\nu}$ and the hadronic tensor $W^{\mu\nu}$ [12]:

$$\frac{d^2\sigma}{dE'\,d\Omega} = \frac{\alpha^2}{2MQ^4}\frac{E'}{E} L_{\mu\nu} W^{\mu\nu}\,, \tag{2.8}$$

where Ω is the solid angle in the laboratory frame and $\alpha = \frac{1}{137}$ the electromagnetic fine-structure constant. The differential cross section can also be expressed in other kinematic variables using

$$\frac{2\pi M\nu}{E'}\frac{d^2\sigma}{dE'\,d\Omega} = \frac{d^2\sigma}{dx\,dy} = x(s-M^2)\frac{d^2\sigma}{dx\,dQ^2}. \tag{2.9}$$

where s is the center-of-mass energy squared of the lepton-nucleon system. The tensor $L_{\mu\nu}$ describes the interaction at the leptonic vertex in the 1-photon exchange, and can be written with the Dirac matrices γ_μ and spinors u, $\overline{u}$:

$$L_{\mu\nu}(k,k',s) = \sum_{s'} \overline{u}(k',s')\,\gamma_\mu\,u(k,s)\,\overline{u}(k,s)\,\gamma_\nu\,u(k',s'). \tag{2.10}$$

The spin four-vector s^ν of the incoming muon is defined by

$$s^\nu = \frac{1}{2m}\overline{u}(k,s)\gamma^\nu\gamma^5 u(k,s)\,, \tag{2.11}$$

and set to be $s^\nu = (0,\vec{s})$ in the rest frame of the particle. The mass of the muon is given by m. In these expressions, the spin vector s is a dimensionless quantity due to the chosen normalization. Using the abbreviated notation $\not{q} = \gamma^\mu a_\mu$, summing over the lepton spins of the final state and employing trace algebra leads to [13]

$$\begin{aligned}
L_{\mu\nu}(k,k',s) &= Tr[(\not{k}' + m)\gamma_\nu(\not{k} + m)\frac{m+\gamma_5\not{s}}{2m}\gamma_\mu] && (2.12)\\
&= 2(k_\mu k'_\nu + k_\nu k'_\mu - \left(kk' - m^2\right) g_{\mu\nu}) + 2im\varepsilon_{\mu\nu\alpha\beta}s^\alpha(k-k')^\beta && (2.13)\\
&\approx 2(k_\mu k'_\nu + k_\nu k'_\mu - kk' g_{\mu\nu}) + 2im\varepsilon_{\mu\nu\alpha\beta}s^\alpha(k-k')^\beta && (2.14)\\
&= L^{(S)}_{\mu\nu}(k,k') + L^{(A)}_{\mu\nu}(k,k',s)\,, && (2.15)
\end{aligned}$$

where $g_{\mu\nu}$ is the metric tensor and $\varepsilon_{\mu\nu\alpha\beta}$ the antisymmetric Levi-Civita tensor. The spin independent terms of the leptonic tensor are symmetric while the spin dependent term is antisymmetric under μ, ν interchange. The two different parts indicated to be symmetric (S) and antisymmetric (A), respectively. The leptonic tensor $L_{\mu\nu}$ can be calculated exactly in QED, but the hadronic tensor $W^{\mu\nu}$ cannot be calculated. Theoretically, $W_{\mu\nu}$ is parametrized by a set of structure functions F_1, F_2, g_1 and g_2, which in turn contain the momentum and spin distribution functions. Imposing symmetry requirements such as Lorentz invariance, gauge invariance, and symmetry of the strong interaction under charge and parity transformation, the symmetric part of the hadronic tensor $W^{\mu\nu}$ can be expressed in terms of two dimensionless structure functions $F_1(x,Q^2)$ and $F_2(x,Q^2)$. The antisymmetric part is parametrized by two others, likewise dimensionless structure functions $g_1(x,Q^2)$ and $g_2(x,Q^2)$:

$$W^{\mu\nu}(P,q,S) = W^{\mu\nu}_{(S)} + W^{\mu\nu}_{(A)}\,, \quad \text{with} \tag{2.16}$$

$$W^{\mu\nu}_{(S)}(P,q) = \left(-g^{\mu\nu} + \frac{q^\mu q^\nu}{q^2}\right) F_1\left(x,Q^2\right) + \left(P^\mu - \frac{P_\lambda q^\lambda}{q^2}q^\mu\right)\left(P^\nu - \frac{P_\lambda q^\lambda}{q^2}q^\nu\right)\frac{F_2\left(x,Q^2\right)}{P_\lambda q^\lambda}, \tag{2.17}$$

$$W^{\mu\nu}_{(A)}(P,q,S) = iM\varepsilon^{\mu\nu\rho\sigma}q_\rho\left[\frac{S_\sigma}{P_\lambda q^\lambda}g_1\left(x,Q^2\right) + \frac{S_\sigma(P_\lambda q^\lambda) - P_\sigma(S_\lambda q^\lambda)}{(P_\lambda q^\lambda)^2}g_2\left(x,Q^2\right)\right]. \tag{2.18}$$

The most general ansatz for the symmetric hadronic tensor $W^{\mu\nu}_{(S)}$ including weak interactions leads to another unpolarized structure function F_3, which is introduced for the parity-non-conserving neutrino scattering, as well as three more polarized structure functions g_3, g_4, and g_5 [12, 14].

Combining the expressions for the leptonic and hadronic tensor one obtains the result of the differential cross section in Eq. 2.8. The unpolarized cross section can be obtained by contracting the symmetric parts of $L_{\mu\nu}$ and $W^{\mu\nu}$ which provide the spin independent cross section. The same procedure can also be applied for the antisymmetric part to obtain the polarized cross section. Both spin-independent and spin-dependent cross section are

$$\frac{d^2\sigma}{dE'\,d\Omega} = \frac{4\alpha^2 E'^2}{Q^4}\left[\frac{2F_1(x,Q^2)}{M_N}\sin^2\frac{\theta}{2} + \frac{F_2(x,Q^2)}{\nu}\cos^2\frac{\theta}{2}\right], \tag{2.19}$$

$$\frac{d^2\Delta\sigma}{dE'\,d\Omega} = \frac{4\alpha^2}{Q^2 M_N \nu}\frac{E'}{E}\left[(E+E'\cos\theta)\cdot g_1(x,Q^2) - \frac{Q^2}{\nu}\cdot g_2(x,Q^2)\right], \tag{2.20}$$

where $\Delta\sigma = \sigma^{\overrightarrow{\Leftarrow}} - \sigma^{\overrightarrow{\Rightarrow}}$ stands for the difference in the cross sections for the nucleon spin anti-parallel and parallel with the beam direction. The unpolarized structure functions parameterize the deviation of the observed experimental cross section from the Mott cross section. There is an analogy to the electric and magnetic form factors in elastic scattering, which are the Fourier transformations of the electric charge distribution and the electric current distribution of the nucleon, respectively. The spin-dependent cross section depends on the polarized structure functions g_1 and g_2. The relevant variables of the structure functions are x and Q^2. In leading order α_s, the strong coupling constant, the structure functions turn out to be Q^2 independent and the residual Q^2 dependence can be used as a most sensitive test for the QCD [15].

2.2 Structure Functions

The Quark Parton Model (QPM) invented by Bjorken [16] and Feynman [2], describes DIS on a nucleon as the sum of the incoherent elastic scattering amplitudes on non-interacting point-like partons. These partons are assumed to carry a four-momentum fraction x of the nucleon in the infinite momentum frame, such that rest masses of the partons as well as transverse momenta to the direction of motion can be neglected. Since the electrically neutral gluons do not interact with the virtual photon in lowest order, only quarks are coupled with the virtual photon in the QPM. In the limit $Q^2 \to \infty$ and $\nu \to \infty$, in which the quark parton model is applicable, the structure functions do not depend on Q^2, but become a function on x only. This formalism leads to the definition of parton distribution functions by summing over

the quark and antiquark flavors. The structure functions are written in the QPM as follows:

$$\begin{aligned} F_1(x) &= \frac{1}{2}\cdot\sum_f e_f^2\left(q_f(x)+\overline{q}_f(x)\right), \\ F_2(x) &= x\cdot\sum_f e_f^2\left(q_f(x)+\overline{q}_f(x)\right), \\ g_1(x) &= \frac{1}{2}\cdot\sum_f e_f^2\left(\Delta q_f(x)+\Delta\overline{q}_f(x)\right), \\ g_2(x) &= 0, \end{aligned} \tag{2.21}$$

where e_f is the fractional charge of the quark flavor f. The relation between F_1 and F_2 is referred to as the Callan-Gross relation [17]:

$$F_2(x) = 2xF_1(x). \tag{2.22}$$

This relation is a consequence of quarks having spin $1/2$, and the experimental data so far has been consistent with this relation as expected for scattering from spin-$1/2$ particles. However, in QCD α_s corrections have to be applied to the Callan-Gross relation.

The distributions $q(x)$ are the unpolarized parton density function (PDF) or quark distribution function, and $\Delta q(x)$ are the polarized quark distribution function. The unpolarized quark distribution $q(x)$ is defined as the sum of the quark distribution function with parallel $q^{\uparrow\uparrow}$ and anti-parallel $q^{\uparrow\downarrow}$ spin with respect to the nucleon spin: Each helcity distribution function $\Delta q(x)$ is defined by the difference between them,

$$\begin{aligned} q(x) &= q^{\uparrow\uparrow}(x)+q^{\uparrow\downarrow}(x), \\ \Delta q(x) &= q^{\uparrow\uparrow}(x)-q^{\uparrow\downarrow}(x). \end{aligned} \tag{2.23}$$

$q(x)$ and $\Delta q(x)$ can be interpreted as the probability of finding an unpolarized and a polarized quark with a certain flavor in the nucleon. In DIS, only the contributions of both quarks and anti-quarks to the spin can be extracted. The integral over the unpolarized parton density function yields the total momentum carried by quarks. It turns out that the nucleon momentum is not completely carried by the quarks. Measurements show that the gluons carry about one half of the nucleon momentum [13]. In the same way, the integration over x of the polarized quark distribution function in the nucleon yields the fraction of the nucleon spin carried by quarks,

$$\Delta q = \int_0^1 \Delta q(x)\,dx. \tag{2.24}$$

The polarized quark distribution $\Delta q+\Delta\overline{q}$ is also called the axial charge in the QCD framework because it is related to the matrix element of the axial current $\overline{\psi}\gamma_\mu\gamma_5\psi$ in the nucleon state.

An important result of the unpolarized structure functions is the scaling violation. If the

constituents of the nucleon would be pointlike and behave like free particles, the structure functions in Eq.2.21 do not depend on Q^2. This phenomenon is the so-called Bjorken scaling. Precise measurements of $F_2^p(x,Q^2)$ show a Q^2 dependency of F_2 for the proton and also for the deuteron. The experimental results for $F_2^p(x,Q^2)$ and $F_2^d(x,Q^2)$ are represented in Fig. 2.2 as a function of Q^2 for various fixed values of x. For values of $x < 0.05$ and $x > 0.3$, the structure function $F_2^p(x,Q^2)$ shows a significant dependence on Q^2, which is not expected in the naive quark parton model. For small values of x, the structure function $F_2^p(x,Q^2)$ rises with increasing Q^2. The opposite is true for large x values. Here the structure function $F_2^p(x,Q^2)$ decreases with increasing Q^2. This can be explained by the existence of sea quarks from arising gluon splitting, which carry a small fraction x of the nucleon momentum. For higher Q^2 values, the sea quarks can be resolved in the scattering process resulting in an increase of the structure function F_2. Correspondingly, the probability of scattering off a parton with a large fraction of the nucleon momentum decreases with increasing resolution associated with higher Q^2 values.

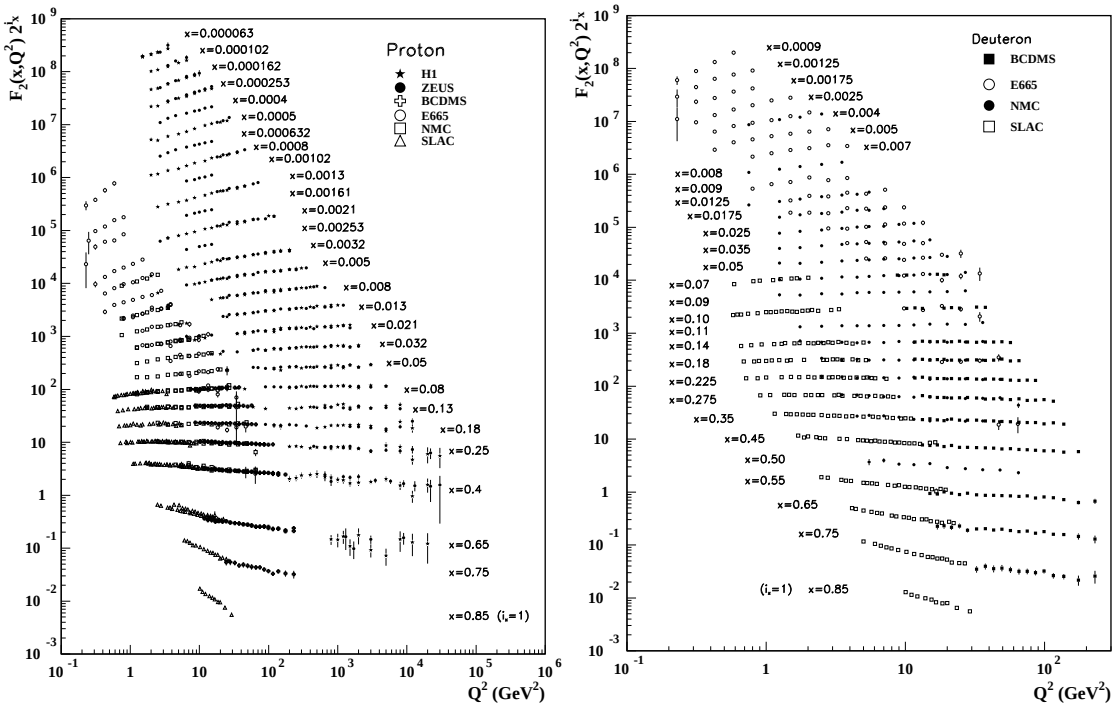

Figure 2.2: The unpolarized proton (left) and deuteron (right) structure function $F_2^{p,d}(x,Q^2)$, measured in deep inelastic lepton nucleon scattering (H1[18], ZEUS[19], BCDMS[20, 21], E665[22], NMC[23] and SLAC[24]). For the purpose of plotting, $F_2^{p,d}(x,Q^2)$ has been multiplied by 2^{i_x}, where i is the number of the x bin. The data are shown as a function of Q^2 for fixed values of x, statistical and systematical errors are shown in both plots. Plots are taken from [14].

The polarized distribution functions only play a role in DIS when the scattered leptons and targets are polarized. The spin structure function $g_1(x,Q^2)$ and $g_2(x,Q^2)$ can be determined with a longitudinal polarized lepton beam via photon-nucleon asymmetries A_1 and A_2 on a longitudinally and transversely polarized target [25]:

$$\begin{aligned} A_1(x,Q^2) &= \frac{\sigma_T^{\frac{1}{2}}-\sigma_T^{\frac{3}{2}}}{\sigma_T^{\frac{1}{2}}+\sigma_T^{\frac{3}{2}}} = \frac{g_1-\gamma^2 g_2}{F_1}, \\ A_2(x,Q^2) &= \frac{2\sigma_{TL}}{\sigma_T^{\frac{1}{2}}+\sigma_T^{\frac{3}{2}}} = \frac{\gamma(g_1+g_2)}{F_1}. \end{aligned} \tag{2.25}$$

The indices $\frac{1}{2}$ and $\frac{3}{2}$ indicate the sums of the photon spin and nucleon spin antiparallel ($\frac{1}{2}$) and parallel ($\frac{3}{2}$) with respect to the virtual photon axis, respectively. The photoabsorption cross section for transverse photons is σ_T. σ_{TL} is the interference between transverse and longitudinal photon cross sections. Introducing R, which is defined as the ratio of the transversely and longitudinally polarized photoabsorption cross section,

$$R = \frac{\sigma_L}{\sigma_T} = (1+\gamma^2)\frac{F_2(x,Q^2)}{2xF_1(x,Q^2)} - 1, \tag{2.26}$$

where γ is the kinematic factor $2Mx/\sqrt{Q^2}$. The definition of A_1 and A_2 can then be combined into the following expression for g_1 and g_2,

$$g_1(x,Q^2) = \frac{F_2}{2x(1+R)}(A_1+\gamma A_2), \qquad g_2(x,Q^2) = \frac{F_2}{2x(1+R)}(\frac{A_2}{\gamma}-A_1). \tag{2.27}$$

Using the earlier measured structure function F_2 as well as the ratio R and neglecting the second asymmetry A_2 due to kinematical suppression, one can extract $g_1(x,Q^2)$ from a measurement of the photon asymmetry A_1 in the DIS process. The asymmetry A_1 is related to the experimental asymmetry $A_{||}$,

$$A_1 \approx \frac{A_{||}}{D} = \frac{1}{D}\frac{\sigma_{\uparrow\downarrow}-\sigma_{\uparrow\uparrow}}{\sigma_{\uparrow\downarrow}+\sigma_{\uparrow\uparrow}}, \tag{2.28}$$

where the two arrows refer to the parallel and antiparallel spin orientations of the lepton beam with respect to the target nucleon, and D is the virtual photon depolarization factor. Like the unpolarized structure functions, it is assumed that the polarized structure function $g_1(x,Q^2)$ possesses a significant Q^2 dependence due to radiative QCD effects. The analysis of the Q^2 dependence in Fig. 2.3 shows that within the range of existing experiments the result is experimentally consistent with being slightly dependent on Q^2. The polarized quark distributions for the proton were determined from global fits to inclusive DIS data obtained by COMPASS, EMC, HERMES, SLAC, and SMC experiments covering a kinematic range

of $0.006 < x < 0.8$ and $0.7 < Q^2 < 80$ (GeV/c)^2. Over the limited Q^2 range accessible by current experiments a slight Q^2 dependence of $g_1(x, Q^2)$ is observed for the proton, whereas the Q^2 dependence is not clearly determined for the neutron and deuteron due to statistical limitations. One can find the experimental measurements of g_1^n in Refs. [26, 27, 28, 29].

The QPM is an approximation, in which the binding of the partons neglect the large transverse momentum reactions. Moreover, massive or massless quark is also not sensitive to calculate the structure functions, and consequently one cannot expect to make a reliable calculation of g_2 within the QPM [12], as shown in Eq.2.21. However, the Operator Product Expansion (OPE) provides a formalism so that g_2 is related to the quark-gloun interactions

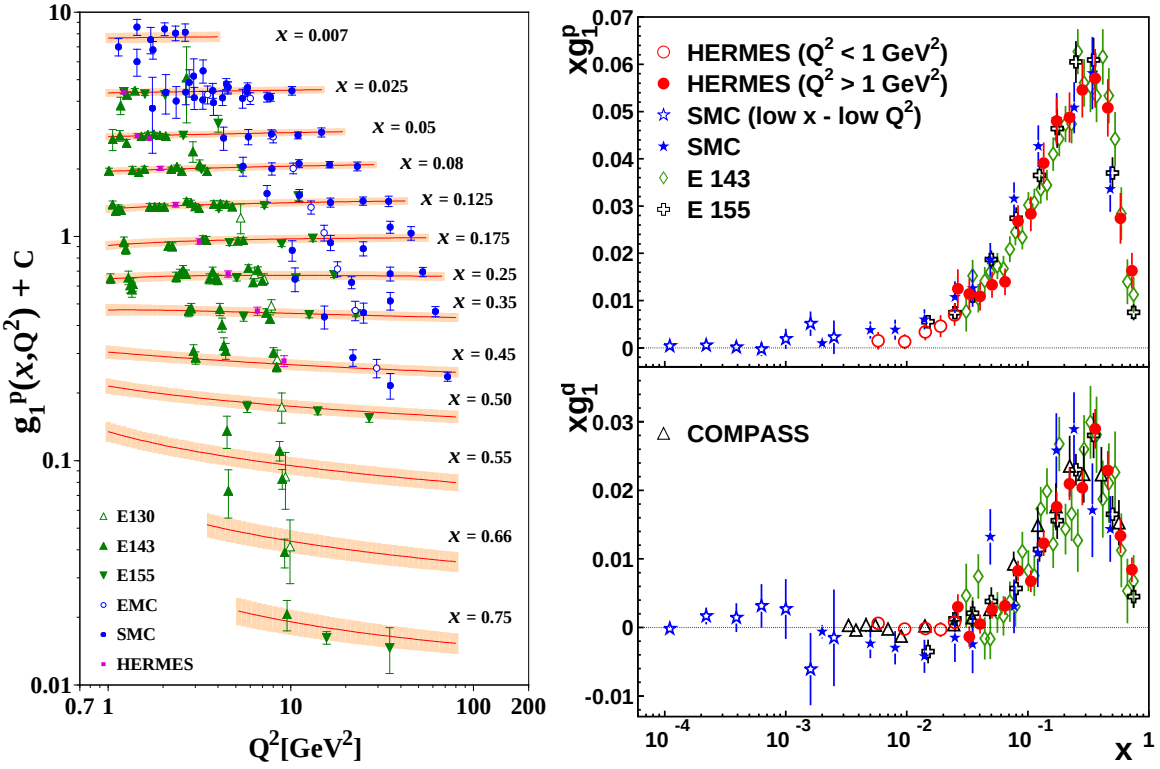

Figure 2.3: On the left, the polarized structure function $g_1^p(x, Q^2)$ measured in deep inelastic lepton-nucleon scattering (E130[30], E143[31], E155[32], EMC[6, 33], SMC[34], HERMES[35]) is shown. The data are shown as a function of Q^2 for fixed values of x. A constant C is added to g_1^p for the purpose of plotting. Global fits were performed by the Asymmetry Analysis Collaboration [36]. In the right figure, the results on xg_1^p and xg_1^d versus x are shown in separate panels. All data are presented as function of x for their measured mean values of $\langle Q^2 \rangle$. The error bars represent the quadrature sum of statistical and systematic uncertainties. The data are taken from HERMES[37], SMC[34, 38], E143[31], E155[32, 39] and COMPASS[40].

through higher twist effects [1] and the calculation of g_2 is extremely sensitive to transverse momenta and whether massive or massless quark are considered [42]. Hence, the introduction of intrinsic k_T and quark masses allow a non-zero value of g_2. The structure function g_2 has been also measured for the proton [31, 43], neutron [44], and deuteron [43] within a kinematic range of $0.02 < x < 0.8$ and $1 < Q^2 < 30$ (GeV/c)^2. The integration of xg_2 is found to be consistent with zero for the proton, neutron and deutron.

2.3 QCD Evolution of Structure Functions

The structure functions F_2 and g_1 vary with Q^2. These scaling violations can be explained in the perturbative regime of QCD by the interaction of quarks and gluons. QCD is the non-Abelian[2] gauge field theory of strong interactions, in which the force is mediated by gluons. The gluons can interact to each other with a scale dependent coupling strength:

$$\alpha_s(Q^2) = \frac{4\pi}{(11 - \frac{2}{3} n_f) \ln(Q^2/\Lambda^2_{QCD})}, \tag{2.29}$$

where $\Lambda_{QCD} \approx 0.3$ GeV is the QCD scale parameter of strong interactions. Λ_{QCD} gives a lower limit for the applicability of the perturbative calculation. n_f is the number of quark flavors f, which have a mass smaller than the momentum scale Q^2. According to the QCD regime, the strong force becomes more feeble for short distance interactions, which is referred to as asymptotic freedom. In the regime of short distances, the strong coupling constant is sufficiently small so that the QCD processes can be calculated by perturbative expansions similar to Quantum Electro Dynamics (QED). However, at low energies the perturbative expansion diverges due to the increase of the coupling constant. Thus QCD does not allow predictions for strong interactions like the confinement of quarks inside hadrons and the fragmentation processes. To deal with the properties of the hadrons themselves, it is necessary to use an approach, which is still valid when the interaction becomes stronger [45]. The value of α_s depends on Q^2, in the limit $Q^2 \to \infty$ it vanishes logarithmically. Applying this limit for small distances, which corresponds to large values of Q^2, the quarks can be treated as free, pointlike particles as it has been done for partons in the QPM. An appropriate value of Q^2 is about 1.0 (GeV/c)^2. For increasing resolution of Q^2 each quark is surrounded by a cloud of quarks and gluons. These partons originate from the splitting of gluons into quark-antiquark pairs. Each of these sea quarks carry a part of the proton momentum. This process leads to a depletion of the parton density at high x with increasing Q^2.

For the quark distribution functions the situation is similar. Quarks can loose momentum

[1] Higher twist is the generic name for $\vartheta(1/\sqrt{Q^n})$ correction to the DIS process [41].

[2] Non-Abelian means that not all the generators commutate with each other. The commutator of any two is a linear combination of the generators: $[T_a, T_b] = i f_{abc} T_c$. If the structure constant f_{abc} of the group is not equal zero, then the group is called non-Abelian.

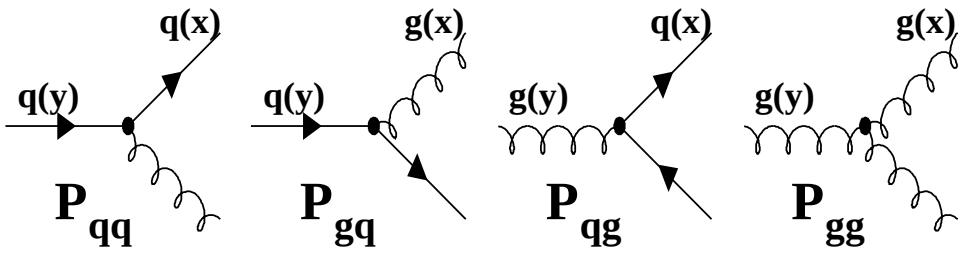

Figure 2.4: Feynman graphs of the lowest order processes with the corresponding splitting functions, the time is oriented rightwards. A quark can emit a gluon. A gluon can split up into a quark-antiquark or a gluon-gluon pair, where the final state partons then have lower momenta.

by emission of a gluon, and they can also be generated by pair production from a gluon. Furthermore, gluons can as well decompose into two gluons. These processes are described by so-called splitting functions $P_{fi}(x/y)$. In Fig. 2.4, the corresponding Feynman diagrams are shown. The splitting functions represent the probability of finding a parton f carrying momentum fraction x in the final state, originating from an initial parton i with momentum fraction y. The partons can either be gluons or quarks, where quark masses and thus flavor dependence are neglected. For the spin dependent case separate quark and gluon distribution functions with helicity dependent splitting functions ΔP_{fi} have to be considered. The calculation of unpolarized [46] and polarized [47, 48, 49] splitting functions are available in Next-to-Leading-Order (NLO). Due to helicity conservation for massless quarks at the quark-gluon vertex, the polarized and unpolarized splitting functions are identical in Leading-Order (LO) [50]. This means that the polarized and unpolarized distribution functions evolve similarly.

The evolution of the distribution functions with Q^2 is given by the Dokshitzer-Gribov-Lipatov-Altarelli-Parisi (DGLAP) equations [51, 52, 53]:

$$\begin{aligned}
\frac{d}{d\ln Q^2}\Delta q_{ns}(x,Q^2) &= \frac{\alpha_s(Q^2)}{2\pi}\left[\Delta P^{ns}_{qq}\otimes\Delta q_{ns}\right](x,Q^2)\,, \\
\frac{d}{d\ln Q^2}\begin{pmatrix}\Delta\Sigma(x,Q^2)\\ \Delta G(x,Q^2)\end{pmatrix} &= \frac{\alpha_s(Q^2)}{2\pi}\left[\begin{pmatrix}\Delta P^s_{qq} & 2n_f\Delta P^s_{qg}\\ \Delta P^s_{gq} & \Delta P^s_{gg}\end{pmatrix}\otimes\begin{pmatrix}\Delta\Sigma\\ \Delta G\end{pmatrix}\right](x,Q^2)\,,
\end{aligned} \tag{2.30}$$

where $\otimes$ denotes a convolution integral defined by

$$\left[a\otimes b\right](x,Q^2) = \int_x^1 \frac{dy}{y} a\left(\frac{x}{y},Q^2\right) b(y,Q^2). \tag{2.31}$$

Here, $\Delta q_{ns}(x,Q^2)$ is the flavor non-singlet distribution, the flavor singlet quark distribution $\Delta\Sigma(x,Q^2)$ and the gluon distribution $\Delta G(x,Q^2)$, respectively. The flavor siglet distribution

$\Delta\Sigma(x,Q^2)$ and non-singlet distribution $\Delta q_{ns}(x,Q^2)$ are defined as

$$\begin{aligned}\Delta\Sigma(x,Q^2) &= \sum_i \Delta q_i = (\Delta u + \Delta\overline{u}) + (\Delta d + \Delta\overline{d}) + (\Delta s + \Delta\overline{s}),\\ \Delta q_{ns}(x,Q^2) &= \sum_i \frac{e_f^2 - \langle e^2\rangle}{\langle e^2\rangle}\Delta q_i = (\Delta u + \Delta\overline{u}) - \frac{1}{2}(\Delta d + \Delta\overline{d}) - \frac{1}{2}(\Delta s + \Delta\overline{s}) \quad (2.32)\end{aligned}$$

with $\langle e^2\rangle = \sum_f e_f^2/n_f$, where n_f is the number of quark flavors f. The important thing to mention is that the Q^2 evolution of the non-singlet term Δq_{ns} does not depend on the gluon contribution, while $\Delta\Sigma$ and ΔG couple to each other. Therefore $g_1(x,Q^2)$ can be used to extract the gluon helicity distribution ΔG from measuring its Q^2 dependence of $\Delta\Sigma$ over a wide range. $\Delta\Sigma$ is the singlet combination of the spin dependent quark distribution functions. The set of equations can be solved numerically, given the distribution functions at a fixed value of Q^2. On the other hand one can fit the distribution functions to the observed scaling violations of structure functions.

In perturbative QCD by means of using OPE, the resulting expressions for the polarized structure function $g_1(x,Q^2)$ are generalized to include gluons. They are written in a form which is convenient for the Q^2 evolution of the structure functions [54, 55, 56]:

$$g_1(x,Q^2) = \frac{1}{2}\langle e^2\rangle \left[\Delta C_{ns} \otimes \Delta q_{ns} + \Delta C_s \otimes \Delta\Sigma + 2n_f \Delta C_g \otimes \Delta G\right]. \quad (2.33)$$

ΔC_{ns}, ΔC_s and ΔC_g are Wilson coefficient functions and correspond to the hard scattering cross section of non-singlet photon-quark, singlet photon-quark and photon-gluon, respectively. The polarized Wilson coefficient functions evolve formally equivalent to the unpolarized ones. In LO, the unpolarized and polarized Wilson coefficient functions are also equal and $\Delta C_{NS}^{(0)} = \Delta C_S^{(0)}$. In addition, the gluon coefficient function is $\Delta C_g^{(0)} = 0$. Thus Eq.2.21 is recovered in QPM. Since the coefficient functions depend on the chosen renormalization scheme at NLO, one can classify the factorization in terms of their treatments in higher order expansion. The Wilson coefficient functions $\Delta C(x,Q^2)$ can be expanded in power series of $\alpha_s(Q^2)$ [57]:

$$\Delta C(x,Q^2) = \Delta C^{(0)} + \frac{\alpha_s(Q^2)}{2\pi}\Delta C^{(1)} + O(\alpha_s^2). \quad (2.34)$$

Using $n_f = 3$ for three active flavors and $\Delta C(Q^2) = \int_0^1 \Delta C(x,Q^2)dx$, the non-singlet and singlet coefficients are given up to third and second order in Q^2 as [58]:

$$\Delta C_{ns}(Q^2) = 1 - \frac{\alpha_s(Q^2)}{\pi} - 3.5833\left(\frac{\alpha_s(Q^2)}{\pi}\right)^2 - 20.2153\left(\frac{\alpha_s(Q^2)}{\pi}\right)^3, \quad (2.35)$$

$$\Delta C_s(Q^2) = 1 - \frac{\alpha_s(Q^2)}{\pi} - 1.0959\left(\frac{\alpha_s(Q^2)}{\pi}\right)^2. \quad (2.36)$$

The coefficients $\Delta C_{s,ns}^{(1)}$ have been calculated in the original work by Kodaira et al.[59]. Coefficients up to $\Delta C_s^{(3)}$, $\Delta C_{ns}^{(4)}$ were calculated in Ref. [60].

2.4 First moments of g_1

The total contribution of the spin of quarks to the nucleon can be derived from the integration of g_1 over x, which is called the first moment. The first moment of g_1 is given by

$$\Gamma_1 = \int_0^1 g_1(x)dx = \frac{1}{2}\int_0^1 \sum_f e_f^2 \Delta q_f(x)dx. \tag{2.37}$$

Since the experiments cover only a limited range in x, extrapolations for large x and small x are needed in order to determine the first moment of the structure function g_1. Under the assumption of $SU(3)_f$ flavor symmetry of the axial vector current in the spin $\frac{1}{2}$ baryon-octet, the matrix elements a_0, a_3, and a_8 can be defined to the first moments for the proton and neutron as

$$\begin{aligned}\Gamma_1^{\mathrm{p,n}} &= \pm\frac{1}{12}(\Delta u - \Delta d) + \frac{1}{36}(\Delta u + \Delta d - 2\Delta s) + \frac{1}{9}(\Delta u + \Delta d + \Delta s) \\ &= \frac{1}{12}(\pm a_3 + \frac{1}{\sqrt{3}}a_8) + \frac{1}{9}a_0.\end{aligned} \tag{2.38}$$

where the minus sign $(-)$ refers to Γ_1^n. The matrix elements a_0, a_3 and a_8 are directly related to the polarized quark and antiquark distribution and can be written as

$$\begin{aligned}a_0 &= \Delta u + \Delta d + \Delta s + \Delta\overline{u} + \Delta\overline{d} + \Delta\overline{s}, \\ a_3 &= \Delta u - \Delta d + \Delta\overline{u} - \Delta\overline{d}, \\ a_8 &= \frac{1}{\sqrt{3}}\left(\Delta u + \Delta\overline{u} + \Delta d + \Delta\overline{d} - 2(\Delta s + \Delta\overline{s})\right).\end{aligned} \tag{2.39}$$

The matrix elements a_3 and a_8 are related to the weak decay constants, while the axial singlet matrix element a_0 cannot be related to the weak decay. In particular, a_3 equals the ratio $|g_A/g_V|$ of the axial vector (g_A) to the vector (g_V) coupling constants. The three matrix elements given in Eq. 2.39 can be estimated from the weak neutron decay constant (a_3) [14], hyperon decays (a_8) [61] and inclusive DIS measurements (a_0) [62]. In the QPM, the singlet axial charge a_0 gives the contribution $\Delta\Sigma$ of all quarks to the nucleon spin and there is no contribution from the gluon.

In QCD this statement is not generally true. QCD corrections induce a Q^2 dependence which breaks Bjoken scaling. The spin dependent structure function g_1 is thus replaced by a Q^2

dependent form as given in Eq. 2.33. In QCD the first moment Γ_1 of the g_1 is modified by [12]

$$\begin{aligned}\Gamma_1(Q^2)^{\mathrm{p,n}} &= \int_0^1 g_1(x,Q^2)dx \\ &= \frac{1}{12}(\pm a_3 + \frac{1}{\sqrt{3}}a_8)\Delta C_{NS}(Q^2) + \frac{1}{9}a_0(Q^2)\Delta C_S(Q^2). \end{aligned} \tag{2.40}$$

Depending on the chosen factorization scheme, $a_0(Q^2)$ can get a contribution from the polarized gluon. In the Modified-Minimal-Subtraction ($\overline{MS}$) scheme [63], $\Delta C_g(Q^2)$ vanishes such that ΔG does not contribute to the first moment in the QPM. Other choices of the renormalization scheme were suggested by Adler and Bardeen (AB) [64] and by Carlitz, Collins and Mueller [65], called the JET [66] scheme. In these approaches, $\Delta\Sigma$ is independent of Q^2 and $C_g(Q^2)$ is non-zero. Therefore $a_0(Q^2)$ would be modified by an anomalous gluon contribution, which corresponds to the interaction between the singlet axial current of the matrix element and the polarized gluon. It suggests that every polarized quark structure function $\Delta\Sigma$ should be corrected due to an anomalous gluon contribution as follows [67, 68]:

$$\Delta\Sigma^{DIS} = a_0(Q^2) = \Delta\Sigma - n_f\frac{\alpha_s}{2\pi}\Delta G(Q^2), \tag{2.41}$$

where $\Delta\Sigma^{DIS}$ is the measured value from a DIS experiment. It is possible that the bare $\Delta\Sigma$ can vanish for a large contribution ΔG. The interpretation of the $\Delta\Sigma$ cannot be directly obtained from the $a_0(Q^2) = \Delta\Sigma^{DIS}$ without information about $\Delta G(Q^2)$. There are straightforward transformations [69, 70] that relate the schemes and their results to each other. Experiments are now taking data to determine the contribution from gluons to the nucleon spin. A first measurement of the gluon polarization was reported by the E581/704 experiment at Fermilab measuring π^0 production with high transverse momentum p_T: The ΔG is qualitatively not so large [71]. Most recently, COMPASS has announced a new determination via the asymmetry in high p_T hadron-pair production, which yields $\Delta G/G = 0.024 \pm 0.089(\mathrm{stat}) \pm 0.057(\mathrm{syst})$ at an average $\langle x_G\rangle = 0.095$ [72]. However, all measurements of the gluon polarization have still large uncertainties both systematic and statistical. Therefore more additional information about ΔG with greater accuracy is necessary for conclusive statements.

Earlier, inclusive DIS experiments on polarized proton targets have already measured Γ_1 with polarized electrons at SLAC, even though in a restricted kinematic range [73, 74]. The first interesting result for Γ_1 was reported by EMC [6] in inclusive DIS, and subsequently confirmed by a number of other experiments [30, 31, 32, 34, 37, 62]: The quark contribution $\Delta\Sigma$ to the nucleon spin is substantially smaller than expected in the QPM [7]:

$$\begin{aligned}\Delta\Sigma^{DIS} &= \Delta u + \Delta d + \Delta s + \Delta\overline{u} + \Delta\overline{d} + \Delta\overline{s} \\ &= 0.29 \pm 0.06 \qquad \text{at } \langle Q^2\rangle = 5\ (\mathrm{GeV/c})^2. \end{aligned} \tag{2.42}$$

If the exact $SU(3)_f$ flavor symmetry and non-gluon contribution are assumed, the SMC results [7] provide an estimate of different contributions from quark flavors with combined hyperon β decay to the nucleon spin. The SMC analysis used to evaluate Δq based on the Bjorken sum rule [75, 76, 77] with proton, neutron, and deuteron data including QCD radiative corrections:

$$\Delta u = +0.82 \pm 0.02, \qquad \Delta d = -0.43 \pm 0.02, \qquad \Delta s = -0.10 \pm 0.02. \tag{2.43}$$

This result indicates a significant negative contribution of *s* quarks to the proton spin, though the interpretation strongly depends on the gluon contribution ΔG to the nucleon spin. If one considers the most recent QCD analysis from COMPASS data [62], the result is very similar at $\langle Q^2 \rangle$ = 3 (GeV/c)^2:

$$\Delta\Sigma^{DIS} = 0.33 \pm 0.03 \pm 0.05, \qquad \Delta s = -0.08 \pm 0.01 \pm 0.02. \tag{2.44}$$

On the other hand, the HERMES group has presented data on the polarized *s* quark from the analysis of semi-inclusive DIS production, where the flavor decomposition from the struck quark to the final state hadron allows the separation of the spin contributions of the *u*, *d*, *s* quarks and their antiquarks. The polarized *s* quark distribution at Q^2 = 2.5 (GeV/c)^2 is compatible with zero: $\Delta s = +0.03 \pm 0.03 \pm 0.01$ [78]. However, this estimation has been questioned due to the fact that corrections of independent fragmentation like diquark fragmentation seem to be large [79, 80], and a considerable uncertainty still remains in the contribution of the polarized $\bar{s}$ quark.

These two different results lead to the interesting question to which extent the *s* and $\bar{s}$ quarks are polarized inside the nucleon, and how well we understand the spin structure of other baryons. A measurement of Λ polarization will be able to give important answers to these questions and motivate further measurements to disclose *s* and $\bar{s}$ quarks in order to make a step towards solving the nucleon spin puzzle. Furthermore, it will be attempted to understand the relevant interconnections of quarks and gluons for other baryons [9].

2.5 The Spin Structure of Λ

In order to calculate the first moment of Γ_1 and Δq for all members of the spin $1/2$ baryon octet $(p, n, \Sigma^{\pm}, \Sigma^0, \Lambda, \Xi^-, \Xi^0)$, one needs to calculate the matrix elements using the current algebra. Generally, one can use the $SU(3)_f$ flavor symmetry to calculate them in terms of the current operators and baryon state [81]. The current operators of the octet axial-vector can be written as:

$$J^i_\mu = \overline{\psi}\gamma_\mu\gamma_5 \left(\frac{\lambda_i}{2}\right)\psi, \quad i = 0, 1, 2, ...8. \tag{2.45}$$

Here, the ψ is the quark field triplet and the conjugate quark field $\overline{\psi}$ is constructed to find the wave functions of baryon octets:

$$\psi = \begin{pmatrix} u \\ d \\ s \end{pmatrix}, \quad \overline{\psi} = (ud-du, ds-sd, us-su), \tag{2.46}$$

where the baryon states act like a row and column vector under SU(3)$_f$ transformations. λ_i are the generator matrices of the group SU(3)$_f$ in the matrix element. Generators may be taken to be any 3^2 - 1 = 8 linearly independent traceless hermitian matrices as a set of unitary 3×3 matrices. These eight matrices are known as the Gell-Mann matrices. The singlet matrix λ_0, the triplet matrix λ_3, and octet matrix λ_8 are given by

$$\lambda_0 = \begin{pmatrix} 1 & 0 & 0 \\ 0 & 1 & 0 \\ 0 & 0 & 1 \end{pmatrix}, \quad \lambda_3 = \begin{pmatrix} 1 & 0 & 0 \\ 0 & -1 & 0 \\ 0 & 0 & 0 \end{pmatrix}, \quad \lambda_8 = \sqrt{\frac{1}{3}} \begin{pmatrix} 1 & 0 & 0 \\ 0 & 1 & 0 \\ 0 & 0 & -2 \end{pmatrix}. \tag{2.47}$$

The hadronic matrix elements from a_0 to a_8 for a specific baryon with spin S, mass m_B, and momentum P are then calculated [12]

$$\begin{aligned} \langle P,S \,|\, J^0_\mu \,|\, P,S \rangle &= 2M_B S_\mu a_0, \\ \langle P,S \,|\, J^i_\mu \,|\, P,S \rangle &= M_B S_\mu a_i \quad (i = 1,2,...8) \end{aligned} \tag{2.48}$$

with the flavor-singlet axial-vector current and the octet of axial-vector currents, respectively. The axial singlet a_0 corresponds to the expectation value of the z-component of all quark spins in the naive QPM. The baryon matrix B sums up each 3×3 matrix of baryon octet fields [81, 82]. It can be described similarly to the λ_i by the representation of Gell-Mann matrices:

$$B = \sum_{i=1}^{8} B_i \lambda_i = \begin{pmatrix} \Lambda/\sqrt{6} + \Sigma^0/\sqrt{2} & \Sigma^+ & P \\ \Sigma^- & \Lambda/\sqrt{6} - \Sigma^0/\sqrt{2} & N \\ \Xi^- & \Sigma^0 & -2\Lambda/\sqrt{6} \end{pmatrix}. \tag{2.49}$$

The baryon matrix B is not hermitian because charge conjugation of a baryon state leads to an antibaryon state. To build an SU(3)$_f$ invariant of matrices, one has to saturate all the indices by taking traces of the product.

The baryon octets are constructed with each matrix element of the octet axial current for two baryon states B_j and B_k. There is a conventional way to combine three matrices to form an SU(3)$_f$ flavor singlet involving the commutator and anticommutator of two of the matices and defining F and D, such that

$$\langle B_j; P,S \,|\, J^i_\mu \,|\, B_k; P,S \rangle = D\,tr(J^i_\mu \{B_k, \overline{B_j}\}) + F\,tr(J^i_\mu [B_k, \overline{B_j}]). \tag{2.50}$$

Only two permutations are independent combinations, the other permutations are identical since the trace is invariant under cyclic permutations. All the spinors, momentum dependence, and the rest of the matrix elements are contained in D and F. Thus, this enables us to relate the invariants in one matrix element to those in another. From the definition of B_i and J^i_μ, one can see the similarity to the λ-matrices because $B_i \sim \lambda_i$ and $J^i \sim \frac{\lambda_i}{2}$, which leads to

$$\begin{aligned} tr\left(J^i_\mu\{B_k,\overline{B_j}\}\right) &\sim \frac{1}{2}tr\left(\lambda_i\{\lambda_k\lambda_j\}\right) = -if_{ijk}, \\ tr\left(J^i_\mu[B_k,\overline{B_j}]\right) &\sim \frac{1}{2}tr\left(\lambda_i[\lambda_k\lambda_j]\right) = d_{ijk}, \end{aligned} \tag{2.51}$$

where d_{ijk} and f_{ijk} are the usual SU(3) group structure constants. The reason for the names of D and F is that the F coupling is proportional to the structure constant f_{ijk}, which is fully antisymmetric under interchange of any pair of indices, while the D coupling is proportional to the symmetric invariant tensor d_{ijk}. From Eq. 2.50 and Eq. 2.51, one can find

$$\langle B_j;P,S\,|\,J^i_\mu\,|B_k;P,S\rangle = 2M_B S_\mu (D\,d_{ijk} - iF\,f_{ijk}). \tag{2.52}$$

The non-zero elements of the symmetric and antisymmetric structure functions for two baryon expectation values are given in Table 2.2. Experimentally, the F and D have been determined from the hyperon β-decays since the same currents are involved [61]:

$$F = 0.463 \pm 0.008, \qquad D = 0.804 \pm 0.008. \tag{2.53}$$

For the Λ hyperon, the calculation of matrix element is straightforward. The relevant Λ state is $|\Lambda\rangle = |B^8\rangle$, and thus it leads to

$$\begin{aligned} \langle\Lambda|\,J^i_\mu\,|\Lambda\rangle &= M_\Lambda S_\mu (D\,d_{i88} - iF\,f_{i88}) \qquad (i=8), \\ &= M_\Lambda S_\mu (-\frac{2}{\sqrt{3}}D). \end{aligned} \tag{2.54}$$

Since the F terms are disappeared by using the Table 2.2, one obtains an expectation value a_3 and a_8 for the Λ hyperon of

$$a_3 = 0, \qquad a_8 = -\frac{2}{\sqrt{3}}D. \tag{2.55}$$

To calculate Γ_1^Λ one needs to create the axial current representation:

$$\Gamma_1^\Lambda = \frac{1}{2}\left(\frac{4}{9}\Delta u_\Lambda + \frac{1}{9}\Delta d_\Lambda + \frac{1}{9}\Delta s_\Lambda\right) = \frac{1}{12}\left(\frac{4}{3}a_0 + a_3 + \frac{1}{\sqrt{3}}a_8\right). \tag{2.56}$$

Using the calculated expectation values of Eq. 2.55 and the axial singlet $a_0 = \Delta\Sigma$, the first moment of Λ is given by

$$\Gamma_1^\Lambda = \frac{1}{18}(2\Delta\Sigma - D). \tag{2.57}$$

Finally, inverting Eq. 2.39 leads to the polarized quark distribution for the Λ hyperon:

$$\Delta u_\Lambda = \Delta d_\Lambda = \frac{1}{3}(\Delta\Sigma - D)$$
$$\Delta s_\Lambda = \frac{1}{3}(\Delta\Sigma + 2D). \tag{2.58}$$

Table 2.3 summarizes the first moments and the polarized quark distributions for all baryon octets in terms of the D, F, and $\Delta\Sigma$ representation. From the available $\Delta\Sigma$ from DIS experiments and estimated F and D (see Eq. 2.53) all predicted values for the baryon octet can easily be calculated assuming the $SU(3)_f$ flavor symmetry. In the QPM, using spin-flavor symmetric wave functions [83], one also obtains the results for the members of the baryon octet. Both calculated values of first momentum and polarized quark distributions in the SU(3) and the QPM are summarized in Table 2.4.

It is clear that some possible spin crisis for the hyperon can be imagined as for the proton. Hyperon spin structures must be found to test the model predictions from general principles in QCD. But unfortunately the spin structure of the hyperons cannot be measured directly due to the lack of stable hyperon targets. Therefore one has to access the spin structure of the hyperons by using the fragmentation process, in which they are formed as a spin polarimeter for the quarks contained. The study of the Λ and $\overline{\Lambda}$ polarization should lead eventually to a deeper understanding of the spin structure of baryons.

Table 2.1: Definitions of kinematic quantities used in the description of the deep inelastic scattering process.

Beam muon	
$k^\mu = (E, \vec{k})$	Four-momentum of the incident muon
$k'^\mu = (E', \vec{k}')$	Four-momentum of the scattered muon
θ, ϕ	Polar and azimuthal muon scattering angles in the lab system
$s^\mu \overset{Lab.}{=} \frac{1}{m_\mu}\left(\lvert\vec{k}\rvert, \hat{\vec{k}}E\right); \hat{\vec{k}} = \frac{\vec{k}}{\lvert\vec{k}\rvert}$	Spin four-vector of the incident muon in the lab system for longitudinal polarization
Target nucleon	
$P^\mu \overset{Lab.}{=} (M, \vec{0})$	Four-momentum of the target nucleon
$S^\mu \overset{Lab.}{=} (0, \hat{\vec{S}})$	Spin four-vector of the target nucleon
Inclusive DIS	
$\nu = \frac{P_\mu q^\mu}{M} \overset{Lab.}{=} E - E'$	Energy transfer to the target
$y = \frac{P_\mu q^\mu}{P_\mu k^\mu} \overset{Lab.}{=} \frac{\nu}{E}$	Fractional energy transfer of the virtual photon
$q^\mu = k^\mu - k'^\mu = (\nu, \vec{q})$	Four-momentum transfer to the target
$Q^2 = -q_\mu q^\mu \overset{Lab.}{\simeq} 4E\,E'\sin^2\frac{\theta}{2}$	Negative squared invariant mass of the virtual photon
$s = (P^\mu + k^\mu)^2 \overset{Lab.}{=} 2ME + M^2$	Squared center of mass energy
$W^2 = (P^\mu + q^\mu)^2 \overset{Lab.}{=} M^2 + 2M\nu - Q^2$	Squared mass of the hadronic final state
$x = \frac{Q^2}{2P_\mu q^\mu} \overset{Lab.}{=} \frac{Q^2}{2M\nu}$	Bjørken scaling variable
Semi inclusive DIS	
$P_h^\mu = (E_h, \vec{p}_h)$	Four-momentum of a detected final state hadron h
$P_{\lvert\rvert}^* = \vec{P}_h^* \cdot \frac{\vec{q}^*}{\lvert\vec{q}^*\rvert}$	Longitudinal momentum of the hadron h in the $\gamma^* N$ center of mass system
$x_F = \frac{P_{\lvert\rvert}^*}{\lvert\vec{q}^*\rvert} \simeq \frac{2P_{\lvert\rvert}^*}{W}$	Feynman scaling variable
$z = \frac{P_\mu P_h^\mu}{P_\mu q^\mu} \overset{Lab.}{=} \frac{E_h}{\nu}$	Fraction of the virtual photon energy carried by a hadron h

Table 2.2: The non-vanishing completely antisymmetric structure constants f_{ijk} and the symmetric constants d_{ijk}

ijk	123	147	156	246	257	345	367	458	678
f_{ijk}	1	1/2	$-1/2$	1/2	1/2	1/2	$-1/2$	$\sqrt{3}/2$	$\sqrt{3}/2$
ijk	118	146	157	228	247	256	338	344	
d_{ijk}	$1/\sqrt{3}$	1/2	1/2	$1/\sqrt{3}$	$-1/2$	1/2	$1/\sqrt{3}$	1/2	
ijk	355	366	377	448	558	668	778	888	
d_{ijk}	1/2	$-1/2$	$-1/2$	$-1/(2\sqrt{3})$	$-1/(2\sqrt{3})$	$-1/(2\sqrt{3})$	$-1/(2\sqrt{3})$	$-1/\sqrt{3}$	

Table 2.3: First moment of g_1 and polarized quark distribution Δ u, Δ d and Δ s for hadrons of the baryon octet in terms of $\Delta\Sigma$, F, and D using SU(3)$_f$ flavor symmetry.

Baryon	Γ_1	Δu	Δd	Δs
p	$\frac{1}{18}(2\Delta\Sigma+D+3F)$	$\frac{1}{3}(\Delta\Sigma+D+3F)$	$\frac{1}{3}(\Delta\Sigma-2D)$	$\frac{1}{3}(\Delta\Sigma+D-3F)$
n	$\frac{1}{9}(\Delta\Sigma-D)$	$\frac{1}{3}(\Delta\Sigma-2D)$	$\frac{1}{3}(\Delta\Sigma+D+3F)$	$\frac{1}{3}(\Delta\Sigma+D-3F)$
Λ	$\frac{1}{18}(2\Delta\Sigma-D)$	$\frac{1}{3}(\Delta\Sigma-D)$	$\frac{1}{3}(\Delta\Sigma-D)$	$\frac{1}{3}(\Delta\Sigma+2D)$
Σ^+	$\frac{1}{18}(2\Delta\Sigma+D+3F)$	$\frac{1}{3}(\Delta\Sigma+D+3F)$	$\frac{1}{3}(\Delta\Sigma+D-3F)$	$\frac{1}{3}(\Delta\Sigma-2D)$
Σ^0	$\frac{1}{18}(2\Delta\Sigma+D)$	$\frac{1}{3}(\Delta\Sigma+D)$	$\frac{1}{3}(\Delta\Sigma+D)$	$\frac{1}{3}(\Delta\Sigma-2D)$
Σ^-	$\frac{1}{18}(2\Delta\Sigma+D-3F)$	$\frac{1}{3}(\Delta\Sigma+D-3F)$	$\frac{1}{3}(\Delta\Sigma+D+3F)$	$\frac{1}{3}(\Delta\Sigma-2D)$
Ξ^0	$\frac{1}{9}(\Delta\Sigma-D)$	$\frac{1}{3}(\Delta\Sigma-2D)$	$\frac{1}{3}(\Delta\Sigma+D-3F)$	$\frac{1}{3}(\Delta\Sigma+D+3F)$
Ξ^-	$\frac{1}{18}(2\Delta\Sigma+D-3F)$	$\frac{1}{3}(\Delta\Sigma+D-3F)$	$\frac{1}{3}(\Delta\Sigma-2D)$	$\frac{1}{3}(\Delta\Sigma+D+3F)$

Table 2.4: In the SU(3)$_f$ column, the predicted values of Δq are calculated by inserting $\Delta\Sigma = 0.28$, $F = 0.459$, and $D = 0.798$ [84], and the QPM results are obtained by replacing $\Delta\Sigma = 1$, $F = 2/3$, and $D = 1$ [85].

Baryon	Δu		Δd		Δs	
	QPM	SU(3)$_f$	QPM	SU(3)$_f$	QPM	SU(3)$_f$
p	4/3	0.82 ± 0.04	$-1/3$	-0.44 ± 0.04	0	-0.10 ± 0.04
n	$-1/3$	-0.44 ± 0.04	4/3	0.82 ± 0.04	0	-0.10 ± 0.04
Λ	0	-0.17 ± 0.04	0	-0.17 ± 0.04	1	0.62 ± 0.04
Σ^+	4/3	0.82 ± 0.04	0	-0.10 ± 0.04	$-1/3$	-0.44 ± 0.04
Σ^0	2/3	0.36 ± 0.04	2/3	0.36 ± 0.04	$-1/3$	-0.44 ± 0.04
Σ^-	0	-0.10 ± 0.04	4/3	0.82 ± 0.04	$-1/3$	-0.44 ± 0.04
Ξ^0	$-1/3$	-0.44 ± 0.04	0	-0.10 ± 0.04	4/3	0.82 ± 0.04
Ξ^-	0	-0.10 ± 0.04	$-1/3$	-0.44 ± 0.04	4/3	0.82 ± 0.04

Chapter 3

Longitudinal Λ Polarization

3.1 The Λ Hyperon as a Spin Polarimeter

The Λ hyperon is a member of the $J^P = \frac{1}{2}^+$ baryon octet with a mass of m_Λ = 1115.683 MeV/c^2 [14] and strangeness $s = -1$. Its predominant decay channels are two body nonleptonic decays:

$$\begin{aligned} \Lambda &\rightarrow p + \pi^- \quad (BR = 63.9 \pm 0.5\%), \\ \Lambda &\rightarrow n + \pi^0 \quad (BR = 35.8 \pm 0.5\%). \end{aligned} \tag{3.1}$$

The prominent decay of $\Lambda \rightarrow p\pi^-$ (see Fig. 3.1) has been well studied from the experimental point of view, because both charged daughter particles can be easily detected. The lifetime of this decay is (2.632 ± 0.020) × 10^{-10} s (cτ = 7.89 cm), and thus allows to identify the Λ without loosing the signal by too much background. The decay of Λ hyperons shows a strong parity violation. This means that its decay particles with respect to the direction of initial Λ

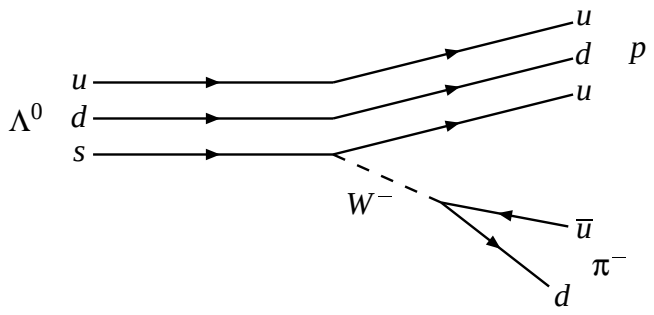

Figure 3.1: Decay of Λ^0 into p and π^- via intermediate W^- Boson in weak interaction.

spin has a large asymmetry in the angular distribution. Since the angular distribution of the decay products reveal the polarization itself, this property is called a self-analyzing decay. This self analyzing property of the Λ makes it particularly interesting for spin physics.

To exploit the angular distributions, one has to move into the Λ rest frame. The coordinate system in this frame is shown in Fig. 3.2, where the z-axis is defined along the Λ spin direction. In the Λ decay, the total angular momentum of the $\Lambda(J^P = \frac{1}{2}^+)$ must be conserved. The quantum numbers of the p and π^- are $J^P = \frac{1}{2}^+$ and $J^P = 0^-$, respectively. Therefore the angular momentum l of the two daughter particles is either $l = 0$ or $l = 1$. If the parity would be conserved, only the p-wave would be allowed due to $P = (-1)^l$. Since the weak decay violates parity, additionally the s-wave contributes to the decay amplitude. Taking into account the Clebsch-Gordan coefficients, one obtains the total wave function for the s-wave and p-wave [86]:

$$\psi_s = a_s Y_0^0 \chi^+, \quad \psi_p = a_p(\sqrt{\frac{2}{3}} Y_1^1 \chi^- - \sqrt{\frac{1}{3}} Y_1^0 \chi^+), \tag{3.2}$$

where a_s and a_p denote the complex amplitude of s-wave and p-wave, Y_m^l are the corresponding spherical harmonics, and $\chi^{\pm}(m_z = \pm\frac{1}{2})$ are the Dirac-spinors, which have two possible spin states of the decay particles with respect to the Λ spin direction. One finally gets the differential angular distribution of the decay particles from the probability, given by

$$\psi\psi^* \propto \frac{dN}{d\cos\theta d\phi} = \frac{N}{4\pi}(1 + \alpha\cos\theta) \quad \text{with } \alpha = -\frac{2Re(a_s a_p^*)}{|a_s|^2 + |a_p|^2}, \tag{3.3}$$

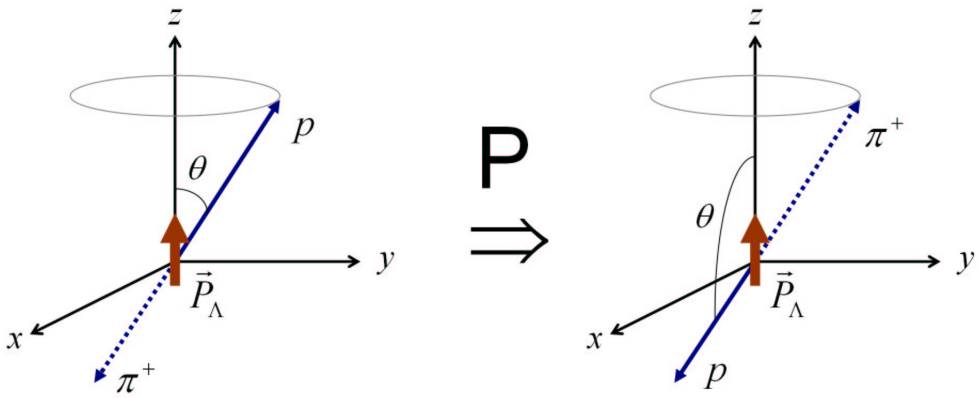

Figure 3.2: The Λ decay process in the Λ rest frame and the effect of the parity operation on the Λ decy: Λ spin direction and momentum vectors of the decay products are given by red and blue arrows, respectively. Due to parity violation the proton prefers to go in the direction of the Λ spin.

being the so-called decay asymmetry parameter. The α can be considered as a measure of the parity violation of the Λ hyperon. Experimentally, α was determined in the reaction $\pi^- p \to \Lambda K^0$. The size of α is found to be $\alpha = 0.642 \pm 0.013$ [14]. θ is the angle between the Λ spin direction and the momentum vector of the outgoing proton in the Λ rest frame. After integration over the azimuthal angle, the normalization constant is $N/2$.

It is easy to see that if the initial spin of the Λ was not exactly along the z-direction, one would write the angular distribution in terms of αP, i.e. including the Λ polarization P:

$$\frac{dN}{d\cos\theta} = \frac{N}{2}(1 + \alpha P \cos\theta), \tag{3.4}$$

where P is the average polarization with respect to the defined quantization axis. The angle θ cannot be defined without a reference axis because the angular distribution should be additionally distorted depending on the initial spin state of the Λ. Thus, one has to choose a well defined quantization axis. There are some choices of the quantization axis with a physical purpose.

If $N^{\uparrow}$ assigns the number of Λs with spin pointing along the quantization axis and $N^{\downarrow}$ the number of Λs with spin pointing in the opposite direction, one can find such a distribution from integration of the angular distribution:

$$\begin{aligned} N^{\uparrow} &= \int_0^1 \frac{N}{2}(1 + \alpha P \cos\theta) d(\cos\theta) = \frac{N}{2}(1 + \frac{\alpha P}{2}), \\ N^{\downarrow} &= \int_{-1}^0 \frac{N}{2}(1 + \alpha P \cos\theta) d(\cos\theta) = \frac{N}{2}(1 - \frac{\alpha P}{2}). \end{aligned} \tag{3.5}$$

Introducing an asymmetry between spin-up state and spin-down state of Λs with respect to the quantization axis, the polarization then can be simplified to [87]

$$\alpha P = 2\left[\frac{N^{\uparrow} - N^{\downarrow}}{N^{\uparrow} + N^{\downarrow}}\right]. \tag{3.6}$$

When the average number of particle spins pointing along the quantization axis is different from zero, this particle is called *polarized*. Additionally, we can obtain the product of αP from a measurement of the number of spin up and down state.

To measure a non-zero polarization, one needs to have both nonzero α and P [88]. For large values of α it is easier to measure the asymmetry of the number of spin-up and spin-down state and hence the Λ polarization. For instance, the decay of $\Sigma^+ \to p\pi^0$ has α near its maximal negative value, making it easy to measure the Σ^+ polarization through its decay mode. On the contrary, the decay of $\Sigma^- \to n\pi^-$ has a small α making it necessary to have a large data sample and good control of systematic errors to get its polarization. In the decay

of $\Xi^- \to \Lambda\pi^-$, information about the spin direction of the Ξ^- is contained in the subsequent Λ decay process. To extract such a Ξ^- polarization, one must use the information from the Λ decay to determine the parent polarization [89].

Table 3.1 is a list of the decay modes, branching ratios, and α parameters for hyperon decays. If one assumes CP invariance, the respective charge-conjugated decay has the opposite sign while the absolute value of the asymmetry parameter for Λ and $\overline{\Lambda}$ will be identical. Hence, their relation is $\alpha_\Lambda = -\alpha_{\overline{\Lambda}}$.

The asymmetry parameter of the Λ hyperon was determined in two different approaches. If one considers the reaction $\pi^- p \to \Lambda K^0$ with unpolarized beam and target, parity conservation in such a strong interaction implies that the Λ hyperon must be polarized with spin transverse to the production plane [86], which is spanned by the two outgoing particles, i.e. $\vec{p}_\Lambda \times \vec{p}_{K^0}$. On the contrary, parity conservation forbids any other polarization of the Λ in the production plane. In this case, one strictly defines the direction of the initial Λ spin transverse to the normal of the production plane and the angular distribution is directly proportional to $1 + \alpha\cos\theta$. Consequently, a measurement of the asymmetry between spin-up state and spin-down state of Λ as in Eq. 3.6 corresponds to a measurement of the asymmetry parameter α. The measured asymmetry parameters of Λ can be found in Refs.[90, 91, 92, 93]. An additional precision in determining α_Λ obtained from the measurement of Ξ polarization in the $K^- p \to \Xi K$ reaction. The decay parameter of the Λ are determined with combining the angular distributions of the $\Xi \to \Lambda\pi$ and subsequent $\Lambda \to p\pi$ decays [94].

Table 3.1: Decay asymmetry parameters of hyperon decay channels [14]. The convention is to use the angular distribution of the decay baryon (i.e. proton for Λ) to determine the polarization.

Hyperon	**Decay channel**	**Branching ratio**	**Asymmetry parameter α**
Λ	$p\pi^-$	63.9 ± 0.5 %	0.642 ± 0.013
Λ	$n\pi^0$	35.8 ± 0.5 %	0.65 ± 0.05
Σ^+	$p\pi^0$	51.57 ± 0.30 %	$-0.980 \pm^{0.017}_{0.015}$
Σ^+	$n\pi^+$	48.31 ± 0.30 %	0.068 ± 0.013
Σ^-	$n\pi^-$	99.848 ± 0.005 %	-0.068 ± 0.008
Ξ^0	$\Lambda\pi^0$	99.522 ± 0.032 %	-0.411 ± 0.022
Ξ^-	$\Lambda\pi^-$	99.887 ± 0.035 %	-0.458 ± 0.012
Ω^-	$\Lambda\pi^-$	67.8 ± 0.7 %	-0.026 ± 0.023
Ω^-	$\Xi^0\pi^-$	23.6 ± 0.7 %	0.09 ± 0.14
Ω^-	$\Xi^-\pi^0$	8.6 ± 0.7 %	0.05 ± 0.21

In practice, the measurement of hyperon polarization is rather difficult due to the fact that the initial spin distribution of the hyperon is not directly accessible. As it was already indicated above, a practical problem is to choose a quantization axis. In the inclusive hyperon production $pN \to HX$ the reference axis is the normal to the production plane, which is spanned by the incoming beam and the outgoing Λ, i.e. $\vec{n}_{trans} \propto \vec{p}_{beam} \times \vec{p}_{\Lambda}$. It is referred to as the transverse Λ polarization.

Spontaneous Λ Polarization

In the middle of 1970's, Λ hyperons produced with 6 GeV polarized protons were found to be polarized [95]. Consecutively, it was discovered that Λ hyperons were also polarized transverse to the production plane in the interaction $pBe \to \Lambda X$ with unpolarized beam and target at Fermilab [96]. They measured a negative polarization of up to $P_T^{\Lambda} = -0.28 \pm 0.08$. This was completely unexpected. The reason is that following the theoretical expectation the spin effects should diminish and finally disappear at high energies because a large number of possible channels contributes to the production cross section with comparable magnitudes. Thus, the polarization in inclusive high energy processes is expected to be small. In contradiction to this, the experimental observation shows that spin effects seems to play an important role even in high energy physics. The observed polarization of hyperons does not depend on the spin states of either beam or target particle and is therefore sometimes called a spontaneous polarization [97].

The polarization effect of an inclusively produced hyperon has been confirmed by many different experiments with various energies of proton beams ranging from 12 GeV at KEK [98] to $\sqrt{s} = 62$ GeV in a collider experiment at CERN [99]. Additionally the polarization for the heavier hyperons have also been observed with similar magnitude. The correct description of spin effects has become a critical test of any theory of hadronic phenomena [100]. Many theories have so far been developed trying to describe the observed polarization effects. In the beginning the idea was that the polarization is primarily a leading particle effect in terms of highly polarized strange quarks. Since only one valence *s* quark needs to be produced for the Λ, whereas for the $\overline{\Lambda}$ all three anti-quarks have to be created, the different polarization between hyperon and antihyperon lies in the source of the *s* quark. However, later measurements of antihyperon destroyed this simple picture [101, 102].

Today there are three classes of dynamical models [103] available for this inclusive production processes in unpolarized high energy hadron-hadron collisions. In the semiclassical picture like the LUND string model, the polarization mechanism is essentially based on a soft process, where perturbative QCD can not be applied any more. When a $s\overline{s}$ pair is produced in the color string field, it is assumed that the *s* quark has a a small transverse momentum which must be compensated by that of the $\overline{s}$ quark. As a result, the $s\overline{s}$ pair has an orbital

angular momentum which induces the Λ polarization. In the recombination model [104], the polarization is explained by Thomas precession with a spin-momentum correlation. To make a Λ from the fragmentation of a target nucleon, one needs to recombine a fast diquark and a slow *s* quark. The effect of Thomas precession arises when the direction of the the recombination force acting on the *s* quark does not coincide with the direction of its motion. The Λ polarization in this model is essentially kinematic and is sensitive to the quark spin rotation. These two models provide simple classical arguments for a qualitative description of hyperon polarization. However, they are unable to make quantitative predictions and fail to explain the antihyperon polarization. In the Regge type models, the Λ production is described by a reggeized meson exchange in hadronic amplitudes. It was proposed that the hadron fragmentation is well described by the Regge trajectory. These theoretical approaches attempt to explain the mechanism of the hyperon polarization. This model has some predictive power, but that contain several key assumptions, which make it not fully convincing. Moreover, it seems to be difficult to extend the approach for hyperon production to other reactions. Reviews of both the experimental and theoretical situation are available in Refs. [103, 105, 106].

A recent phenomenological approach is based on the perturbative QCD factorization schemes. The main idea of M. Anselmino et al. [107] is to use new polarized fragmentation functions which include intrinsic k_T to describe the fragmentation process of an unpolarized quark into a polarized hyperon. A similar approach based on polarized fragmentation function was also presented by D. Hui et al. [108] with numerical calculations. These models describe the qualitative features of all experimental data for $pN \to \Lambda X$ correctly, but do not predict the $\overline{\Lambda}$ polarization. The parametrization of polarized fragmentation functions in this model can also be used to make consistent predictions for the reaction $lN \to l'HX$ [109]. This provides the opportunity to test the universal properties of the hyperon polarization. However, appropriate kinematic regions need to be detected, where perturbative QCD can be used, in order to be able to compare the data with predictions. All of these efforts give an intuitive picture of the hyperon polarization. However, there is still no conclusive theory to include all facts.

COMPASS can also measure the spontaneous transverse polarization of Λ hyperons produced in quasi-real photoproduction. The spontaneous Λ polarization with lepton beams should allow to give information about the various contributions to the Λ polarization coming from the dynamics of the elementary partonic processes.

3.2 Λ Production in Semi-Inclusive DIS

The idea of using Λ and $\overline{\Lambda}$ as a spin polarimeter of quarks in semi-inclusive DIS reaction was originally proposed by F. Baldracchini et al. in 1981 [110]. The main idea is a spin transfer reaction, which transfers the spin from the transversely polarized nucleon to the final

state Λ hyperon. Using the longitudinally polarized beam and target one can extend the measurement to the longitudinal Λ spin transfer via Λ polarization pointing along the virtual photon direction. A first theoretical study of the longitudinal Λ polarization to investigate the spin transfer mechanism from an unpolarized quark to a Λ was suggested by I. Bigi [111], and later pointed out by X. Artru and M. Mekhfi [112]. Theoretical and experimental approaches concerning the longitudinal Λ polarization in the semi-inclusive DIS will be discussed in the following section.

3.2.1 Fragmentation in Semi-Inclusive DIS

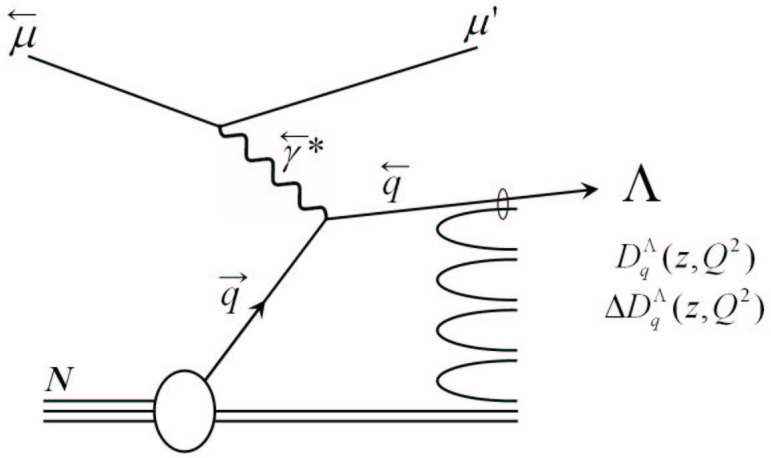

Figure 3.3: Λ production in semi-inclusive DIS process. The struck quark q hadronizes into a Λ. The produced Λ is described by the unpolarized $D_q^\Lambda(z,Q^2)$ and polarized $\Delta D_q^\Lambda(z,Q^2)$ fragmentation functions.

An insight into the contributions of the individual quark flavors to the spin of a hadron may be obtained from the analysis of polarized semi-inclusive DIS, where at least one hadron of the final state X is detected in coincidence with the scattered muon. Fig. 3.3 shows an illustration of the Λ production in semi-inclusive DIS. Hadrons are produced by the scattering of a virtual photon γ^* off either a sea quark or a valence quark. As indicated by the arrows, a beam of negative helicity emits a polarized γ^*. For reasons of helicity conservation the γ^* can only scatter off a quark q with opposite helicity. This fixes the spin orientation of the struck quark, i.e. the outgoing quark has the same helicity as γ^*. The struck quark has to pick up either an antiquark or at least two more quarks in order to form a color-singlet final state (a meson or baryon). The hadron has a fractional energy $z = \frac{E_h}{\nu}$ of the virtual photon. This process of forming an observable hadron from a struck quark or target remnant is known as the fragmentation or also hadronization. It cannot be described in perturbative QCD due to

the confinement properties of this theory [13] and because long-range interactions between the struck quark and the target remnant are involved. When the stuck quark and diquark move apart, the coupling constant becomes large, and thus prohibits a perturbative expansion in powers of α_s. Therefore it is a non-perturbative QCD process.

Despite this fundamental problem encountered in the calculation of fragmentation functions, there are theoretical models to deal with the fragmentation process. QCD supports the idea of factorization in a theoretical framework, which is valid in the Bjorken limit. One can separate the hard scattering process, which can be treated with perturbative methods, from the fragmentation process. Since the fragmentation into the hadronic final state is independent of the absorption of the virtual photon by the quark. To describe the fragmentation of quarks into hadrons, one uses an analogous treatment to the one introduced in Section 2.3 to describe the quark distribution functions inside the nucleon.

Symbolically, the cross section for the semi-inclusive DIS process can be seen as a convolution of three sub-processes:

$$\sigma = \text{Quark distribution} \otimes \text{Hard scattering} \otimes \text{Fragmentation}. \tag{3.7}$$

The differential cross section for the semi-inclusive DIS can be written as

$$\frac{d\sigma}{dxdzdQ^2} = \frac{d\sigma_{incl}}{dxdQ^2} \frac{\sum_q e_q^2 q(x,Q^2) D_q^h(z,Q^2)}{\sum_q e_q^2 q(x,Q^2)}, \tag{3.8}$$

where σ_{incl} is the inclusive DIS cross section (see Eq.2.19) and the sum runs over all allowed quarks and antiquarks for both the quark distribution and fragmentation functions. The fragmentation functions $D_q^h(z,Q^2)$ are the probabilities to find a quark to fragment into a hadron at momentum scale Q^2 and with energy fraction z. The fragmentation functions are normalized to conserve the energy and total average hadron multiplicity:

$$\begin{aligned} \sum_h \int_0^1 z D_q^h(z,Q^2) dz &= 1, \\ \sum_h \int_{z_0}^1 D_q^h(z,Q^2) dz &= < n_h(Q^2) >, \end{aligned} \tag{3.9}$$

where z_0 is the threshold energy for producing a hadron of mass m with a minimum multiplicity. It is assumed that the fragmentation functions also depend on W^2 since the experiment shows that the multiplicity of the final state hadron usually rises logarithmically with W^2 [113].

For a non-zero spin final state hadron, one usually separates the fragmentation functions into a combination of polarized and unpolarized fragmentation functions. If one defines the

probability for a quark q with a given helicity to fragment into a hadron with the same helicity ($\uparrow\uparrow$) or opposite helicity ($\uparrow\downarrow$), the unpolarized and polarized fragmentation for single hadron production can be expressed in the form:

$$\begin{aligned} D_q^h(z) &= D_{q\uparrow\uparrow}^h + D_{q\uparrow\downarrow}^h, \\ \Delta D_q^h(z) &= D_{q\uparrow\uparrow}^h - D_{q\uparrow\downarrow}^h. \end{aligned} \tag{3.10}$$

A requirement for the spin dependent fragmentation functions in Eq. 3.10 is that the polarized fragmentation functions are constrained by the unpolarized fragmentation functions:

$$|\Delta D_q^h(z)| \leq D_q^h(z). \tag{3.11}$$

An ansatz satisfying this condition is

$$\Delta D_q^h(z) = C_q^h \cdot D_q^h(z) \tag{3.12}$$

with coefficients C_q^h, which can be used to make theoritical predictions for the polarized fragmentation functions [114].

For Λ production, there are formally 6 quarks and 6 anti-quarks leading to 12 possible quark fragmentation functions. If one neglects contributions from heavy flavors, and uses SU(3) flavor symmetry, two independent fragmentation functions remain:

$$\begin{aligned} \Delta D_u^\Lambda(z) &= \Delta D_{\bar{d}}^\Lambda(z) = \Delta D_s^\Lambda(z) \quad \text{favored}, \\ \Delta D_{\bar{u}}^\Lambda(z) &= \Delta D_d^\Lambda(z) = \Delta D_{\bar{s}}^\Lambda(z) \quad \text{unfavored}. \end{aligned} \tag{3.13}$$

In general the favored fragmentation functions are more probable than the unfavored, as the observation in semi-inclusive measurement shows that $\Delta D_{\text{favored}} > \Delta D_{\text{unfavored}}$. Thus one can neglect unfavored fragmentation functions as they are usually suppressed.

3.2.2 Fragmentation in e^+e^- Annihilation

The factorization theorem of QCD implies another feature of the fragmentation function. It demands that the fragmentation process is universal no matter whether the hadronization process was determined by a DIS measurement or by a $q\bar{q}$ pair production in e^+e^- annihilation. Thus the measurement of the e^+e^- annihilation into a Λ hyperon plays a role as fundamental as the one of the corresponding crossed semi-inclusive DIS process. Here, the underlying $e^+e^- \to Z^0, \gamma^* \to q\bar{q}$ scattering cross section can be calculated in the electroweak theory. In this theory quarks produced at the Z^0 pole are naturally polarized because the coupling to fermions violates parity and favors certain helicity states. This implies that not even beam polarization is required since the parity-violating Z^0 coupling automatically generates a net polarization of the quarks.

An analytical expression for the cross section of a semi-inclusive process $e^+e^- \to \Lambda + X$ can be given when focusing on the fragmentation part $\sigma \propto \sum_q D_q^\Lambda(z,Q^2)$ only. All calculable quantities of the cross section are obtained by summing over the fragmentation functions from all possible quarks and antiquarks of any flavor. Hence, the extraction of the polarized fragmentation functions $\Delta D_q^\Lambda(z,Q^2)$ is relatively straightforward for e^+e^- experiment. Moreover, flavor tagging in e^+e^- annihilation is much easier to be accomplished than in polarized DIS. The ALEPH and OPAL collaborations at the LEP Collider of CERN have reported results of Λ polarization in semi-inclusive e^+e^- annihilation. Their results are discussed in Section 3.4. More detailed theoretical discussions about the QCD expression of the fragmentation functions for e^+e^- annihilation can be found in Refs. [85, 115].

3.2.3 Connection between Fragmentation and Parton Functions

The quark distribution function $q(x,Q^2)$ and the quark fragmentation function $D_q^h(z,Q^2)$ are two fundamental quantities to describe the structure of hadron. It would be obviously convenient to have a relation between those two functions. If simple connections exist between them in a specified physical region, then one can exploit the accurate information to predict the quark distribution function of a final state hadron by measuring the fragmentation functions. Such a relation has been used as a helpful ansatz to model the quark fragmentation functions based on predictions of quark distributions functions, such that one can predict the poorly known $D_q^h(z,Q^2)$ with the help of the rather well known $q(x,Q^2)$.

As a matter of fact, a relation connecting the structure functions of quarks and the fragmentation is given in Refs. [116, 117]. It is the so-called Gribov-Lipatov reciprocity relation. V. Gribov and L. Lipatov proved in their classical paper [118] that the nonsinglet splitting functions for DIS and e^+e^- annihilation are equal in leading order calculation. It was necessary to check the validity of these theoretical arguments by means of phenomenological studies. It turned out that the structure functions predicted by the traditional Gribov-Lipatov relation are below the data in e^+e^- annihilation. Thus the idea was not supported by phenomenological evidence [116]. Recently, a revised form of the Gribov-Lipatov relation [117] has been suggested as an approximate relation in the large z limit,

$$\frac{1}{z}D_q^h(z) = q(2-\frac{1}{z}). \tag{3.14}$$

By adopting the known parameterizations of parton distributions from the data of DIS experiments on the nucleon, it was possible to predict the fragmentation functions and provide a comparison to the available experimental data on the nucleon production in e^+e^- annihilation. With distinction between the valence and sea quarks, the prediction using this phenomenological ansatz was found to be compatible with data. Parameterizations support the validity of the revised Gribov-Lipatov relation.

It is quite interesting to note that an immediate application can be derived from this for Λ

production in DIS. Such a relation can provide a successful description of the quark distributions of the Λ based on the available Λ polarization data. The fragmentation function of the Λ is expected to be related to the spin structure of the Λ hyperon at $z \to 1$ at an input energy scale Q^2.

3.3 Theoretical Models of Longitudinal Λ Polarization

In the case of a longitudinally polarized lepton beam and a longitudinally polarized nucleon target as given for the COMPASS experiment, there are two potential sources of Λ polarization. Either the polarization is induced by interaction with the polarized beam or it comes from the polarized quark in the target nucleon.

The complete expression describing spin-1/2 baryon production for longitudinal and transverse polarization at tree level in semi-inclusive DIS can be found in Ref. [119]. In this thesis the leading order prediction integrated over the intrinsic transverse momentum of quark is considered for the Λ production in a DIS process. In this approximation the Λ polarization is given as an asymmetry of cross sections:

$$\begin{aligned} P_\Lambda(x,y,z) &= \frac{d\sigma^{\overrightarrow{l}\overrightarrow{N}\to l'\overrightarrow{\Lambda}X} - d\sigma^{\overrightarrow{l}\overrightarrow{N}\to l'\overleftarrow{\Lambda}X}}{d\sigma^{\overrightarrow{l}\overrightarrow{N}\to l'\overrightarrow{\Lambda}X} + d\sigma^{\overrightarrow{l}\overrightarrow{N}\to l'\overleftarrow{\Lambda}X}} \\ &= \frac{\sum_q e_q^2 \left[P_B D(y)\, q(x) + P_T\, \Delta q(x)\right] \Delta D_q^\Lambda(z)}{\sum_q e_q^2 \left[q(x) + P_B D(y)\, P_T\, \Delta q(x)\right] D_q^\Lambda(z)}, \end{aligned} \tag{3.15}$$

where the Λ is polarized parallel or antiparallel along the muon and nucleon spin direction. e_q is the charge of the quark, P_B and P_T are the beam and target longitudinal polarizations, $q(x)$ and $\Delta q(x)$ are the unpolarized and polarized quark distribution functions of the nucleon, and $D_q^\Lambda(x)$ and $\Delta D_q^\Lambda(x)$ are the unpolarized and polarized fragmentation functions, respectively. Note the nonlinear dependence of the Λ polarization on the beam and target polarization in Eq. 3.15. $D(y)$ is commonly referred to as the longitudinal depolarization factor of the virtual photon with respect to the incident lepton:

$$D(y) = \frac{1-(1-y)^2}{1+(1-y)^2}, \tag{3.16}$$

where y is the energy fraction of the incident lepton carried by the virtual photon. In the special case of using an unpolarized target [120], the expression of Eq. 3.15 can be simplified to

$$P_\Lambda(x,y,z) = P_B D(y) \cdot \frac{\sum_q e_q^2\, q(x)\, \Delta D_q^\Lambda(z)}{\sum_q e_q^2\, q(x)\, D_q^\Lambda(z)}, \tag{3.17}$$

since the terms P_T are absent. The factor $P_B D(y)$ depends on the experimental conditions. Typically this value is about 0.42 in the case of the COMPASS experiment, so that the Λ polarization becomes rather large.

In order to compare the results with those from different measurements of the Λ polarization, it is useful to introduce a quantity which is known as the longitudinal spin transfer coefficient:

$$C^{\Lambda}_{LL'}(x,z) = \frac{P_\Lambda}{P_B D(y)} = \frac{\sum_q e_q^2 q(x) \Delta D_q^\Lambda(z)}{\sum_q e_q^2 q(x) D_q^\Lambda(z)}, \tag{3.18}$$

where L is the primary quantization axis, that is directed along the virtual photon momentum. The spin transfer coefficient $C^{\Lambda}_{LL'}(x,z)$ describes the probability that the polarization of the struck quark is transferred to the Λ hyperon along the quantization axis L'. In principle, the spin transfer can be studied experimentally for any direction with an angle to the defined axis L'. For the longitudinal spin transfer, the direction of the virtual photon momentum is defined as the quantization axis L' ($C^{\Lambda}_{LL'}(x,z) = C^{\Lambda}_{LL}(x,z)$). Another choice of the spin quantization axis L' has been studied to prove their compatibility in Section 5.6.7.

Assuming isospin symmetry $D_u^\Lambda = D_d^\Lambda$ and $\Delta D_u^\Lambda = \Delta D_d^\Lambda$, and neglecting the unfavored functions originating from the sea quarks in both quark distribution and fragmentation functions, one obtains an approximation for the spin transfer $C^{\Lambda}_{LL}(x,z)$ from Eq. 3.18:

$$C^{\Lambda}_{LL}(x,z) \approx \frac{(4u+d)\,\Delta D_u^\Lambda(z) + s\,\Delta D_s^\Lambda(z)}{(4u+d)\,D_u^\Lambda(z) + s\,D_s^\Lambda(z)}. \tag{3.19}$$

A similar expression also holds for the $\overline{\Lambda}$ with some additional terms, which come from nonleading contributions. Since contributions from the sea quarks cannot simply be suppressed in the $\overline{\Lambda}$ case, it is not easy to find approximate expressions for $C^{\overline{\Lambda}}_{LL}(x,z)$. If isospin symmetry is applied here as well, the spin transfer $C^{\overline{\Lambda}}_{LL}(x,z)$ can be expressed by [109]

$$C^{\overline{\Lambda}}_{LL}(x,z) \approx \frac{(4\overline{u}+\overline{d})\,\Delta D_{\overline{u}}^{\overline{\Lambda}}(z) + \overline{s}\,\Delta D_{\overline{s}}^{\overline{\Lambda}}(z) + (4u+d)\,\Delta D_{\overline{u}}^{\overline{\Lambda}}(z) + s\,\Delta D_{\overline{s}}^{\overline{\Lambda}}(z)}{(4\overline{u}+\overline{d})\,D_{\overline{u}}^{\overline{\Lambda}}(z) + \overline{s}\,D_{\overline{s}}^{\overline{\Lambda}}(z) + (4u+d)\,D_{\overline{u}}^{\overline{\Lambda}}(z) + s\,D_{\overline{s}}^{\overline{\Lambda}}(z)}. \tag{3.20}$$

Note that contrary to the case of Λ, the leading and nonleading contributions are a mixture of quark distributions and fragmentation functions with terms of the form $q\Delta D_{\overline{q}}^{\overline{\Lambda}}$ and $\overline{q}\Delta D_{\overline{q}}^{\overline{\Lambda}}$. Therefore the kinematic dependence of the spin transfer for $\overline{\Lambda}$ have to be handled with more care. The difference of spin transfer for $\overline{\Lambda}$ and Λ considering the spin transfer can simply be seen from the comparison of Eq. 3.20 with Eq. 3.19.

The spin transfer of Λ mainly depends on the ratio of the polarized and unpolarized fragmentation function. After integrating over x_{Bj} in the quark distribution, Eq. 3.18 leads to a remarkably simple expression, which gives direct access to the polarized fragmentation functions:

$$C^{\Lambda}_{LL}(z) \approx \frac{\Delta D_q^\Lambda(z)}{D_q^\Lambda(z)}, \tag{3.21}$$

which has already been assumed as C_q^h in Eq. 3.12. The basic assumption is that the Λ polarization in the COMPASS experiment arises due to the fragmentation of an unpolarized quark. Despite simplifying assumptions that have been made in deriving Eq. 3.21, it is a useful starting point for developing a qualitative understanding of $C_{LL}^{\Lambda}(z)$. This relation provides the base to study the properties of the polarized fragmentation functions by utilizing the longitudinal Λ polarization. From the Gribov-Lipatov relation as mentioned in Section 3.2.3, one can further relate the quark fragmentation function of the Λ to the corresponding quark distribution for the Λ in case of $z \to 1$.

All hyperons are polarized in proton-proton interactions. In the same way, one would expect the hyperons to be polarized in DIS as well. A contribution to the Λ polarization comes from the decay of possibly polarized heavier hyperons. If a Λ is produced from such a hyperon decay, its polarization will reflect that of its parent particle. When the polarized heavier hyperon decays into a Λ, its polarization can be transferred to the Λ. The most prominent candidates are summarized in Table 3.2 in case of the QPM. The Σ^* and Ξ^* cannot be derived from the proton spin structure through the $SU(3)_f$ rotation because they are not members of the baryon octet. To obtain values of P_{Ξ^*}, it is assumed that P_{Ξ^*} and P_{Ξ^0} are the same. Such as Ω^-, J/ψ and Λ_c decay channels are assumed to be very small to the Λ production in COMPASS kinematic, and thus they can be neglected. In principle, the contribution of Σ^0 could be excluded from direct Λ events by vetoing events with detection of a photon in the ECAL detector, but technically it could not be dealt with. Alternatively, the fraction of the heavier hyperon decays is estimated with a Monte Carlo simulation. However, theoretical approaches for the contribution of the heavier hyperons show a strong model dependence since there are quite different expectation values of the polarized quark distribution for heavy baryons according to $SU(3)_f$ or QPM scheme.

Table 3.2: Contributions of hyperon decays to the Λ polarization. Ξ is indicated for both the Ξ^- and Ξ^0. The data are taken from Ref. [114].

Decay channel	Branching ratio	Resulting P_Λ	interaction
$\Sigma^0 \to \Lambda\,\gamma$	∼100%	$-\frac{1}{3}P_{\Sigma^0}$	Electroweak
$\Sigma^*(1385) \to \Lambda\,\pi$	∼88%	$P_{\Sigma(1385)}$	Strong
$\Xi \to \Lambda\,\pi$	∼99%	$\sim 0.9 P_{\Xi}$	Weak
$\Xi^*(1530) \to \Xi\pi \to \Lambda\,\pi\,\pi$	∼100%	$\sim 0.9 P_{\Xi^*(1530)}$	Weak

3.3.1 The Current Fragmentation Region

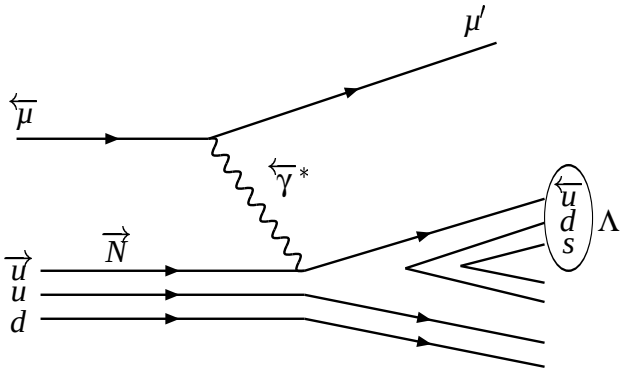

Figure 3.4: Λ production in the current fragmentation region: a negatively polarized γ^* is absorbed by a *u* quark in the target nucleon with a spin direction opposite to that of γ^*. The Λ consists of the scattered *u* quark and additional components of *d* and *s* quark from the fragmentation process.

The Λ production in semi-inclusive DIS can be distinguished in two different kinematic regions, which are characterized by the Feynman scaling variable x_F:

$$x_F = \frac{2P_*^{\parallel}}{W}, \tag{3.22}$$

where $P_*^{\parallel}$ is the longitudinal component of the hadron momentum in the $\gamma^* N$ center-of-mass system. If the x_F variable is negative, the region is called the target fragmentation region. The hadron is then in the backward hemisphere of the $\gamma^* N$ rest frame. In the target fragmentation region, hadrons consist of the debris of the target. On the other hand, the kinematic domain $x_F > 0$ corresponds to the so-called current fragmentation region. Selected are only particles moving forward in the $\gamma^* N$ rest frame. For the requirement $x_F > 0$, the remnant target contribution is assumed to be small and it is more probable that the hadron contains the struck quark. To detect events of the struck quark, it is necessary to select a hadron with a high enough x_F. Strictly speaking, the notion of quark fragmentation has only a meaning in the current fragmentation. A production mechanism of Λ in the current fragmentation region is shown in Fig. 3.4.

The underlying dynamics of hyperon production and its polarization in the fragmentation process cannot be described by perturbative QCD, Therefore some phenomenological approach has to be considered. Various assumptions are included in the different models describing the

Λ polarization and the spin transfer in the current fragmentation region for the general case of Eq. 3.15. The following subsections introduce the theoretical approaches for the longitudinal Λ polarization and spin transfer in the current fragmentation region.

Quark Parton Model

The most simple model is the QPM, which is based on the spin-flavor SU(6) wave functions. It assumes that a Λ is composed of three non-interacting quarks with zero orbital angular momentum, and that the spin of the Λ comes entirely from the constituent quarks. The spin of the Λ is completely carried by the *s* quark and the spin contribution from the *u* and *d* quarks to the Λ are equal to zero, i.e. $\Delta s^{\Lambda} = 1$, $\Delta u^{\Lambda} = \Delta d^{\Lambda} = 0$. This means that if the Λ is produced in the fragmentation of *u* and *d* quarks, one expects that $P_{\Lambda} \sim 0$. Therefore, the polarization of a directly produced Λ is determined by the polarization of the *s* quark, while the *ud* pair is assumed to be a spinless singlet state in the fragmentation. It is also possible to extend the calculation of the spin transfer to heavier hyperons. The contributions from heavier hyperons were taken into account in the model by I. Bigi, G. Gustafson and J. Häkkinen (BGH) [114]. In this simple approach, the spin transfer for each individual quark is independent of the kinematic variable *z*, but due to the contributions from the decay of heavier hyperons, the spin transfer shows a slight *z* dependence.

Model predictions for the Λ polarization is mostly obtained by means of a Monte Carlo simulation. A. Kotzinian et al. [121] have predicted the Λ polarization on the basis on the BGH model with Monte Carlo simulation. The calculation of the polarization has been performed in different experimental conditions for the COMPASS experiment. In the current fragmentation at $z > 0.2$, the polarization is expected to be about -12% for Λ. For $\overline{\Lambda}$ negative values of -15% have been predicted in the considered scheme. In this work, an important effect of the target polarization on the Λ polarization is presented. The difference ΔP_{Λ} of the Λ polarizations for parallel and anti-parallel target polarization in reference to the beam, namely $\Delta P_{\Lambda} = P_{\Lambda}^{\uparrow\uparrow} - P_{\Lambda}^{\uparrow\downarrow}$, is predicted as a function of the kinematic variables x_{Bj} and *z*. This approach leads to a similar prediction for ΔP_{Λ} and $\Delta P_{\overline{\Lambda}}$ within a few percent. The signs of ΔP_{Λ} and $\Delta P_{\overline{\Lambda}}$ are negative. However, the predictions are slightly different for Λ and $\overline{\Lambda}$ produced at high x_{Bj} since the contributions of quark flavors are different. A validation of these models may be possible in COMPASS conditions with a longitudinally polarized muon beam and a longitudinally polarized ^{6}LiD target.

SU(3)$_f$ Symmetry Model

A more sophisticated method for calculating the Λ spin transfer is to use SU(3)$_f$ symmetry together with experimental results for the proton. It was assumed that the spin transfer from

a polarized quark q to a polarized Λ is proportional to the Λ spin carried by that flavor, i.e. to g_1^Λ, which is defined in analogy to the polarized quark distribution functions of the Λ as given in Eq. 2.56. The prediction of the Λ spin transfer with SU(3)$_f$ symmetry was studied first by M. Burkardt and R. Jaffe (BJ) [122], who assumed that the spin crisis exists not only for the nucleon, but also for other octet baryons. They used the proton data of the EMC analysis [6] to decompose the first momentum of g_1^Λ and took into account the hadronic matrix elements. A value of $\Gamma_1^\Lambda = -0.042 \pm 0.019$ was obtained and its Δu, Δd, and Δs contributions to the Λ spin were also separately estimated. The values of Δq obtained by this approach are given in Table 3.3. Later on, this model was updated by Jaffe [120] with proton data of the SMC experiment and various additional assumptions.

A prediction of Λ polarization based on the BJ model was made by A. Kotzinian et al. [121] for different experiments. In the most simple one (BJ I) only the valence quarks contribute to the Λ spin, whereas in the more advanced model (BJ II) also contributions from the sea quarks and antiquarks are considered. The estimated spin transfer from quark to Λ varied from -20% to -14% for u and d quark and the contribution of s quarks to the Λ spin transfer is about 60% and 66% in the BJ I and BJ II, respectively. According to this estimation, Λ and $\overline{\Lambda}$ polarization are predicted to be as small as -5%, and thus much smaller than suggested in the BGH model mainly due to the different values in the spin transfer from u or d quarks. No significant differences between Λ and $\overline{\Lambda}$ were expected in the current fragmentation. In the BJ I and BJ II model, the spins of the u and d quarks and antiquarks are directed opposite to the spin of the Λ hyperons. Since polarized s quarks are relatively rare in the nucleon and their squared charge is only 1/9, while polarized u quarks are abundant and their squared charge is 4/9, the u quark make the dominant contribution to the Λ spin even though they have a small value of polarization. Jaffe pointed out that for HERMES and COMPASS kinematics the Λ polarization should be dominated by the u quark [120], and hence a polarization points to a non-zero polarized u quark fragmentation.

The SU(3)$_f$ symmetry model was modified by D. Ashery and H. Lipkin with proton data of the SLAC experiment in Ref. [123], so that the valence quarks and sea quarks contribute separately to the Λ. In this model the sea quarks in the proton is assumed to SU(3)$_f$ singlets and to be not polarized. The contribution from the sea quarks was subtracted from the total Δq, leaving the valence quarks only. The values of Δq for valence quarks are used for calculating the Λ spin transfer produced in the fragmentation. The dependence of the Λ spin transfer on x_F were shown using Monte Carlo simulation within the kinematic of the E665 experiment. The results presented by Ashery-Lipkin are compared with this analysis in Section 6.1.3.

If such an SU(3)$_f$ symmetry is applied to the Λ with recent semi-inclusive HERMES data [78], values favoring a much smaller polarization of the s quark are obtained instead. The unpolarized and polarized quark distribution functions have also been calculated using a non-perturbative lattice simulation for the Λ. Lattice QCD analysis [125] finds small u and d

Table 3.3: Comparison of estimations for the polarized quark distribution of the Λ based on the QPM, different SU(3)$_f$, and lattice QCD.

Model	$\Delta u_\Lambda = \Delta d_\Lambda$	Δs_Λ
Quark Parton model [114]	0	1
SU(3)$_f$ BJ [122]	-0.23 $\pm$ 0.06	+0.58 $\pm$ 0.07
SU(3)$_f$ BJ I [120]	-0.20 $\pm$ 0.03	+0.60 $\pm$ 0.04
SU(3)$_f$ BJ II [120]	-0.14 $\pm$ 0.03	+0.66 $\pm$ 0.04
SU(3)$_f$ Ashery-Lipkin [123]	-0.07 $\pm$ 0.04	+0.73 $\pm$ 0.04
SU(3)$_f$ Semi-Inclusive [124]	-0.09 $\pm$ 0.04	+0.47 $\pm$ 0.04
Lattice QCD [125]	-0.02 $\pm$ 0.04	+0.68 $\pm$ 0.04

quark polarizations and high s quark polarization. The results of Lattice QCD indicate that the flavor symmetry breaking has just a little effect on the internal spin structure.

SU(3)$_f$ Symmetry Breaking Model

It is known experimentally that the SU(3)$_f$ symmetry is broken for the sea quark in the nucleon. The Chicago-Columbia-Fermilab-Rochester (CCFR) [126] collaboration presented the asymmetry for the s quark and light quarks in the nucleon in the NLO-QCD analysis of neutrino charm production. The s quark is suppressed by a factor of two compared to that of the non-s quarks. Furthermore, an evidence of asymmetry for the s and $\overline{s}$ quark distribution was found. It could be more than twice one of the light quark distribution at small x_{Bj}. The baryon-meson fluctuation model [127, 128] also suggested the same behavior of $s < \overline{s}$ at small x_{Bj}. Another phenomenological support for $s \neq \overline{s}$ was provided by a global QCD analysis of structure functions [129]. More recently, the constraints on the s and $\overline{s}$ quark distributions have been reconsidered using dimuon data from the NuTeV collaboration. They have shown that the asymmetry of s and $\overline{s}$ lies in a small range from -0.001 to $+0.004$ integrating over the measured x_{Bj} region. However, the functional behavior is clearly varying in the different x_{Bj} regions [130]. Although the size of the asymmetry of s and $\overline{s}$ is still quite uncertain, it was suggested to be that the asymmetry of quark distributions may produce an observable contribution to the different behaviors of Λ and $\overline{\Lambda}$ polarization [131, 132].

The possible asymmetry for quark distributions in the nucleon have been intensively studied by B. Ma et al. [132]. Not only did they consider an asymmetry of s and $\overline{s}$ but also another case with an additional contribution of $\overline{d} > d$ in the target nucleon. They used the Monte Carlo parameterizations as input for the quark distributions of the nucleon and found that the different behaviors of Λ and $\overline{\Lambda}$ could be explained due to the quark-antiquark asymmetries

in the nucleon sea, although there is a strong model-dependence for quark distributions in this interpretation. Fig. 3.5 shows the calculated results for the spin transfer of Λ and $\overline{\Lambda}$ using different sets of the quark distribution. The asymmetry of quark and antiquark distribution in the nucleon plays an important role in these plots. However, it needs to be mentioned that there is an alternative explanation for the different behavior of the spin transfer for the Λ and $\overline{\Lambda}$. The quark and antiquark fragmentation functions could also be a source for the differences in the spin transfer of Λ and $\overline{\Lambda}$. Due to large uncertainties in the data, it is still too early to arrive at some definite conclusion. To clearly distinguish the quark-antiquark asymmetry, whether in the fragmentation functions or in the quark and antiquark distribution functions of the target nucleon, further experimental efforts are needed.

Quark Diquark Model

A model by J. Ellis, A. Kotzinian, and D. Naumov [133, 134] was suggested using Monte Carlo simulation in the QPM and SU(3)$_f$ scheme. A key assumption in this approach is that the beam energies in current experiments on the Λ polarization are not high enough for the current fragmentation to be populated by $q \to \Lambda$ fragmentation only. Therefore this model takes into account that Λ is also originating from the remnant diquark fragmentation even in the current fragmentation region. In this approach, the hyperon may inherit the polarization

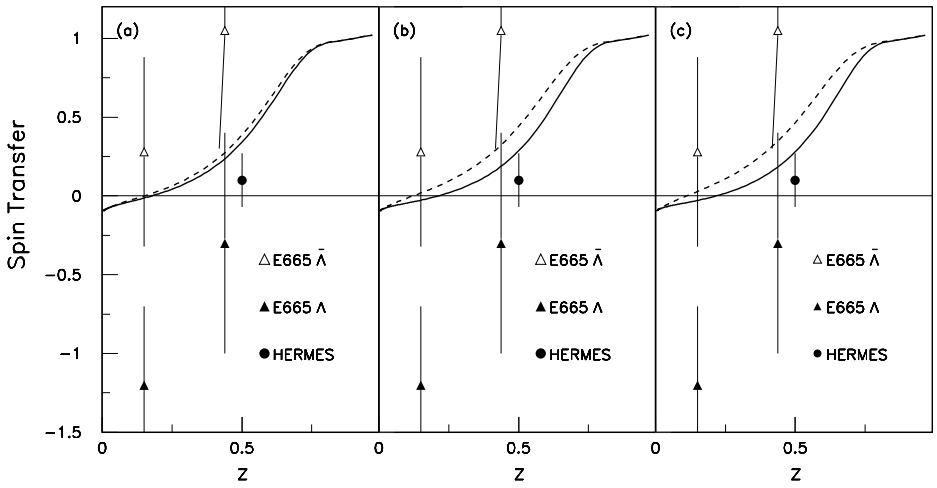

Figure 3.5: The z dependence of the Λ and $\overline{\Lambda}$ spin transfer in polarized lepton DIS on the nucleon. The solid and dashed curves correspond to the Λ and $\overline{\Lambda}$ spin transfer respectively with: (a) default of the CTEQ5 parameterization, (b) including the $\bar{s} > s$, and (c) including an additional contribution of $\overline{d} > d$ in the target nucleon. The fragmentation functions are predicted by the SU(6) Quark-Diquark model. The data point from HERMES is the average spin transfer for Λ.

either from the struck quark or from the remnant diquark. In order to treat the diquark polarization, it was assumed that the polarization of remnant diquark is correlated with possible polarization of intrinsic strangeness *s* quark. The idea of the polarized intrinsic strangeness model will be covered in more detail in Section 3.3.2. The spin correlations between the struck quark and the intrinsic strangeness *s* quark have been defined for the valence and sea quarks as free parameters. The spin correlations are then fixed by a fit with data from the NOMAD experiment in deep inelastic ν scattering [133]. The spin transfer of Λ and $\overline{\Lambda}$ are then calculated using the LUND string fragmentation model as incorporated into the JETSET [135, 136] simulation. Since all hadrons generated in the string fragmentation model are ordered in the rank from the diquark and quark ends of the string, the Λ events are tagged according to this rank. The predicted spin transfer of Λ and $\overline{\Lambda}$ for the COMPASS kinematics were performed for two different cases. In the simple one (Model A) the Λ and $\overline{\Lambda}$ contain the diquark or struck quark, while in the more realistic one (Model B) the Λ and $\overline{\Lambda}$ originate from the middle of the string.

Fig. 3.6 shows the predictions of spin transfer for Model A and Model B for Λ and $\overline{\Lambda}$ at the COMPASS kinematics as functions of x_{Bj}, y and x_F. In the case of Λ the two models differ in their prediction for the three different kinematic regions, since the quark and diquark fragmentation contribute differently to the Λ production. On the other hand, for the $\overline{\Lambda}$ case, the prediction of Model A and B are almost same due to the assumption of no spin transfer to an antihyperon in the diquark fragmentation. As can be seen in Fig. 3.6, the spin transfer of $\overline{\Lambda}$ is significantly larger than that of Λ at large x_F. The reason is that the $\overline{\Lambda}$ is produced manily from $\bar{s}$ quark at $x_F > 0.5$. Hence, it was expected that the measurement of the $\overline{\Lambda}$ spin transfer could give a crucial information on the $\bar{s}$ quark in the nucleon. In addition, a comparison between the QPM and BJ approach for baryon spin structure was represented for the COMPASS kinematics. The spin transfer of the BJ approach for both Λ and $\overline{\Lambda}$ were found to be smaller than the one of QPM. An influence of quark distribution functions on the spin transfer was studied as well. It was found that the CTEQ [130] parton distribution results in larger spin transfer than GRV98 [137] for both Λ and $\overline{\Lambda}$.

Polarized Fragmentation Model

D. de Florian et al. [138] and M. Anselmino et al. [139] have predicted the spin transfer to Λ by evolving the unpolarized fragmentation functions obtained from data of e^+e^- experiments, which are based on a QCD analysis in NLO according to the DGLAP formalism. Since the polarized fragmentation functions are not well known so far, the relation between the spin dependent and the unpolarized Λ fragmentation functions at the input scale for the Q^2 evolution is estimated using three distinct scenarios: The first scenario corresponds to the QPM, the second one is based on a $SU(3)_f$ symmetry, and in the last scenario all three quarks contribute equally to the Λ polarization. The polarized fragmentation functions were

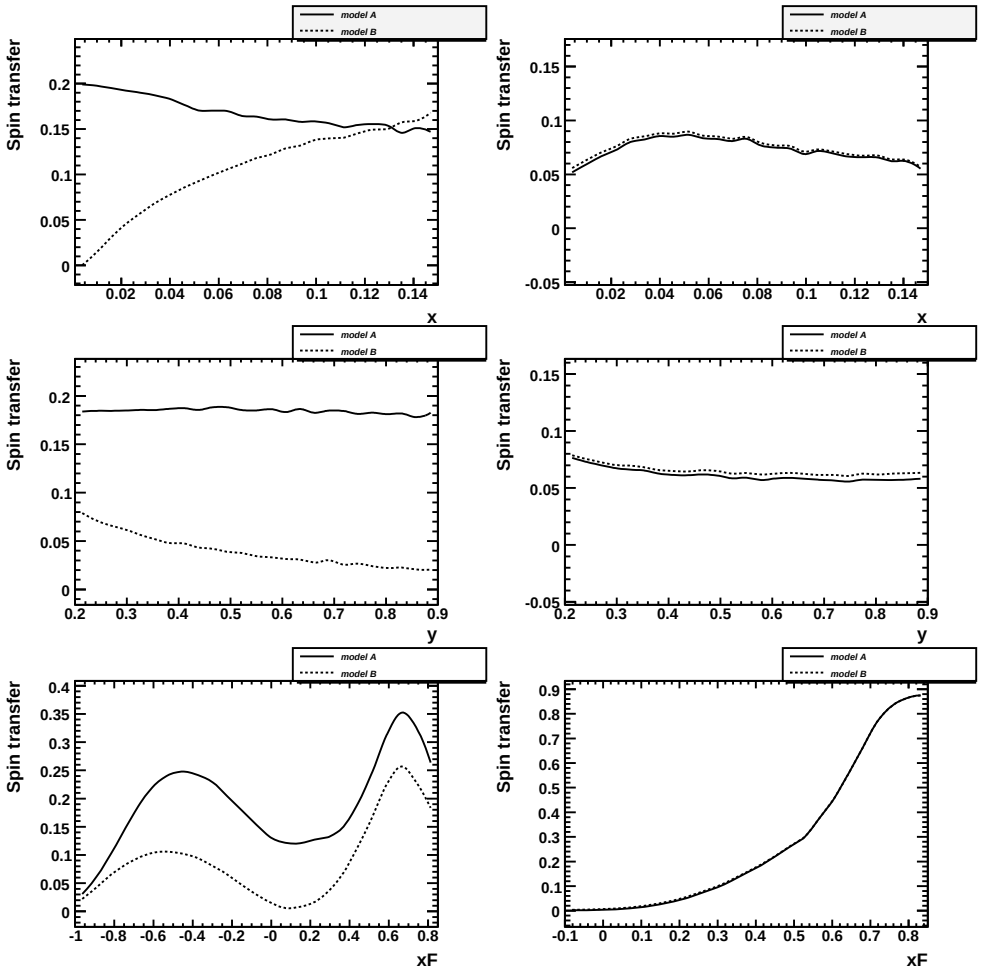

Figure 3.6: Comparison of the spin transfer predictions for Model A (solid line) and Model B (dashed line) for Λ (left) and $\overline{\Lambda}$ (right) hyperons at COMPASS energy as functions of x_{Bj}, y and x_F. The parton distribution function of GRV98LO and the SU(6) model of the baryon spin structure are used.

calculated by numerical computations according to these three different scenarios. In this approach, the gluon contribution is also included in order to analyze the effect of imposing a different boundary condition for the polarized gluon fragmentation function. The three quite different scenarios for fragmentation functions yield very different results in the polarization. The QPM scenario is consistent with zero polarization and does not show any dependence on z, but the other two scenarios even differ in their sign. In Fig. 3.7, the predictions resulting from fragmentation functions as functions of y and x_{Bj} for the three cases are shown at fixed Q^2 and z. Comparing the experimental results with such predictions should immediately allow to draw clear conclusions and to learn about quark fragmentation properties.

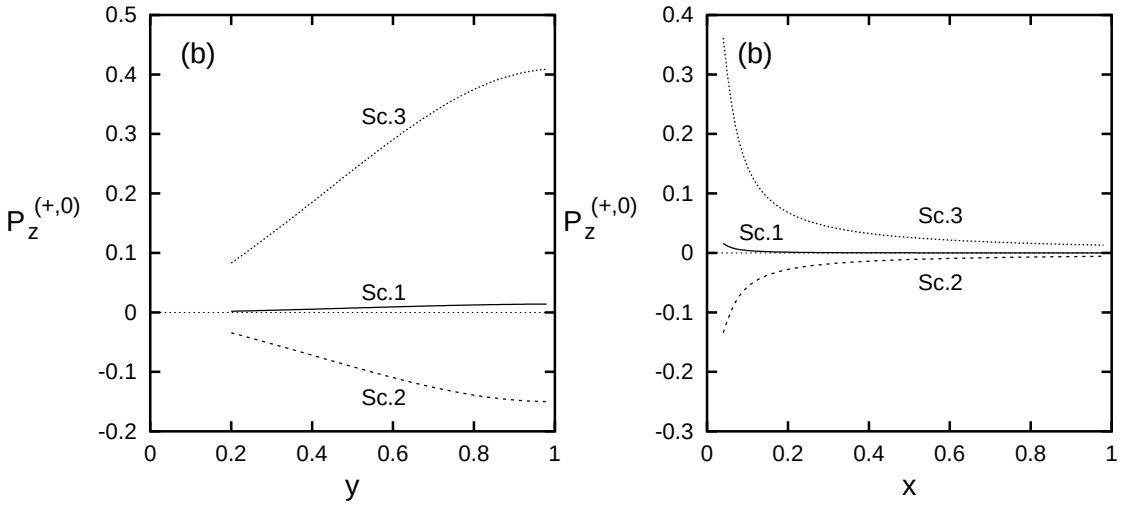

Figure 3.7: The Λ polarizations predicted by using polarized fragmentation functions are shown as functions of y and x_{Bj} at fixed values of $Q^2 = 1.7$ (GeV/c)^2 and $z = 0.5$ for three different scenarios (Scenario 1: QPM, Scenario 2: SU(3)$_f$, and Scenario 3: same contributions of all three quarks).

It is important to note that the COMPASS experiment has measured not only the Λ polarization but also the $\overline{\Lambda}$ polarization. Since the polarization of the antihyperon in semi-inclusive DIS is more sensitive to the sea quarks, it is thus instructive to make a more detailed study for the sea quarks. For Λ production where the valence quark contributions dominate, one expects the $u \to \Lambda$ process to dominate and P_Λ should be small. But for $\overline{\Lambda}$ for which there is no contribution from the valence quark, one expects that $\overline{u} \to \overline{\Lambda}$ and $\overline{s} \to \overline{\Lambda}$ give comparable contributions to the $\overline{\Lambda}$ production and $P_{\overline{\Lambda}}$ should be mainly determined by $\overline{s}$. This implies that $P_{\overline{\Lambda}}$ should be positive and in size much larger than P_Λ. Recently, D. Hui et al. [140] have shown the qualitative features of $\overline{\Lambda}$ polarization with comparisons between hyperons and antihyperons. The unpolarized and polarized fragmentation functions have been assumed using a hadronization model and the Gribov-Lipatov relation. The dependence of the polarization on the kinematic variable x_F has been estimated for all kinds of hyperons and antihyperons. The results for Λ and $\overline{\Lambda}$ are shown in Fig. 3.8. The difference between Λ and $\overline{\Lambda}$ is only significant for larger x_F.

Other Models

The spin transfer to Λ and $\overline{\Lambda}$ in semi-inclusive DIS reactions has also been described in several other theoretical papers. A negative spin transfer from u and d quarks of -0.09 was predicted using an effective QCD Lagrangian [141]. Further theoretical predictions for Λ and $\overline{\Lambda}$ spin transfer can be found in the covariant Quark-Diquark model in Ref. [142], the MIT bag model in Ref. [143], and the perturbative QCD model in Refs. [144, 145, 146].

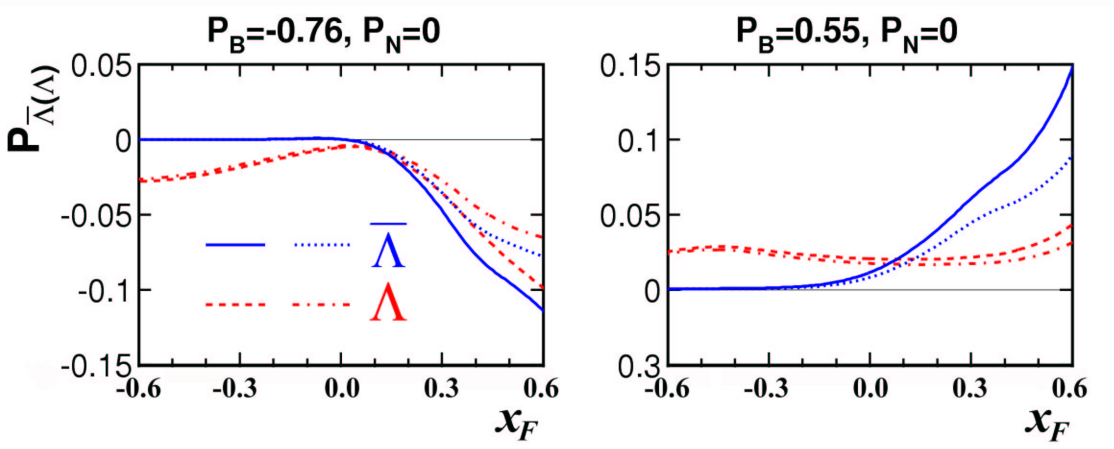

Figure 3.8: Comparison of the polarizations of antihyperons with those of the corresponding hyperons as a function of x_F in the reaction $l^+p \to l^+\overline{\Lambda}(\Lambda)X$ at E_{μ^+}=160 GeV (in the left figure) and at E_{e^+}=27.6 GeV (in the right figure). The solid and dashed lines denote the results obtained by using QPM, while the dotted and dashed-dotted lines denote those by using SU(3)$_f$.

3.3.2 The Target Fragmentation Region

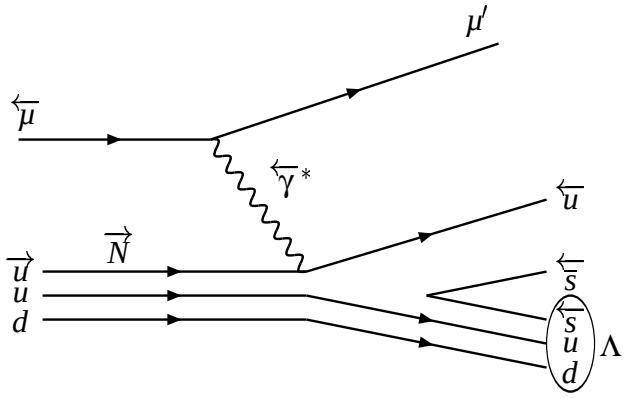

Figure 3.9: Λ production in the target fragmentation region: Λ hyperon consists of a remnant diquark and an additional *s* quark from the sea in the nucleon. The Λ does not contain the struck quark.

The spin structure of an *s* quark in the nucleon is still not understood at a fundamental level, despite having been intensively studied both theoretically and experimentally during the past

several years. In principle, it is possible to measure Δs of the nucleon using the polarization of Λ particles produced in the target fragmentation region as an indirect measurement. A dominant production mechanism in the target fragmentation region is shown in Fig. 3.9. If a remnant diquark and an additional *s* quark in the target nucleon keep the angular momentum, a polarization may be carried by the *s* quark and transferred to the produced Λ, while the remnant *ud* diquark is to be in a spin singlet state.

Intrinsic Strangeness Model

J. Ellis et al. [147] suggested a qualitative Λ polarization model due to polarized intrinsic $s\bar{s}$ pair in the nucleon. A significant contribution of $s\bar{s}$ pairs to the nucleon spin has been motivated by the indication of a violation of the Okubo-Zweig-Iizuka (OZI) rule in $p\bar{p}$ collisions [148]. The OZI rule is based on the idea that diagrams with disconnected quark loops are suppressed compared to connected quarks. Thus $s\bar{s}$ mesons are not preferably produced in the interaction of non-strangeness particles. Hence, the predicted ratio of ϕ and ω mesons produced in $p\bar{p}$ reactions should be equal due to the assumption of no $s\bar{s}$ pair states in the proton. However, experiments at the Low Energy Antiproton Ring (LEAR) found a factor of 30-50 more ϕ mesons than expected [149]. Consequently, the OZI rule is apparently violated. To explain this violation, a considerable fraction of intrinsic $s\bar{s}$ was suggested in the nucleon wave function [150].

It is convenient to distinguish between extrinsic and intrinsic $s\bar{s}$ pair following M. Burkadrdt and B. Warr [127]. Extrinsic strangeness appears due to $q\bar{q}$ pair production from gluons, which can be described perturbatively since the $q\bar{q}$ pair has components which too short a lifetime to interact with the rest of the proton. Intrinsic strangeness can be seen as a result of the $q\bar{q}$ pair connecting with valence quarks in the proton, which can be described as a non-perturbative QCD effect. The $q\bar{q}$ pair does not recombine immediately. One major difference between extrinsic and intrinsic $s\bar{s}$ pairs is that intrinsic ones can be found at large values of x_{Bj} where they have time to reach an energetically more favorable state.

From QCD it is known, that the condensate of a $s\bar{s}$ pair in the QCD vacuum is not small compared with the condensate of light quarks [150, 151]:

$$< 0|\bar{s}s|0 >= (0.8 \pm 0.1) < 0|\bar{q}q|0 > \quad \text{with } q = (u,d). \tag{3.23}$$

Additionally, there are now quite a lot of experimental indications that the proton and neutron wave function contain a fraction of $s\bar{s}$ pairs comparable to the one of the $u\bar{u}$ and $d\bar{d}$ pairs. Therefore, the proton wave function with an intrinsic strangeness component can be decomposed to:

$$|P >= \alpha \sum_{X=0}^{\infty} |uudX > + \beta \sum_{X=0}^{\infty} |uuds\bar{s}X >, \tag{3.24}$$

where X stands for any number of gluons and light $q\overline{q}$ pairs. Furthermore $|\alpha|^2 + |\beta|^2 = 1$. The magnitude of the probability for the intrinsic $s\overline{s}$ pair is consistent with the limit of $0.01 \leq |\beta^2| \leq 0.19$ derived from the strangeness production in $\overline{p}N$ annihilation.

Such a $s\overline{s}$ pair in the nucleon can be regarded as a spin singlet state $^1S_0$ corresponding to the pseudoscalar $J^{PC} = 0^{+-}$ channel and as a spin triplet state $^3P_0$ in the scalar $J^{PC} = 0^{++}$ channel. Experimental result showed in the reaction $p\overline{p} \to \Lambda\overline{\Lambda}$ at the PS185 experiment [152] that the spin of the $s\overline{s}$ pairs oriented opposite to the proton spin ($S_z(s\overline{s}) = -1$). Therefore, one can conclude that the $s\overline{s}$ pair is to be in the spin triplet state $^3P_0$. In the original intrinsic strangeness model [147], the spin projection of $s\overline{s}$ was only taken to be $S_z(s\overline{s}) = -1$. Thus a maximal anticorrelation between the polarization of the struck quark and the s quark was assumed. The Λ polarization is expected to be negative, large, and equal to the polarization of the $\overline{\Lambda}$ in the target fragmentation region. An indication for this effect was measured in the neutrino-nucleon DIS scattering experiments at WA59 and NOMAD, which correctly reproduced the sign and magnitude of the Λ polarization.

Contrary to the PS185 experiment, CLAS data on the reaction $ep \to e'K^+\Lambda$ [153] indicated that the $S_z(s\overline{s}) = 0$ state of the $s\overline{s}$ pair could be possilble. In the extended intrinsic strangeness model [133], it was considered that two contributions of $S_z(s\overline{s}) = -1$ and $S_z(s\overline{s}) = 0$ have an equal probability in the nucleon wave function. The polarization of Λ has been predicted to be negative and small in this case. The difference between Λ and $\overline{\Lambda}$ polarizaiton is expected to be quite significant as $P_{\overline{\Lambda}} = 3P_\Lambda$ [154]. Prediction of this model are in good agreement with the NOMAD data. However, for the charged lepton DIS measured at E665, HERMES and COMPASS more statistics are needed to make a detailed comparison. Finally, it needs to be mentioned that the measurement of the $\Lambda\overline{\Lambda}$ correlations in the target fragmentation region in DIS is important to test whether the spin of the $s\overline{s}$ is really anticorrelated with the proton spin [147, 150].

Meson Cloud Model

The simplest way to model a polarized s quark would be in terms of a polarized hyperon accompanying a non-perturbative cloud of kaons [155]. As the π-cloud model provides a natural explanation of the isospin symmetry breaking in the unpolarized proton sea, a kaon cloud in the nucleon due to mesonic degrees of freedom would be a possible mechanism to obtain a polarized s quark. This probability of a ΛK^+ state in the nucleon can be revealed by the measurement of polarized Λ production. One can also expect that the contributions from higher possible fluctuations with vector mesons, like ΛK^*, will lead to non-zero Λ polarization. However, the estimate of relative probability for this state is less than 10% with respect to the ΛK^+ state. This model expects a zero polarization with an unpolarized target for the Λ and the same for the $\overline{\Lambda}$. However, the Λ polarization is almost 100% correlated with

the target polarization, the difference of Λ polarization for the parallel and opposite target polarization is expected to be $|\Delta P_\Lambda| = 2$.

In the model of S. Brodsky and B. Ma [128] it is assumed that the distributions of nonvalence quarks and antiquarks may be asymmetrically generated by $SU(3)_f$ symmetry breaking in the nucleon sea. The authors investigated the asymmetries of intrinsic $q\overline{q}$ pairs in the nucleon wave function, which are generated by the meson-baryon (ΛK^+) fluctuations. This model predicts that the intrinsic d and s quarks in the nucleon sea are negatively polarized, whereas the intrinsic $\overline{d}$ and $\overline{s}$ quarks give zero contributions to the proton spin. Expected results are that the Λ polarization will be negative, and a vanishing or slightly positive polarization for the $\overline{\Lambda}$ can be expected in the target fragmentation region .

Diquark Model

An alternative proposition is a significant contribution from diquark fragmentation to Λ and $\overline{\Lambda}$ polarization. It was pointed out by the EMC collaboration that the production rates of Λ and $\overline{\Lambda}$ are roughly equal for $x_F > 0$. However, the $\overline{\Lambda}$ production rate decreases rapidly for $x_F < -0.2$, while the Λ remains nearly constant. The observed difference of production rates is directly related to the different production mechanism of Λ and $\overline{\Lambda}$ [156]. The $\overline{\Lambda}$ can only be produced by creating a diquark-antidiquark pair in the target fragmentation. Such a process requires an opposite spin of the antidiquark with respect to the diquark. Therefore the $\overline{\Lambda}$ may inherit the polarization from the spin configuration of the fragmented antidiquark.

For the time being, no clear experimental evidence for any of the models has been found. The currently favored model is intrinsic strangeness, but due to small statistics the conclusions are unclear. Especially the experimental situation for $\overline{\Lambda}$ is rather scarce and not more than a few hundred events have been observed. All presented models can be tested in the COMPASS experiment. The measurement of the Λ and $\overline{\Lambda}$ polarization in the target fragmentation region can provide insight about polarized s and $\overline{s}$ quarks in the nucleon and could discriminate between different models.

3.4 A Brief Overview of the Experimental Situation

Several experiments, where hyperons are produced in DIS reactions and in e^+e^- annihilation, published data on the longitudinal polarization of Λ and $\overline{\Lambda}$. The measured polarizations for different fragmentation regions for Λ and $\overline{\Lambda}$ are summarized in Table 3.4. The longitudinal polarization of Λ was first observed in bubble chamber neutrino and anti-neutrino experiments. The results varied from -0.29 to -0.63 increasing with the absolute value of x_F in the target fragmentation region. Although the intrinsic strangeness model explain these results successfully, these early experiments suffered from low statistics. Therefore the results from bubble chamber experiments cannot be considered conclusive. Particularly, the result could not lead to a conclusion for the current fragmentation region.

The NOMAD [160] collaboration has measured the Λ polarization with a ν_μ beam energy of 43 GeV in the charged current interaction $\nu_\mu N \to \mu^- \Lambda X$. In this process the interaction is mediated via the exchange of a W^+ boson. The weak current W^+ couples only to left handed d quarks or right handed $\overline{u}$ quarks and involves a flavor change. For this process the polarization of the Λ is given by the following expression [160]:

$$P_x^\Lambda(x,y,z) = -\frac{q_d(x)\Delta D_u^\Lambda - (1-y)^2 q_{\overline{u}}(x)\Delta D_{\overline{d}}^\Lambda}{q_d(x)D_u^\Lambda + (1-y)^2 q_{\overline{u}}(x)D_{\overline{d}}^\Lambda}, \tag{3.25}$$

where $q_d(x)$ and $q_{\overline{u}}(x)$ are the quark distribution function of the d quark and $\overline{u}$ quark and $D_u(z)$ and $D_{\overline{d}}(z)$ are the fragmentation function of the u quark and $\overline{d}$ quark, respectively. The contribution of s quarks in the nucleon are neglected for the sake of simplicity. If a small contribution from the $\overline{u}$ quark is assumed, a measurement of Λ polarization in the current fragmentation region provides directly information on the spin transfer C_{LL}^Λ with the same statistical error. This fact derives to the relation of $P_x^\Lambda = -C_{LL}^\Lambda$. The spin transfer presented by the NOMAD experiment can be consequently compared with other experiments. The observed average spin transfer in the current fragmentation region is $C_{LL}^\Lambda = +\,0.09 \pm 0.06$ (stat.) $\pm$ 0.03 (sys.). It was found that the spin transfers are slightly different in the target fragmentation and in the current fragmentation region.

The E665 [161] and HERMES [124] experiments provide a quite similar environment to the one at COMPASS, thus the results are expected to be similar. HERMES has measured the spin transfer in the reaction $e^+N \to e^{+'}\Lambda X$. A longitudinally polarized positron beam with a lower beam energy of 27.6 GeV than COMPASS is interacting on various unpolarized gas targets, and the kinematic region is slightly different. The HERMES results are based on a data sample containing 7,300 Λ events. The observed spin transfer is $C_{LL}^\Lambda = +0.11 \pm 0.10$(stat.) $\pm$ 0.03(sys.) in the region $x_F > 0$, which is in good agreement with the NOMAD result. The systematic error was estimated from the normalization uncertainty with a positive-negative beam helicity and a positive-negative hadron pair, which do not originate from Λ decay. Most theoretical models predict a gradual increase at high values of x_F and z for

Table 3.4: Present results for Λ and $\overline{\Lambda}$ polarization for different x_F regions. For E665 and HERMES, the spin transfer coefficient C_{LL} are presented instead of the polarization P_x. For OPAL and ALEPH, where x_F is undefined, $x_E \equiv 2E_\Lambda/\sqrt{s}$ is used. The statistical errors of $P_x(C_{LL})$ are included in the table.

Experiment Λ	Reaction	$\langle$ E$_{beam}\rangle$	x_F	N_Λ	P_x^Λ (C_{LL}^Λ)
WA21 [157] (1985)	$\nu_\mu p$	51 GeV	Full sample	289	-0.10 ± 0.14
			$x_F < 0$	203	-0.29 ± 0.18
			$x_F > 0$	86	$+0.53 \pm 0.30$
WA21 [157] (1985)	$\overline{\nu}_\mu p$	40 GeV	Full sample	267	-0.24 ± 0.17
			$x_F < 0$	210	-0.38 ± 0.18
			$x_F > 0$	57	$+0.32 \pm 0.35$
WA59 [158] (1992)	$\overline{\nu}_\mu Ne$	40 GeV	Full sample	469	-0.56 ± 0.13
			$x_F < 0$	403	-0.63 ± 0.13
			$x_F > 0$	66	-0.11 ± 0.45
E632 [159] (1994)	$\nu_\mu Ne$	150 GeV	Full sample	258	-0.38 ± 0.16
			$x_F < 0$	190	-0.43 ± 0.20
NOMAD [160] (2000)	$\nu_\mu N$	43.8 GeV	Full sample	8087	-0.15 ± 0.03
			$x_F < 0$	5608	-0.21 ± 0.04
			$x_F > 0$	2479	-0.09 ± 0.06
E665 [161] (2000)	$\mu^+ N$	470 GeV	$0 < x_F < 0.3$	750	-1.2 ± 0.5 (C_{LL}^Λ)
			$x_F > 0.3$		-0.32 ± 0.7 (C_{LL}^Λ)
HERMES [124] (2006)	$e^+ N$	27.6 GeV	Full sample	7300	
			$x_F > 0$	6746	0.11 ± 0.10 (C_{LL}^Λ)
ALEPH [163] (1996)	$e^+ e^-$	91.2 GeV	$x_E > 0.3$	≈ 8000	-0.32 ± 0.07
OPAL [162] (1998)	$e^+ e^-$	91.2 GeV	$x_E > 0.3$	8309	-0.33 ± 0.06
Experiment $\overline{\Lambda}$	Reaction	$\langle$ E$_{beam}\rangle$	x_F	N_Λ	$P_x^{\overline{\Lambda}}$ ($C_{LL}^{\overline{\Lambda}}$)
E665 [161] (2000)	$\mu^+ N$	470 GeV	$0 < x_F < 0.3$	650	0.26 ± 0.6 ($C_{LL}^{\overline{\Lambda}}$)
			$x_F > 0.3$		1.1 ± 0.8 ($C_{LL}^{\overline{\Lambda}}$)
NOMAD [164] (2001)	$\nu_\mu N$	43.8 GeV	Full sample	649	-0.07 ± 0.12
			$x_F < 0$	248	0.23 ± 0.20
			$x_F > 0$	401	-0.23 ± 0.15

charged lepton scattering. Although this data explored up to higher values of x_F and z, no clear evidence of a kinematic dependence on x_F and z was observed for the spin transfer of Λ.

The E665 experiment at Fermilab has measured the spin transfer of Λ with a 470 GeV/c polarized μ^+ beam. The result obtained by the E665 experiment is contrary to the results of NOMAD and HERMES since a negative spin transfer for Λ was observed in the current

fragmentation region. Nevertheless, the E665 result seems to be consistent with the model prediction, which is expected to show a trend towards positive spin transfer with increasing x_F and a large difference in spin transfer between target and current fragmentation region.

The results of HERMES and NOMAD are a contrast to the Λ polarization observed in e^+e^- annihilation at OPAL and ALEPH as well. The OPAL [162] and ALEPH [163] data show a large negative Λ polarization and a pronounced rise of Λ polarization at high values of z. This difference between e^+e^- annihilation and DIS experiment can be explained by the fact that the Λ production on the Z^0 pole is dominated by the fragmentation of strongly polarized s quarks, whereas in DIS the dominantly fragmenting u quarks are polarized very weakly. A comparison between experimental results from e^+e^- annihilation and calculated results based on the BGH model seems to agree reasonably well, but this is not unique explanation. The predictions of the BJ models based on the $SU(3)_f$ symmetry are also consistent with the data. The available data from OPAL and ALEPH are still far from accurate and not enough statistics to give a decisive conclusion which model describes appropriately the properties of Λ polarization.

In the target fragmentation, the Λ polarization is negative and large. A clear difference of the Λ polarization between target and current fragmentation region is observed. This means that the production mechanisms of Λ particles should differ in the target and current fragmentation region, and thus the polarizations are changed. If one assumes that all $s\bar{s}$ pairs are coupled to a $^3P_0$ state and the s quarks are polarized negatively, the results of E665 and NOMAD experiments for $x_F < 0$ can be explained by this simple intrinsic strangeness model. A negative polarization at $x_F < 0$ would also agree with the expectation based on the extended intrinsic strangeness model, which considers equal probability of $^1S_0$ and $^3P_0$ state. The polarization of Λ and $\overline{\Lambda}$ is expected to be different in this regime. The difference of the polarization between Λ and $\overline{\Lambda}$ in the target fragmentation region observed by WA59 and NOMAD as given in Tab. 3.4 can successfully be explained as predicted by the model of extended intrinsic strangeness.

The experimental information on the polarization and spin transfer of $\overline{\Lambda}$ is even more scarce. The result of NOMAD [164] is based on 650 events sample for $\overline{\Lambda}$. Similarly, 650 events has been collected by the E665 experiment. HERMES has not performed the measurement of $\overline{\Lambda}$ polarization. The results are compatible with zero in the target fragmentation region. In current fragmentation region, the obtained results for the spin transfer of $\overline{\Lambda}$ by the NOMAD experiment seems to be positive $C_{LL}^{\Lambda} = +0.23 \pm 0.15(\text{stat.}) \pm 0.08(\text{sys.})$. The positive spin transfer $C_{LL}^{\Lambda} = +1.1 \pm 0.8$ was also obtained by the E665 experiment. The results are consistent with the expected trend towards positive spin transfer with increasing x_F. However, improved statistics on the $\overline{\Lambda}$ are needed for a decision on which model showed be favored. In this work, the result of $\overline{\Lambda}$ will especially contribute to the improvement of the error on $C_{LL}^{\overline{\Lambda}}$ with much higher statistics than other experiments in the current fragmentation region.

Chapter 4

COMPASS Experiment

COMPASS is a fixed target experiment located at the north area of CERN. It is situated at the end of the M2 beam line of the Super Proton Synchrotron (SPS). The main purpose of the COMPASS experiment is to investigate hadron structure and hadron spectroscopy by using high intensity muon and hadron beams. In 2002, the experiment had the first year of data taking with almost the complete setup using a muon beam. Some new detectors were added in 2003 and 2004. After the break of 2005 due to the SPS shutdown, data taking with a muon beam was resumed in 2006 and continued up to now [165].

In this chapter, the main detectors of the experiment are briefly described. The COMPASS experiment uses a beam of longitudinally polarized positive muons and a longitudinally or transversely polarized ^{6}LiD target, which can be regarded as a polarized deuteron target. The target consists of two target cells with opposite spin directions. Polarized beam and target are described in Section 4.1 and 4.2, respectively. In order to cover the large scattering angle and thus large Q^2 region, the spectrometer is designed in two stages, a large angle and a small angle spectrometer. Two parts of the spectrometer are built up around and after the target to select and register potentially useful scattering events. The next section describes the general layout of tracking detectors and particle identification in the COMPASS spectrometer. Particle identification is provided by a ring-imaging Čerenkov detector (RICH), the muon filters (MF), which distinguish muons from hadrons, an electromagnetic calorimeter (ECAL), and two hadronic calorimeters (HCAL), which are also part of the trigger system. In Section 4.4, the concept of the trigger system is presented in more detail. The data acquisition system (DAQ) with read-out electronics and detector control system (DCS) are addressed in the last Section. An extensive description of the COMPASS experiment can be found in Refs. [166].

4.1 The Polarized Muon Beam

The COMPASS muon program uses the longitudinally polarized muon beam from the CERN M2 beam line [169]. The beam line can also transport hadrons with energy up to 300 GeV

for the COMPASS hadron program by removing the absorbers and tuning the magnets. Only the muon beam, which is relevant for the analysis of Λ polarization, will be described in this Section.

The polarized muon beam for the COMPASS experiment is produced by collision of high energy protons on a production target. A schematic view of the various accelerators involved is shown in Fig. 4.1. A primary proton beam is first accelerated by the Proton Synchrotron (PS), where it obtains an energy of E_P = 14 GeV and an intensity of 3.4×10^{13} protons per PS cycle. Then the protons are injected into the SPS. After the protons are accelerated in the SPS, they are extracted from the SPS accelerator toward the north experimental area of

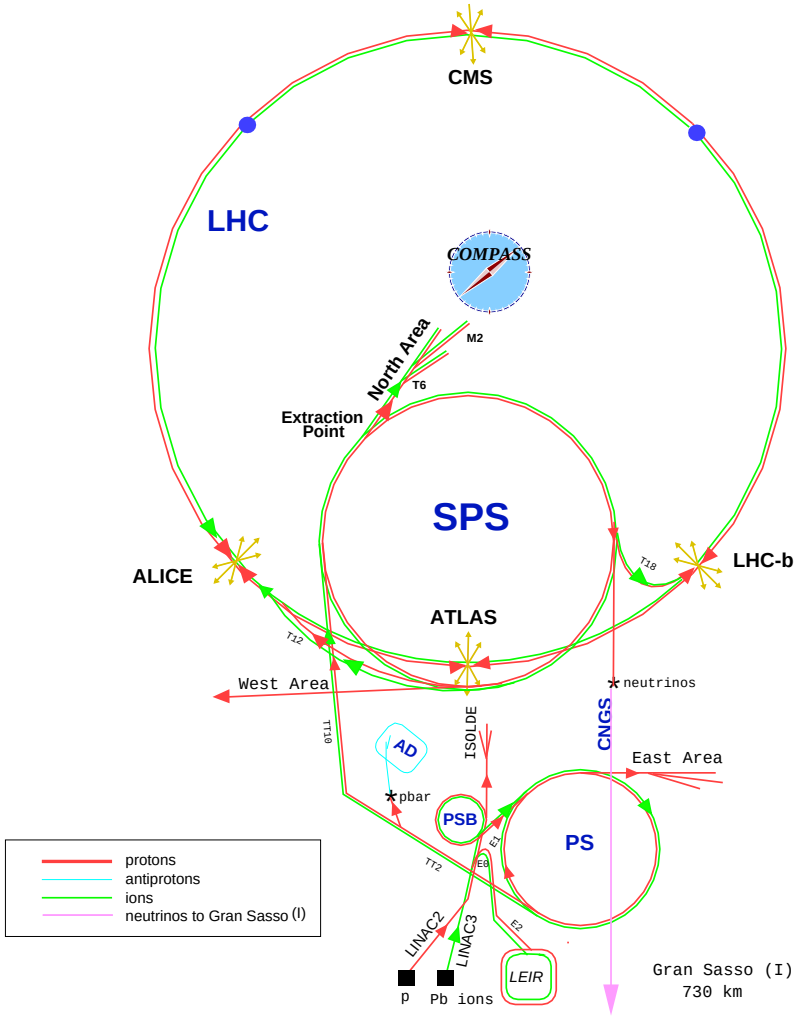

Figure 4.1: The accelerator complex at CERN (not drawn to scale), showing the two accelerators PS, SPS, and the position of the experimental area of COMPASS.

CERN. A beam energy E_P = 400 GeV protons are directed onto the T6 beryllium target with an incident intensity in the range from 2×10^{12} to 1.2×10^{13} protons per SPS cycle, during the 4.8 s on-spill time followed by an off-spill time of 12.0 s adding up to a total cycle length of 16.8 s. The SPS cycle is sketched in Fig. 4.2, where the solid line displays the intensity of protons in the SPS. During acceleration the intensity remains constant. In this time, protons are debunched, so that their flux is distributed random and constant. The M2 beam line is about 1 km long and serves both for the transport of the primary beam from the SPS to the experimental area and for the production of secondary beams. The scheme of M2 beam line is shown in Fig. 4.3.

The key feature of generating the muon beam is the decay channel right after the T6 target [167]. A set of bending magnets B1-B3 and scrapers select the produced hadrons with a momentum of 172 GeV/c and a momentum spread of $\pm$10%. The collisions of protons and nuclei of the beryllium target (T6) produce mainly pions and kaons. The produced hadrons are transported in a 600 m long decay section, in which about 5% of the hadrons decay into muons and neutrinos. Electron production is suppressed by a factor of approximately 10^{-4} because of helicity conservation [168]. At the end of this section, remaining hadrons are removed by means of beryllium absorbers and only muons pass to the double bend upward. The muons loose about a momentum of 2 - 3 GeV/c on their way through the hadron absorber [169]. Muons with a momentum of 160 GeV/c and a momentum spread of approximately $\pm$3% are selected by two bending magnets B4-B5 and scrapers in the next 330 m section. The scrapers are special collimators made of magnetized iron that deflect low momentum particles away from the beam.

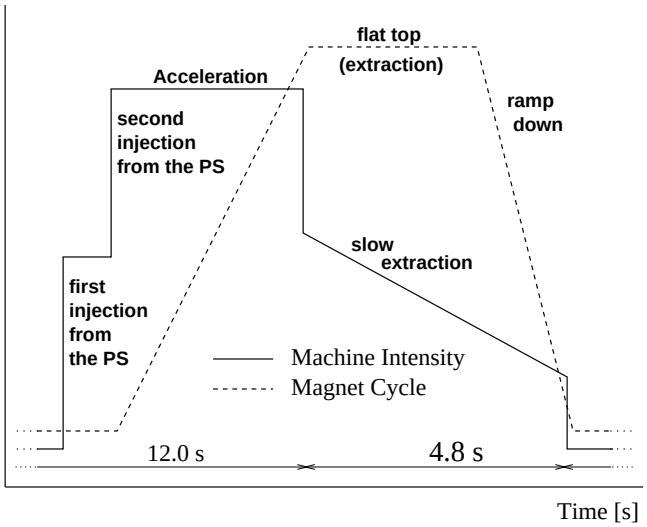

Figure 4.2: The SPS spill structure (not drawn to scale). The solid line is the proton intensity within the SPS, the dashed line the magnet current of the SPS.

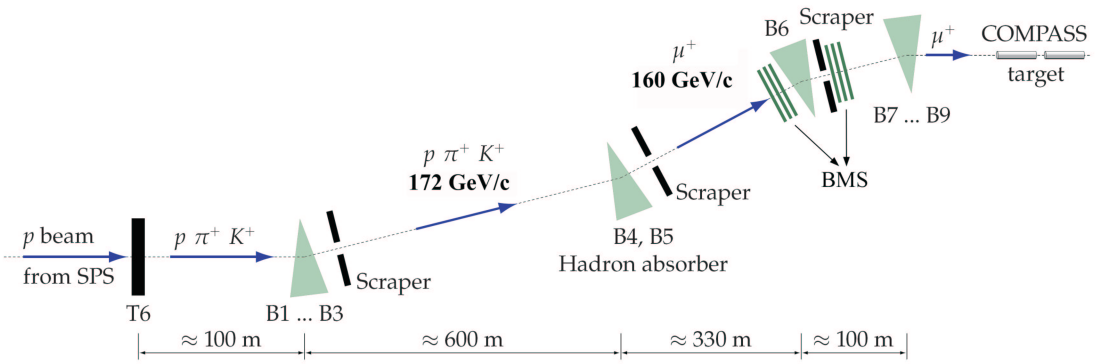

Figure 4.3: Schematic view of the M2 muon beamline in vertical plane (not drawn to scale). Pions and kaons produced in the proton-beryllium collisions in T6 decay in a hadron decay section. The fraction of hadrons is further reduced by an absorber, before the muons are selected by their momentum with an arrangement of bending magnets and scrapers. The muon momentum is measured by the beam momentum station (BMS) approximately 100 m upstream of the COMPASS target.

The produced muon beam is led from the underground SPS level up to the experimental hall by two groups of bending magnets, such that it travels almost horizontally towards the COMPASS target. The momentum of each muon is measured by the Beam Momentum Station (BMS). The BMS consists of six scintillator planes placed between 60 m and 140 m in front of the COMPASS target. Three planes are located upstream and the other three downstream of bending magnet B6. Different momenta of each beam particle leads to different transverse displacement in the vertical bending plane, which allows to measure the momenta of each beam particle [170]. At the end of the beam line a set of multiple quadrupole magnets B7-B9 focuses the beam onto the COMPASS target.

Due to the parity violating weak decay of the charged pions and kaons the muon beam is naturally polarized. The muon polarization depends on the fraction of the parent pion momentum carried by decay muon [171]. This dependence is illustrated in Fig. 4.4. Assuming a fixed parent pion momentum of 172 GeV/c, the beam polarization is shown as a function of muon momentum. The beam polarization is optimized to a value of $-80 \pm 4\%$ with a muon beam momentum of 160 GeV/c and a beam flux of 2×10^8 muons per SPS cycle in 2004. This final muon polarization value also includes a correction due to the kaon component of the hadron beam. The beam spot size at the polarized COMPASS target is also important because it determines the diameter of the target cells. The beam size is about $\sigma_x \sim \sigma_y \sim 8$ mm. The nominal parameters of the muon beam for COMPASS are summarized in Table 4.1.

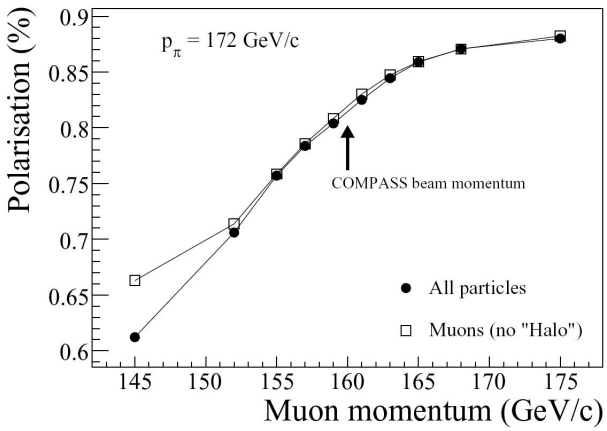

Figure 4.4: The muon beam polarization as a function of muon momentum, assuming a hadron momentum of 172 GeV/c.

Table 4.1: Characteristics of the muon beam during data taking in 2004.

Beam parameters	Measured
Mean beam energy	160 ± 5 GeV/c
Beam intensity	2.8×10^8 μ^+ /spill
Beam polarization	-0.80 ± 0.04
Beam diameter	$\sigma_x \sim \sigma_y \sim 8.0$ mm
Beam divergence	$\sigma_{\theta_x} < 0.4$ mrad, $\sigma_{\theta_y} < 0.8$ mrad

4.2 The Polarized Target

NH_3 and ^{6}LiD are ideal solid materials available as polarized proton and deuteron targets, respectively. If the measurements with both materials are combined, the structure of the neutron can be extracted. While NH_3 is a rather well known target material, ^{6}LiD was chosen as the target material in the data taking 2002-2006 because of its high polarizability [172]. ^{6}LiD can in a simple picture be thought of as being composed of a spinless α (^{4}He) particle and two spin-1 deuteron.

In order to make a asymmetry measurement, the target consists of two independently and oppositely polarized cells. They have a diameter of 3.0 cm and 60 cm length each as pictured in Fig. 4.5. The two target cells are separated by a gap of 100 mm and in the middle of the gap a microwave stopper made from a 0.1 mm copper foil is installed to isolate the microwave frequencies present in each cell.

The target is polarized longitudinally with respect to the direction of the muon beam as shown in Fig. 4.6. The polarization of the target is obtained via dynamic nucleon polarization (DNP) with microwave frequency modulation technique at a temperature of 200 to 300 mK [173]. ^{6}LiD is placed inside a microwave cavity orientating the spin direction by irradiating the material with microwaves slightly above or below the electron spin resonance (Larmor) frequency. This causes a transfer of the high electron polarization to the nucleons by resonant absorption of the microwave radiation. To perform this transition efficiently, a 2.5 T longitudinal field is produced by a superconducting magnet system.

The change of the spin configuration is performed in the two ways [174]. The first one is the so-called microwave reversal, which is used by DNP. The microwave reversal needs about 1 week to reach the maximum polarization and is not adequate for frequent spin reversals. However, it is performed at least once in the beam time for each year in order to test for systematic errors. With this microwave reversal, the spin configuration of target cells can be changed from the 1^{st} to the 3^{rd} configuration and from the 2^{nd} to the 4^{th} shown in Fig. 4.6. The second method is the so-called field rotation, which is done by changing the solenoid current. The spin reversal by field rotation is based on the fact that the nuclear spin follows

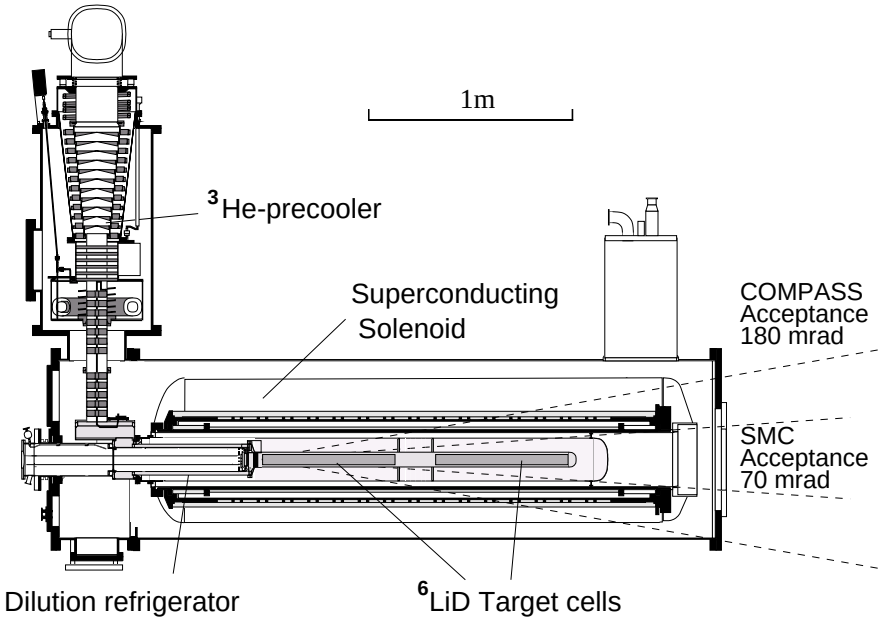

Figure 4.5: Schematical side view of the ^{6}LiD target system. The two 60 cm target cells are placed inside a superconducting magnet. The dilution refrigerator is responsible for cooling the target material. The acceptance of the presently used SMC solenoid is shown in comparison with the proposed acceptance of the COMPASS magnet. The angle is not drawn to scale.

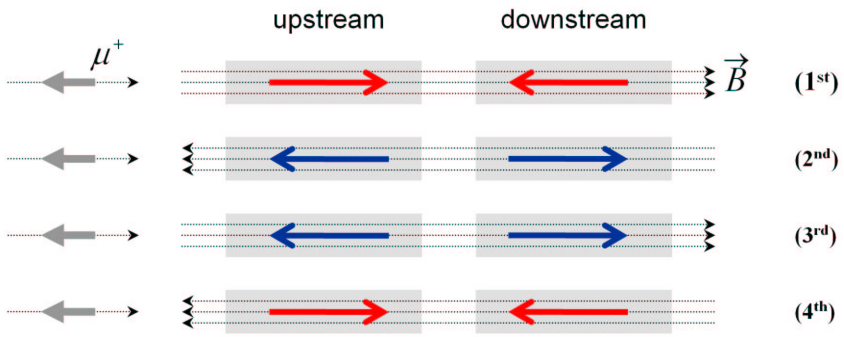

Figure 4.6: The four configurations of the longitudinally polarized target with two opposite magnetic fields: The negatively polarized muon traverses from the left side.

the direction of the external magnetic field. This is one of the special features of the polarized COMPASS target. This setup requires that the spin directions of the target are reversed every 8 h to reduce possible systematic influences due to the spectrometer acceptance and the different amount of material in the two target cells. By using the field rotation, the spin configuration of target cells can be changed from the 1^{st} to the 2^{nd} configuration and from the 3^{rd} to the 4^{th} in Fig. 4.6. The polarization of ^{6}LiD is determined by using a nuclear magnetic resonance (NMR) probe [175]. The average target polarization has been measured to be $|P_T^{\mathrm{up}}|$ = 54% in the upstream cell and $|P_T^{\mathrm{down}}|$ = 47% in the downstream cell.

The COMPASS muon program also contains the measurement of the transverse spin-dependent structure function with a transversely polarized target. Such a spin configuration can be realized by holding the nuclear polarization at a low temperature and stopping the field rotation of the solenoid. The transverse spin direction of two target cells are maintained by a transverse dipole field of 0.42 T. To avoid thermal relaxation the target material is cooled down below 100 mK, where in the frozen spin mode the polarization has a lifetime in the order of 1000 h.

4.3 The COMPASS Spectrometer

The COMPASS spectrometer used for the physics programs is designed in two stages. The first and second stage of the spectrometer are located downstream of the target, and extend over a total length of 50 m. These are distinguished as a Large-Angle Spectrometer (LAS) and a Small-Angle Spectrometer (SAS). Each of the two spectrometer stages is built around a dipole analyzing magnetic. The first stage is based on the spectrometer magnet (SM1) with a bending power of 1.0 Tm, which has been designed to ensure a $\pm$ 180 mrad polar acceptance and is referred to as LAS. Since the deflection angle in a magnetic field depends on the ratio between field strength and particle momentum, the first spectrometer magnet with the lower magnetic field is used to deflect and split up tracks of particles in the lower momentum range. In the second stage particles with high momentum emerging under smaller angles are detected. The SAS covers the inner $\pm$ 30 mrad, accordingly the second spectrometer magnet (SM2) has a higher bending power of 4.4 Tm. The full detector setup for the year 2004 is sketched in Fig. 4.7. The various components of the spectrometer are summarized in Table 4.2.

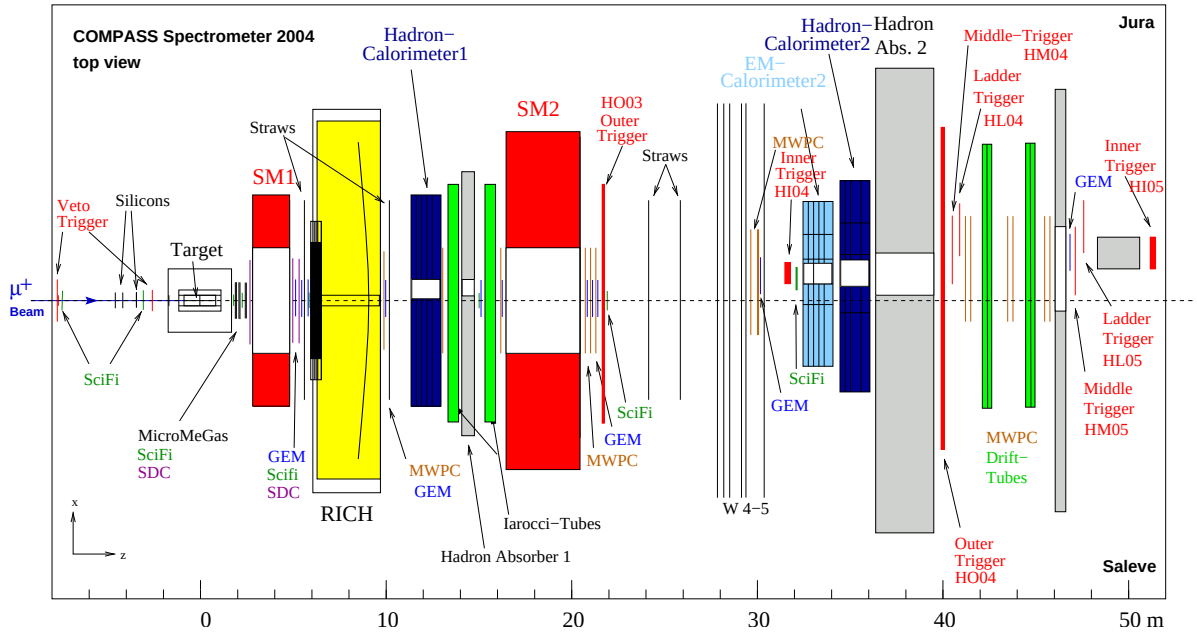

Figure 4.7: Top view of the COMPASS muon beam setup as for 2004. The muon beam is entering from the left side. The target is located at $z = 0$. The positions of the two magnets (SM1 and SM2) can be seen with red boxes. Each of the two spectrometers are followed by different size trackers and completed by a hadron calorimeter (HCAL) and by a hadron absorber (MF). A RICH detector is part of the LAS setup. The SAS includes an electromagnetic calorimeter (ECAL). The trigger hodoscopes (HO, HI, HL, HM) are positioned in the downstream part of the spectrometer behind SM2 and the second MF. Jura indicates the horizontal direction x.

Table 4.2: Overview of detector setup used in COMPASS. It shows a list of target, magnets and different detectors used in 2004, together with their respective main characteristics, grouped according to their geometrical positions along the beam line and functions in the spectrometer. In the last column, projections are given as X for a horizontal axis, Y for a vertical axis, U for a counter-clockwise rotated x-axis, and V for a clock-wise rotated x-axis. The angle of rotation depends on the detector type and ranges from 5° to 45°. Typical values for resolutions of the detectors at standard muon beam conditions are given including contributions from pile-up, magnetic fringe fields, or reconstruction inefficiencies. σ_x denotes the r.m.s. spatial resolution along one coordinate, σ_t the r.m.s. time resolution. The types of tracking detectors are divided into three groups as a Very Small Area Trackers (VSAT), a Small Area Trackers (SAT), and a Large Area Trackers (LAT) according to their designs. The following subsections describe the general features of the detectors for the tacking and particle identification.

Table 4.2: Overview of detector setup used in COMPASS.

	Name	Position in cm	Type	Active area in cm^2	Planes (Projections), Spatial σ_x, Time σ_t resolution
Beam	BMS 1-6	$\sim$ -10000	VSAT	60 $\times$ 230	6 planes (Y), σ_x = 0.6-2.5 mm , σ_t = 0.3 ns
	Veto BL	-2000	Trigger	50 $\times$ 50	segmented plane with hole
	Veto I1,O1	-740	Trigger	250 $\times$ 320	segmented plane with hole
	Veto I2	-265	Trigger	30 $\times$ 30	segmented plane with hole
	SciFi 1,2	-760 - -288	VSAT	3.9 $\times$ 3.9	4 planes (XY), σ_x = 130 μm, σ_t = 0.4 ns
	Si 1, 2	-570 - -350	VSAT	5.0 $\times$ 7.0	8 planes ($XYUV$), σ_x = 8-11 μm, σ_t = 2.5 ns
Target	Target	-100 - 30	Target	-	^{6}LiD, 2 cells, each 60 cm long with 3 cm diameter
LAS	SciFi 3,4	124 - 214	VSAT	5.3 $\times$ 5.3	6 planes (XYU), σ_x = 130 μm, σ_t = 0.4 ns
	MM 1,2,3	140 - 251	SAT	40 $\times$ 40	36 planes ($XYUV$), σ_x = 90 μm, σ_t = 9 ns
	DC 1	260	LAT	180 $\times$ 127	8 planes ($XYUV$), σ_x = 190 μm
	SM 1	313 - 413	Magnet	-	1.0 Tm integrated field strength
	GEM 1,2,3	477 - 564	SAT	31 $\times$ 31	12 planes ($XYUV$), σ_x = 70 μm, σ_t = 12 ns
	DC 2,3	462 - 511	LAT	180 $\times$ 127	16 planes ($XYUV$), σ_x = 190 μm
	Straw 3	534 - 558	LAT	280 $\times$ 320	6 planes ($XYUV$), σ_x = 190 μm
	SciFi 5	584	VSAT	8.4 $\times$ 8.4	2 planes (XY), σ_x = 170 μm, σ_t = 0.4 ns
	RICH	600 - 950	PID	60 $\times$ 120	$\pi/K/p$ separation up to 43 GeV/C
	MWPC A*	952	LAT	178 $\times$ 120	4 planes ($XYUV$), σ_x = 1.6 mm
	GEM 4	960	SAT	31 $\times$ 31	4 planes ($XYUV$), σ_x = 70 μm, σ_t = 12 ns
	Straw 4	1012 - 1021	LAT	280 $\times$ 320	3 planes (XYV), σ_x = 190 μm
	HCAL 1	1217 - 1317	PID	420 $\times$ 300	$\frac{\Delta E}{E} = \frac{0.59}{\sqrt{E}} \oplus 0.08$
	MF 1	1430 - 1490	PID	633 $\times$ 633	60 cm iron in between MW1
	MW 1	1399 - 1543	PID	473 $\times$ 405	16 planes (XY), σ_x = 2.8 mm
SAS	GEM 5,6	1385 - 1579	SAT	31 $\times$ 31	8 planes ($XYUV$), σ_x = 70 μm, σ_t = 12 ns
	MWPC A1,2	1375 - 1570	LAT	178 $\times$ 120	6 planes (UXV), σ_x = 1.6 mm
	SciFi 6	1500	VSAT	10 $\times$ 10	3 planes (XYV), σ_x = 210 μm, σ_t = 0.4 ns
	SM 2	1600 - 2000	Magnet	-	4.4 Tm integrated field strength
	GEM 7-10	2021 - 3139	SAT	31 $\times$ 31	16 planes ($XYUV$), σ_x = 70 μm, σ_t = 12 ns
	MWPC A3-6,11	2011 - 3099	LAT	178 $\times$ 120	15 planes (UXV), σ_x = 1.6 mm
	SciFi 7,8	2128 - 3198	VSAT	12.3$\times$ 12.3	4 planes (XY), σ_x = 210 μm, σ_t = 0.4 ns
	HO 3	2100	Trigger	200 $\times$ 100	2 planes (Y) with hole
	Straw 5,6	2447 - 2587	LAT	280 $\times$ 320	6 planes ($XYUV$), σ_x = 190 μm
	W45	3034 - 3071	LAT	500 $\times$ 250	24 planes ($XYUV$), σ_x = 0.5 mm
	HI 4	3200	Trigger	17 $\times$ 32	1 plane (X)
	ECAL 2	3300 - 3400	PID	245 $\times$ 184	$\frac{\Delta E}{E} = \frac{0.06}{\sqrt{E}} \oplus 0.02$
	HCAL 2	3526 - 3626	PID	440 $\times$ 200	$\frac{\Delta E}{E} = \frac{0.66}{\sqrt{E}} \oplus 0.05$
	MF 2	3700 - 3940	PID	904 $\times$ 904	240 cm concrete before triggers
	HO 4	4005	Trigger	480 $\times$ 225	1 plane (Y) with hole
	HM 4	4024	Trigger	120 $\times$ 102	4 planes (XY)
	HL 4	4056	Trigger	128 $\times$ 40	1 plane (X)
	MWPC B1-6	4188 - 4627	LAT	178 $\times$ 90	9 planes (XUV), σ_x = 1.6 mm
	MW 2	4244 - 4524	PID	447 $\times$ 202	6 planes (XYV), σ_x = 0.6-0.9 mm
	MF 2'	4650 - 4690	PID	904 $\times$ 904	40 cm iron before triggers
	GEM 11	4711	SAT	31 $\times$ 31	4 planes ($XYUV$), σ_x = 70 μm, σ_t = 12 ns
	HM 5	4784	Trigger	150 $\times$ 120	4 planes (XY)
	HL 5	4808	Trigger	168 $\times$ 48	1 plane (X)
	MF 3	4905 - 5065	PID	303 $\times$ 303	160 cm iron before HI5
	HI 5	5100	Trigger	35 $\times$ 51	1 plane (X)

4.3.1 Tracking System

Different tracking detectors are employed in regions at different distance from the beam axis, to match the rate requirements as well as the size of the surface to be instrumented and the required space and time resolution. The tracking detectors are located around the magnets, and they are divided into three groups. These are the VSAT, SAT, and LAT, respectively.

Very Small Area Trackers (VSAT)

In VSAT, three types of tracking devices are used for measuring of the beam particle momentum in COMPASS. Because of the high intensity beam, fast trackers are positioned in the beam, thereby requiring high granularity detectors. The BMS is responsible for beam momentum measurements at the very first stage in front of the target (see Section 4.1). In combination with the BMS, beam tracking is done by three silicon microstrip (SI) [176] detectors and two scintillating fiber (SciFi) [177, 178] stations upstream of the target. The SciFi detectors have a good time resolution in the order of 350 to 500 ps and a spatial resolution of 130 to 250 μm. In contrast with this, the SI detectors have a good spatial resolution of better than 11 μm due to their small pitch, while the time resolution is about 2.5 ns. Therefore the SciFi mainly contribute the timing, and the SI gives the precise spatial information for the beam tracking. The other 6 SciFi detectors are used to provide tracking of the scattered muon and calculating the scattering point, which is the vertex of the primary reaction. These SciFi detectors were installed behind the target throughout the whole spectrometer in 2004.

Small Area Trackers (SAT)

The intermediate region at a radial distance of 2.5 cm to 40 cm is covered by the Small Area Trackers (SAT) in a region with a large number of hadron multiplicity from the interactions and a high flux from the halo muons. Two novel gaseous devices are employed as SAT in this region. Three Micro Mesh Gaseous (Micromegas) [179] chambers are located between the target and SM1, and eleven Gas Electron Multiplier (GEM) [180] stations are distributed throughout the spectrometer. Micromegas are gaseous detectors using a parallel plate electrode structure with an active area of 40×40 cm^2. The detector consists of a thin metal anode grid (micromesh) stretched at a small distance above the microstrip readout electrodes. They have a spatial resolution of about 90 μm and a time resolution of 9 ns. The GEM detectors are realized with an active area of 31×31 cm^2 as triple GEMs, which consists of a metal-clad polymer foil. Two GEM detectors are mounted back-to-back, forming one GEM station. The spatial resolution of GEMs are on average 70 μm, and the time resolution is about 12 ns. A central dead zone with a diameter of 5 cm is deactivated for both detectors in order to avoid too high occupancies on the central strip. Partial overlap with a large area tracker located at the same position along the beam guarantees complete track reconstruction and alignment.

Large Area Trackers (LAT)

Tracking has to be ensured for the full acceptance for particles traversing the detector under larger angles. Therefore a second class of detectors is used providing full coverage of the acceptance. In the outer regions more distant to the beam, large area trackers (LAT) are distributed over the full length between the target and behind the second muon filter. The LAT system incorporates Drift Chambers (DC) [181], Straw Tube drift chambers (ST) [182], Multi Wire Proportional Chambers (MWPC) [183] and the W45 chambers (DW) [184]. Three identical DC are installed closely behind the target with a large active area, fully covering the acceptance. In order to avoid too high rates near the beam a central dead zone of 30 cm diameter was implemented. One pair of ST stations are located in the front and behind the RICH. Another pair of ST stations are installed after the SM2. Three different types of MWPCs are composed of partly different geometrical dimensions, different size of dead zone and active area, and number of layers. They are mostly distributed after SM1 throughout the full spectrometer with a combination of SAT detector. The DW have much larger surface than all other detectors in the category of LAT. DWs are located further downstream behind SM2.

4.3.2 Particle Identification

Particle identification (PID) is provided by a Ring-Imaging Čerenkov detector (RICH) [185], which identifies outgoing hadrons into pions, kaons, and protons up to momenta as large as 43 GeV/c. The scattered muons are detected in the Muon Wall tracking detectors (MW) [186] combined with Muon Filters (MF), which distinguish muons from other charged particles. Two Hadron calorimeters (HCAL) [187, 188] measure the hadron energy and are also part of the trigger system, described in Sect. 4.4. An electromagnetic calorimeter (ECAL) [189] measures the energies of the γ's and e's emitted at small angles.

Muon Identification

The muon identification is performed by two muon filtering systems in the LAS and SAS. Since high energy hadrons do not traverse the absorber, they cannot give a signal in the detector after the absorber. Only muons can pass through the material and make a signal in the detector due to their larger penetration ability. Thus the muon detectors are combined with an absorber. In the LAS, the muon filtering system consists of the first MW1 with iron of 60 cm thickness (MF1). The MF1 is placed behind the first hadron calorimeter. The basic element of MW1 is a gaseous wire chamber of plastic mini drift tubes (Iarocci-Tubes). Because the spatial resolution of MW1 is worse than that of other tracking detectors, it can only be used to decide whether there was a muon or not. In the SAS, the identification of muons behind SM2 is performed by the second MW2 with a 2.4 m thick concrete absorber

(MF2). The principle of MW2 is similar to the one of MW1, except that MW2 consists of drift tubes.

The RICH

Hadron identification in the COMPASS experiment is performed by means of a RICH, which is a part of the large angle spectrometer. According to the requirements of the COMPASS experiment, the RICH has to separate pions, kaons and protons with momenta between 5 GeV/c and 43 GeV/c and has to cover the whole angular acceptance of $\pm$250 mrad in the horizontal and $\pm$200 mrad in the vertical plane. The Čherenkov photons emitted in the gas are reflected by spherical mirrors towards the photon detectors. These detectors are placed either on the top or bottom half and far away from the beam line. The surface of the photon detector is covered with eight segmentations of MWPCs. In each MWPC, the photons are converted to electrons by CsI photo-cathodes. The resolution for pion and kaon separation at the 2.5 σ level is up to 43 GeV/c during the years 2002-2004.

Hadronic Calorimeters

The HCAL1 and HCAL2 mainly serve two purposes in the COMPASS setup. Both hadronic calorimeters measure the energy of hadrons produced in the target and participate in the triggering of scattered muon. Both HCALs are sampling calorimeters using stacks of iron or lead and plastic scintillator plates for the detection of hadronic showers. These are generated by cascades of interactions within the steel and scintillator. Both HCALs have a modular structure in the form of a matrix with central and corner parts partly removed. The calorimeters have a hole of sufficient dimension to let pass the high intensity beam. The hole is shifted to the Jura side because of the beam deflection in SM1 and SM2. To avoid electromagnetic contamination, HCAL1 and HCAL2 is shielded with lead walls and ECAL2, respectively. The energy resolution of the HCALs for hadron energies between 10 and 100 GeV are given in Table 4.2.

Electromagnetic Calorimeter

ECAL2 is a homogeneous calorimeter consisting of lead glass modules. It is located before HCAL2 in part of the SAS and measures the energy of $e^{\pm}$ and γ. Hadrons traversing the ECAL can only be detected by complete absorption in the HCALs due to their larger interaction length, but $e^{\pm}$ and γ are fully absorbed by ECAL2. Measuring the energy of $e^{\pm}$ and γ in ECAL provides a PID for particles electromagnetically interacting. The measured energy resolution of ECAL2 is given in Table 4.2. Although it was originally planned to install two ECALs in each SAS and LAS stage, up to 2004 only the second stage was set up. In 2006, a second electromagnetic calorimeter (ECAL1) was also installed and operated in the LAS.

4.4 The Trigger System

A trigger system is designed to select the scattered muons using dedicated trigger hodoscopes, HCALs, and a veto system [190]. Two main classes of events are selected by the trigger system in COMPASS. The first one covers inclusive DIS events with $Q^2 \gtrsim 1$ (GeV/c)^2 using only information from the scattered muon. These triggers are especially important for the determination of Λ polarization. The second type is implemented for quasi-real photon events with small four momentum transfer $Q^2 \lesssim 1$ (GeV/c)^2 and selects scattered muons with a certain minimum energy loss together with a fast calorimetric trigger rejecting hadrons in the final state.

The hodoscope system is divided into four parts consisting of two hodoscope stations each, the inner, the ladder, the middle and the outer system, which are abbreviated HI, HL, HM, and HO. They give access to different geometrical regions. The HI and HL contain only vertical

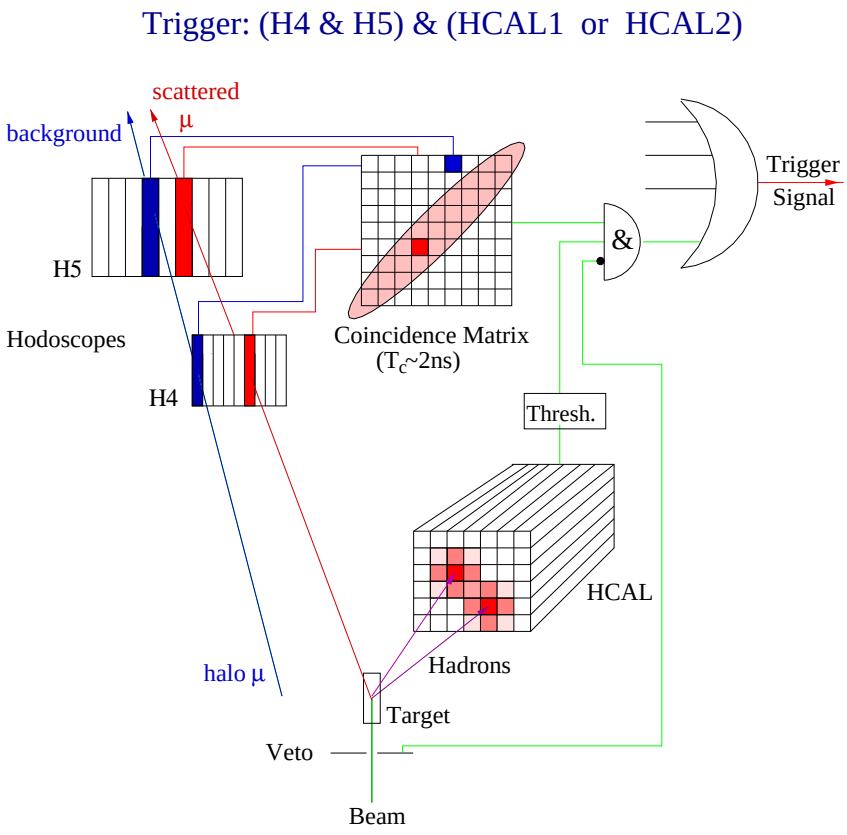

Figure 4.8: Principle Scheme of the trigger decision for DIS events. Halo muons, whose tracks do not point back to the target, are rejected by the coincidence matrix. In addition, a minimum energy deposition in at least one of the two hadron calorimeters is required for the detection of the scattered muon.

elements, whereas the HO has only horizontal planes, and the HM features both projections. In addition, muon selection requires an absorber in front of the hodoscopes to reject hadrons and electrons. HI is set closer to the beam and covers low y events with scattering angles below 5 mrad. The HL covers a region further away from the beam and complements high y events. The HM selects DIS events as well as quasi-real photon events with scattering angles between 4 and 12 mrad. The HO selects only DIS events with large scattering angles. Since there is a contamination of halo muons in the trigger hodoscopes, the different triggers can individually be combined with the information coming from the veto counters. The veto acts as an anticoincidence, thus only events without a hit in the veto counters are recorded. Enable combination with trigger hodoscopes, HCALs and veto system can be realized using a coincidence matrix.

DIS Trigger

In order to ensure that the virtual photon made a deep inelastic reaction, one usually requires its four-momentum Q^2 to be more than 0.1 (GeV/c)^2. In COMPASS, the DIS trigger selects events with a Q^2 between 0.5 and 50 (GeV/c)^2 in the y range from 0 to 0.9. The HM and HO are mainly used to trigger DIS events. This DIS trigger is implemented as geometrical trigger. The horizontal scintillators of the HM4 and HM5 measure the vertical projection of the scattered muon and check its compatibility with the target position (vertical target pointing). Therefore, the two hodoscopes are positioned approximately 10 m apart, as shown in Fig. 4.9. The field of view from the two hodoscope segments defines the volume, which cannot distinguish from the target. If the trajectory of the scattered muon points back from the coincidence signal of two segments to the target, this event will be accepted. Two additional vertical scintillators of the HM4 and HM5 also measure the horizontal projection and allow to

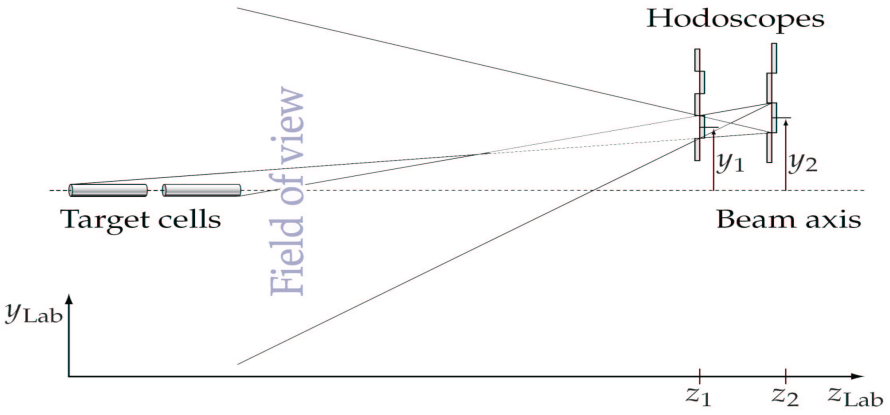

Figure 4.9: Selection of DIS events with geometrical trigger: By requiring a coincidence of pairs of horizontal hodoscope segments the origin of the scattered muons is constrained to the field of view which includes the target. The figure is taken from [191].

perform a coarse energy cut, but it is only used in the trigger for quasi-real photoproduction. The HO3 and HO4 consist of horizontal scintillator slabs only, therefore the HO checks the vertical target pointing. Only veto signals, but no information from the calorimeter, is required to suppress the background.

The Trigger for Quasi-Real Photoproduction

The trigger system for processes induced by quasi-real photons has to select events with a very small four momentum transfer $Q^2 \ll 1$ (GeV/c)^2, corresponding to muon scattering angles close to $\theta \approx 0$ mrad. At the same time, it is required that the photon has a minimum energy fraction of the muon energy y_{min}. This minimum energy loss of the scattered muon is needed to provide a sufficient photon polarization. The energy loss trigger is performed by measuring two different positions along the beam. As is shown in Fig. 4.10, two vertical hodoscopes measure the horizontal positions of the deflected track by magnet, and the momentum can be obtained by measuring the deflection angle in the bending plane. The minimum energy loss of the muon can be determined from the above informations. In order to suppress halo muons, the calorimeter signal has to be correlated with the hodoscope signal.

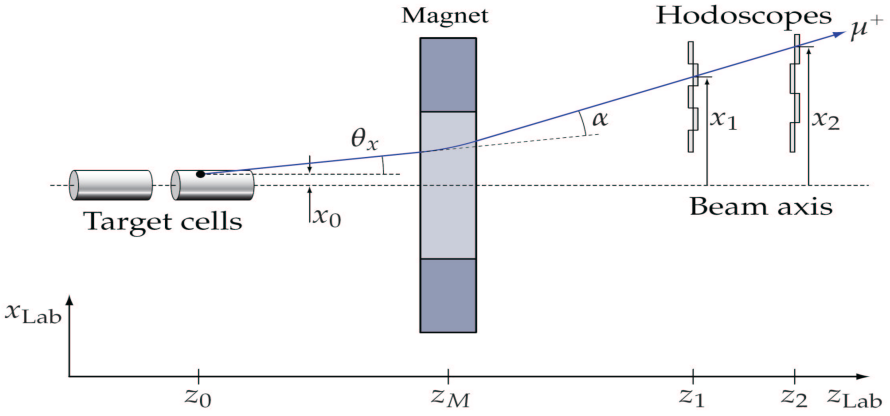

Figure 4.10: Selection of Quasi-Real Photoproduction events with the energy loss trigger: The energy of the scattered muon is determined by measuring its deflection angle in the bending plane of the spectrometer with vertically segmented hodoscope planes. The figure is taken from [191].

Calorimetric Trigger

Events with accidental coincidences by halo muon, which is deflected like a scattered muon in the SM1 and SM2, can lead to pile up in the hodoscope system. Such events can be minimized by triggering on the hadronic calorimeters with an energy deposition exceeding

that of a single muon. Hadronic cascades in the calorimeters are usually spread over several neighboring calorimeter cells and thus form a large cluster. The typical cluster size of hadrons is of the order of the interaction length squared, while the cluster of a muon is localized along its track. The total energy deposition of a halo muon and a hadron can thus be compared by summing over the area around the impact point. After the determination of the energy deposition, a threshold has to be set for an effective suppression of halo muon tracks. A threshold of 6 GeV corresponds to approximately 3 times the energy deposit of the typical single muon and thus rejects those events with an efficiency of more than 90%. Independently a calorimetric trigger is used without connecting the hodoscope system. A second threshold for the calorimetric trigger is set to approximately 9 times the single muon response. The purpose of this trigger is twofold: it extends the kinematic range to large Q^2 values and also allows an evaluation of the hodoscope trigger efficiencies.

Veto System

One of the main tasks of the trigger system is the reduction of halo muons traversing the trigger hodocope. A veto system, which leaves only a small hole for the beam to pass, is therefore installed in front of the target to discriminate the unwanted triggers. An anticoincidence with the veto triggers inhibits the formation of a trigger signal in the two hodoscopes planes. The first veto hodoscope V_1 and second smaller one V_2 are only fully efficient for tracks with a slope greater than roughly 8 mrad due to the limited size of hole in the beam line. Therefore, a third veto hodoscope V_{bl} with a large hole in the beam line was placed further upstream of the target to reject tracks passing through both holes of V_1 and V_2. The reduction of the trigger rate by including the veto system is in the order of 87%.

Trigger Performance

The maximum trigger rate is limited by the event size and the bandwidth of the data transmission from the COMPASS data farm to the CERN data storage system, which is about 30 MByte/s. In 2004, the trigger rates of 14 k and 7 k per spill were achieved for the inner trigger (IT) and the ladder trigger (LT) in coincidence with the calorimetric trigger, 18 k and 9.5 k for the middle trigger (incMT) and outer trigger (OT) without calorimeters and 22 k for the calorimetric trigger (Calo). Summing up to all types of combined triggers lead to a total of approximately 70 k events per spill. The different trigger configurations during the data taking are summarized in Table 4.3. The kinematic range in Q^2 versus y and Q^2 versus x_{Bj} covered by the trigger subsystems are illustrated in Fig. 4.11. The IT and LT cover the low and medium Q^2 region. IT is used to cover the kinematic region $y < 0.4$, while LT covers mainly the region $y > 0.6$. The HO selects muons up to $Q^2 \approx 20$ (GeV/c)^2. The calorimeter is used to extend the kinematic range to very large Q^2 values which can not be covered by the hodoscopes.

Table 4.3: Trigger rates of the different trigger conditions with the nominal beam intensity of 2 $\times 10^8$ in three different years. $V_{1'}$ is part of the hodoscope V_1.

Name	Trigger condition	Rate in 2002 [192]	Rate in 2003 [190]	Rate in 2004 [166]
IT	HI4/5 + Calo1/2	11 K	11 K	14 K
LT	HL4/5 + Calo1/2 + $\overline{V}_{1',bl}$	6 K	6 K	7 K
MT	HM4/5 + Calo1/2 + $\overline{V}_{1,2,bl}$	1.1 K	1 K	1.6 K
OT	HO3/4 + $\overline{V}_{1,2,bl}$	6 K	8 K	9.5 K
Calo	Calo1/2 + $\overline{V}_{1,2,bl}$	–	5 K	22 K
incMT	HM4/5 + $\overline{V}_{1,2,bl}$	11K	20 K	18 K

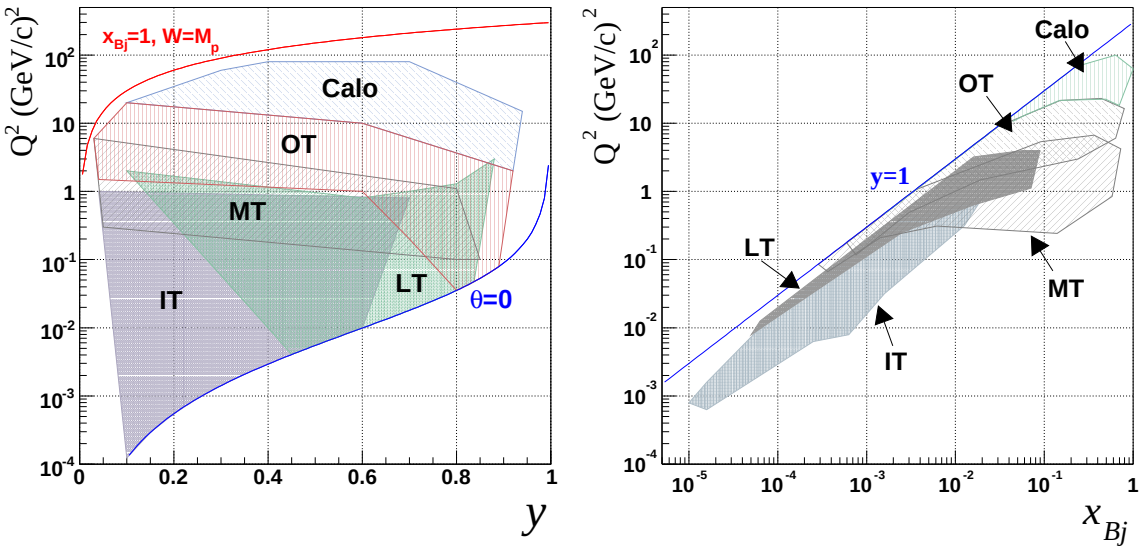

Figure 4.11: Left: The kinematic coverage in y and $Q^2$for the five different trigger subsystems. The line x_{Bj} = 1, W = M_p and θ = 0 show the kinematic limits of elastic scattering and forward scattering, respectively. Right: Region in x_{Bj} and Q^2 selected by different trigger subsystems. The line y = 1 shows the kinematic constraint. Events with a hodoscope trigger are excluded for the Calorimeter trigger.

4.5 Data Acquisition System and Detector Control

4.5.1 Data Acquisition System

The COMPASS experiment consists of approximately 1400 single detector elements and 250,000 electronic channels. The readout electronics has been adopted to cope with an event size of 35 KByte at a trigger rate about 10 kHz for the muon beam. This is done by a pipelined and dead-time free readout scheme. The architecture of the DAQ system [193, 194] in COMPASS is chosen to be very flexible and expandable to allow for upgrades and modifications. A general layout of the data flow is given in Fig. 4.12.

In COMPASS the detectors employed four different types of frontend boards depending on their specific needs. The RICH detector uses the GASSIPLEX chip [195], the calorimeters are read out by fast integrating ADC modules (FIADC). The GEM and silicon trackers on the other hand use a readout based on the APV25 chip [196] developed by CMS. Most tracking detectors are read out via the F1-TDC chip [197] developed by the University of Freiburg. The F1-TDC was designed with flexibility to fulfill all requirements, such as a capability of high data rate and a deadtime free readout with widely different types of detectors.

The digitized data from several frontend devices are transferred to distributed readout driver modules named COMPASS Accumulate, Transfer and Control Hardware (CATCH) [168, 198] or GEm SIlicon Control and Acquisition (GeSiCA) [191], which were developed at the university of Freiburg and TU Munich, respectively. The main task of these readout driver modules are a fast readout of the frontend boards and the local subevent building at data rates of up to 160 MByte/s. In parallel, the Trigger Control System (TCS) [191] provides the trigger signals, time synchronization, and an information on event identification to the CATCH and GeSiCA. The TCS also distributes a reference clock needed for precise time measurement, and provides additional means of control like artificial triggers for calibration. The trigger signals from the TCS are transferred via the CATCH to all connected frontend boards. At the beginning of a data taking the CATCH initializes all connected frontend boards. The GeSiCA works similar to the CATCH, but is optimized for the readout of GEM and Silicon detectors.

Through optical fibers (S-link) [199] the data collected from CATCH or GeSiCA are then transferred to readout buffer PCs (ROB). The ROBs store the received data on PCI cards called spillbuffers. The regrouping and event building of the data streams is supported by those spillbuffers. These allow to make use of the break in the SPS accelerator's duty cycle to reduce the sustained data rate to a third of the onspill rate. Four spillbuffers per ROB can be mounted. A S-link multiplexer (SMUX) module was developed to minimize the number of spillbuffers. Four CATCH modules can be connected to a SMUX.

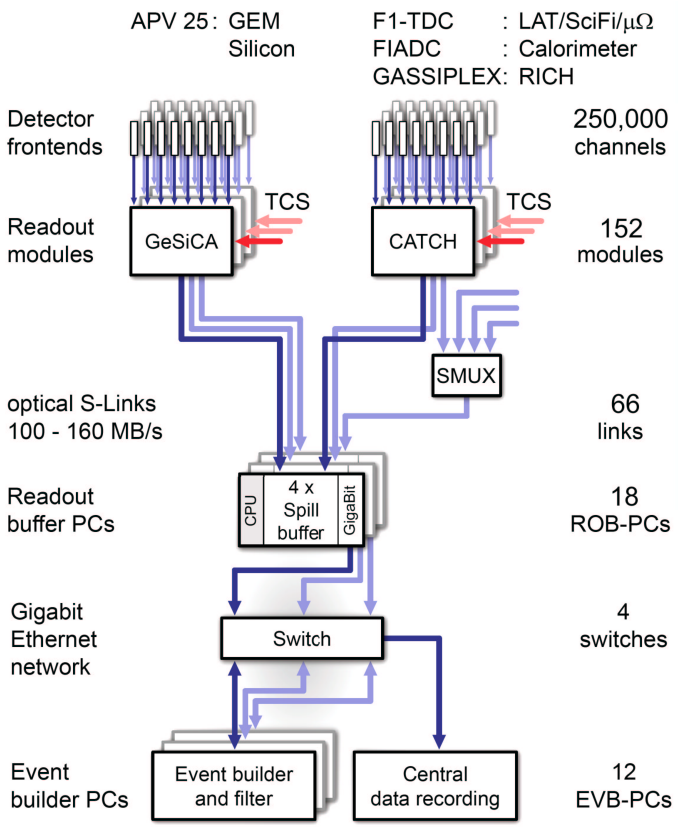

Figure 4.12: General architecture of the DAQ system. Digitized data from the front-ends are combined on the readout modules (CATCH and GeSiCA) close to the detectors. The storage of the data during the spill and the event building is performed locally. The data are recorded at the CERN computer center.

For further processing the information of each subevent in the ROBs, which do not contain the full information from all detectors, are transferred via three Gigabit Ethernet switches to the event builder (EB) computers. The subevents arriving from different ROBs are combined together according to the complete event blocks, which include the data of all detectors. The total bandwidth available for event building amounts to 12 GBit/s. Starting with the beam time in 2004, an online filter was used to reduce the event size. The online filter increases the purity of the triggers and allows for a cost effective reduction of the amount of tapes, as well as providing a reduced CPU time for the reconstruction of the data.

The finalized and filtered events in the EBs are asynchronously transferred through the network via a dedicated Gigabit Ethernet switch to the central data recording system, where they are temporarily stored on disk, before they get migrated to the tapes of the CERN Advanced STORage system (CASTOR) [200]. Typically, 50,000 events were recorded per spill of 4.8

s at a trigger rate of 10^4/s. With an average event size of 35 kByte this equals to an onspill data rate of 356 MByte/s. Due to the buffering the data rate results in a sustained rate of 106 MByte/s before the online filter. The online filter discarded 23% of the data in 2004, thus further reducing the data rate to 80 MByte/s. The total amount of raw data recorded in the beam times 2002-2004 with longitudinal target polarization was 612 TByte.

The main software used for the COMPASS data acquisition is based on the Alice DATE [201] package, which provides components for event building, run control, information logging, and event sampling. Few modifications have been applied to the readout routines of the ROBs to optimize the input and output.

4.5.2 Detector Control and Monitoring System

The main task of the Detector Control System (DCS) is to provide an interface for experimental setting and reading all the relevant parameters during the operation of the various detectors. High and low voltage, VME crate status, gas mixtures, temperatures, and magnetic fields are displayed as a function of time and are controlled in a graphical user interface (GUI). The readout chain and the front-end electronics of the detectors are monitored by a software tool called MurphyTV [202]. Failures of the read-out chain are detected by error words generated by the electronic boards, or by inconsistent formats of the data structure. A software named COOOL has been designed to read COMPASS raw data streams and produces histograms for each detector plane in form of a ROOT [203] tree. A large variety of informations from online monitoring, trigger conditions, DAQ system, SM1 and SM2, COOOL histograms, beam line, and target polarization are stored to keep track of the experimental setup in a MySQL database which is maintained through a web interface [204].

Chapter 5

Data Analysis

The main focus of the research presented in this thesis is understanding the spin transfer from a quark to hyperons in the fragmentation process. This chapter describes techniques used to extract the spin transfer of the Λ hyperon. Section 5.1 introduces some general information about the software used in the data analysis. This section can also be understood as a snapshot of the data processing procedures. In Section 5.2, the event selection and the topology of the Λ, $\overline{\Lambda}$, and K^0 decays are described including applied cuts and treatment of background processes. A Monte Carlo simulation is employed to correct acceptance effects in the COMPASS apparatus. Section 5.3 explains how the Monte Carlo data were generated and reconstructed. In addition a comparison of data and Monte Carlo is addressed to verify the accuracy of the acceptance correction. The coordinate system as well as the method to extract the polarization from the selected data sample are then thoroughly explained in Section 5.4. After summarizing the overall results from 2002-2004 data samples in Section 5.5, the uncertainties of the results are evaluated from various systematic studies, which are described in Section 5.6. Especially the possible sources of systematic errors from Monte Carlo will be addressed in more detail. In the last Section 5.7 the dependence of the spin transfer for Λ and $\overline{\Lambda}$ on the various kinematic variables is presented.

5.1 Data Reconstruction

The analysis is based on the data taken with longitudinally polarized target and muon beam in the years 2002, 2003, and 2004. The raw data files produced by the DAQ system contain the digitized detector informations. The raw data is divided into so-called runs with 200 spills, which correspond to roughly one hour of beam time. Before a physics analysis can be performed, the physical information has to be extracted from the raw data, which is done by the COMPASS Reconstruction and Analysis software (CORAL) [205]. It is a fully object oriented program with a modular architecture written in C++.

Two initial processing phases are needed to prepare the track and vertex reconstruction [166].

In the first phase called decoding, the hit information of the detector channel is extracted from the raw digits. In a second phase, detector channels are grouped together according to the passage of the same particle. During this so-called clusterization phase, the information on the measured position in each detector plane is used to calculate the coordinate of the cluster in the main reference system of the apparatus. The geometrical position of each detector plane is retrieved from a data file which was determined either from the alignment procedure or the Monte Carlo package. The clusters are then pre-selected on the basis of time information i.e., time calibration. When Monte Carlo data files are processed, the decoding phase is replaced by a digitization phase, in which the response of the detector is simulated and hits are produced on the basis of the particle trajectory and detector resolution. After clusterization, charged and neutral particles are reconstructed and particle identification is performed. The information of tracking detectors is used to reconstruct the trajectories of charged particles through the spectrometer, while the calorimeter clusters are used to separate muons from hadrons and to measure the energy and impact coordinates of photons.

The procedure of track reconstruction [206, 207] is divided into three phases corresponding to pattern recognition, bridging, and global fitting. The pattern recognition selects sets of clusters which show patterns that agree with track segments found in the various zones of the spectrometer. For this purpose, the spectrometer is divided into 5 zones, in which the tracks are expected to be straight lines. Such zones are defined by particular spectrometer parts from the target to MF2. Track candidates are separately searched for in every zone and for each available projection, based on the number of clusters and on the azimuthal angle of the track. The track segments found in several distinct zones are then combined by extrapolation to build a full track. The successfully combined track segments are fitted and then sorted according to a quality function, which takes into account the χ^2 of the fit. The combination with the best quality function is retained, while combinations of previously accepted segments are discarded. This process is iterated until the list is exhausted. In the third step of the track reconstruction, the magnetic fields and material maps are used to get the best estimate of trajectory parameters and error matrix of charged particles. The parameters and error matrices of the bridged tracks are calculated using a Kalman fit method [208, 209]. This fit starts from the first cluster of the found track and then the calculated track parameters are propagated to the next detector surface. The same process is repeated for all found clusters. The Kalman fit is performed twice, first in the direction of the beam and then in the opposite direction, in order to provide the track parameters at the first and last measured point of the track.

After the track reconstruction, the stage is moved into the vertexing procedure [210], which is performed to identify the primary interaction point and subsequent decays of neutral particles with all reconstructed tracks. To reconstruct the primary interaction point, the beam and the scattered muon have to be identified. Since more than one beam track can exist in the time slot for one event, as many primary vertices as the number of existing beam tracks can be reconstructed in this phase. A first approximation of the primary vertex is obtained by

computing the closest point between one beam track and all possible outgoing tracks, which are not too far away from the center of the target. The tracks surviving the initial selection are used to perform the global fit of the vertex position by an inverse Kalman filter. During the first iteration, all tracks are used to estimate the parameters of the vertex, and the relative χ^2 value of each track to the fit is computed. If the largest χ^2 exceeds a certain threshold, the corresponding track is removed from the list and the procedure is iterated once more with the remaining tracks. Secondary vertices are searched for by combining all pairs of two tracks with opposite charge, regardless of their association to primary vertices.

The output of the vertexing procedure are the vertex coordinates and the fitted parameters of the tracks associated with the vertex. The results of the tracking and vertexing reconstruction are stored in so-called Data Summary Table (DST) files. In addition, the Mini Data Summary Tape (mDST) files can be simultaneously produced with the Physics Analysis software Tool (PHAST) [211] in CORAL. This means that the mDST files are either produced from the raw data directly or converted from DST files. The mDST files contain only events with at least one reconstructed vertex, either primary or secondary vertex. In case of Monte Carlo events, mDST files contain the generated information as well as the reconstructed information.

The reconstructed data in the mDST files is analyzed with PHAST. One can select the interesting events for the purpose of an analysis and save them into a tree class derived from the ROOT framework or into reduced mDST in the same format. The data reduction factor between the input raw data and the output mDSTs is about 80. The total size of all mDST files for this analysis with longitudinal target polarization is 7.6 TByte and contains 5.6×10^6 events. The analysis of Λ and $\overline{\Lambda}$ polarization was performed with a cluster of 200 PCs with a batch system at CERN, at the Grid Computer Centre Karlsruhe (Gridka) [212] and at a powerful local computer cluster at Freiburg. To process the data, a $Q^2 > 0.9$ (GeV/c)^2 cut is applied and the results are saved in so-called nano-DST (nDST) files, which contain only the DIS events needed for the Λ and $\overline{\Lambda}$ analysis. In the last step, the Λ and $\overline{\Lambda}$ events are extracted from nDST files and collected in classes of ROOT trees. Such files can then be easily analyzed further on an event-by-event basis within the standard ROOT software, which has been developed at CERN for high energy physics and which is a powerful tool for displaying, fitting and storing complex data structures. At the time of this work, the mDST production was constantly being updated, the slots in Table 5.1 correspond to the date of production versions for the mDST files.

Table 5.1: Summary of data sets used for the present analysis. The slots are correspond to the produced version and date of mDSTs [213]. The nDST Data sets are preselected applying $Q^2 > 0.9$ (GeV/c)^2 for DIS candidate events.

Period	Slot	mDST file size [GByte]	Number of events [10^6]	Number of events $Q^2 > 0.9$ (GeV/c)^2 [10^6]
2002/P1C	2	166	117.038	4.840
2002/P2A	2	288	223.635	9.794
2002/P2D	3	174	134.973	5.619
2002/P2E	2	251	178.741	7.751
2002/P2F	2	121	82.002	3.741
2002/P2G	2	200	164.716	6.340
2002		1200	910.222	38.088
2003/P1A	1	182	156.010	8.834
2003/P1B	1	145	130.449	8.219
2003/P1C	1	166	141.225	9.389
2003/P1D	1	204	172.001	11.938
2003/P1E	1	284	212.824	15.093
2003/P1F	1	199	169.254	11.518
2003/P1I	3	272	202.695	13.208
2003/P1J	2	442	325.133	21.079
2003		1894	1509.595	99.281
2004/W22	2	584	402.309	21.756
2004/W23	3	363	244.877	10.707
2004/W26	2	376	236.196	14.168
2004/W27	2	215	136.127	8.125
2004/W28	2	232	185.131	12.407
2004/W29	1	213	166.830	11.088
2004/W30	2	315	224.947	13.226
2004/W31	2	293	210.151	12.506
2004/W32	2	416	300.973	17.923
2004/W37	3	450	336.027	20.457
2004/W38	2	547	360.236	21.288
2004/W39	2	314	204.816	11.635
2004/W40	3	229	150.617	8.863
2004		4546	3159.242	184.155
Overall		7640	5579.059	321.525

5.2 Event Selection

The neutral Λ particle cannot be seen as a track in the spectrometer. The only way to identify Λ in the COMPASS experiment is to look for their charged decay products in the decay channel $\Lambda \to p\pi^-$. The Λ is not the only particle that decays with such a signature, there is actually a whole class of two-particle decays. They exhibit a V-shaped decay structure, and that is why this kind of decay is called V^0. The typical topology of a V^0 event is shown in Fig. 5.1. A V^0 appears as two tracks emerging from a secondary vertex, which is usually located downstream of the target, with the reconstructed total momentum pointing back to the primary vertex.

In principle the identification of particles can be done using a RICH detector. However, the RICH is not employed to identify the tracks from the V^0 decay particles, because of the rather high pion and proton thresholds. The identification of protons for the RICH requires that their momentum is larger than 18 GeV/c. It turns out that the mean momentum of proton from the V^0 decay lies below this threshold, so that no RICH information is used in this analysis. The background to the V^0 signals coming from primary vertex tracks and low momentum tracks can be effectively separated from the signal by using appropriate cuts and track selection. Consequently, the Λ selection relies purely on kinematic information. After the reconstruction of tracks and vertices as described in Section 5.1, a series of cuts is therefore applied to reduce background events and enrich the sample with Λs.

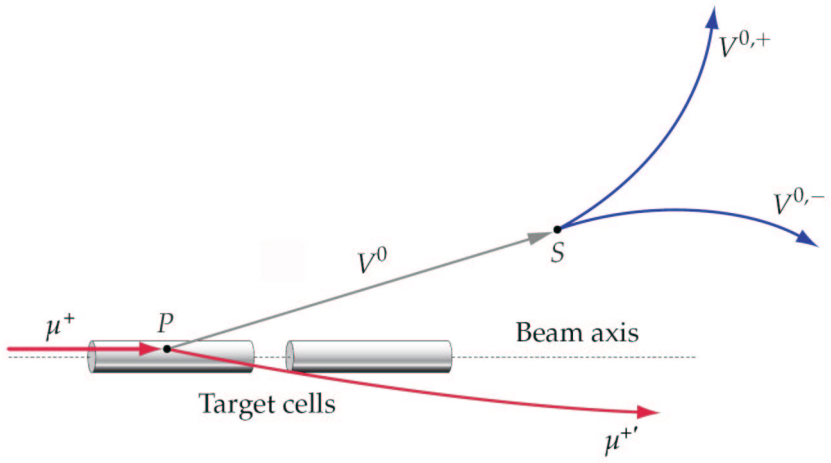

Figure 5.1: V^0 event signature: An incoming beam muon scatters off a target nucleon in the primary interaction point P and creates a V^0 particle, which is neutral and thus cannot be seen by the apparatus. Some distance apart from the primary vertex the V^0 decays into two tracks of opposite charge at the interaction point S. The figure is taken from [191].

5.2.1 Selection of Primary Vertex

Events were selected in which the primary vertex contains at least two charged tracks, a beam track, a scattered muon and two additional tracks to form a secondary vertex. The primary vertex has to have exactly one incoming beam particle and one scattered muon. Since there may be several candidates of primary vertices in one event, events have been selected with the best primary vertex, which is the one with the maximum number of tracks and smallest χ^2 of vertex [214]. The scattered muon is identified using the function predefined in PHAST. A track is identified as a scattered muon, if it has a hit in the hodoscope behind the second muon filter, and if the extrapolated track points within 5 cm radius to the entrance of the target and has a distance to the beam axis of less than 2 cm. The identification of the scattered muon is improved by the requirement that they traverse an amount of material, which corresponds to more than 30 radiation length. If the event has been triggered by the calorimeter trigger and no scattered muon is identified in the hodoscopes, the first muon filter is used to recover the scattered muon. Such a track must have at least 6 hits in the 8 planes of the detector which are located behind the first hadron absorber.

In order to select DIS events, Q^2 is required to be larger than 1 (GeV/c)^2. The cut on $Q^2 >$ 1 (GeV/c)^2 drastically reduces the statistics since about 90% of the data are below $Q^2 < 1$ (GeV/c)^2. To ensure a constant data quality, bad runs and spills with obvious problems were excluded. The lists of bad runs and spills [215] are generated by checking the time evolution of the average number of primary vertices, beam tracks, outgoing tracks, and the number of tracks associated with the primary vertices. If one of the parameters deviates more that 5σ from the average value, if it has too low statistics, or if it exhibits a large systematic shift with respect to the neighboring spills in the variables mentioned before, this spill is marked as bad. Most of such deviations are correlated to detector problems or changes of the trigger settings. In total about 13% of the spills are marked as bad ones, but they contain on average less events than the good spills. The exclusion of bad runs and spills has been done on a spill-by-spill level in this analysis.

The primary vertex has to be inside the target, this is ensured by demanding, that the z-coordinate of the primary vertex is in the upstream target cell $-100 < z_{prim} < -40$ cm or in the downstream target cell $-30 < z_{prim} < 30$ cm along the beam axis. Its radius R_{prim} has to be smaller than 1.4 cm, which is a bit below the true target cell radius of 1.5 cm, to compensate the imperfect alignment of the target and its movement due to the changing solenoid field. Additionally, it was found that the target cells are not completely filled with material, so the y-coordinate of the primary vertex is required to be $y_{prim} < 1.0$ cm. For these target geometry cuts, a reference frame associated to the inclined target [216] is used instead of the nominal coordinates. In addition, the extrapolated beam muon trajectory is required to completely traverse both target cells in order to equalize the beam flux through both target cells. In Fig 5.2, the distribution of primary vertices along the beam axis and the distribution

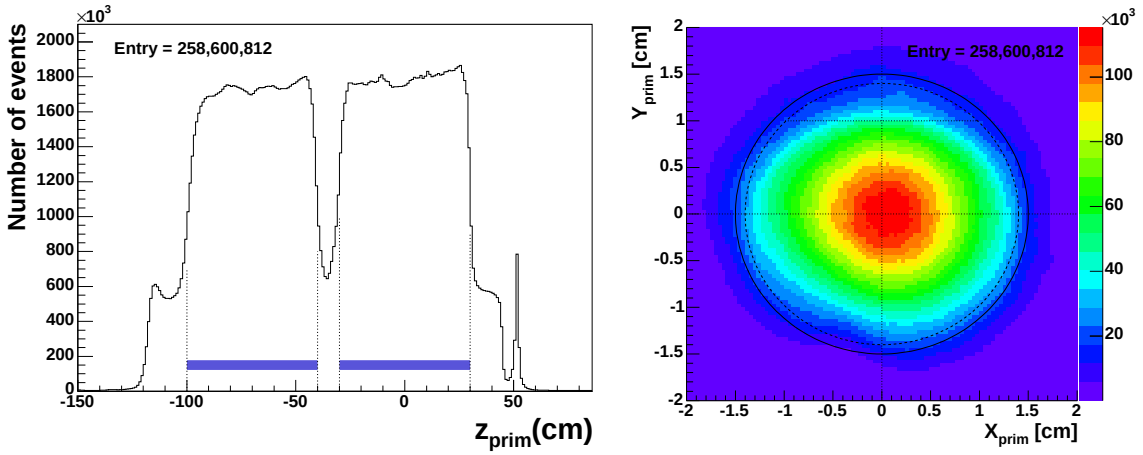

Figure 5.2: Left: Distribution of primary vertex position along the beam axis before applying the beam crossing and the target cuts. Blue bars in horizontal direction and dotted lines in vertical direction correspond to the two target cells. These two cells are clearly separated in the vertex reconstruction. The peak at $z_{prim} \approx 50$ cm is caused by the window of the target microwave cavity (see Fig. 4.5). Right: Radial distribution of the position of the primary vertex. The outer circle corresponds to the nominal target radius, the dashed inner circle indicates the applied cut $R_{prim} < 1.4$ cm. The effect of $y_{prim} < 1.0$ cm indicated by a dashed line is shown in the top region of the target.

of radial positions before applying the beam crossing and target cuts are shown.

In the track reconstruction a particle is tagged as a scattered muon if it fulfills one of two criteria [214]. The scattered muon track must be compatible with the trigger hodoscope hits as given in the trigger matrix. In the case of a track ending before the hodoscope, an event has been also accepted if there is a cluster due to the multiple scattering within one slab size of the extrapolated track. To ensure the muon identification quality the scattered muon track is additionally required to have at least one hit in both hodoscopes corresponding to the event trigger type. This leads to the rejection of events with multiple scattering in the trigger hodoscopes.

The fractional virtual photon energy y specifies which fraction of the lepton energy in the laboratory system is transferred to the nucleon. It is required to fulfill the condition $0.2 < y < 0.9$. High y events are discarded because they are affected by radiative effects, and their systematic uncertainties become too large to be incorporated. In addition, the agreement between data and Monte Carlo decreases rapidly for $y > 0.9$. The lowest value corresponds to the minimum of y which is only possible with the trigger system in COMPASS. The low y events are mainly selected by the inner trigger, they correspond to quasi-real photon events with small Q^2. Quasi-real photon events can be effectively suppressed with a cut on $y > 0.2$.

Furthermore, the efficiency of the inner trigger is drastically reduced in the range below 0.2 [190]. The above cuts are summarized in Table. 5.2. They select a sample of 65,883,218 events with a good definition of a primary vertex. The selected events contain on average 2.77 V^0 candidates per primary vertex. Fig. 5.3 show the invariant mass plots of the selected V^0 sample with $m_{p\pi^-}$, $m_{\overline{p}\pi^+}$ and $m_{\pi^+\pi^-}$ for the Λ, $\overline{\Lambda}$ and K^0 hypothesis. Since the V^0 samples contain a lot of background, an additional set of cuts on the V^0 candidates are introduced to reduce the background under the Λ and $\overline{\Lambda}$ signal in the following subsection.

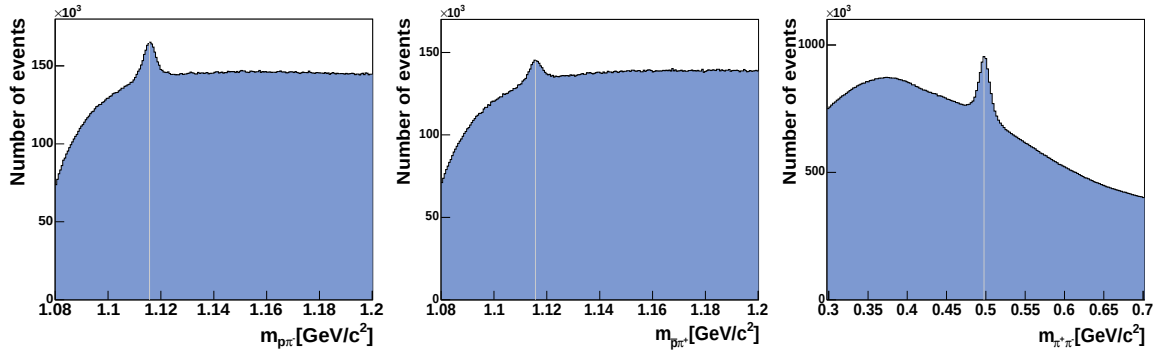

Figure 5.3: Invariant mass distribution of the V^0 sample for the $m_{p\pi^-}$, $m_{\overline{p}\pi^+}$ and $m_{\pi^+\pi^-}$ for the Λ, $\overline{\Lambda}$ and K^0 hypothesis after the selection of a primary vertex. The lines indicate the PDG values of the Λ, $\overline{\Lambda}$ and K^0.

Table 5.2: Summary of the event selection cuts: The table lists how the different cuts reduce the absolute and relative number of events.

Cut	Number of Events	
	[10^6]	[%]
Initial data set	5579.09	100.00
Best primary vertex	5003.57	88.48
Definition of scattered μ' : $X/X_0 > 30.0$	3388.84	60.80
DIS events : $Q^2 > 1.0$ (GeV/c)^2	288.54	5.15
Exclusion of bad spills and runs	258.60	4.62
Beam crossing through the target	200.25	3.57
Events in target ($R_{prim} > 1.4$ cm, $y_{prim} > 1.0$ cm)	164.67	2.94
At least one hit of scattered μ' in both trigger hodoscopes	147.69	2.64
$0.2 < y < 0.9$	65.88	1.18

5.2.2 Selection of V_0 Events

A secondary vertex formed in the reconstruction is required to have no incoming track and to be separated from the primary interaction point. Because of the finite spatial resolution of the measured charged particles V^0 vertices close to the primary vertex could be the result of wrong track combinations. This effect is suppressed by demanding that the V^0 vertex is located downstream of the primary vertex.

The ratio of signal over background and the mass resolution of the Λ hyperon depends on the z_{V_0} position of the decay vertex. If the Λ decays inside the target cells, the background increases strongly as shown in the Fig. 5.4. A good compromise to keep as many Λ as possible and get a much better resolution of the mass spectrum is to take secondary vertices with $z_{V_0} > 35$ cm. There is also an upper limit to the position z_{V_0} of the decay vertex, where one of the decay tracks traversed the Micromegas with their high spatial resolution and therefore provide a precise track reconstruction leading to a good mass resolution. Consequently z_{V_0} is restricted to values smaller than 140 cm, which is the position of the first Micromegas. In

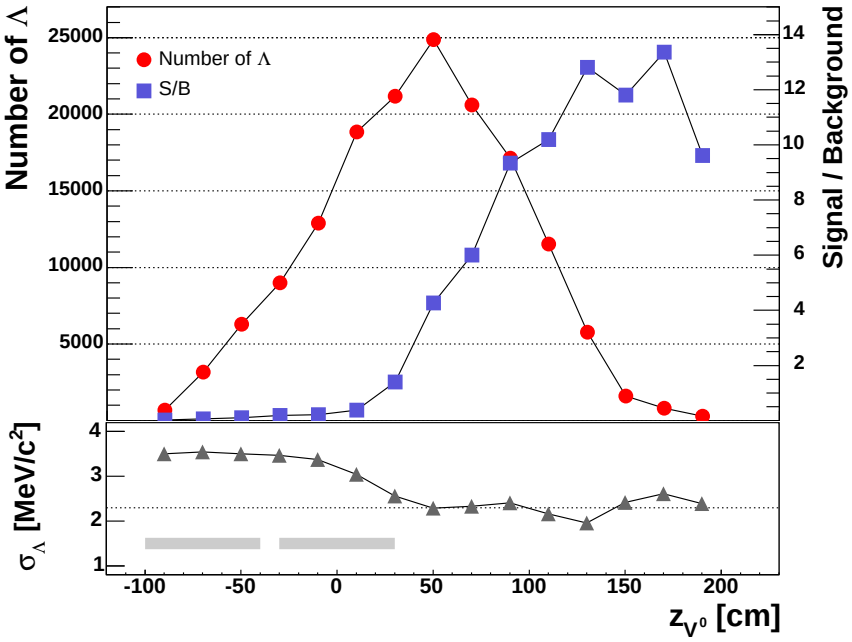

Figure 5.4: Decay position of Λ. The figure shows the dependence of the absolute number of events (red circles) and signal to background ratio (blue squares) on the decay position. Additionally, the width of the Λ mass resolution is given in the lower plot (grey triangles). The position of the two target cells is sketched for reference as grey bars between -100 cm and 30 cm. The plot was produced with final cuts applied, except for a cut on the longitudinal position of the decay vertex.

addition, it has been found that the number of reconstructed V^0 in data and Monte Carlo is slightly different for $z_{V_0} > 140$ cm. For consistency of data and Monte Carlo it is better to apply the cut $z_{V_0} < 140$ cm.

The reconstruction of the V^0 vertex is generally performed in CORAL. The precision of the vertex determination depends on momentum vectors and covariance matrices of the two tracks. A least-square estimator called Kalman filter was employed to calculate the most probable position and corresponding error matrices by combining all pairs of tracks at the V^0 vertex. The hit information of the tracking detector are not used in the vertex fit. Input for the vertex fit are five parameters per track, which are x, y, dx/dz, dy/dz, $1/p$ at certain z positions of the vertex. Output of the vertex fit are three parameters (dx/dz, dy/dz, $1/p$) per track and the position of the vertex (x, y, z) [217]. It is assumed that tracks originate from the same vertex position. Thus the number of degrees of freedom (ndf) for the vertex fit is

$$\text{ndf} = 5 \cdot n_{\text{out}} - (3 \cdot n_{\text{out}} + 3) = 2 \cdot n_{\text{out}} - 3, \tag{5.1}$$

where n_{out} is the number of outgoing tracks in the vertex. For the V^0 vertex two outgoing tracks are involved, so that the ndf of the V^0 vertex fit is fixed to 1. In the V^0 vertex finding algorithm large χ^2/ndf values are rejected by a threshold value of 10. However, the cut χ^2/ndf < 10 is too mild to make sure of true Λ and $\overline{\Lambda}$ in practice. To improve the reconstruction quality of the secondary vertex, the reduced χ^2 of the secondary vertex is required to be below 2. The distributions of the reduced χ^2 values of the secondary vertex is shown after and before the cut was applied in the top and left plot of Fig. 5.5. To make a judgment about the goodness-of-fit of the V^0 vertex in the selected V^0 sample, the χ^2 probabilities are used. The calculation of the probability for a χ^2 and a ndf are based on the gamma function. The relevant quantity of a χ^2 probability is the integral [218]

$$P(\chi^2, \text{ndf}) = \int_{\chi^2}^{\infty} P(\chi'^2, \text{ndf}) d\chi'^2. \tag{5.2}$$

For two different ndfs, the corresponding χ^2 probabilities are shown in the top and right plot of Fig. 5.5. By requiring the reduced χ^2 to be less than 2.0, the V^0 candidates are selected with a χ^2 probability to be larger than 0.157. The effect of cut on $\chi^2 < 2.0$ is shown for the $m_{p\pi^-}$ and $m_{\overline{p}\pi^+}$ invariant mass distribution in the bottom panel of Fig. 5.5.

In the first part of the spectrometer region, the fringe fields of the target solenoid and SM1 dipole magnet overlap. Tracks with very low momenta are particularly sensitive to the magnetic field. This makes track and vertex reconstruction more difficult and results in a less precise momentum measurement for small momentum tracks due to the complicated interplay of two fields. To avoid this problem, the momentum of the V^0 daughters is required to be larger than 1 GeV/c. In order to ensure a precise measurement of the momentum of the V^0 decay particles and thus of the reconstructed V^0 mass, the daughter tracks are required to have

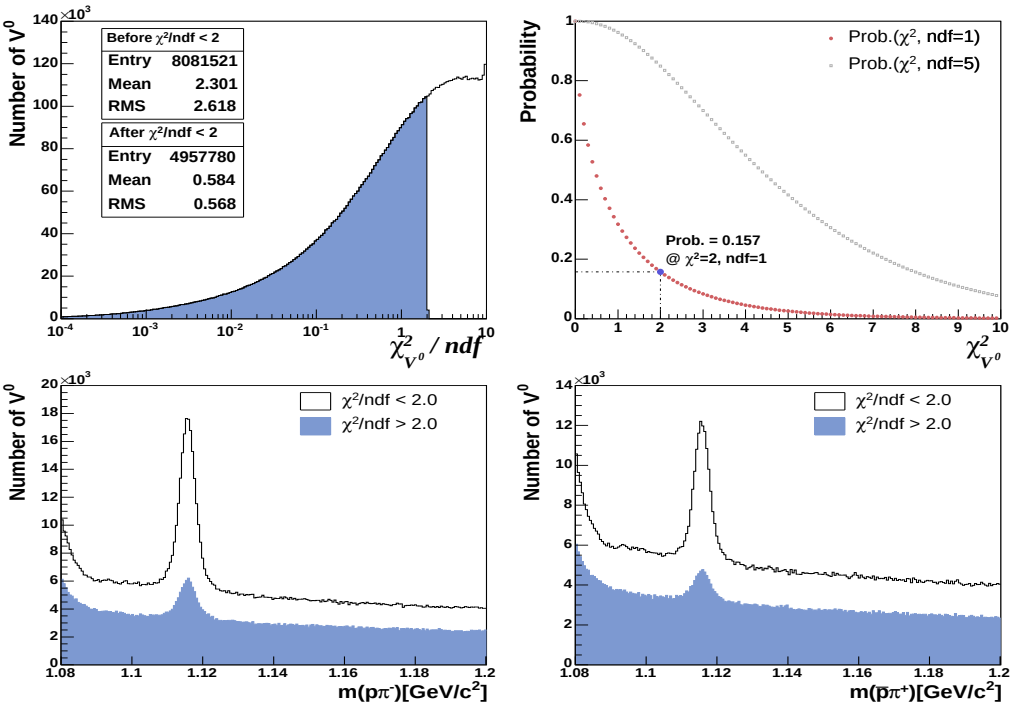

Figure 5.5: Top: Distribution of χ^2/ndf for the reconstructed V^0 vertices (left). The filled histogram shows the events with $\chi^2/\text{ndf} < 2$. χ^2 probabilities are shown for ndf = 1 and ndf = 5 (right). The blue point at $\chi^2 = 2.0$ corresponds to the applied cut with ndf = 1. Bottom: The invariant mass histograms of $m_{p\pi^-}$ and $m_{\overline{p}\pi^+}$ hypothesis are plotted with the applied cut on $\chi^2/\text{ndf} < 2$. The blue areas show the rejected events with a cut on $\chi^2/\text{ndf} > 2$.

passed through the first spectrometer magnet SM1. This is accomplished by demanding the last measured point with an z larger than 350 cm. This criteria was introduced because it was found that the fringe field tracks, which ended before the SM1 magnet, have significantly different reconstruction precision. A comparison between the momentum measurement of two tracks by demanding $h^{\pm} > 1$ GeV/c and h^+ or $h^- < 1$ GeV/c has been made for the $m_{\pi^+\pi^-}$ invariant mass distribution in the left plot of Fig. 5.6. In the right plot of Fig. 5.6 the $m_{\pi^+\pi^-}$ invariant mass distributions is shown as well as by requiring the cuts on $z^{\pm}_{last} > 350$ cm and z^{+}_{last} or $z^{-}_{last} < 350$ cm, separately. If two tracks are reconstructed with insufficient momenta and length, the reconstructed invariant mass under the $m_{\pi^+\pi^-}$ assumption does not contribute to the signal. The situations are the same for the $m_{p\pi^-}$ and $m_{\overline{p}\pi^+}$ assumptions for Λ and $\overline{\Lambda}$. Consequently, these cuts reduce efficiently the background contribution to the V^0.

The Λ hyperon has two main production mechanisms. On the one hand, it can be produced directly in the primary interaction. On the other hand it can be a decay product from heavier hyperons like Σ or Ξ. These decay channels are experimentally difficult to separate. If the Λ

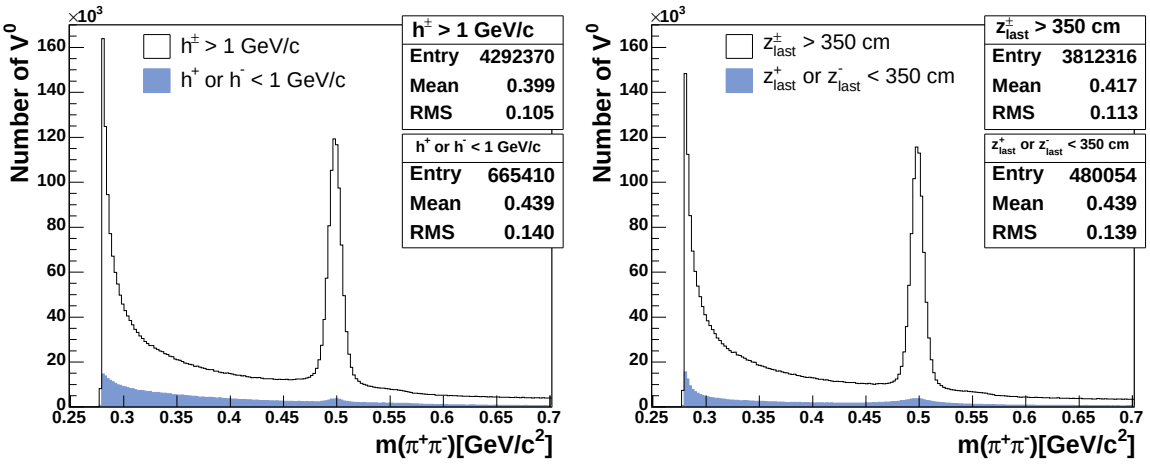

Figure 5.6: Left: The invariant mass histograms of hadron pair assuming $m_{\pi^+\pi^-}$ hypothesis are plotted with an applied cut on $h^{\pm} > 1$ GeV/c and h^+ or $h^- < 1$ GeV/c (filled histogram), separately. Right: The $m_{\pi^+\pi^-}$ invariant mass distributions by demanding $z^{\pm}_{last} > 350$ cm and z^+_{last} or $z^-_{last} < 350$ cm (filled histogram).

originates from a decay of heavier hyperons, the Λ would have a higher transverse momentum with respect to the heavier hyperons because of an additional γ or π track. The fraction of direct Λ can be enhanced by imposing a cut on the angle between the reconstructed Λ momentum direction and the direction connecting the primary and the Λ vertex, which is called the collinearity angle. The θ_{col} distribution of V^0 events for the overall data sample is shown in the top and left panel of Fig. 5.7. In the top and right panel of Fig. 5.7, the θ_{col} distribution of the true Λ events for the Monte Carlo sample is compared with the selected V^0 data sample. Most of true Λ events in Monte Carlo is not affected by the collinearity cut. From the Monte Carlo study it has been found that a limit of $\theta_{col} < 0.01$ rad is optimal for direct Λ events [219]. The $m_{p\pi^-}$ and $m_{\overline{p}\pi^+}$ invariant mass distributions are shown to see the effect of the cut on $\theta_{col} < 0.01$ rad in the bottom panel of Fig. 5.7.

The Λ and $\overline{\Lambda}$ still sit on a non-vanishing background. A further cleanup of the Λ and $\overline{\Lambda}$ sample is achieved by cutting on the region of low transverse momenta p_T of the decay products with respect to the direction of V^0. A cut on $p_T > 0.023$ GeV/c was applied to reject the remaining background of e^+e^- pairs from γ conversion. The decay $\gamma \to e^+e^-$ has a very small phase space leading to a prominent broad line at low p_T. The e^+e^- pairs of the V^0 candidates can be easily visualized in the so-called Armenteros-Podolanski plot, which will be discussed in more detail in the following section. Table 5.3 summarizes the applied V^0 selection cuts. The final data sample consists of 1,252,173 V^0 vertices, that will define the Λ and $\overline{\Lambda}$ samples used for the polarization analysis.

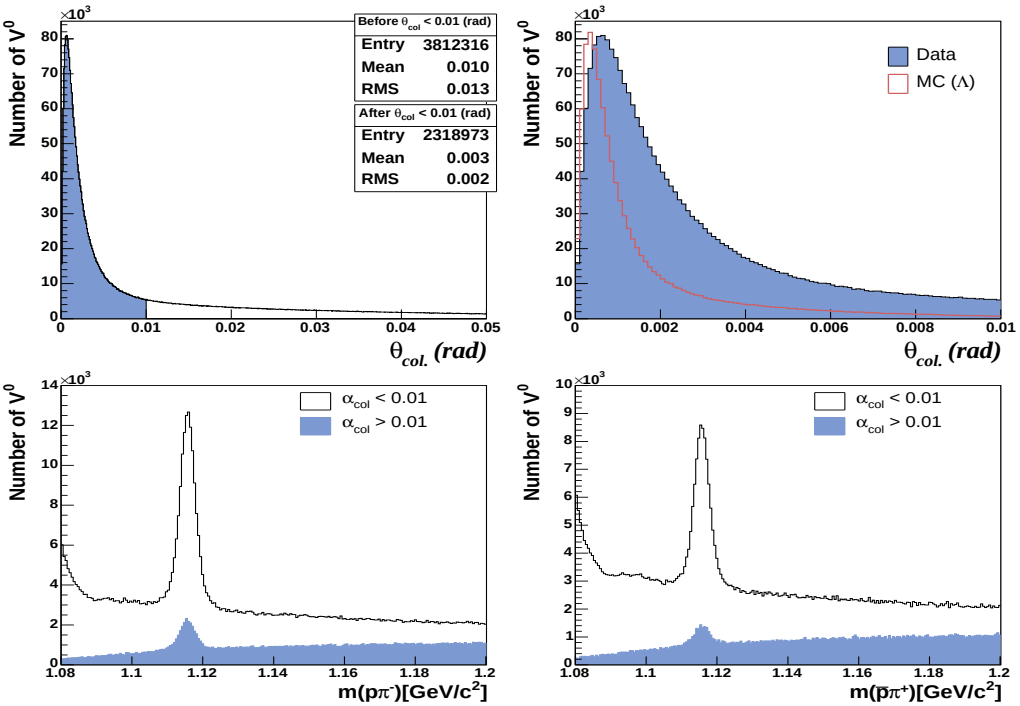

Figure 5.7: Top: θ_{col} distributions of the reconstructed V^0 vertices (left). The filled histogram shows the events with $\theta_{col} < 0.01$. θ_{col} distribution of the reconstructed true Λ for Monte Carlo is compared with V^0 candidates for the data sample (right). Bottom: The invariant mass histograms of $m_{p\pi^-}$ and $m_{\overline{p}\pi^+}$ hypothesis are plotted with the applied cut on $\theta_{col} < 0.01$. The blue areas show the rejected events with cut on $\theta_{col} > 0.01$.

Table 5.3: Overview of the applied cuts for the V^0 events: Table shows the absolute and relative reduction of the number of V^0 candidates by the different cuts.

Cut	Number of V^0 vertices	
	[10^6]	[%]
After the primary vertex selection	182.34	100.00
V^0 vertex position : $z_{V^0} > z_{prim}$	110.87	60.80
V^0 vertex position : 35 cm < z_{V^0} < 140 cm	8.08	4.40
χ^2 of V^0 vertex : $\chi^2 < 2.0$	4.95	2.71
Momentum of both daughter particles : $p > 1$ GeV/c	4.29	2.35
Removal of fringe field tracks : $z_{last} > 350$ cm	3.81	2.09
Angle of collinearity : $\theta_{col} < 0.01$ rad	2.31	1.27
Transverse momentum of decay particle : $p_T > 0.023$ GeV/c	1.25	0.68

5.2.3 Armenteros-Podolanski Plot

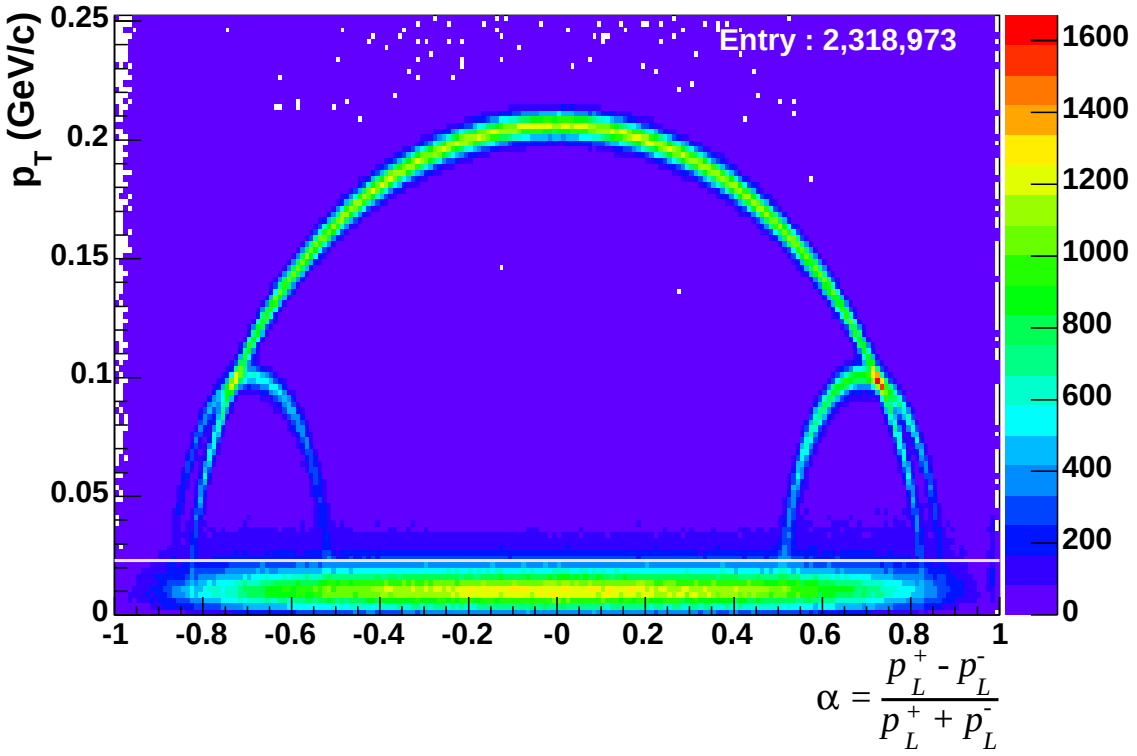

Figure 5.8: Armenteros-Podalanski plot of the V^0 samples after V^0 selection cuts. The transverse and longitudinal momenta of the decay particles are compared in this plot. The three noticeable structures correspond to different V^0. $\Lambda \to p\pi^-$ are located with a small arc at the right side and $\overline{\Lambda} \to \overline{p}\pi^+$ are distributed on the left side. The large symmetrical arc corresponds to $K_s^0 \to \pi^+\pi^-$. The decay $\gamma \to e^+e^-$ has a very small phase space leading to a prominent broad line at low p_T. The horizontal line indicates the cut on $p_T > 0.023$ GeV/c.

In 1953, R. Armenteros and J. Podolanski [220] developed a method of analyzing the V^0 decays to search for new neutral particles in terms of the measured four momentum of the two daughter particles. The method is based on calculating two variables, namely transverse momentum p_T and longitudinal momentum asymmetry α. If the direction of motion of the V^0 rest frame in the laboratory frame is defined as the longitudinal direction L, the longitudinal momentum p_L^* of decay particles in the V^0 rest frame is simply defined by $p_L^* = p\cos\theta$, where p is a momentum and θ is a polar angle with respect to the V^0 direction. For two decay particles one has a relation as $p_L^{*+} = -p_L^{*-}$ in the V^0 rest frame. If β is a velocity of the V^0 in the laboratory frame, the Lorentz transformation from the V^0 rest frame to the laboratory

frame gives the following relation:

$$\begin{aligned} p_L^{\pm} &= \gamma(p_L^{*\pm} + \beta E^{*\pm}), \\ \text{where} \qquad E^{*\pm} &= \frac{1}{2m_{V^0}}(m_{V^0}^2 + (m^{\pm})^2 - (m^{\mp})^2) \text{ and } \gamma = (1-\beta^2)^{-\frac{1}{2}}. \end{aligned}$$

The longitudinal momenta $p_L^{\pm}$ in the laboratory frame depend on the velocity β, and are combined to the the momentum asymmetry α:

$$\begin{aligned} \alpha &= \frac{p_L^+ - p_L^-}{p_L^+ + p_L^-} \\ &= \frac{\gamma(p\cos\theta + \beta E^+) - \gamma(-p\cos\theta + \beta E^-)}{\gamma(p\cos\theta + \beta E^+) + \gamma(-p\cos\theta + \beta E^-)} \\ &= \frac{2p\cos\theta + \beta(E^+ - E^-)}{\beta(E^+ + E^-)} \\ &= \frac{2p\cos\theta + \beta((m^+)^2 - (m^-)^2)/m_{V^0}}{\beta m_{V^0}} \\ &= \frac{2\sqrt{(p^2 - p_T^2)}}{\beta m_{V^0}} + \alpha_c \qquad \text{with } \alpha_c = \frac{(m^+)^2 - (m^-)^2}{m_{V^0}^2}. \end{aligned} \tag{5.3}$$

By plotting p_T versus α, the so-called Armenteros-Podolanski plot, the different V^0 decays can be distinguished by collecting the V^0 events to different elliptic arcs. Thus it is a convenient way of identifying the different decays of Λ, $\overline{\Lambda}$ and K^0s. If the masses of the decay particles are equal, α is distributed symmetrical around $\alpha = 0$. If the originating decay particles have different masses, the center of the arc is shifted to positive or negative value in the α variable. The center of the arc for the different V^0 can be easily calculated by α_c, and the maximum p_T is given by [221]

$$p_T^{max.} = \frac{\sqrt{(m_{V^0}^2 - (m^+ + m^-)^2)(m_{V^0}^2 - (m^+ - m^-)^2)}}{2m_{V^0}}. \tag{5.4}$$

For K^0 the maximum p_T available is $p_T^{max.} = 0.206$ GeV/c and $p_T^{max.} = 0.101$ GeV/c for Λ and $\overline{\Lambda}$.

Fig. 5.8 represents the Armenteros-Podolanski plot of the reconstructed V^0 sample. Two intense regions arise from the Λ and $\overline{\Lambda}$, a prominent is from $K^0 \to \pi^+\pi^-$ and a narrow ellipse from $\gamma \to e^+e^-$ can clearly be seen. Since the photons are located in the low p_T region, they can therefore be excluded easily by demanding $p_T > 0.023$ GeV/c. The overlap of the Λ and $\overline{\Lambda}$ arcs with the K^0 at $|\alpha| \approx 0.75$ and $p_T \approx 0.100$ GeV/c, is more difficult to separate because they have the same kinematic signature. In principle, an elimination of the K^0 peak

by an invariant mass cut can be used to reduce the background in the Λ and $\overline{\Lambda}$ invariant mass distribution. However, such a cut is not profitable, because it removes a non-negligible fraction of the Λ. Applying the K^0 exclusion, the reduction rate of Λ is found to be about 20%. Since the sample of K^0 can be easily managed in Monte Carlo and may be used to study the systematics with high statistic, it was therefore decided to keep the K^0 as a main background in the polarization analysis. From this Armenteros-Podolanski plot, it is apparent that the Λ and $\overline{\Lambda}$ are distributed with opposite sign of α. A cut on $\alpha > 0$ for Λ and $\alpha < 0$ for $\overline{\Lambda}$ are obvious due to their positions in the Armenteros-Podolanski plot.

5.2.4 Selection of Current Fragmentation

In order to calculate x_F, one needs to assume a mass for the reconstructed hadron. It means that the x_F of reconstructed V^0 events must be separately calculated with the mass of Λ, $\overline{\Lambda}$ and K^0. Fig. 5.9 shows the x_F distribution of the Λ data in the year 2004. The x_F distribution is obtained for the Λ events in the signal region after the subtraction of background. It can be seen that most of the data comes from the current fragmentation region, and the statistic in the target fragmentation region is unfortunately too small to allow for an extraction of the kinematic dependence for the polarization. Low momentum particles decay with large angle in the laboratory system. Mostly, those events correspond to the target fragmentation. The interest in this analysis is in particular the spin transfer in the current fragmentation region. Therefore, a cut of $x_F > 0.05$ is applied to select the current fragmentation region for V^0 event.

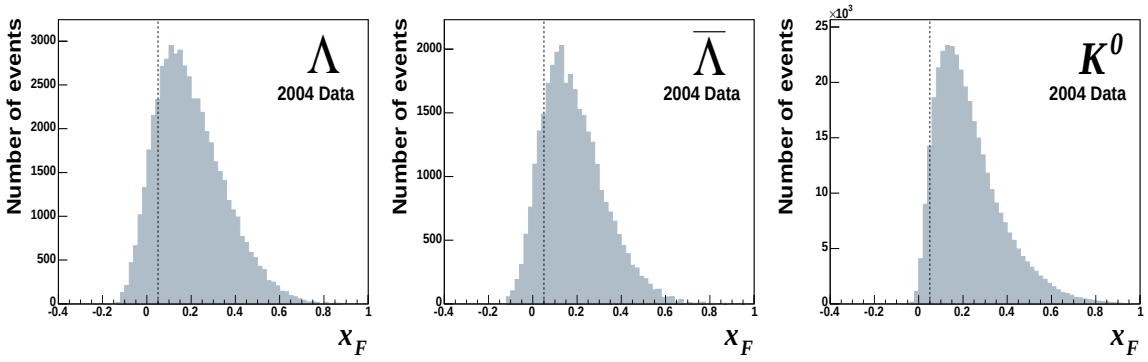

Figure 5.9: x_F distributions for the Λ, $\overline{\Lambda}$ and K^0 sample in 2004. The x_F distributions are obtained after the subtraction of the background in the signal region.

5.2.5 Invariant Mass Distribution

V^0 events which passed all introduced cuts, the invariant masses are calculated by making a mass assumption for the two decay particles. Track combinations for which the assumption is correct will pile up in a peak close to the V^0 mass. The natural widths of the peaks depend on the lifetime of the particles (2.50 μeV for Λ and $\overline{\Lambda}$, 7.35 μeV for K^0), but are smeared out by the measured widths $\sigma_\Lambda \approx 2.3$ MeV/c and $\sigma_{K^0} \approx 6.3$ MeV/c. Therefore the measured widths purely reflect the resolution of the spectrometer.

Fig. 5.10 shows the invariant mass plots for the Λ, $\overline{\Lambda}$, and K^0 hypotheses with data obtained in the years from 2002 to 2004, separately. The Λ and $\overline{\Lambda}$ peaks are located on a non-vanishing background, which is mostly the background from kaon events. An irregular structure around $m_{p\pi^-}(m_{\overline{p}\pi^+}) \approx 1.09$ GeV/c^2 in the Λ and $\overline{\Lambda}$ invariant masses in Fig. 5.10 is caused by two different contributions of background. The $\gamma \to e^+e^-$ start at the kinematic border of 1.077 GeV/c^2, but the $K^0 \to \pi^+\pi^-$ contribute above 1.09 GeV/c^2 and produce an edge in this mass region.

The invariant mass histograms of Λ are fitted with a function, which is defined as the sum of a Gaussian, a first order polynomial, and scaled K^0 background from the Monte Carlo:

$$f(m_{p\pi^-}) = \frac{N}{\sqrt{2\pi}\sigma} exp[-\frac{(m_{p\pi^-} - \overline{m})^2}{2\sigma^2}] + p_0 + p_1 m_{p\pi^-} + K^0(m_{p\pi^-}), \tag{5.5}$$

where N is the number of Λ under the Gaussian peak, σ the width, and $\overline{m}$ the mean value of the peak. The fit function has five free parameters. For the Λ a fit range from 1.09 GeV/c^2 to 1.2 GeV/c^2 was used. The lower bound is naturally motivated by the limitation of K^0 background. For the $\overline{\Lambda}$ the fit function is defined in the same way, except for the mass assumption $m_{\overline{p}\pi^+}$. To take into account the K^0 background in the fit procedure, one needs to prepare an extra histogram from the Monte Carlo. Events in this histogram must have passed through the applied cuts and been verified as a K^0 by the generated Monte Carlo. It is a part of the total background. For the fit of the K^0 histogram the situation is reversed, the background is defined with Λ and $\overline{\Lambda}$ events from the Monte Carlo.

The numbers of Λ, $\overline{\Lambda}$ and K^0 events obtained by the Gaussian fit have increased about twice in each year. The final Λ and $\overline{\Lambda}$ consist of 79,000 and 46,000 candidates. This leads to a ratio between Λ and $\overline{\Lambda}$ of 1.72. The obtained signal width for the Λ and $\overline{\Lambda}$ is about 2.3 MeV/c^2, for the K^0 it is 6.3 MeV/c^2. The mean positions are close to the Particle Data Group (PDG) value of 1.1157 GeV/c^2 for Λ and $\overline{\Lambda}$. and of 0.4976 GeV/c^2 for K^0. From the very good agreement in the mean positions it can be concluded that calibration and alignment of the COMPASS detector are very well for this analysis. The peak shapes of Λ and $\overline{\Lambda}$ are successfully described by the Gaussian distribution. The reduced χ^2 values of the fit are below 2.0. But the

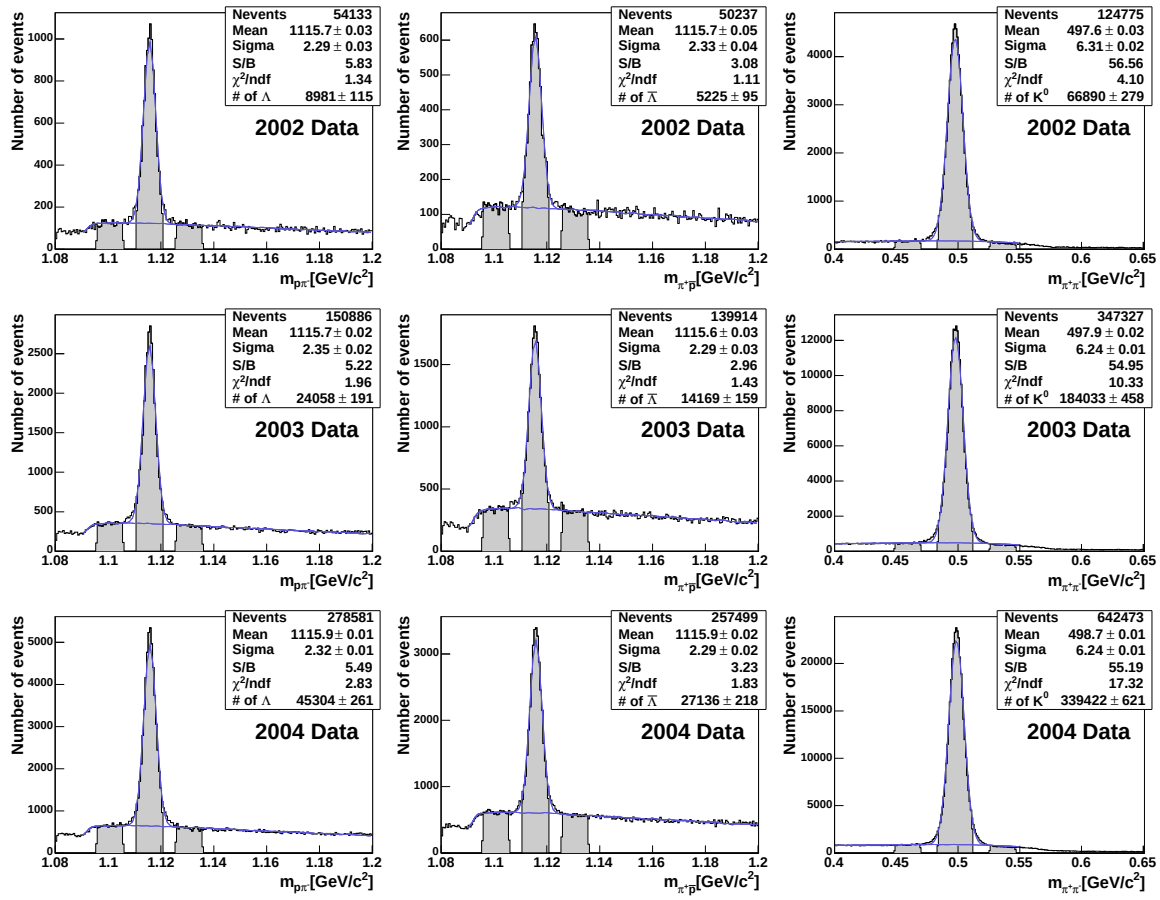

Figure 5.10: Invariant mass distributions for Λ, $\overline{\Lambda}$,and K^0 hypothesis are shown after the application of the final cut for the three different years. The histograms of Λ and $\overline{\Lambda}$ are fitted with the sum of a Gaussian, a first polynomial and K^0 background. Inversely, a background defined by Λ and $\overline{\Lambda}$ are used to fit the histograms of K^0. The fitting procedure is described in the text. One can see the mean positions close to the Λ and $\overline{\Lambda}$ mass of 1.1157 GeV/c^2 and K^0 mass of 0.4976 GeV/c^2. The sigma of the Gaussian is about 2.3 MeV/c^2 for Λ and $\overline{\Lambda}$. For K^0 it is 6.3 MeV/c^2. The three filled region in the plots indicate the signal and sidebands, which are used for background subtraction in the kinematic distributions.

available high statistics of the K^0 sample show that the fit method has a weak point. This means that the mass peak is a sum of different Gaussians, which reflect the different resolutions of the various tracking sets. Despite the obvious fault of the one Gaussian, the χ^2 of the K^0 fit is improved by subdividing the data sample in $\cos\theta$ bins for the polarization analysis. The shape of the peak can generally be improved by a double Gaussian fit. Nevertheless, the use of a double Gaussian is problematic when statistics are insufficient which is the case for 2002 data.

In each histogram, the signal and two background regions are defined to be used for background subtraction in the kinematic distributions. The kinematic distributions under the signal band, such as momentum, should differ from the sideband regions, and the events in the signal band contain background events as well as signal events. In order to correct the properties of the signal events, the distributions of two sidebands are subtracted from the respective histograms of the peak band. Bands of $2\sigma = 5$ MeV/c^2 width were chosen for each region, the center of the side bands is 6σ away from the peak.

Reconstructed V^0 particles from each year have a slightly different acceptance due to different detector setups. In the polarization analysis the reconstructed V^0 particles are therefore treated separately for different years. Also, the Monte Carlo data of Λ, $\overline{\Lambda}$ and K^0 are simulated for the three years independently. The widths of the mass peaks were found to be smaller in reconstructed Monte Carlo compared to real data showing that still some more knowledge about the detector needs to be implemented in Monte Carlo.

5.3 Monte Carlo Simulation

For the determination of the Λ polarization, one needs the best description of the spectrometer to correct the detector acceptance. Furthermore, it is important to know the contributions from the different production processes to the measured Λs. Since it is not possible to separate all production processes in real data, a Monte Carlo simulation must be used to understand the Λ production. This chapter will show how the Monte Carlo simulations were generated and how the reconstructed Monte Carlo describes the hadronic final state and kinematic variables with respect to the data.

The simulation has to model the physics processes and the detector response, therefore the Monte Carlo simulation proceeds in two steps: First, event generators simulate all the particles that are produced in the primary interaction and their eventual decay processes. After that, all generated particles are passed to a detector simulation . The detector simulation has to be extensively described with respect to geometrical shapes, positions, and amount of material of detector components. In this analysis, the complete Monte Carlo chain consists of the Monte Carlo generator LEPTO 6.5 [222] and COMGEANT 0.0.72 [223], which is a simulation package of the COMPASS detector and is based on GEANT 3.21 [224]. These are the two main parts of the simulation process and they can be done independently. The Monte Carlo data are then reconstructed using CORAL. It includes some additional information specific for the Monte Carlo, detector efficiencies and resolutions, that are only taken into account when reconstructing the Monte Carlo data and not already in COMGEANT. In this section only the topics relevant for this analysis will be mentioned.

5.3.1 Event Generation

The event generator used for the simulation of DIS events at COMPASS is LEPTO. The Monte Carlo generator LEPTO provides as an output the information of momentum, energy and identity of the produced particles as well as information about the simulated process, i.e. which scattering took place within the given cross section. In LEPTO, the cross section of scattering processes are realized by three first order hard QCD processes. The main process is the leading order DIS (L.O.DIS). The QCD-compton (or gluon radiation) and photon-gluon fusion (PGF) process appear as background processes. In the low Q^2 range, the interaction does not only occur in a hard scattering process, but also involves many soft interactions by real photons. Therefore, LEPTO is not suitable for the analysis of the $Q^2 < 1$ (GeV/c)^2 region. Fig. 5.11 shows the obtained event processes in Λ and $\overline{\Lambda}$ production after application of the final cuts. More than 80% of the events come from the DIS process, and the background processes can be neglected in a leading order consideration.
In the DIS process, there is the possibility of QED radiation at the lepton-photon vertex as well as a QCD radiation of the struck quark which emits partons before and after the photon-quark interaction. If an event contains a radiated photon, the kinematic variables which describe the virtual photon and which can be used to generate the final hadronic state can be different from the true kinematics. This can be corrected either by estimating the smearing of the kinematic variables or by an extra program like RADGEN [225], which is used to calculate the radiative corrections according to their cross sections. However, comparisons between data and Monte Carlo for the muon kinematics show good agreements without radiative correction. Therefore the Monte Carlo for Λ production does not contain radiative correction. The effect of QCD radiation can also be treated using a parton shower as a higher order effect. Since the calculation of the Λ polarization is only considered in leading order, the QCD radiative corrections are not included in Monte Carlo for this analysis.

The generation of events with LEPTO has been restricted to kinematic regions accessible with the COMPASS spectrometer and relevant for this analysis. On the generator level, the Monte Carlo sample has been generated applying the following preselection cuts:

- $Q^2 > 0.9$ (GeV/c)^2
- $0.0001 < x_{Bj} < 0.999$
- $\nu < 250$ GeV
- $0.09 < y < 0.91$
- $P_{\Lambda,\overline{\Lambda}} > 3.0$ GeV/c, $P_{K^0} > 2.0$ GeV/c

The cuts on the momenta were motivated by the momentum distributions of the data (see Fig. 5.16). Since the detector configuration and reconstruction procedure for 2002, 2003 and 2004 differ, the Monte Carlo samples have been treated to the full detector simulation for each

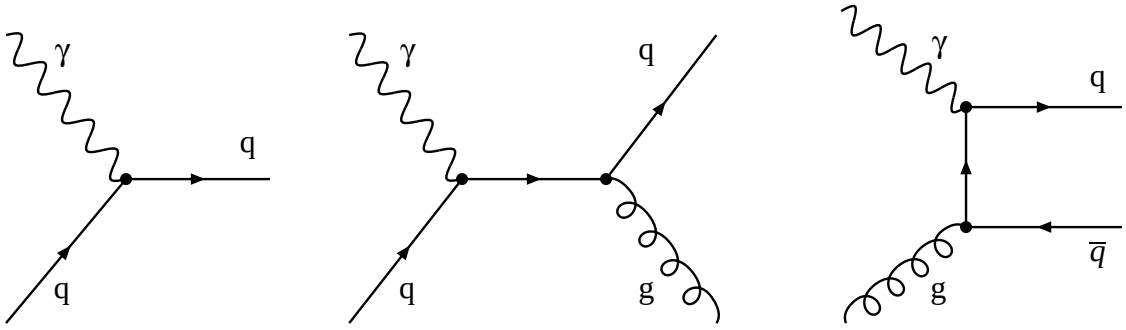

(a) L.O. DIS (b) QCD-Compton (c) PGF

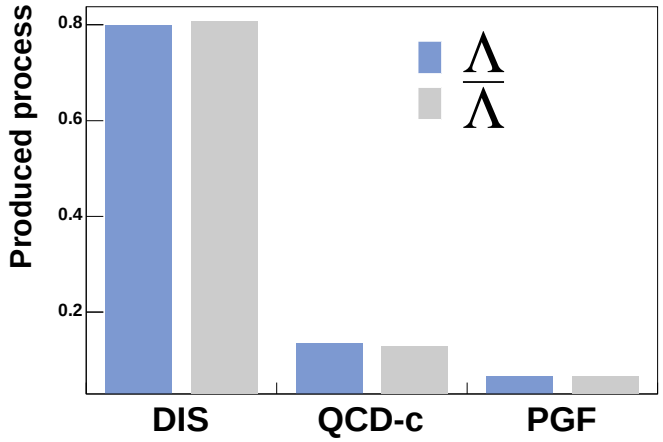

Figure 5.11: Λ and $\overline{\Lambda}$ production processes due to leading order DIS, QCD-Compton, and photon-gluon fusion (PGF) process after application of the Λ and $\overline{\Lambda}$ cuts.

of the 3 years separately. In fact, the data samples in each year were periodically produced by different CORAL versions. The influence of the CORAL version used in the reconstruction procedure is found to be negligible. Therefore, the comparison of data with Monte Carlo and the extraction of polarizations are separated for the three years. Also, the Monte Carlo samples for each year have been generated with three different production modes, where the production contains at least one Λ, $\overline{\Lambda}$ or K^0. The total event statistics were about 9×10^6 for hyperons and about 12×10^6 for K^0 per year. The ratio of the production was 30% (Λ) : 30% ($\overline{\Lambda}$) : 40% (K^0). Since the background statistics is limited by the lack of sufficient computing power and available time, the description of background is not completely optimized. However, absolute statistics of background in Monte Carlo are sufficient to compare with the background of the data samples. Finally, some part of LEPTO parameters have been modified as described in the following subsections.

5.3.2 Parton Distribution Function

An important underlying ingredient of the Monte Carlo is the probabilistic description depending on the kinematic variables. The parton distribution function $q(x, Q^2)$ describes the probability to find a parton q of flavor f with a momentum fraction x_{Bj} at a momentum scale Q^2. Since the absolute form of parton distribution functions cannot be calculated in perturbative QCD, a parametrization of these distributions has been obtained using experimental data and the Q^2 dependence according to the QCD evolution. Historically, many different parameterizations were developed by various authors and were collected together in the CERN library program PDFLIB [226].

In this analysis, the parton distribution function GRV94LO [227] parametrization at leading order has been used. The influence of the choice of parton distributions was tested by using alternatively CTEQ2L [228], CTEQ5L [229], and GRV98LO [137] parameterizations in the systematic study. Significant effects on the parameterization could not be detected which is not surprising since all parton distributions model the quark distribution in the valence region equally well. Fig. 5.12 shows the distributions for up, down and strange quarks, and gluons for the GRV94 parametrization in leading order as a function of the momentum fraction x_{Bj} at a fixed $Q^2 = 3.5$ (GeV/c)^2, which corresponds to the mean value of the Λ data sample.

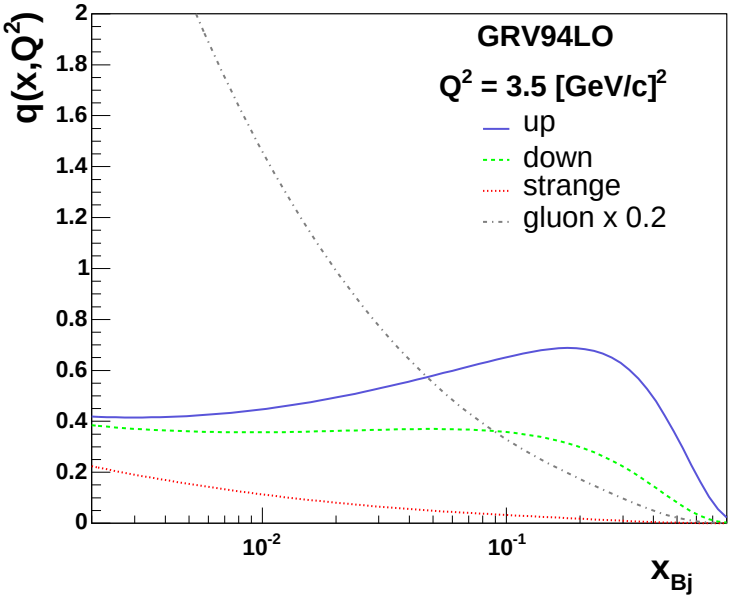

Figure 5.12: GRV94LO [227] parton distribution function: The distributions for up, down, strange quarks, and gluons in leading order as a function of the momentum fraction x_{Bj}. The distributions are obtained with a fixed $Q^2 = 3.5$ (GeV/c)^2.

5.3.3 Fragmentation Model

High energy collisions between 2 particles create many particles in the final state depending on the center-of-mass energy. The large number of final state particles lead to a very complex structure of the matrix elements. Theoretical calculations of the transformation of the resulting colored partons into colorless hadrons is not established up to day. Therefore the process of fragmentation can only be described through a phenomenological approach. The production of hadron in DIS is analogous to the e^+e^- annihilation since the fragmentation is universal [230]. The explanation of the observed hadronic final states in e^+e^- annihilation events are realized by the development of various models with Monte Carlo technique.

The most important approach to the fragmentation is the LUND string model [231]. The string description intuitively depicts the quark confinement in QCD. In this model, baryons and mesons are produced by breaking of the one-dimensional string, which can be imagined as a cylindrical flux tube with about 1 fm in diameter and tension κ. The string constant (field energy density) κ is known to be $\kappa \approx 1$ GeV/fm from hadron spectroscopy. When a quark has been kicked out by the virtual photon, the remnant nucleon is treated as a diquark. As they move apart, the gluon field stretches in between quark and diquark. If the separation is large enough, the string can break by creating quark-antiquark pairs or diquark-antidiquark pairs from the available field energy within the color flux. The resulting two strings can split again according to the same scheme, until an energy threshold is reached.

The quark and antiquark pair is produced at the breaking point and tunnels out with some finite longitudinal and transverse momentum gained from the field energy. The total transverse momentum is locally compensated between the quarks since the string is assumed to have no transverse excitations. The LUND model assumes a Gaussian distribution for p_T with a width $\sigma \approx 0.36$ GeV/c. Additionally, a small admixture of a second broader Gaussian with larger width is introduced. Thus, the probability for the production of a $q\overline{q}$ pair with quark mass m and transverse momentum p_T is proportional to

$$P \sim exp(-\frac{\pi m_T^2}{\kappa}) = exp(-\frac{\pi m^2}{\kappa})exp(-\frac{\pi p_T^2}{\kappa}), \tag{5.6}$$

where $m_T^2 = m^2 + p_T^2$ is called the transverse mass. This mechanism is the basis for the LUND symmetric string fragmentation function as an ansatz.

The LUND string model in LEPTO is realized by the JETSET 7.4 [232] program which allows to adjust the parameters of the model. In JETSET, fragmentation functions give the probability of finding a hardron emerging from a quark with energy fraction z:

$$f(z) = \frac{1}{z}(1-z)^a exp(-\frac{bm_T^2}{z}), \tag{5.7}$$

with the free parameters a and b . The default values of a and b are 0.3 and 0.58 GeV^{-2}, respectively. The parameters a and b are modified to improve the description of the Monte Carlo shape of the momentum, x_F and z distributions of hadrons. Fig. 5.13 illustrates the influence of the changes on the fragmentation function $f(z)$. The fragmentation function $f(z)$ has been shifted with the modified settings to lower z for both Λ and K^0 production. The Gaussian distribution of the transverse momentum is also adjusted to improve the description of transverse momenta for generated hadrons. The width of the broad Gaussian is taken to be a factor 2.5 (3.0) larger than first Gaussian for Λ (K^0) production and the admixture of a broader Gaussian in the first Gaussian is set to 8% (10%) for Λ (K^0) production. In Fig. 5.14 the modified and default settings are shown with two Gaussian curves each. The second broader Gaussians are enlarged by a factor 20 for default setting and by a factor 5 for modified Λ setting. The first Gaussian from the modified Λ setting has a smaller amplitude than the default setting. In contrast, the second Gaussian from the modified Λ setting has a larger amplitude than the default setting.

Eq. 5.6 also implies a dependence on quark masses, which leads to the relative occurrence of flavors. The relative occurrence of flavors is implemented by a suppression of heavy quark production:

$$u\overline{u} : d\overline{d} : s\overline{s} : c\overline{c} \approx 1 : 1 : 0.3 : 10^{-11}. \tag{5.8}$$

The charm quark and heavier ones are hence not expected to be produced in the fragmentation process. The probability to create an $s\overline{s}$ pair is suppressed by 0.3 compared to the $u\overline{u}$ and $d\overline{d}$ pair production. The suppression of $s\overline{s}$ production can be adjusted by changing a parameter in JETSET. The modified $P(s)/P(u)$ leads to a change of momentum, z and x_F distribution. For three productions the suppression of $s\overline{s}$ production are found to be 0.4.

JETSET contains different scenarios for baryon production. In the simplest picture, baryon production can be obtained by various diquark-antidiquark pairs instead of quark-antiquark pairs in a string. All possible quark-diquark combinations are related to SU(6) symmetry. Due to the higher mass of diquarks compared to quarks, diquark-antidiquark pair production is suppressed by 0.1. In this work, this parameter of $P(qq)/P(q)$ is modified to a value of 0.2 to improve the description of hadronic kinematics. A more general framework for baryon production is the so-called popcorn mechanism, in which diquarks as such are never produced, but rather baryons appear from the successive production of several $q_i\overline{q}_i$ pairs. It could happen that the color of the produced quark-antiquark pair does not match the color of the initial quark. Hence there will still be a string which will break forming more $q\overline{q}$ pairs. Those pairs will continue to pop out from the vacuum. Consequently, together with the original quark q_1 and the antiquark $\overline{q}_1$, a baryon $B(q_1q_2q_3)$ and antibaryon $\overline{B}(\overline{q}_1\overline{q}_2\overline{q}_3)$ can be produced. In principle, even more pairs can be created leading to additional mesons M generated in between the hadrons resulting in a $BM\overline{B}$ configuration. Those baryon production ratios can also be adjusted by changing the probability but they are left untouched in this work since no apparent improvements on the kinematic spectra were observed.

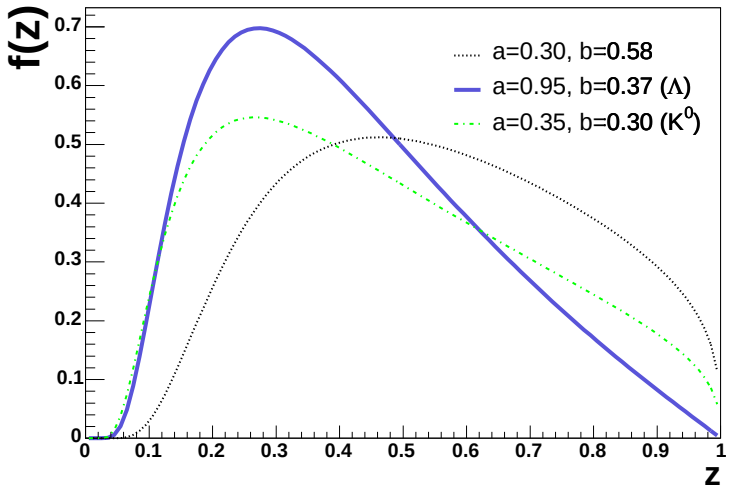

Figure 5.13: LUND fragmentation function $f(z)$: The black dotted curve shows the fragmentation function Eq. 5.7 with default values. The solid and dot-dashed curve corresponds to the Λ and K^0 production with modified values.

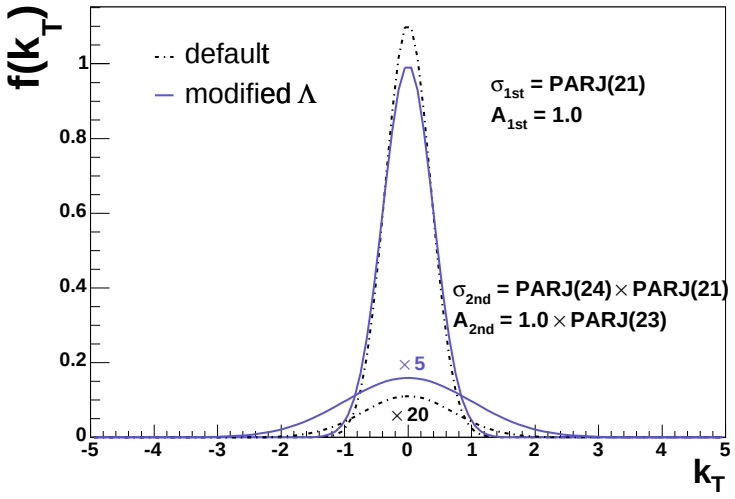

Figure 5.14: Transverse momentum in the fragmentation: The dot-dashed curves display the default settings. The solid curves are obtained with the modified parameters for the Λ production.

In Table 5.4, the modified parameters used in the Monte Carlo simulation are summarized. For this analysis modifications have mainly been applied to the fragmentation process with respect to the default setting. The determination of the parameters was realized by looking

Table 5.4: List of the modified Monte Carlo parameters for hyperons and K^0 production.

Parameter		Default value	modified Λ,$\overline{\Lambda}$	modified K^0
LST(15)	PDF	4046(CTEQ2L)	5005(GRV94LO)	5005(GRV94LO)
PARJ(1)	$\frac{P(qq)}{P(q)}$	0.1	0.2	0.2
PARJ(2)	$\frac{P(s)}{P(u)}$	0.3	0.4	0.4
PARJ(21)	Transverse momentum	0.36 GeV/c	0.4 GeV/c	0.36 GeV/c
PARJ(23)	Admixture of 2nd Gaussian	0.01	0.08	0.1
PARJ(24)	Width of 2nd Gaussian	2.0	2.5	3.0
PARJ(41)	LUND fragmentation *a*	0.3	0.95	0.35
PARJ(42)	LUND fragmentation *b*	0.58 GeV^{-2}	0.37 GeV^{-2}	0.3 GeV^{-2}

at the flatness of data over Monte Carlo. Two main categories can be classified according to correlate parameters. Since parameters PARJ(1,2,41,42) influence only the shape of the p, z, and x_F distributions, a scan dedicated to this parameter space was performed to achieve the improvement of the ratio of data over Monte Carlo . The change of p_t distribution and scattering angle θ_{hadron} with respect to the virtual photon is a direct consequence of the modification by parameters PARJ(21, 23, 24). These two categories could be fixed independently since they are not significantly correlated to other parameters. The ratio of data over Monte Carlo of kinematic distributions for the Λ with 2003 data sample are shown as an example in Fig. 5.15. It can be seen that the modified parameters improved the distributions of p_T, p, and z. The choice was made in favor of getting the best improvement of the momentum spectrum and high x_F. An improvement at high momentum and in the high z region compared to the default setting is clearly visible. This was motivated by the fact that the Λ polarization should be highly increased in the current fragmentation. Therefore, the high z region has to be reasonably well described by Monte Carlo as well as the high x_F region. It leads to the conclusion that the reconstructed Monte Carlo distributions can be directly used for acceptance corrections.

Additional parameters PARJ(2-7, 11-17, 43-45) for spin effects and extra suppressions in special cases were also studied but were left at the default value since no apparent improvements on the kinematic spectra could be achieved. The NOMAD experiment used completely different tuning parameters in its Λ analysis, but their parameters distort the agreement of kinematic distributions for COMPASS. Therefore it could not be used for the Monte Carlo tuning for the COMPASS experiment. Results listed in Table 5.4 are finally to be used for the description of Λ, $\overline{\Lambda}$ and K^0 DIS events.

5.3.4 Comparison of Data and Monte Carlo

To make sure that the Monte Carlo is in good agreement with real data, all kinematic distributions of V^0 are compared with data samples after final cuts in each year as listed in the previous Section. The sideband regions of V^0 particles are subtracted from the kinematic distribution of the signal region in order to select only the expected signal (see Section 5.2.5). The comparison of the momentum spectra of data and Monte Carlo simulation are depicted for reconstructed V^0s and their decay particles in Fig. 5.16. The histograms represent the Monte Carlo samples and the points show the data samples in the first nine plots. The ratio of data over Monte Carlo is also shown in the next nine plots. The comparisons of 2002 and 2003 data can be found in Appendix A. In general, the main features of the data are well reproduced by the Monte Carlo description. Reasonable agreement was also found with data and Monte Carlo for the year 2004. The agreement of data with Monte Carlo for the $\overline{\Lambda}$ and K^0 is quite similar to Λ.

In Fig. 5.17 and Fig. 5.18, the comparison of the inclusive variables x_{Bj}, Q^2, y, W^2 for the Λ and $\overline{\Lambda}$ data in 2004 is shown. The inclusive spectra of the distribution for x_{Bj} and Q^2 show good agreement between data and Monte Carlo while the resulting spectra on the other inclusive distribution y and W^2 show the necessity for improvements for the Λ. One reason for the discrepancy lies in the thresholds of the calorimeters for the triggering of scattered muons. If the thresholds of the HCALs were adjusted for the Monte Carlo sample, the ratio of data over Monte Carlo for the y and W^2 description could be improved [233]. However, the correct values are still not determined at present analysis. Future tuning efforts will profit from precise HCAL information so that the improvements of the y and W^2 spectrum will be refined.

Fig. 5.19 and Fig. 5.20 show the hadronic variables. The azimuthal angle ϕ in the laboratory system and transverse momentum p_T for both Λ and $\overline{\Lambda}$ are shown in Fig. 5.19. The ratios of data over Monte Carlo show a perfect agreement. One can conclude that the measured azimuthal angle ϕ will not dilute the measurement of the polarization. The same holds for the transverse momentum p_T of Λ with respect to the virtual photon. The semi-inclusive variables x_F and z are plotted in Fig. 5.20. One finds discrepancies in the x_F and z distribution since the spectra are not described well. The distribution of x_F and z is only suited to compare data with Monte Carlo at high x_F and z, which is the important region for this analysis. Hence, the influence of polarization on the imperfect distributions must be tested by using alternative parameterizations. This will be discussed in more detail in Section 5.6.3.

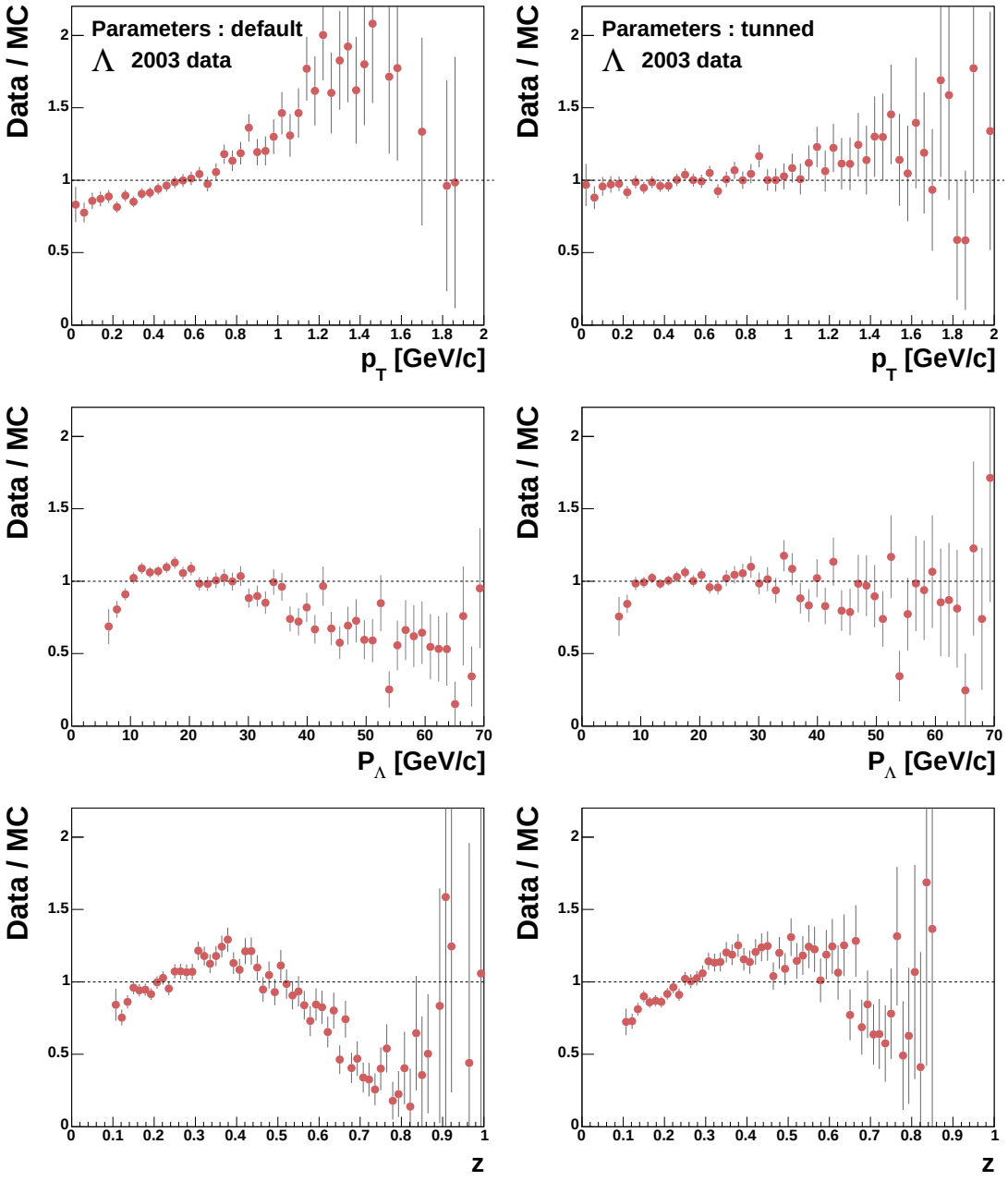

Figure 5.15: Comparison of default (left) and tuned (right) kinematics with modification of parameters for the Λ. The ratios of data over Monte Carlo are shown in each plot. For this study data and Monte Carlo were used for the year 2003.

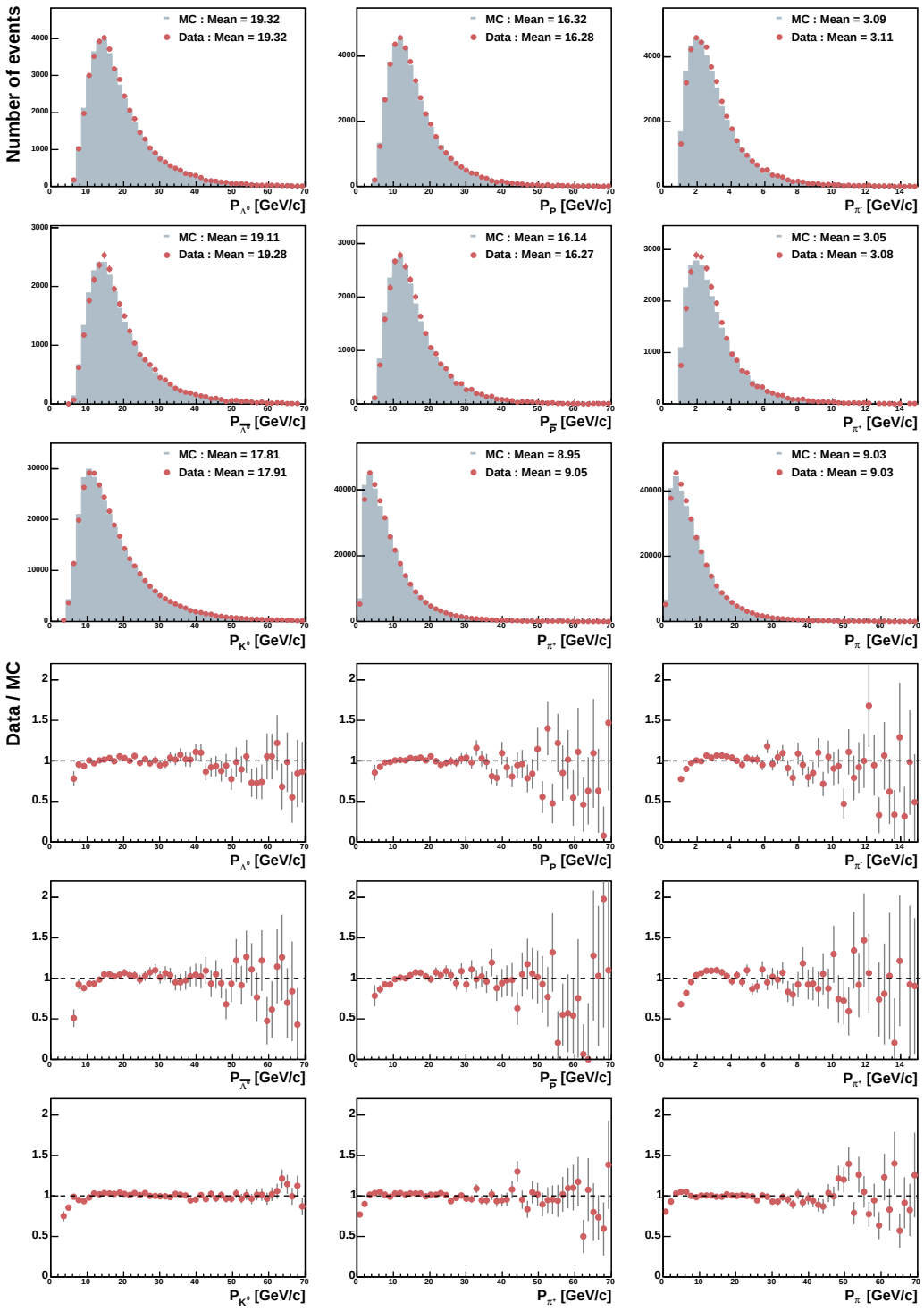

Figure 5.16: Comparison of 2004 data with Monte Carlo for the momentum distributions of reconstructed particles in V^0 events. The histograms represent the Monte Carlo samples and the points show the data samples. The distributions are normalized to the total number of entries. The means of the distributions are also given.

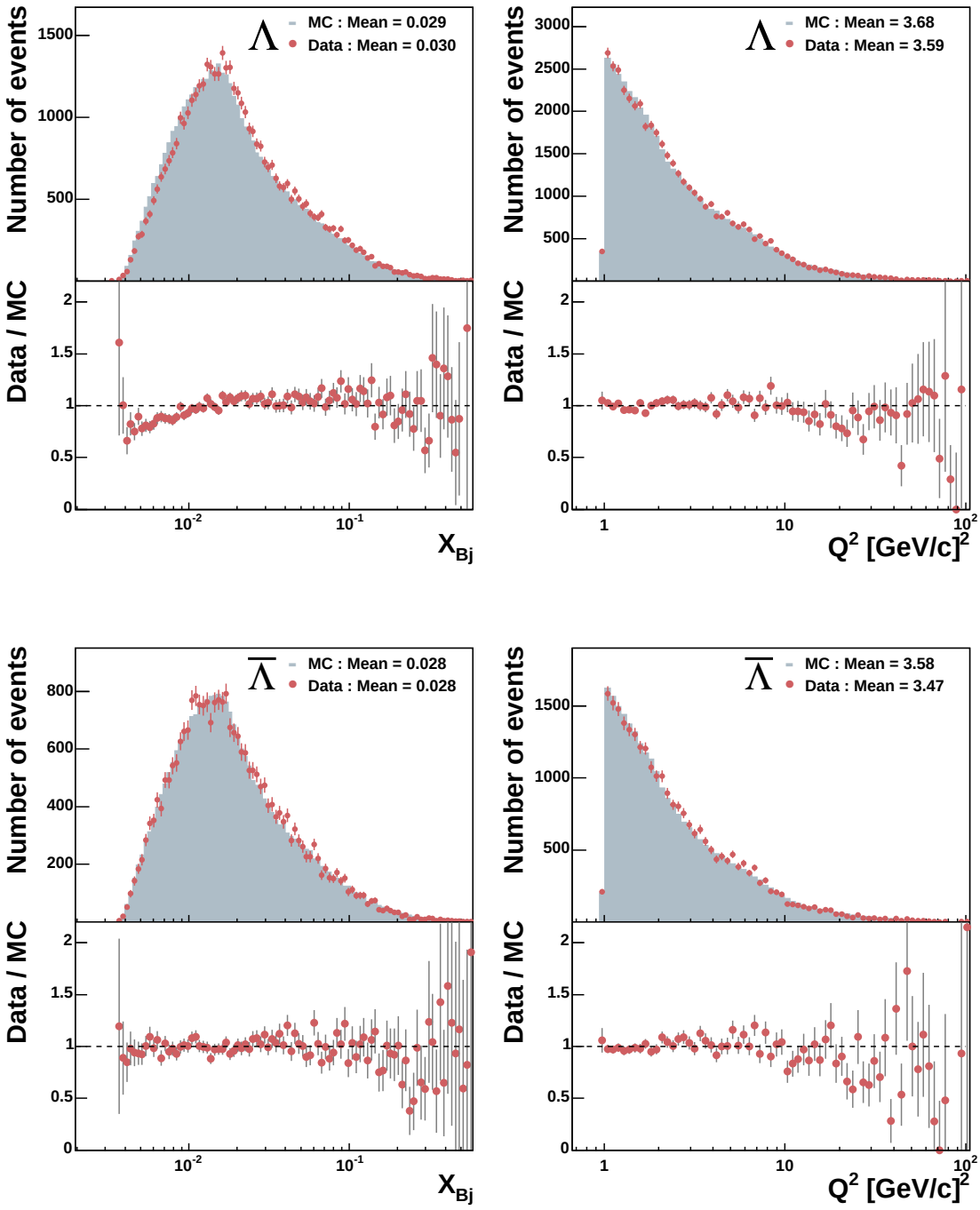

Figure 5.17: Comparison of 2004 data with Monte Carlo for the inclusive kinematic variables x_{Bj} and Q^2 for Λ and $\overline{\Lambda}$ events. The filled areas represent the Monte Carlo samples and the points show the data samples. The distributions are normalized to the total number of entries. The means of the distributions are also given.

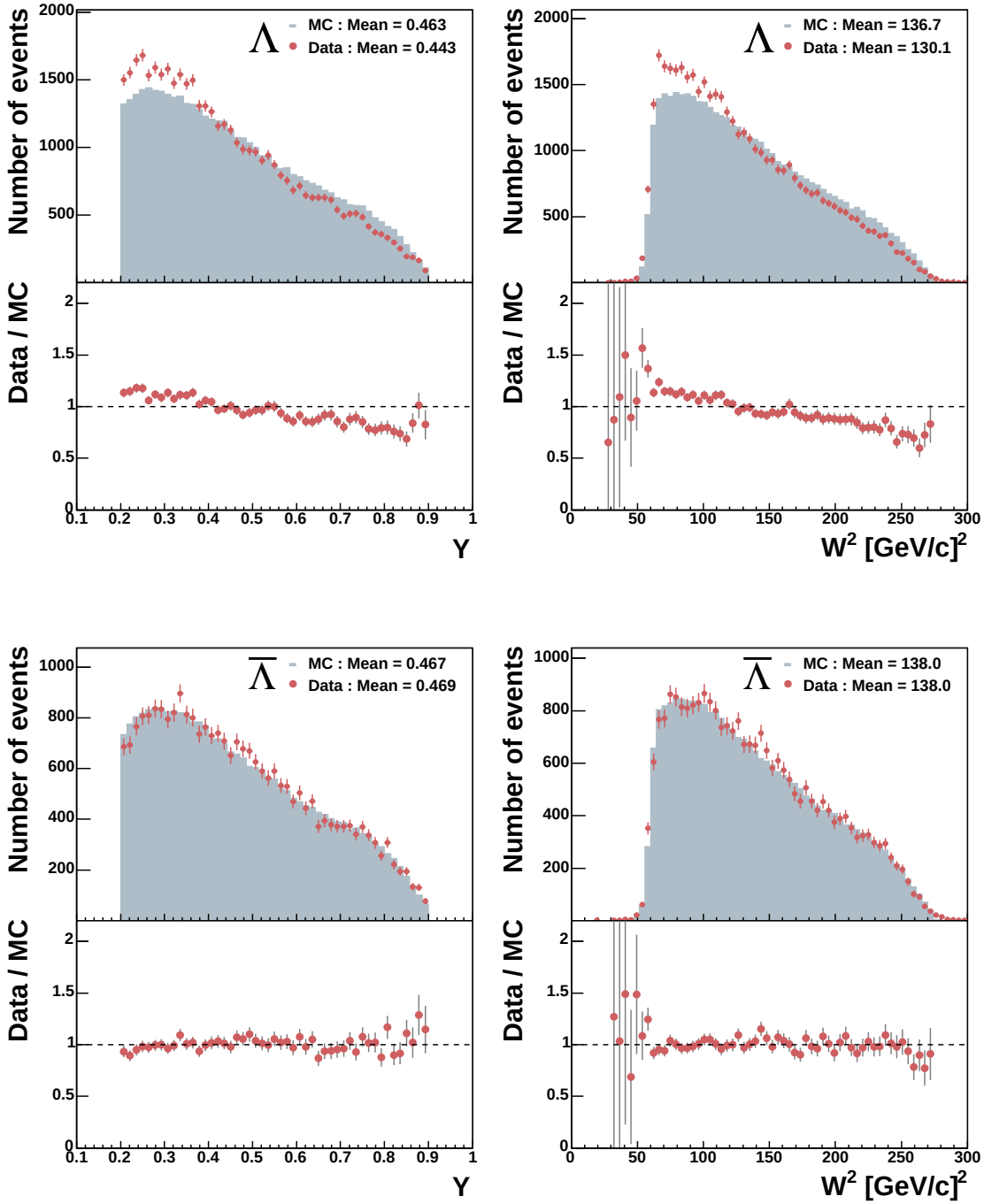

Figure 5.18: Comparison of 2004 data with Monte Carlo for the inclusive kinematic variables y and W^2 for Λ and $\overline{\Lambda}$ events. The filled areas represent the Monte Carlo samples and the points show the data samples. The distributions are normalized to the total number of entries. The means of the distributions are also given.

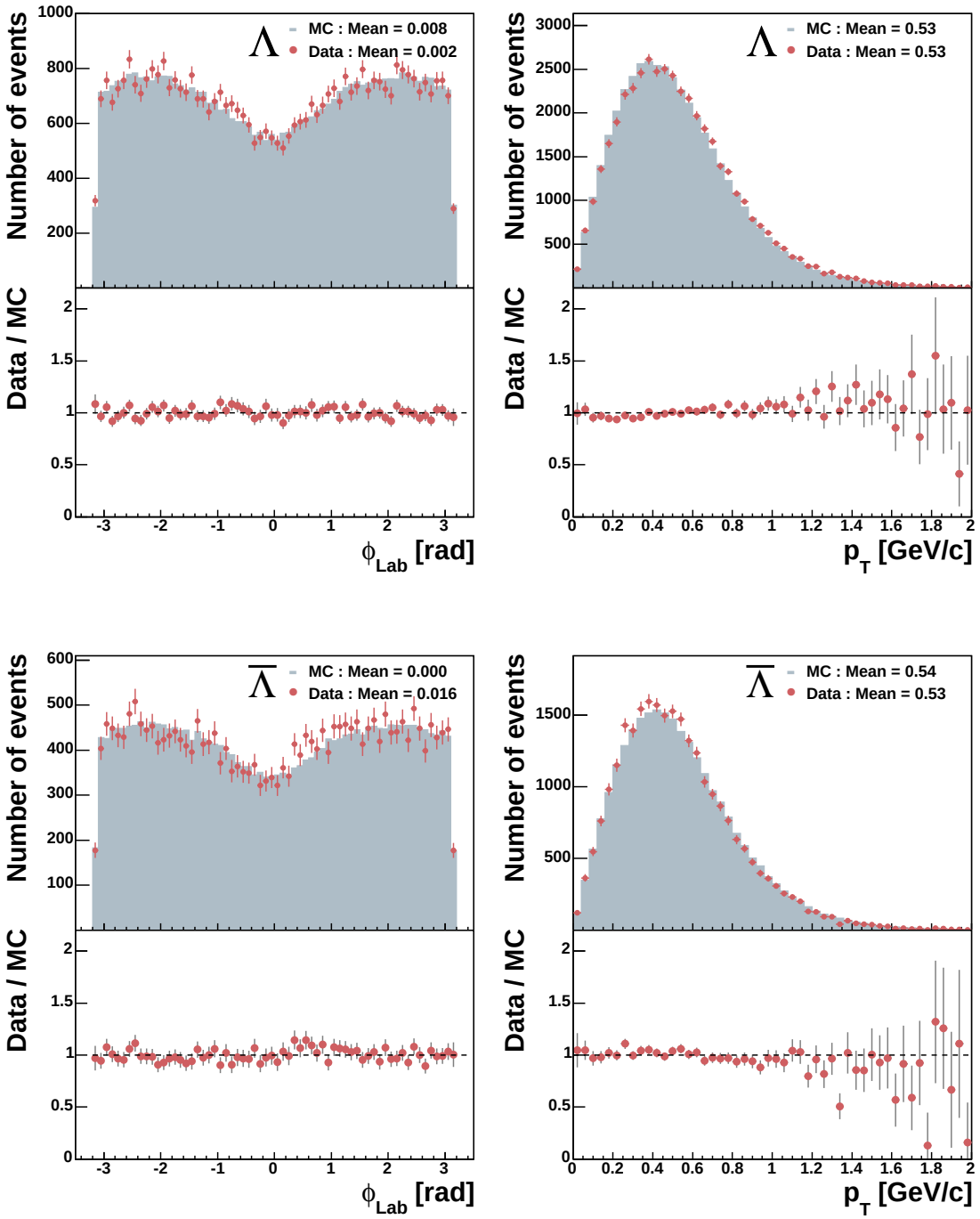

Figure 5.19: Comparison of 2004 data with Monte Carlo for the semi-inclusive kinematic variables ϕ and p_T for Λ and $\overline{\Lambda}$ events. The filled areas represent the Monte Carlo samples and the points show the data samples. The distributions are normalized to the total number of entries. The means of the distributions are also given.

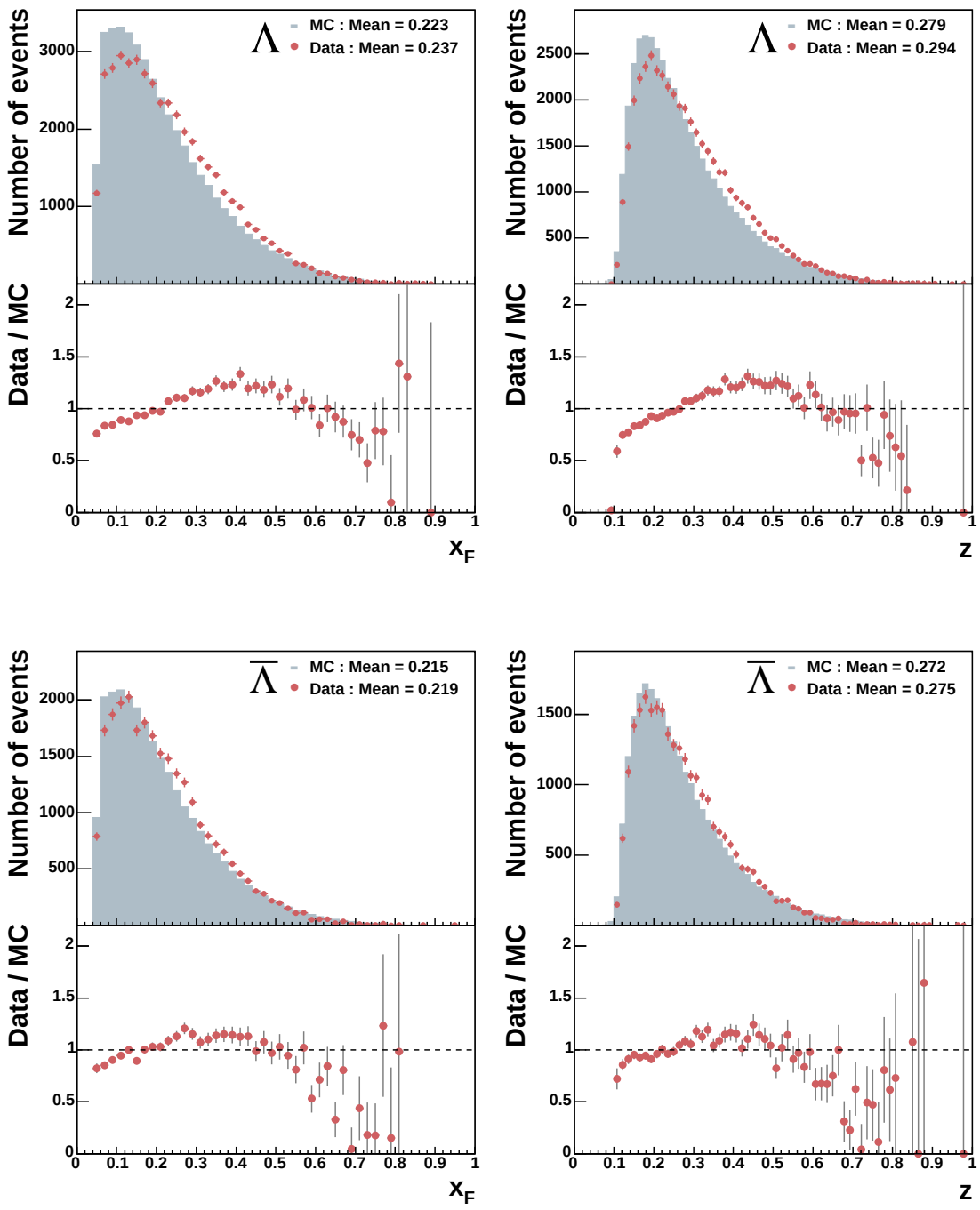

Figure 5.20: Comparison of 2004 data with Monte Carlo for the semi-inclusive kinematic variables x_F and z for Λ and $\overline{\Lambda}$ events. The filled areas represent the Monte Carlo samples and the points show the data samples. The distributions are normalized to the total number of entries. The means of the distributions are also given.

5.4 Polarization Analysis

5.4.1 Reference System

Having identified Λ and $\overline{\Lambda}$ produced in DIS one can try to extract their preferred spin orientation with respect to a physical vectors of the event. Fig. 5.21 shows the reference system in the laboratory frame for the Λ production. The Λ is produced in the scattering of a virtual photon γ^* emitted by the muon beam μ off the target nucleon N together with unidentified particles X. One may choose one of the unit vectors with the help of the three reference planes. The incoming muon beam μ and the outgoing scattered muon μ' define the scattering plane, which is rotated with respect to the production plane by an angle ϕ around the direction of the virtual photon γ^*. To compute the Lorentz 4-vector of the γ^* the information of μ and μ' is used. The production plane is made up of both the virtual photon γ^* and the Λ for the laboratory frame, or it can be spanned by the virtual photon γ^* and the target nucleon N for the Λ rest frame. The decay plane which is formed by the two decay particles of the Λ hyperon is rotated around the production plane by an angle ϕ' at the momentum direction of the Λ. The momentum direction of the Λ is defined as the $\vec{n}_\Lambda$ axis.

For the measurement of longitudinal polarization the direction of the γ^* has to be boosted into the rest frame of the Λ, where the angular distribution of the positive decay particle is analyzed. Fig. 5.22 shows the reference system in the Λ rest frame. The x-axis is chosen along the direction of the reconstructed γ^* momentum. The y-axis is orthogonal to the production plane $\hat{y} = \hat{\gamma}^* \times \hat{N}$, where $\hat{N}$ is the unit vector of the target nucleon in the Λ rest frame. To complete the right-handed coordinate system, the z-axis is set to $\hat{z} = \hat{x} \times \hat{y}$. The definition of the reference system can thus be rewritten as

$$\hat{x} = \frac{\vec{p}_{\gamma^*}}{|\vec{p}_{\gamma^*}|}, \qquad \hat{y} = \frac{\vec{p}_{\gamma^*} \times \vec{p}_N}{|\vec{p}_{\gamma^*} \times \vec{p}_N|}, \qquad \hat{z} = \hat{x} \times \hat{y}. \tag{5.9}$$

The x-axis is the main quantization axis, which is the so-called *longitudinal* direction. A possible polarization is then extracted from the angle between the direction of the positive decay particle and the quantization axis defined in this coordinate system. This reference system will be used throughout the polarization analysis.

As already discussed in Section 3.3, there is some freedom in choosing the reference system. Another choice for the spin quantization axis of the final-state Λ is along the direction of the momentum of the Λ, which is invariant under a Lorentz transformation to the Λ rest frame. The additional test of longitudinal Λ polarization has been done with this alternative system, i.e, the Λ momentum direction instead of γ^* direction. The results in this system are compared with the value of the longitudinal polarization with the γ^* direction in Section 5.6.7.

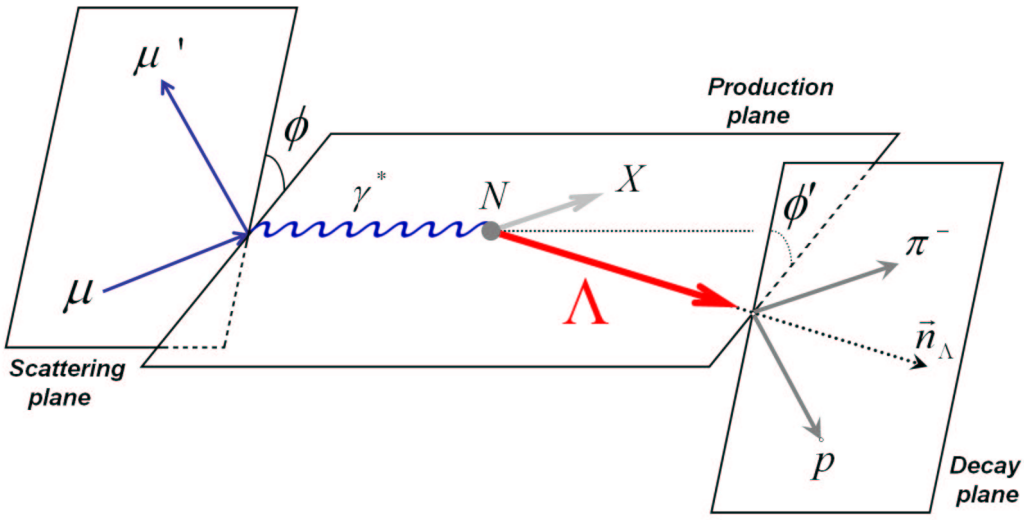

Figure 5.21: Definition of the reference system in the laboratory frame for the semi-inclusive Λ production.

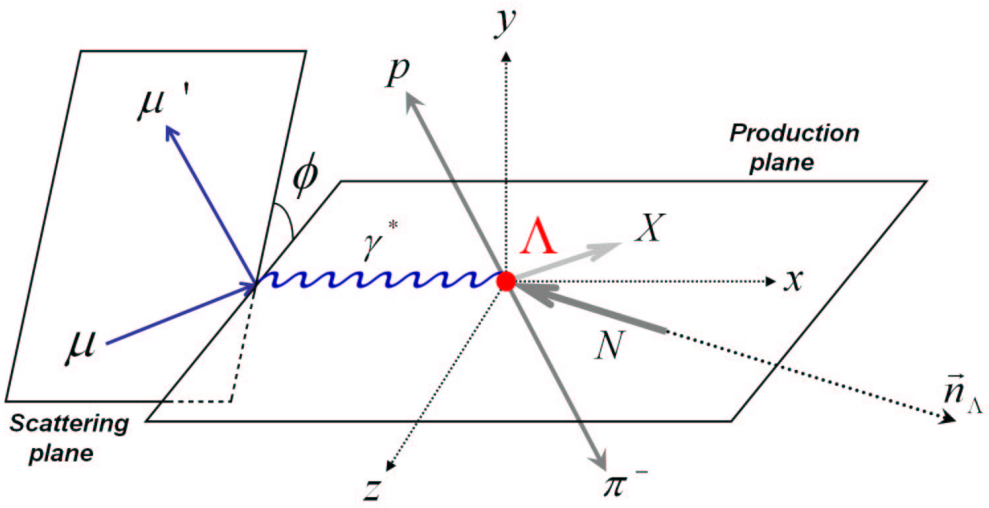

Figure 5.22: Definition of the reference system in the Λ rest frame: For the measurement of longitudinal Λ polarization $\vec{x}$ has been defined to be in the direction of the γ^*. From the angle between the direction of the positive decay particle and the γ^* direction $\vec{x}$ the longitudinal Λ polarization can be extracted.

It is important to demonstrate the ability of our detector to reconstruct correctly the direction of the quantization axis in the defined reference system. To verify this, an angle θ between the quantization axis *x* and the momentum direction of decay proton is defined. Fig. 5.23 shows the obvious correlation between the generated and reconstructed angular variable $\cos\theta_x$ of the decay proton with respect to the *x*-axis. From this one can conclude that the resolution of quantization axis does not smear the polarization.

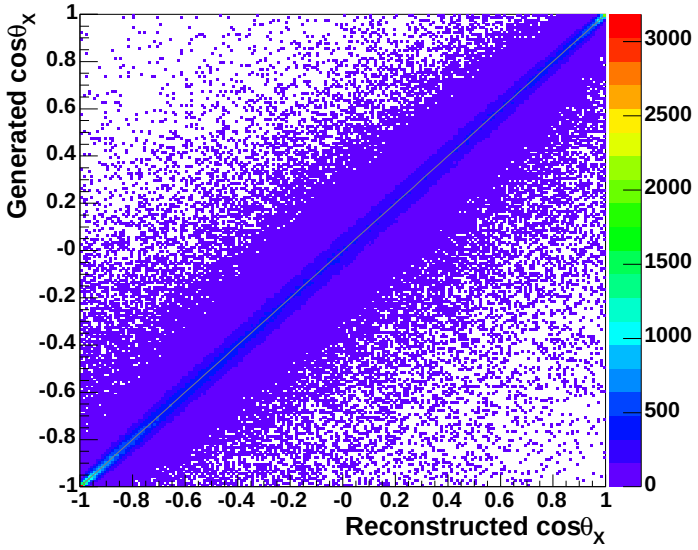

Figure 5.23: Correlation between the generated and reconstructed $\cos\theta_x$ distribution for Λ.

5.4.2 Extraction Method of Polarization

The measurement of the Λ polarization is possible via the parity violation of the weak interaction. As explained in Section 3.1, a possible longitudinal Λ polarization is experimentally extracted from the measured angular distribution of the decay proton with respect to the direction of the γ^* in the Λ rest frame according to

$$\frac{dN}{d\cos\theta_x} = \frac{N}{2}(1+\alpha P\cos\theta_x). \tag{5.10}$$

However, this ideal formula is not applicable to the measurement in practice, because the measured angular distributions are convoluted with the detector acceptance. The COMPASS spectrometer has an inherent asymmetry due to the dipole magnets. When particles fly into the left or the right part of the spectrometer, they are bent into or out of the acceptance depending on the charge. The measured angular distribution has to be corrected, because otherwise acceptance effects might induce a false polarization, which is not distinguishable from a real polarization. The acceptance describes how the average detection efficiency depends

on kinematic variables, geometrical acceptance of the apparatus, dead-time, detector efficiencies, efficiency of the reconstruction process, and cuts applied during the event selection. All effects may cause losses of events. The acceptance is determined using a Monte Carlo simulation. The angular distribution in the Monte Carlo before reconstruction has been generated without polarization, so the observed distortions of angular distributions after reconstruction of Monte Carlo data will only be due to the detector acceptance.

The corrections are included in the so-called acceptance function $A(\cos\theta_x)$. The acceptance function $A(\cos\theta_x)$ is usually obtained by the measured ratio of the number of reconstructed events and the number of generated events:

$$A(\cos\theta_x) = \frac{N_{MC}^{rec}(\cos\theta_x)}{N_{MC}^{gen}(\cos\theta_x)}, \tag{5.11}$$

where $N_{MC}^{rec}(\cos\theta_x)$ is the number of Monte Carlo events accepted and reconstructed after all analysis cut and $N_{MC}^{gen}(\cos\theta_x)$ is the number of generated Monte Carlo events in a certain range of $\cos\theta_x$. Since the acceptance function enters the ideal angular distribution of the data, the angular distribution can be modified:

$$\frac{dN_{Data}}{d\cos\theta_x} = \frac{N_{Data}}{2}(1+\alpha P\cos\theta_x)\cdot A(\cos\theta_x). \tag{5.12}$$

In order to keep systematic errors on the polarization as small as possible, a large amount of Monte Carlo data is required.

Since the Monte Carlo events have been generated without polarization, i.e, $P_{MC} = 0$ the angular distribution of the Monte Carlo simulation can be simplified:

$$\frac{dN_{MC}^{gen}}{d\cos\theta_x} = \frac{N_{MC}^{gen}}{2}(1+\alpha P_{MC}\cos\theta_x) = \frac{N_{MC}^{gen}}{2}. \tag{5.13}$$

Using Eq. 5.11 and Eq. 5.13, Eq. 5.12 can be rewritten as:

$$\frac{dN_{Data}}{d\cos\theta_x} = \frac{N_{Data}}{N_{MC}^{gen}}\frac{dN_{MC}^{rec}}{d\cos\theta_x}(1+\alpha P\cos\theta_x). \tag{5.14}$$

In this equation there is an unknown ratio N_{Data}/N_{MC}^{gen}. To estimate this ratio the following relation can be used:

$$\frac{N_{MC}^{rec}}{N_{MC}^{gen}} = \frac{N_{Data}^{rec}}{N_{Data}}. \tag{5.15}$$

The ratio between the number of reconstructed events and generated events in the Monte Carlo are assumed to be the same as the ratio of the reconstruced and real events in the data.

By introducing the acceptance corrected angular distribution $w(\cos\theta_x)$ and using Eq. 5.15 the Eq. 5.14 can be simplified to:

$$w(\cos\theta_x) = \frac{\frac{dN^{rec}_{Data}}{d\cos\theta_x}}{\frac{dN^{rec}_{MC}}{d\cos\theta_x}} \frac{N^{rec}_{MC}}{N^{rec}_{Data}} = 1 + \alpha P \cos\theta_x. \tag{5.16}$$

Here, N^{rec}_{Data} and N^{rec}_{MC} are the total number of reconstructed events for data and Monte Carlo, respectively.

Consequently, the goal is to determine the normalized number of hyperons within a certain range of $\cos\theta_x$ without background. To calculate the acceptance corrected angular distribution $w(\cos\theta_x)$, the quantity of $1/N^{rec}_{Data} \cdot (dN^{rec}_{Data}/d\cos\theta_x)$ and $1/N^{rec}_{MC} \cdot (dN^{rec}_{MC}/d\cos\theta_x)$ have to be extracted from the data and Monte Carlo separately. Fig. 5.24 shows the number of normalized event for data and Monte Carlo after the background subtraction in ten $\cos\theta_x$ bins for the 2004 data sample. The number of Λ's exhibits an asymmetric distribution, whereas the number of K^0's has a symmetric distribution. However, due to the fact that COMPASS has a limited acceptance, the angular distribution for the K^0's is also not flat.

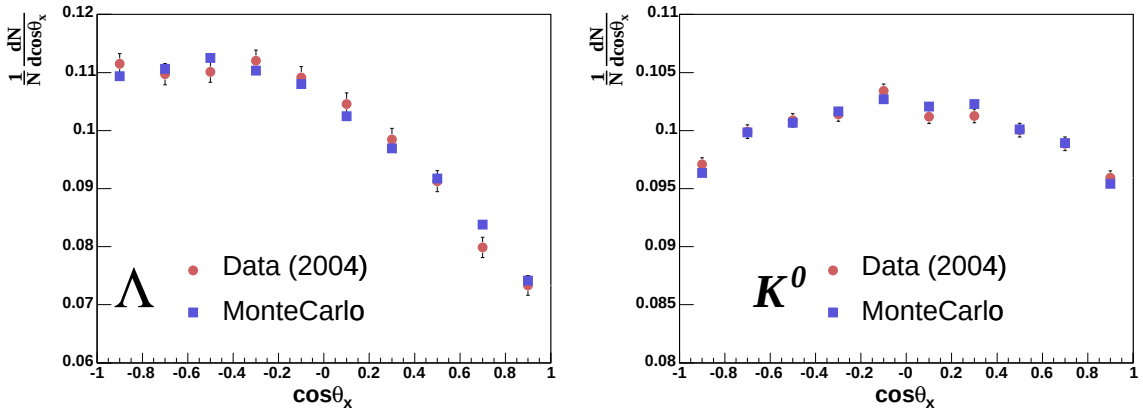

Figure 5.24: Left: The angular distribution in 10 $\cos\theta_x$ bins for the Λ in 2004 data. The $\cos\theta_x$ distribution of Λ strongly deviates from a flat distribution. Right: The $\cos\theta_x$ distribution of K^0. Due to acceptance the distribution is not perfectly flat as expected.

Since an event-by-event identification of the hyperon decays cannot be done, a bin-by-bin method is applied. $\cos\theta_x$ is divided in 5 bins each with a width of 0.4. The main reason for using only 5 $\cos\theta_x$ bins is to ensure that there is still reasonable statistics in each bin for the 2002 data sample after dividing the sample into several kinematic bins. For each $\cos\theta_x$ bin the invariant mass histograms of data and Monte Carlo are made for each sample. Fig. 5.25 shows the invariant mass spectra for the Λ in data and Monte Carlo in each $\cos\theta_x$ bin.

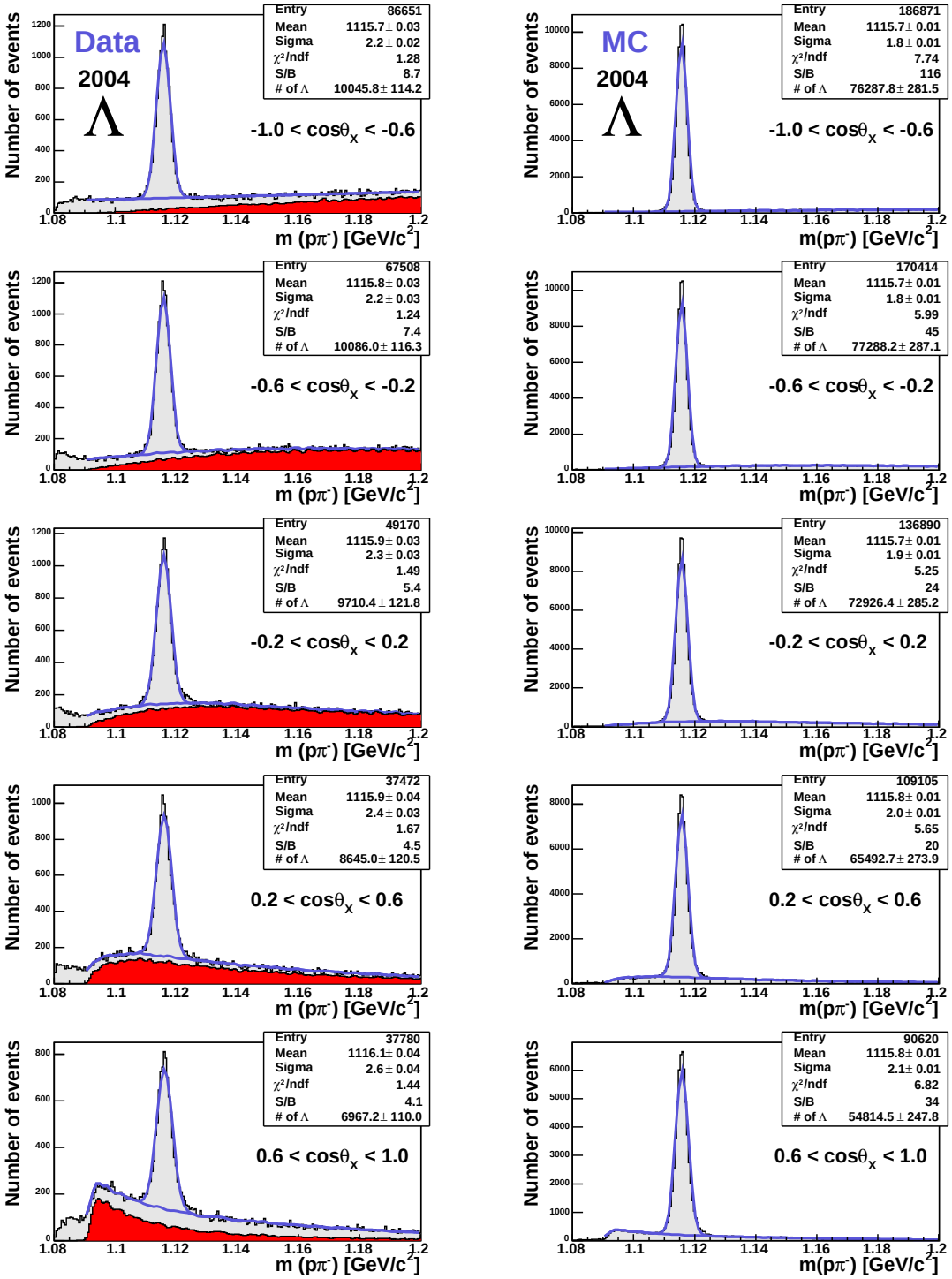

Figure 5.25: Left: Invariant mass distribution of data for the Λ in 5 $\cos\theta_x$ bins. The red histograms indicate the K^0 background, which is estimated from Monte Carlo. Right: Invariant mass distribution of Monte Carlo events in the same $\cos\theta_x$ bins.

One can clearly see that the shape of the histograms differs from the first bin, $-1.0 < \cos\theta_x < -0.6$, to the last bin, $0.6 < \cos\theta_x < 1.0$. The number of hyperons in the subsamples are obtained by fitting the sum of a Gaussian, a first order polynomial and K^0 background as explained in Section 5.2.5. The mass shapes as well as the background are described in the data samples successfully for the Λ. The high statistics of the Monte Carlo sample show that the fit method with one Gaussian does not perfectly describe the mass peak. The reduced χ^2 values are more than 5 and the mass resolutions are slightly different in each $\cos\theta_x$ bin. To overcome the weakness of mass description in Monte Carlo, one either needs to provide a lot of background to make a similar mass shape in the Monte Carlo sample or one can explicitly test the fit method with a polarized Monte Carlo sample. Since it is rather time consuming to simulate the same amount of Monte Carlo as the data sample, a 50% polarized Monte Carlo sample was created and analyzed to check if this shortcoming in description of the mass spectrum in the Monte Carlo has an effect on the polarization. This will be discussed in Section 5.6.2.

From the $w(\cos\theta_x)$ distribution the polarization is directly calculated by combining the number of events from data and Monte Carlo according to Eq. 5.16. The slope of the acceptance corrected angular distribution $w(\cos\theta_x)$ is proportional to the Λ polarization. The polarization is finally extracted by a straight line fit to the acceptance corrected angular distribution $w(\cos\theta_x)$.

5.5 Results

While in the previous chapter the selection criteria for V^0, that define the hyperon samples, was explained as well as the method to extract their polarization, the following section presents the results of the Λ and $\overline{\Lambda}$ polarization and the spin transfer.

5.5.1 Results of Longitudinal Polarization

In a first step, the acceptance corrected angular distribution $w(\cos\theta_x)$ was extracted for the full samples of Λ, $\overline{\Lambda}$, and K^0 in five $\cos\theta_x$ bins. Fig. 5.26 shows the results of polarization for three particles in the three different years. A straight line fit $w(\cos\theta_x) = 1 + c\cos\theta_x$ yields a slope. The slope c is always extracted from the angular distribution of the positive particle, i.e., p^+ for Λ and π^+ for $\overline{\Lambda}$. In principle, this would result in an inverted slope for the $\overline{\Lambda}$, but as the asymmetry parameter α of Λ and $\overline{\Lambda}$ has opposite sign, the effect drops out again when going from the slope of the fit to the polarization P_x.

The measured polarizations as well as the mean values of basic kinematic variables are summarized in Table 5.5 to Table 5.7. The $\overline{\Lambda}$ polarizations are significantly negative, whereas the Λ polarizations are consistent with zero in $1\sigma_{stat}$ of the statistical error. The straight lines fit the data points well with a reasonable χ^2 and probability (goodness of fit), which can be obtained from the CERNLIB routine PROB [14]. In the 2004 data sample, the Λ polarization is measured with a probability of 44% and for the $\overline{\Lambda}$ a probability of 22% is achieved as a worst case. However, it is still compatible with the straight line hypothesis. To average the results for the three year, a standard weighted least-squares procedure is applied:

$$\overline{x} \pm \delta\overline{x} = \frac{\sum_i w_i x_i}{\sum_i w_i} \pm \Big(\sum_i w_i\Big)^{-1/2}, \qquad \text{where} \quad w_i = 1/(\delta x_i)^2. \tag{5.17}$$

Here x_i and δx_i are the polarization values and statistical error obtained in the ith year.

A useful background sample is provided by K^0, which should not show a polarization along any direction since it is spinless. The K^0 polarization is extracted from the angular distribution of the positive pion π^+ in the same manner as for Λ. In the calculation of the K^0 polarization, a decay asymmetry parameter α = 1 was used, so that the K^0 polarization can directly be compared to the null hypothesis assumption. The results of K^0 are consistent with absence of polarization along the γ^* direction. This gives confidence that possible apparatus effects are quite small and that the acceptance correction with Monte Carlo is working properly.

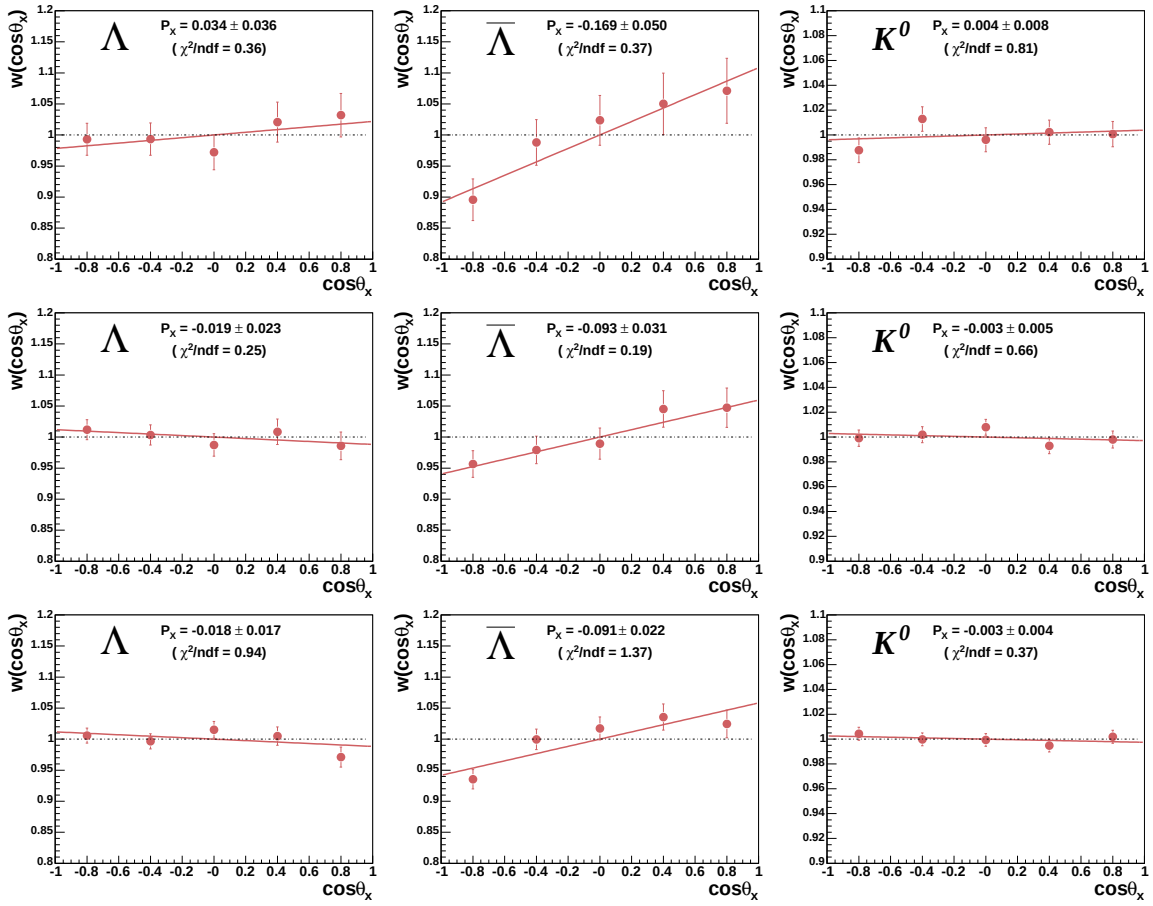

Figure 5.26: Acceptance corrected angular distributions $w(\cos\theta_x)$ for Λ, $\overline{\Lambda}$ and K^0 in the years 2002, 2003 and 2004. The points are fitted with a straight line. The obtained slopes from the fit are directly proportional to the polarizations. Only for $\overline{\Lambda}$ a significantly negative polarization is obtained. The reduced χ^2 of the fit are also shown.

Table 5.5: Polarization of Λ as extracted from the samples plotted in Fig. 5.26. The mean values for kinematic variables are also included. Errors of polarization are statistical only.

		Λ		
year	2002	2003	2004	total
P_x	$+0.034 \pm 0.036$	-0.019 ± 0.023	-0.018 ± 0.017	-0.012 ± 0.013
$\sum N_{\Lambda}^{data}$	9031.9 ± 23.0	24180.7 ± 38.5	45434.3 ± 52.1	78646.9 ± 68.7
χ^2/ndf	0.28	0.25	0.94	-
goodness-of-fit	0.89	0.92	0.44	-
$< Q^2 >$ (GeV/c)^2	2.91	3.39	3.59	3.45
$< x_{Bj} >$	0.027	0.029	0.030	0.029
$< y >$	0.43	0.44	0.44	0.44
$< W^2 >$ (GeV/c^2)^2	127.7	131.0	130.1	130.1
$< x_F >$	0.23	0.24	0.24	0.24
$< z >$	0.29	0.29	0.29	0.29
$< p >$ (GeV/c)	18.7	19.4	19.3	19.3
$< p_T >$ (GeV/c)	0.53	0.53	0.53	0.53

Table 5.6: Polarization of $\overline{\Lambda}$ as extracted from the samples plotted in Fig. 5.26. The mean values for kinematic variables are also included. Errors of polarization are statistical only.

		$\overline{\Lambda}$		
year	2002	2003	2004	total
P_x	-0.163 ± 0.049	-0.099 ± 0.031	-0.091 ± 0.022	-0.100 ± 0.017
$\sum N_{\overline{\Lambda}}^{data}$	5269.2 ± 19.3	14265.0 ± 31.9	27087.6 ± 43.4	46621.8 ± 57.2
χ^2/ndf	0.37	0.19	1.37	-
goodness-of-fit	0.83	0.94	0.24	-
$< Q^2 >$ (GeV/c)^2	2.84	3.34	3.47	3.36
$< x_{Bj} >$	0.024	0.027	0.028	0.027
$< y >$	0.43	0.44	0.47	0.46
$< W^2 >$ (GeV/c^2)^2	127.7	131.0	138.0	134.7
$< x_F >$	0.22	0.22	0.22	0.22
$< z >$	0.28	0.28	0.28	0.28
$< p >$ (GeV/c)	19.2	19.6	19.3	19.4
$< p_T >$ (GeV/c)	0.54	0.53	0.53	0.53

Table 5.7: Polarization of K^0 as extracted from the samples plotted in Fig. 5.26. The mean values for kinematic variables are also included. Errors of polarization are statistical only.

	K^0			
year	2002	2003	2004	total
P_x	$+0.004 \pm 0.008$	-0.003 ± 0.005	-0.003 ± 0.004	-0.002 ± 0.003
$\sum N_{K^0}^{data}$	66972.4 ± 55.8	184417.7 ± 94.4	339952.8 ± 125.2	591342.9 ± 166.4
χ^2/ndf	0.81	0.66	0.37	-
goodness-of-fit	0.52	0.62	0.83	-
$< Q^2 >$ (GeV/c)^2	2.80	3.29	3.47	3.34
$< x_{Bj} >$	0.025	0.027	0.028	0.027
$< y >$	0.45	0.46	0.46	0.46
$< W^2 >$ (GeV/c^2)^2	133.5	136.3	135.9	135.8
$< x_F >$	0.25	0.24	0.24	0.24
$< z >$	0.27	0.27	0.26	0.26
$< p >$ (GeV/c)	17.7	18.1	17.9	17.9
$< p_T >$ (GeV/c)	0.48	0.48	0.48	0.48

5.5.2 Results of Spin Transfer

The spin transfer coefficient can be calculated by using Eq. 3.18. To extract the spin transfer, the longitudinal depolarization factor $D(y)$ of the virtual photon is calculated using the formula $D(y) = (1-(1-y)^2)/(1+(1-y)^2)$ (see Eq. 3.16). For the kinematic constraint of $0.2 < y < 0.9$, the allowed region of $D(y)$ is $0.219 < D(y) < 0.980$. The calculation of $D(y)$ is performed on an event by event basis. The distributions of $D(y)$ for the three years are shown in Fig. 5.27. Here, each $D(y)$ is plotted after background subtraction. The mean values of $D(y)$ are used to calculate the spin transfer coefficient. The measured beam polarization P_B are different for each year. For 2002, P_B is 77%, 76% for 2003, and 80% for 2004. The average errors of the beam polarization are estimated to be about 4% for all years, and they will be taken into account in the systematic error, which will be discussed in Section 5.6.6.

The data suggest in general that the spin transfer of Λ is compatible with zero within the statistical error. The overall spin transfer of Λ was measured resulting in an average value of $C_{LL}^{\Lambda} = +0.030 \pm 0.031$. The negligible spin transfer values for the K^0 in all years indicate that the method used is basically functional. The average spin transfer of K^0 is $C_{LL}^{K^0} = +0.005 \pm 0.007$. The most interesting result is for $\overline{\Lambda}$. Using the same methods as for the Λ, the average spin transfer of $\overline{\Lambda}$ is found to be high with a measured value of $C_{LL}^{\overline{\Lambda}} = +0.232 \pm 0.039$. The difference of the spin transfer between Λ and $\overline{\Lambda}$ is significant.

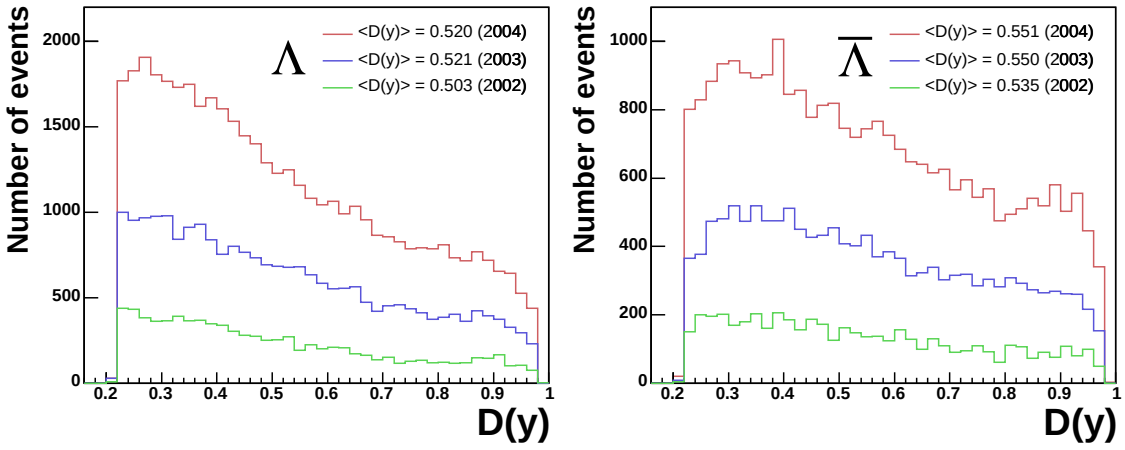

Figure 5.27: Longitudinal depolarization factor $D(y)$ of the virtual photon for Λ and $\overline{\Lambda}$: The plots are obtained after background subtraction. Each histogram is shown here without normalization.

Table 5.8: Spin transfer coefficient of Λ, $\overline{\Lambda}$, and K^0: Errors of the spin transfer are statistical only. Average spin transfer coefficients are given in the last column.

		$C_{LL} = \frac{P_x}{P_B \cdot D(y)}$		
year	P_B	Λ	$\overline{\Lambda}$	K^0
2002	-0.77	-0.088 ± 0.093	$+0.410 \pm 0.121$	-0.010 ± 0.020
2003	-0.76	$+0.048 \pm 0.058$	$+0.222 \pm 0.074$	$+0.007 \pm 0.012$
2003	-0.80	$+0.043 \pm 0.041$	$+0.206 \pm 0.050$	$+0.007 \pm 0.009$
$<C_{LL}>$		$+0.030 \pm 0.031$	$+0.232 \pm 0.039$	$+0.005 \pm 0.007$

5.6 Systematic Study

This section will discuss the influence of essential biases of the presented analysis method on the results in the last section. Given the high statistics of the polarization measurements, a number of systematic studies have been done to determine or to estimate the size of possible systematic errors.

The following potential sources of systematic errors have been studied in the present analysis. A good indication for false polarization are the kaons, which are available in very large numbers and also contribute to the background in the Λ and $\overline{\Lambda}$ invariant mass histograms. The fitting procedure of the invariant mass histograms might introduce biases in particular for each cosθ bin, where the invariant mass distribution shows a nontrivial shape. The polarizations are determined from the slope of the straight line fit in $w(\cos\theta_x)$, thus the stability of the fit procedure has to be checked. It also has to be verified, whether the acceptance correction with the Monte Carlo works correctly and whether the polarization results are stable over the various data taking periods.

Possible systematic effects might in addition be caused by the positive or negative longitudinal polarization of the target or might influence the event type and on the location in which the interaction took place in the upstream or downstream target cells. Possible influences of up-down and left-right asymmetries of the apparatus have to be compensated by means of the acceptance correction from the Monte Carlo. The polarizations have been evaluated splitting data in different samples according to the different triggers in order to find systematic effects originating from the detected scattered muon. All of these systematic issues are addressed in this section.

5.6.1 Systematic of the K^0 Background

The K^0, being spinless and having a similar decay topology as the Λ and $\overline{\Lambda}$, provides a good way to verify that the polarization analysis is free of obvious biases. As a cross-check the results of the K^0 polarization are obtained in the same way, so that the K^0 polarization can directly be compared with respect to the Λ and $\overline{\Lambda}$ polarization. The average K^0 polarization contributes to the calculation of the total systematic error for both Λ and $\overline{\Lambda}$ with a systematic error of 0.002 (see Table 5.7).

5.6.2 Systematics of the Estimation Method

Systematics of the Background Subtraction

To test the background subtraction in the fitting procedure, a Monte Carlo sample with polarized Λ is created and substituted instead of the data sample in the code. The polarizations

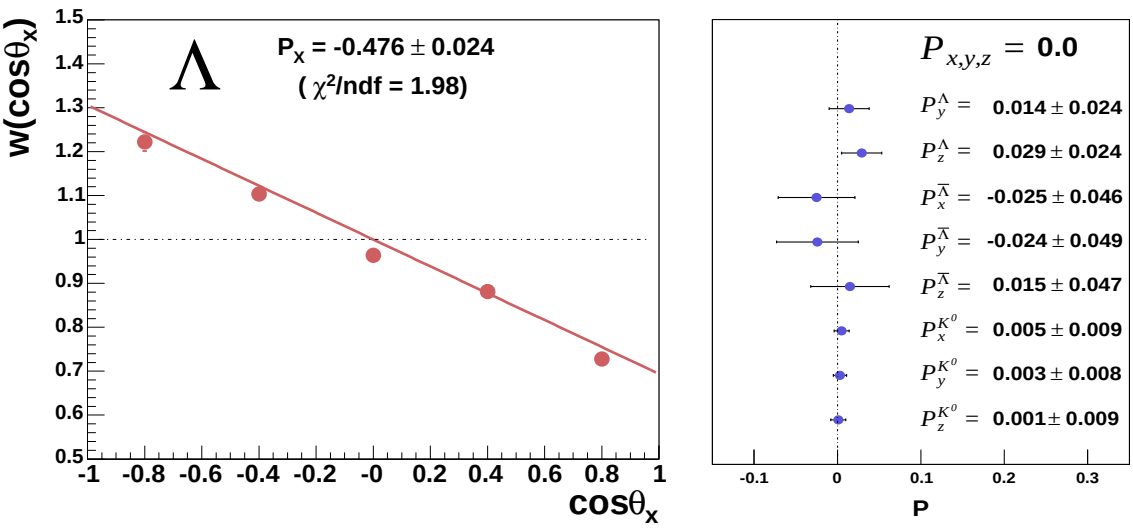

Figure 5.28: Polarized Monte Carlo are simulated with the 2002 set-up. The Monte Carlo Λ sample is polarized with $P_x = -0.5$.

are extracted in exactly the same manner as in the data analysis. Such a procedure allows to study the systematics for the possible influence of the background subtraction method from the fit.

The Λ's in the Monte Carlo sample have a polarization of $P_x = -0.5$, $P_y = 0.0$ and $P_z = 0.0$. $\overline{\Lambda}$ and K^0 are generated without any polarization in all directions [234]. Fig. 5.28 shows the result of Λ polarization with 50% polarized Monte Carlo sample in the left plot. The result of polarizations for the other directions and particles are shown in the right plot, where zero polarizations are expected. The test is quite convincing on the quality of the fit procedure. One can conclude that the fit procedure with a Gaussian function for the background subtraction is valid and quite stable.

The deviation of the mean values from the expected values is at the level of below one sigma of the statistical error. To precisely estimate the systematic error due to the fit procedure, a quantity called pull is introduced. This quantity is defined as

$$\mathbf{P}_i = \frac{P_{x,i}^{\text{analyzed}} - P_{x,i}^{\text{simulated}}}{\sqrt{\sigma^2_{P_{x,i}^{\text{analyzed}}} - \sigma^2_{P_{x,i}^{\text{simulated}}}}}, \tag{5.18}$$

where $P_{x,i}^{\text{analyzed}}$ refers to the observed polarization obtained for the i^{th} sample. $P_{x,i}^{\text{simulated}}$ is the expected polarization. σ^2 is the corresponding variance, and the difference between the analyzed and simulated polarization is used to take into account the complete correlations

between $P_{x,i}^{\text{analyzed}}$ and $P_{x,i}^{\text{simulated}}$ [235]. Pulls should be normally distributed with mean equal to 0 and standard deviation equal to 1. Thus they are a convenient tool to estimate the possible systematic errors. Here, the test cannot be performed as a Gaussian fit to a histogram since there are only 9 pull values. The mean and standard error of the pulls was calculated directly by a Gaussian estimate [236]. Assuming a zero error of the simulated polarization, which is free of any bias, the best estimate for the mean and standard error is then leading to

$$\overline{\mathbf{P}} \pm \overline{\delta\mathbf{P}} \;=\; \frac{\sum_i \mathbf{P}_i}{n} \pm \frac{1}{\sqrt{n}} \cdot \sqrt{\frac{\sum_i (\mathbf{P}_i - \overline{\mathbf{P}})^2}{n-1}} = 0.35 \pm 0.12. \tag{5.19}$$

Taking into account the shifted mean value with respect to the reference mean and two standard deviation of the error on the mean, the systematic uncertainty can be obtained by

$$\begin{aligned} \sigma_{\text{sys}}^{\text{Fit(Gauss)}}(P_x) &= \overline{\mathbf{P}}\sigma_{\text{stat}} + 2 \times \overline{\delta\mathbf{P}}\sigma_{\text{stat}} \\ &= \begin{cases} 0.59 \times 0.013 = 0.008 & \Lambda \\ 0.59 \times 0.017 = 0.010 & \overline{\Lambda} \\ 0.59 \times 0.003 = 0.002 & K^0 \end{cases}. \end{aligned} \tag{5.20}$$

The systematic uncertainty from the fit procedure corresponds to 59% of the statistical error σ_{stat} for each particle. The errors are obviously dominated by statistics. Here, the systematic error has only been determined with a Monte Carlo simulation for 2002 data and is assumed to be of the same size for 2003 and 2004.

Systematics of the Linear Fit

Since the statistics of Λ in the Monte Carlo is about 8 times the statistic in data, the normalization of the total number of events for the data and the Monte Carlo samples is quite important. If the fit procedure does not properly estimate the total number of events in the histogram of each $\cos\theta_x$, the polarization manifests itself as an offset in the $w(\cos\theta_x)$ distribution. The effect has been tested by using a different fit function:

$$w_0(\cos\theta_x) = A_0 + \alpha P_x \cos\theta_x. \tag{5.21}$$

The data are fitted by a first order linear function with a non-fixed parameter A_0. The polarizations are virtually identical to the ones from the fit of $w(\cos\theta_x)$ according to Eq. 5.16. The A_0 parameters of the Λ, $\overline{\Lambda}$, and K^0 fits by $w_0(\cos\theta_x)$ agree with the expected value 1. The difference of the two fits is of the order of 10^{-4}, which can be completely neglected. This demonstrates that the acceptance corrections successfully compensate the different size of the data and the Monte Carlo sample.

The error on $\cos\theta_x$ is set to zero in the standard analysis, but some alternative consideration as a systematic effect can be made. The resolution of $\cos\theta_x$, $\Delta\cos\theta_x$, is considered to be

$1/\sqrt{12}$ times the bin width, because the angular distributions can be taken as a rectangular distribution. The measured polarizations, however, remain unchanged, even if $\Delta\cos\theta_x$ is increased to its higher values. It is thus apparent that the change of the polarizations due to the error on the $\cos\theta_x$ bins can be neglected.

In order to extract the polarization the samples are divided in five $\cos\theta_x$ bins, which results in the $w(\cos\theta_x)$ distribution. To study the influence of the choice of the number of $\cos\theta_x$ bins, the analysis was performed with only four $\cos\theta_x$ bins as well as with ten $\cos\theta_x$ bins. Fig. 5.29 shows an example of $\overline{\Lambda}$ in the 2004 data sample. It can be seen that the deviation from the standard result of $\overline{\Lambda}$ is negligible. However, the derived systematic errors due to the binning of $\cos\theta_x$ are used for the calculation of the total systematic error for the sake of completeness. The systematic error is determined in the following way. A maximum value of deviations with respect to the standard result using five $\cos\theta_x$ bins was found for all V^0 in each year, separately. The found values are shown in the Table 5.9. Then the weighted means of the absolute values of the maximum deviations for each particle were calculated to see the pure effect. The results finally yield the systematic errors for all V^0s:

$$\sigma_{\mathrm{sys}}^{\mathrm{Fit(Linear)}}(P_x) = \begin{cases} 0.004 & \Lambda \\ 0.007 & \overline{\Lambda} \\ 0.001 & K^0 \end{cases} . \tag{5.22}$$

Again, the errors are found to be very small compared to the statistical errors. Fig. 5.30 shows how the values for the polarizations are changed by the conditions of the linear fit as mentioned above and the detailed values are listed in Appendix B.

Table 5.9: The results shown here finally yield the systematic error for all V^0 using the absolute values of the maximum deviations due to the binning of $\cos\theta_x$.

	$\lvert P_x^{5\cos\theta_x} - P_x^{4,10\cos\theta_x}\rvert_{max}$		
year	Λ	$\overline{\Lambda}$	K^0
2002	0.009	0.004	0.001
2003	0.001	0.012	0.002
2004	0.005	0.006	0.001

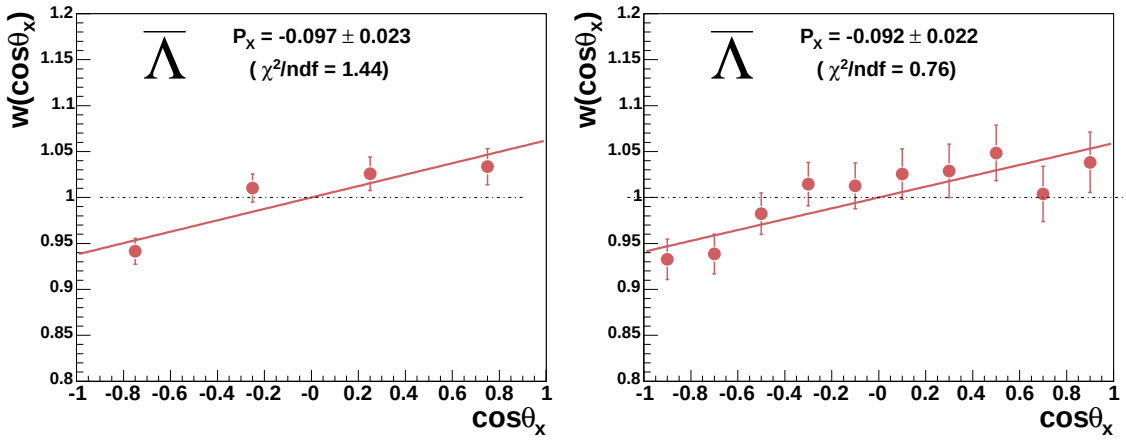

Figure 5.29: Acceptance corrected angular distributions ($w\cos\theta_x$) of the $\overline{\Lambda}$ sample in 2004 are fitted with 4 and 10 $\cos\theta_x$ bins. In both cases the straight lines fit the data well with reduced χ^2 of 1.44 and 0.76 The results are consistent with the result of 5 $\cos\theta_x$ bins.

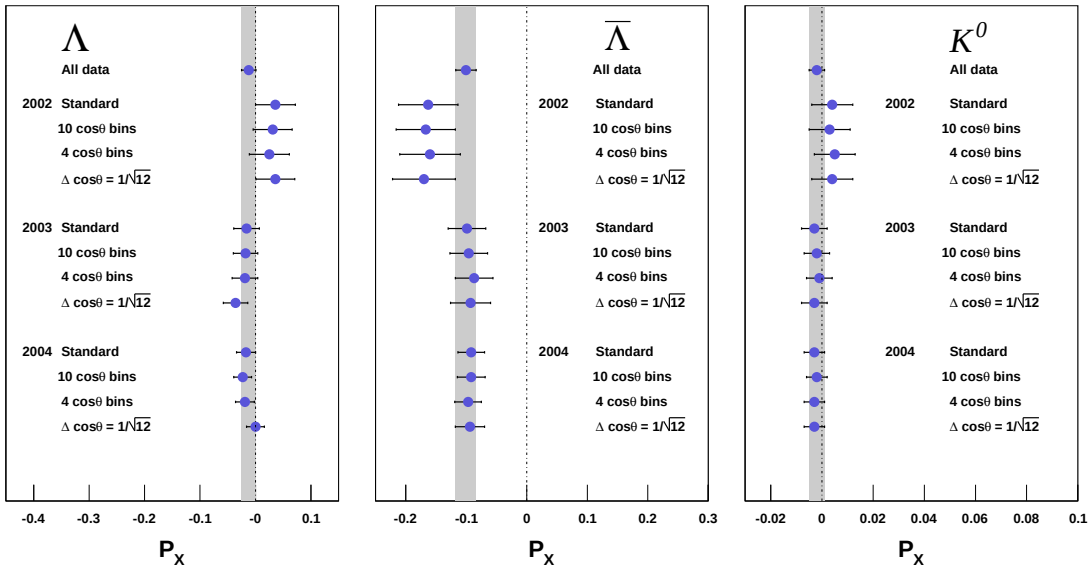

Figure 5.30: Dependence of Λ, $\overline{\Lambda}$, and K^0 polarizations for different binning in $\cos\theta_x$ and $\Delta\cos\theta_x$. The standard indicates results of 5 $\cos\theta_x$ bins with $\Delta\cos\theta_x$=0. 10 and 4 $\cos\theta_x$ bins are obtained with $\Delta\cos\theta_x$=0. The results of $\Delta\cos\theta_x$=$1/\sqrt{12}$ are obtained with 5 $\cos\theta_x$ bins. The values show no significant systematic effect of $\Delta\cos\theta_x$ on the polarization. The bands indicate the values of the overall Λ, $\overline{\Lambda}$, and K^0 polarization, respectively.

5.6.3 Verification of the Acceptance Correction

The acceptance correction calculated using Monte Carlo compensates the asymmetry of the apparatus, which is mainly caused by the spectrometer dipole magnets. The modified parameters in Monte Carlo have been chosen to get good agreement between data and Monte Carlo in the distributions of different kinematic variables. This is not trivial, because a variation of parameters can lead to a better agreement for one kinematic variable, but at the same time the agreement for another can become worse. To study the influence on the polarization by tuning only one parameter is not practical due to the limitations in terms of production time. Therefore the influence on the results for the polarization have been simultaneously studied for the change of the parameters of the fragmentation and the use of different parameterizations for the parton distribution functions. Three different Monte Carlo samples were prepared by changing the parton distribution function (CTEQ2L,CTEQ5L,GRV98LO) and different fragmentation parameters (PARJ(1,2,21,22,23,24,41,42)). The parameters used for the Monte Carlo production are summarized for three different settings in Table. 5.10.

The GRV98LO parametrization used in the standard analysis was replaced by CTEQ2L in 2002, CTEQ5L in 2003, and GRV98LO in 2003. The change of parton distributions affects the shapes of inclusive distributions of x_{Bj}, Q^2, W^2 and y. The fragmentation parameters PARJ(1,2,21,22,23,24,41,42) are changed in addition without distinguishing between the hyperons and K^0 Monte Carlo, which leads immediately to a worse agreement between data and Monte Carlo for the K^0 background. For the default settings of the transverse momentum parameters PARJ(21,23,24), the agreement of data with Monte Carlo is by far not as good as for the tuned ones, which have been used in the standard analysis. In the same manner, the change to the default value of parameters PARJ(1,2,41,42) lead to a disagreement between the

Table 5.10: Summary of the parameters of three different Monte Carlo samples for systematic studies.

Parameter	Meaning	2002(default)	2003(default)	2003(tuned)
LST(15)	PDF	4017(CTEQ2L)	4046(CTEQ5L)	5012(GRV98LO)
PARJ(1)	$\frac{P(qq)}{P(q)}$	0.1	0.1	0.2
PARJ(2)	$\frac{P(s)}{P(u)}$	0.3	0.3	0.4
PARJ(21)	Transverse momentum	0.36 GeV/c	0.36 GeV/c	0.4 GeV/c
PARJ(23)	Admixture of 2nd Gaussian	0.01	0.01	0.08
PARJ(24)	Width of 2nd Gaussian	2.0	2.0	2.5
PARJ(41)	LUND fragmentation a	0.3	0.3	0.97
PARJ(42)	LUND fragmentation b	0.58 GeV^{-2}	0.58 GeV^{-2}	0.37 GeV^{-2}

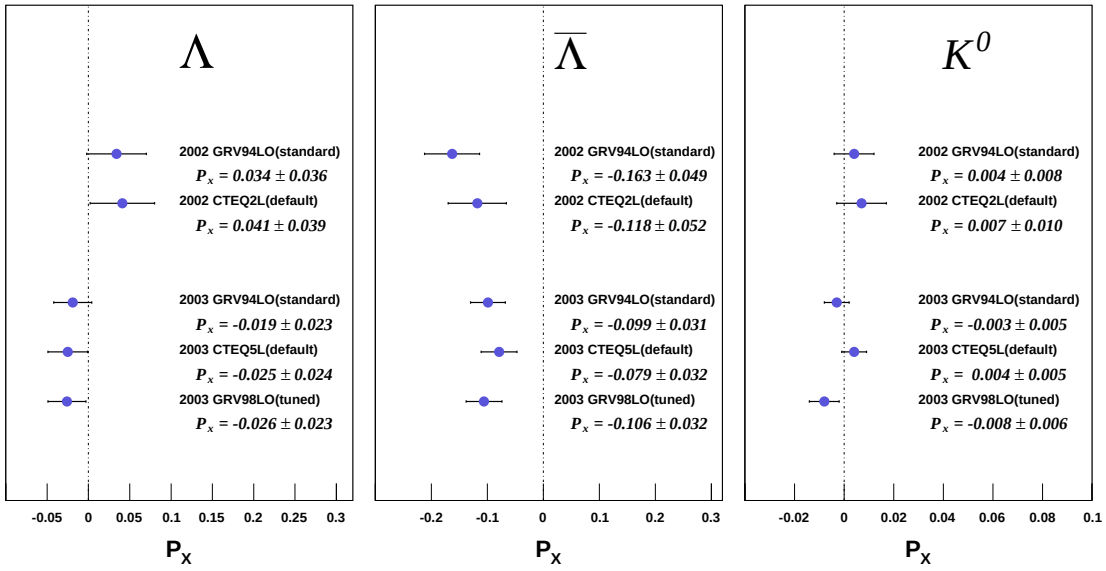

Figure 5.31: Λ, $\overline{\Lambda}$, and K^0 polarizations obtained with three different Monte Carlo samples are compared with standard Monte Carlo.

data and Monte Carlo for the momentum spectra of all reconstructed and decay particles. In contrast, the agreement of x_F and z distributions get much better for the target fragmentation region. These different Monte Carlo samples allow to estimate the effect of these modified parameters on the acceptance correction. These systematic studies have been performed for the 2002 and 2003 data and Monte Carlo sample only. The result of these studies is assumed to be of the same for 2004.

Fig. 5.31 shows that the influence on the polarization is not significant. The differences between the modified setting and the other Monte Carlo are comparable with each other, which means they are within less than one statistical error and can be regarded as a statistical fluctuation. The systematic effect of the acceptance correction is calculated with the pull method as described before. The shifted mean and twice the standard error of the mean values are used to estimate the systematic uncertainty.

$$\begin{aligned} \sigma_{\mathrm{sys}}^{\mathrm{MC}}(P_x) &= \overline{\mathbf{P}}\sigma_{\mathrm{stat}} + 2 \times \overline{\delta\mathbf{P}}\sigma_{\mathrm{stat}} \\ &= \begin{cases} 0.29 \times 0.013 = 0.004 & \Lambda \\ 0.29 \times 0.017 = 0.005 & \overline{\Lambda} \\ 0.29 \times 0.003 = 0.001 & K^0 \end{cases} . \end{aligned} \tag{5.23}$$

The calculation of a systematic error only gives a significant value for Λ and $\overline{\Lambda}$.

A further test was done to check possible effects of the acceptance correction determined

from Monte Carlo. To study this effect, the polarizations were evaluated dividing the data samples according to the kinematic variables $x_{Bj}, Q^2, W^2, y, z, x_F, p_T$ in 5 different bins and their means were compared with the standard results. In total 315 pulls for the Λ, $\overline{\Lambda}$, and K^0 polarizations were prepared. As an example, Fig. 5.32 shows the z dependence of polarizations for the standard Monte Carlo and two different Monte Carlo samples. The deviations from the standard analysis are statistically compatible with what is expected in the absence of systematic effects. The pulls are computed for all kinematic variables and plotted in the right panel of Fig. 5.32. The mean of the pull is found to be centered around zero and the values of pull are distributed mostly within one statistical error. The result still shows no evidence for the presence of a systematic error, even though the data samples used to evaluate the polarization are limited in statistics. It seems that the angular distribution is not distorted by changing the Monte Carlo setting. To conclude, this test gives an independent indication that the acceptance correction with Monte Carlo is correct. The systematic error due to acceptance correction by means of the Monte Carlo is considerably smaller than the statistical errors.

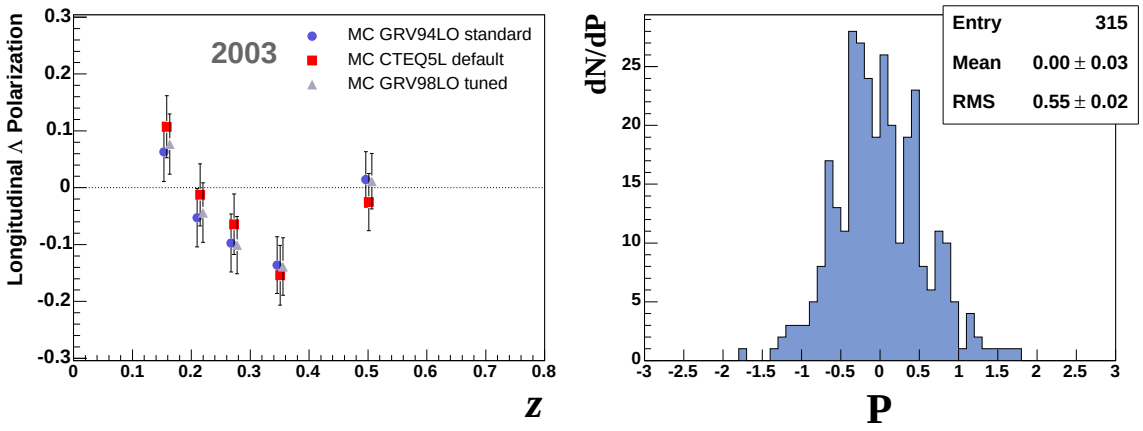

Figure 5.32: Left: Polarization of Λ with the standard Monte Carlo setting is compared with two other Monte Carlo settings in the kinematic variable z and the year of 2003. Right: Distribution of pulls for the evaluated Λ, $\overline{\Lambda}$ and K^0 polarization in 7 kinematic variables and 5 different bins.

5.6.4 Systematic Errors from the Detector Setup

Stability of the Time Variation

During data taking some detectors and the spectrometer setup was improved by repairing, rearranging or adding new detectors. Additionally the reconstruction software was updated continuously, so that the mDST data of the different periods in the data set were produced by different versions of CORAL. To investigate the stability of the spectrometer in time, the compatibility of the polarization results obtained separately for all the data taking periods have been tested. The data samples were collected in 23 periods from 2002 to 2004 altogether and the test was performed separately for Λ, $\overline{\Lambda}$ and K^0.

In Fig. 5.33 the results for the Λ and $\overline{\Lambda}$ mass shift and the mass resolution are given period by period. The shift of the mass spectrum from the PDG is below 1.0 MeV/c^2, which is much smaller than the mass resolution. The sigma of the mass spectrum is approximately constant in time. It was not possible to measure the polarization for one period due to the small statistics, therefore two data periods were combined to extract a polarization, except for period W22. Fig. 5.34 shows that the results do not show any dependence of the polarization on time.

Influence of the V^0 Direction

The COMPASS spectrometer is neither left-right symmetric nor up-down symmetric due to the geometry of the spectrometer magnets. If the acceptance correction fails to compensate the asymmetry in the spectrometer, this could lead to a false polarization in different parts of the spectrometer.

To verify the reliability of the correction, the polarization has been evaluated dividing the data samples according to the azimuthal angle ϕ of the reconstructed particles in the laboratory system. For 2002 and 2003 the data samples were divided depending on the quadrant, in which the V^0 have been reconstructed in the apparatus. This corresponds to the up-left, down-left, up-right, and down-right part of the V^0 momentum direction in the laboratory system. For 2004 each of the data samples is combined in a way such that each sector has a 45° segment of ϕ, which corresponds to eight divisions in the direction of the V^0 momentum. In Fig. 5.35 the longitudinal (x) and transverse (y) component of the Λ momentum is plotted with the whole data sample. Fig. 5.36 summarizes the results for Λ, $\overline{\Lambda}$, and K^0 polarization. The results do not show a large deviation from the average polarization and again do not provide any evidence for systematic effects in their distributions. All calculations have been performed using available precision upto three digits of the polarization values. The numbers can be found in Appendix B.

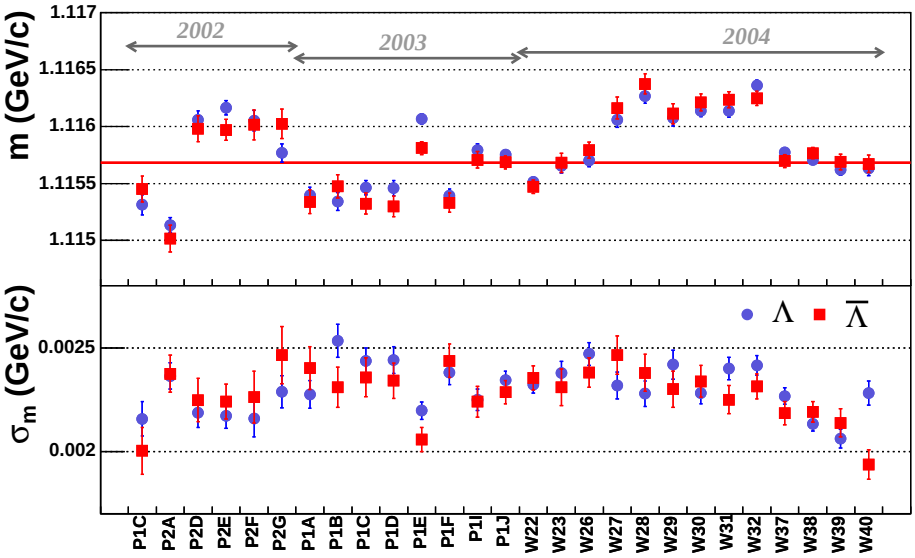

Figure 5.33: Periodical dependence of mean mass and sigma: The blue circles denote the Λ, the $\overline{\Lambda}$ is indicated by red squares, The PDG value is additionally shown as a red line in the upper plot.

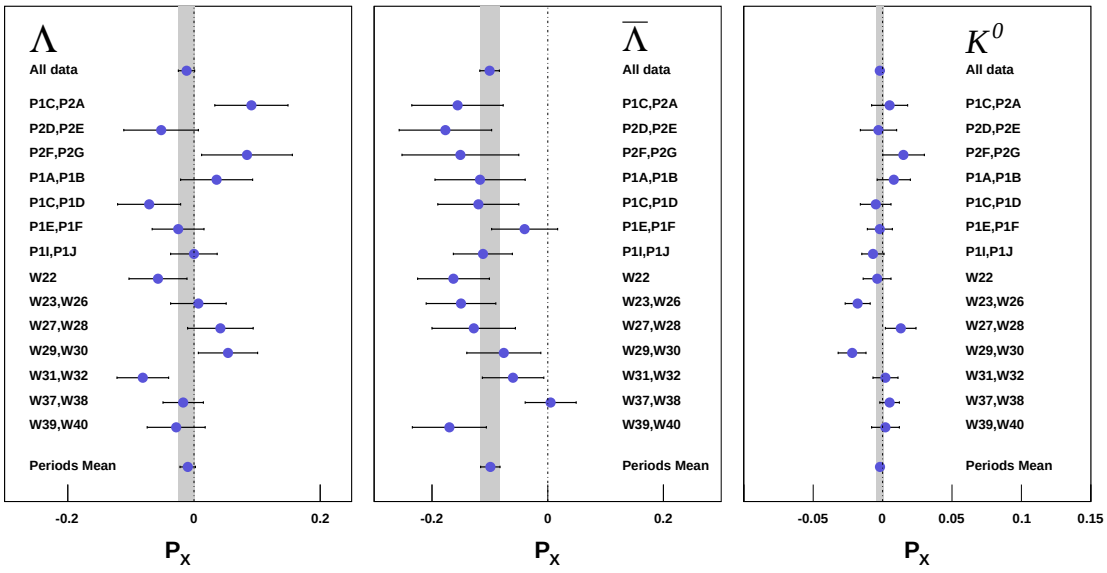

Figure 5.34: Dependence of Λ, $\overline{\Lambda}$, and K^0 polarizations on the various data taking periods: The polarizations fluctuate within the statistical error. The weighted mean of all polarization values agrees with the respective overall polarization, that is indicated by the band.

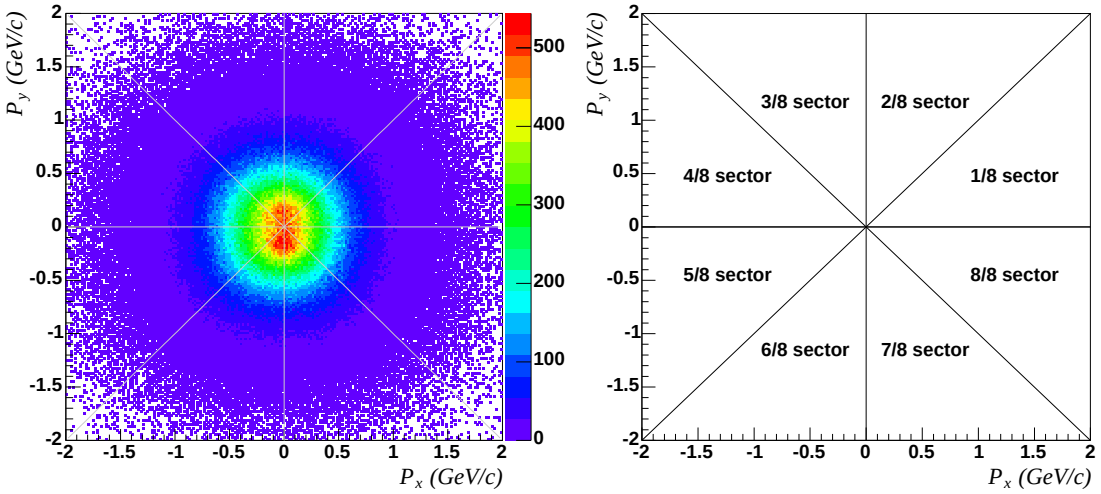

Figure 5.35: The longitudinal (x) and transverse (y) component of the Λ momentum is plotted with the whole data sample (2002-2004) in the laboratory system. The grey lines divide the area into 8 segments.

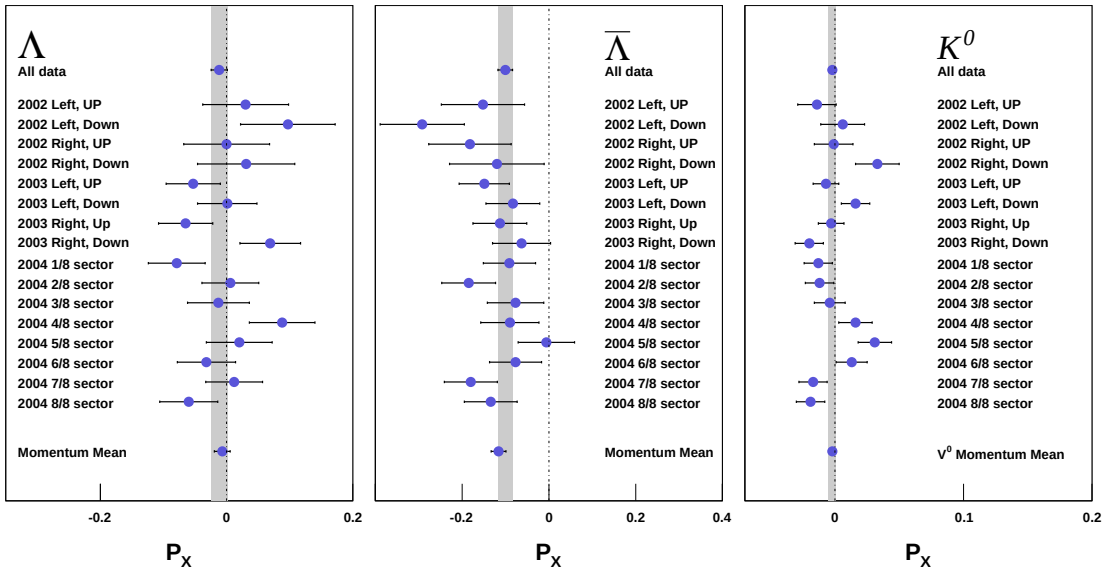

Figure 5.36: Dependence of Λ, $\overline{\Lambda}$ and K^0 polarizations on the various momentum directions: The polarizations fluctuate within the statistical error. The grey bands indicate the overall results for each V^0.

Influence of the Trigger Setup

Possible acceptance effects on the physics results from the trigger were tested by checking the compatibility of the polarizations evaluated after splitting the data according to the trigger type of each event. The inclusive kinematic variable Q^2 is plotted versus y for the different triggers in Fig. 5.38. Usually trigger combinations cover different kinematic regions, but there are no clear boundaries of the kinematic regions due to the overlap of the active region of the triggers. Events of MT with coincidence of calorimeters are not included because of the large overlap of MT and incMT.

Since the IT has been designed for low Q^2 events, it does not play an important role in the Λ analysis. Therefore the events of IT are added with LT events, which cover roughly the same kinematic region. The data were splitted in 5 groups of trigger combinations except for the 2002 data, because the calorimeter trigger was not included in data taking before 2003. Fig. 5.39 shows that the results for the polarization are statistically compatible. The small deviations in the results is not surprising, since the triggers correspond to different kinematic regimes.

Influence of the Target Setup

During the operation of the spectrometer both target cells are longitudinally polarized with opposite spin direction and the orientation of the target polarization is reversed periodically by flipping the solenoid field. For the measurement of the longitudinal Λ polarization the data from both target cells have been added and the absolute value of the target polarization P_T is assumed to be zero. To confirm this assumption, the data has been taken with two different target spin orientations, either target cell is polarized positively or negatively with respect to the spin direction of the beam as given in Fig. 5.37. If the number of V^0 events is well balanced for the two spin orientations, the false polarization due to the target polarization should have canceled out. To simplify the spin direction of the targets, the beam polarization refers to the defined target spin orientation. The mean component of the target polarization is calculated for the two spin orientation of the target in summing over all events:

$$\Delta|P_T| = \frac{1}{N^+_{tot}}|\sum_{N^+_i} P^+_T| - \frac{1}{N^-_{tot}}|\sum_{N^-_i} P^-_T| = 50.359(\%) - 50.444(\%) = -0.085(\%), \qquad (5.24)$$

where the $+$ and $-$ sign indicate the same and opposite spin orientation with respect to the beam polarization. The magnitude of the effective target polarization cancels out completely.

The longitudinal polarizations of Λ, $\overline{\Lambda}$ and K^0 are calculated for the target polarizations of each cell. The results for the polarizations of the upstream and downstream target cell are given in Fig. 5.41. The polarizations are compatible with zero within two standard deviations as expected. One has to keep in mind that the effect of target polarization is essential in

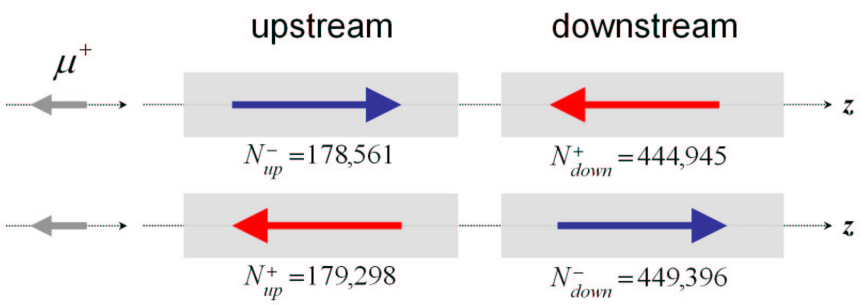

Figure 5.37: Target polarization of the reconstructed V^0 events in each target configuration. The data are selected before the cut on $x_F > 0.05$.

the measurement of Λ polarization, because the Λ polarization could be severely affected by target polarization.

The acceptance difference for V^0 events is clearly visible in Fig. 5.37 as well as in the primary vertex distribution (see also Fig. 5.2), the event ratio of the two target cells is found to be $N_u/N_d \sim 0.4$. It is necessary to investigate the potential influence of different acceptance in the two target cells. To do this, two kinds of effects were considered for the target geometry. The first effect was tested by splitting the two target cells in two halves. The data samples in each target cell is divided in the upstream and the downstream along the z-direction. The second one selects the data samples by dividing the target in quadrants of *x*-*y* plane. The polarizations were then calculated and were statistically compatible as shown in Fig. 5.40. The tests performed in these categories did not give any evidence for the presence of systematic effects.

The dependence of the Λ and $\overline{\Lambda}$ polarization on the target polarization can be measured with different target polarizations of the two target cells at COMPASS. The difference of the Λ and $\overline{\Lambda}$ polarization between positive and negative polarizations of target are measured as following:

$$\begin{aligned} \Delta P_\Lambda = P_\Lambda(P_T^+) - P_\Lambda(P_T^-) &= (-0.011 \pm 0.017) - (-0.007 \pm 0.018) \\ &= -0.004 \pm 0.025, \\ \Delta P_{\overline{\Lambda}} = P_{\overline{\Lambda}}(P_T^+) - P_{\overline{\Lambda}}(P_T^-) &= (-0.107 \pm 0.024) - (-0.102 \pm 0.024) \\ &= -0.005 \pm 0.034. \end{aligned} \tag{5.25}$$

No significant dependence of the polarization on the target polarization has been observed and the results of Λ and $\overline{\Lambda}$ are quite similar. These results are not in qualitative agreement with the theoretical predictions of A. Kotzinian et al., where the differences are expected negative within a few percent for both Λ and $\overline{\Lambda}$. (see Section 3.3.1).

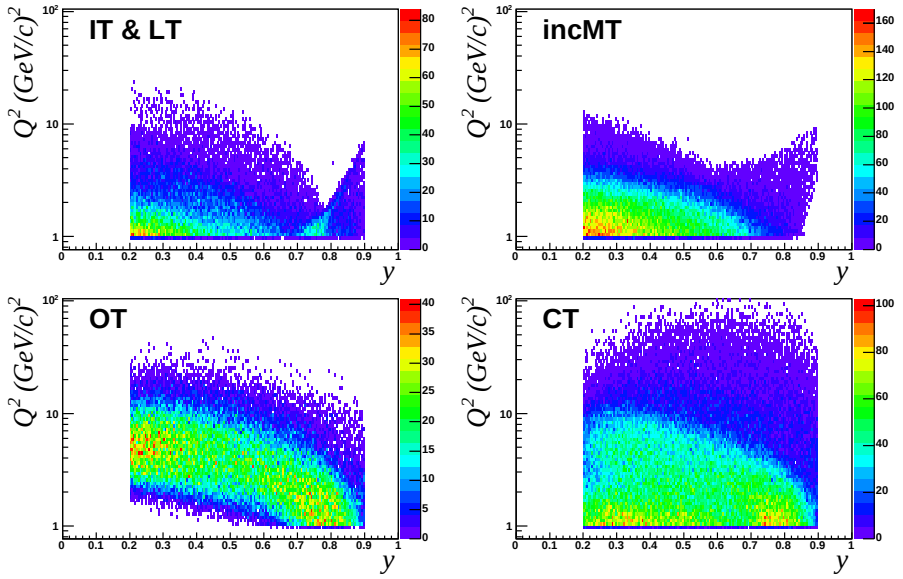

Figure 5.38: Q^2 vs. y for the different triggers: The LT selects events with low Q^2 and large y. The incMT covers the region of intermediate to large Q^2, whereas the OT covers high Q^2 events. $Q^2 > 10$ (GeV/c)^2 are mainly selected by the CT. The CT usually fires in coincidence with one of the hodoscope triggers and covers the whole kinematic region.

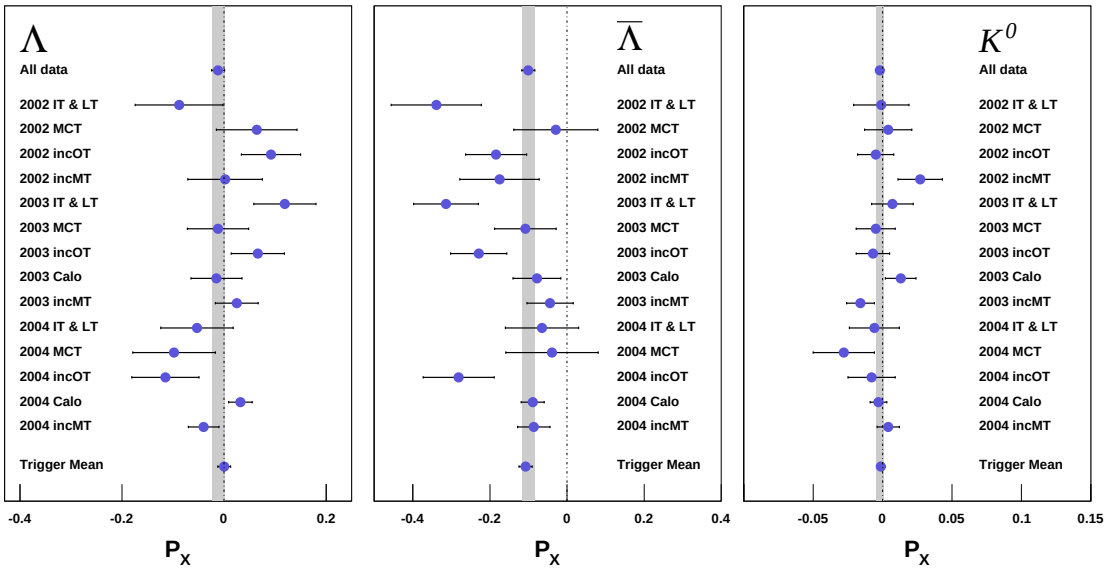

Figure 5.39: Dependence of Λ, $\overline{\Lambda}$, and K^0 polarizations on the different triggers: The polarizations fluctuate within the statistical error. The grey bands indicate the overall results for each V^0.

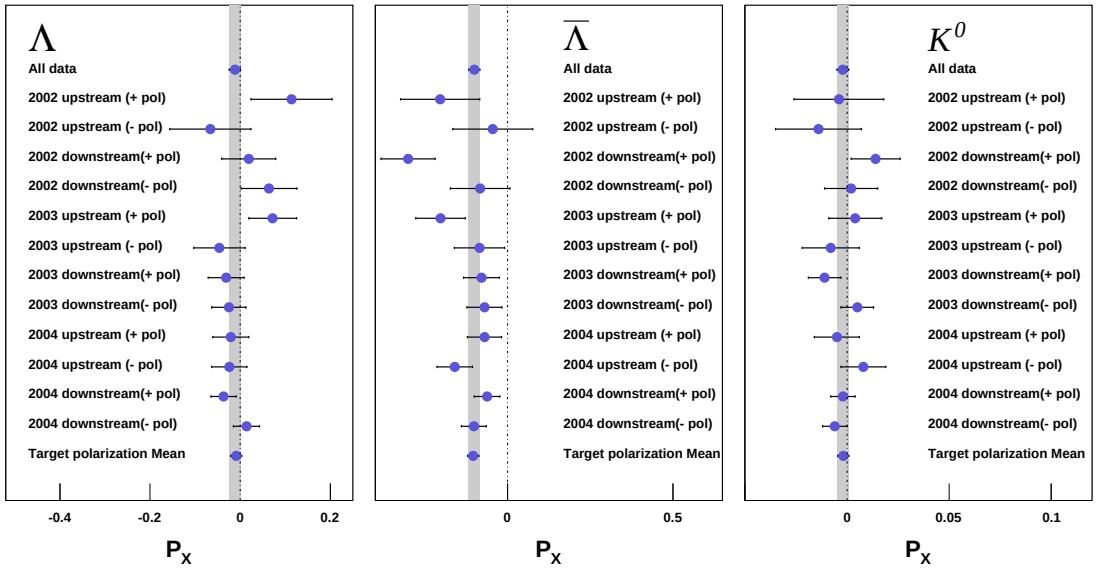

Figure 5.40: Dependence of Λ, $\overline{\Lambda}$, and K^0 polarizations on the different target polarization: The polarizations fluctuate within the statistical error. The grey bands indicate the overall results for each V^0.

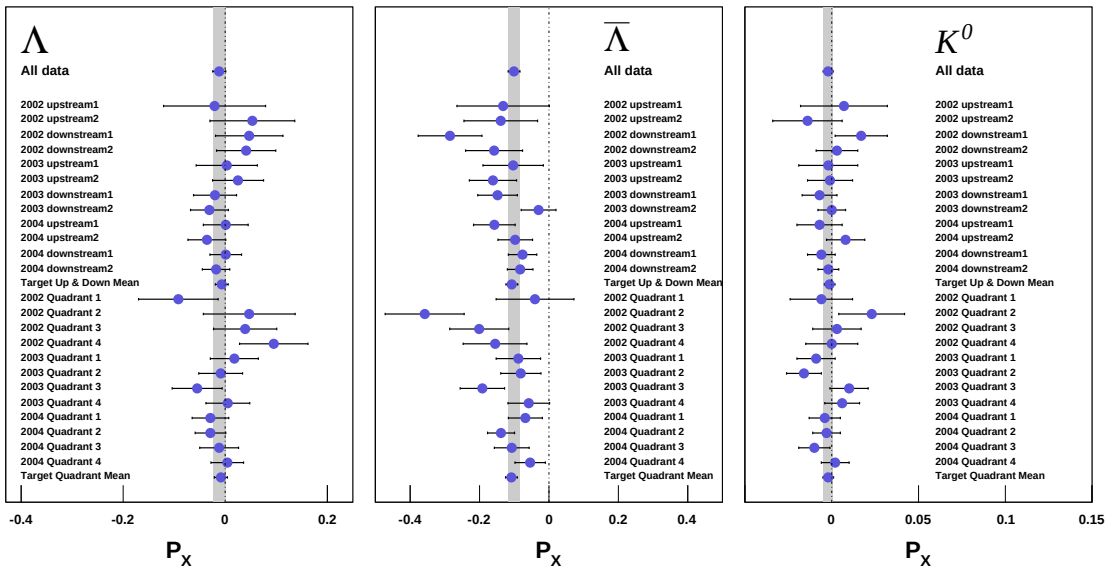

Figure 5.41: Dependence of Λ, $\overline{\Lambda}$, and K^0 polarizations on the different target position: The polarizations fluctuate within the statistical error. The grey bands indicate the overall results for each V^0.

Total Systematic Error of the Detector Setup

Since in the various tests of the detector setup no indication for systematic effects could be observed, it was concluded that the systematic errors due to acceptance for the time, spectrometer, trigger and target are considerably smaller than the statistical errors. As in the previous case, the total systematic error of the detector setup was estimated from the distribution of pulls, in which the polarizations in each category were compared with the results obtained from the overall data, as shown before. In total there are 240 values of pulls from the 3 particles and 4 categories. The distribution of the pulls for all subsamples is shown in Fig. 5.42. The pulls are centered around zero with a sigma of 1 as expected for a data sample following a Gaussian distribution. A very good agreement with purely statistical fluctuations has been seen for all the various subsamples of the polarizations. The systematic errors are estimated in terms of the shift of the mean and their error with 2 standard deviations.

$$\begin{aligned} \sigma_{\rm sys}^{\rm MC}(P_x) &= \overline{\mathbf{P}}\sigma_{\rm stat} + 2 \times \overline{\delta\mathbf{P}}\sigma_{\rm stat} \\ &= \begin{cases} 0.06 \times 0.013 = 0.001 & \Lambda \\ 0.06 \times 0.017 = 0.001 & \overline{\Lambda} \\ 0.06 \times 0.003 = 0.000 & K^0 \end{cases} . \end{aligned} \tag{5.26}$$

The systematic error for Λ and $\overline{\Lambda}$ can be neglected, but for completeness these values were used for the estimation of the the total systematic error. For the polarization of K^0 the effects of the detector setup turned out to be negligible on a level of 10^{-4}.

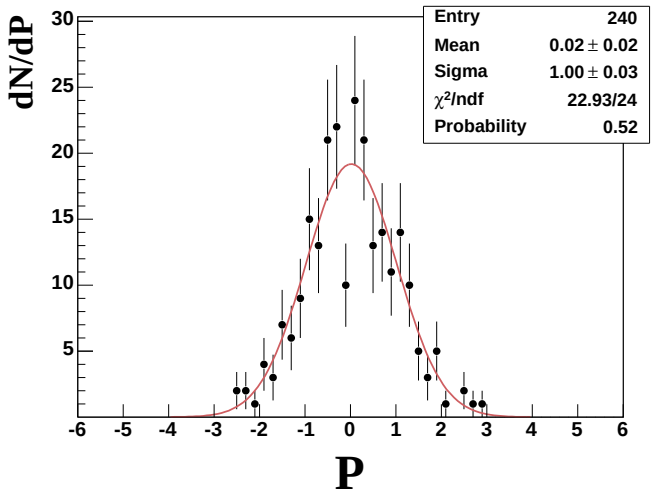

Figure 5.42: Distribution of pulls for the Λ, $\overline{\Lambda}$ and K^0 polarization. The shape of the distribution is well described by the Gaussian and fits the pulls successfully with a reduced χ^2 = 0.96 and a probability of 52%.

5.6.5 Systematic Error on α

For the polarization values established in Section 5.5, the cited errors were just the errors on the slope of the straight line fit to the acceptance corrected angular distribution $w(\cos\theta_x)$ using a constant decay asymmetry parameter α. If the statistics of the data sample is increased, the systematic error of α will become important. Taking additionally into account the error on the measured $\alpha = 0.642 \pm 0.013$, the relative error of the polarization changes by a fraction of $\frac{\delta\alpha}{\alpha} = 0.02$. This yields the systematic error of the polarization due to the error of α:

$$\begin{aligned} \sigma^{\alpha}_{\mathrm{sys}}(P_x) &= |P_x| \times \left(\frac{\delta\alpha}{\alpha}\right) \\ &= \begin{cases} 0.012 \times 0.02 = 0.0002 & \Lambda \\ 0.100 \times 0.02 = 0.0020 & \overline{\Lambda} \end{cases}. \end{aligned} \tag{5.27}$$

Again, the errors are found to be very small compared to the statistical errors.

5.6.6 Total Systematic Error

Total Systematic Error for Polarization

To obtain the total systematic error of the measured polarization, the errors discussed so far are combined in the following way:

$$\sigma^{\mathrm{tot}}_{\mathrm{sys}}(C_{LL}) = \sqrt{(\sigma^{K^0}_{\mathrm{sys}})^2 + (\sigma^{\mathrm{Gauss}}_{\mathrm{sys}})^2 + (\sigma^{\mathrm{Linear}}_{\mathrm{sys}})^2 + (\sigma^{\mathrm{MC}}_{\mathrm{sys}})^2 + (\sigma^{\mathrm{Setup}}_{\mathrm{sys}})^2 + (\sigma^{\alpha}_{\mathrm{sys}})^2}. \tag{5.28}$$

The maximum estimate of the systematic error is obtained by adding all the contributions in quadrature. The results for the systematic errors are summarized for Λ, $\overline{\Lambda}$, and K^0 in Table 5.11. The largest influences on the polarization result arise from the fit procedure, but are still smaller than the statistical error. Including the systematic error on the longitudinal polarization leads to the following results for Λ, $\overline{\Lambda}$, and K^0 in the years from 2002 to 2004:

$$\begin{aligned} P_x^{\Lambda} &= -0.012 \pm 0.013(\mathrm{stat.}) \pm 0.010(\mathrm{sys.}) \\ P_x^{\overline{\Lambda}} &= -0.100 \pm 0.017(\mathrm{stat.}) \pm 0.014(\mathrm{sys.}) \\ P_x^{K^0} &= -0.002 \pm 0.003(\mathrm{stat.}) \pm 0.002(\mathrm{sys.}) \end{aligned} \tag{5.29}$$

Total Systematic Error for Spin Transfer

The systematic uncertainty on the spin transfer coefficient C_{LL} is determined from the overall systematics of the longitudinal polarization and additionally the error of the beam polarization and depolarization factor. The beam polarization P_B is obtained from a parametrization based on a Monte Carlo simulation and has a relative error of 5%. The error on the depolarization

Table 5.11: Summary of systematic errors on the Λ, $\overline{\Lambda}$, and K^0 polarizations.

	$\sigma_{\rm sys}$		
Category	Λ	$\overline{\Lambda}$	K^0
K^0 polarization	0.002	0.002	–
Fit procedure	0.008	0.010	0.002
Linear fit	0.004	0.007	0.001
Tuning of Monte Carlo	0.004	0.005	0.001
Setup of spectrometer	0.001	0.001	0.000
Parameter α	0.000	0.002	–
Total systematic	0.010	0.014	0.002

factor $D(y)$ is calculated from the kinematic variable y. The relative error on $D(y)$ is taken to be 5%. When these two sources of systematics are combined in quadrature, the errors give a global scale uncertainty of 7.1%. Combining the systematic errors due to the error of the longitudinal polarization and the other sources leads to results of a total systematic error for the spin transfer of

$$\begin{aligned}
\sigma^{\rm tot}_{\rm sys}(C_{LL}) &= \sqrt{(\sigma^{P_x}_{\rm sys})^2+(\sigma^{P_B,D(y)}_{\rm sys})^2} = \sqrt{(\sigma^{P_x}_{\rm sys})^2+\left(|C_{LL}|\times\sqrt{(\frac{\delta P_B}{P_B})^2+(\frac{\delta D(y)}{D(y)})^2}\right)^2} \\
&= \begin{cases} \sqrt{(0.010)^2+(0.030\times0.071)^2} = 0.010 & \Lambda \\ \sqrt{(0.014)^2+(0.232\times0.071)^2} = 0.022 & \overline{\Lambda} \\ \sqrt{(0.002)^2+(0.005\times0.071)^2} = 0.002 & K^0 \end{cases} . \qquad (5.30)
\end{aligned}$$

The results of the spin transfer determined in the present analysis are given with systematic errors in the years from 2002 to 2004:

$$\begin{aligned}
C^{\Lambda}_{LL} &= +0.030\pm0.031({\rm stat.})\pm0.010({\rm sys.}) \\
C^{\overline{\Lambda}}_{LL} &= +0.232\pm0.039({\rm stat.})\pm0.022({\rm sys.}) \qquad (5.31) \\
C^{K^0}_{LL} &= +0.005\pm0.007({\rm stat.})\pm0.002({\rm sys.})
\end{aligned}$$

Based on these results, the overall systematic error of the measured spin transfer is estimated to be below 60% of the statistical error. The systematic uncertainty on the final results is obviously small.

5.6.7 Further Study

The angular distribution of decay proton is expressed in terms of the quantized axis. In the present analysis, θ_x is defined as the angle between the proton momentum and the virtual photon γ^* momentum in the Λ rest frame. Another choice of the spin quantization axis $L^{'}$ for the final state Λ is considered to test the influence of the reference system. Instead of the γ^* momentum, one can take the quantization axis along the direction of the Λ momentum as an axis of the longitudinal direction for the determination of the spin transfer. Both possibilities of $C_{LL'}$ determination are directly compared using the two quantization vectors in Fig. 5.43. It can be seen that the spin transfers from the axis of $\vec{P}_{\gamma^*}$ and $\vec{P}_\Lambda$ give consistent results within two standard deviations in the kinematic variable z. The trends of the spin transfer with two different quantization axes are very similar. The small discrepancies can be caused by the incompleteness of the fit procedure for the $\vec{P}_\Lambda$ direction. In the measurement of polarization with the $\vec{P}_\Lambda$ direction, the induced background of invariant mass distributions for each $\cos\theta$ has a nontrivial shape with a different ratio of signal over background. This means that the selection criteria are not properly optimized for the description of the background, which leads to difficulties in the fit procedure. The correct comparison can only be performed after finding a flat backgrounds. Therefore these results are only used to estimate an approximation for the influence of the choice of the reference system. This can be considered as another independent check of the final results. Based on this result, it can be assumed that the choice of the quantization axis of the hyperon in the measurement of spin transfer should be consistent.

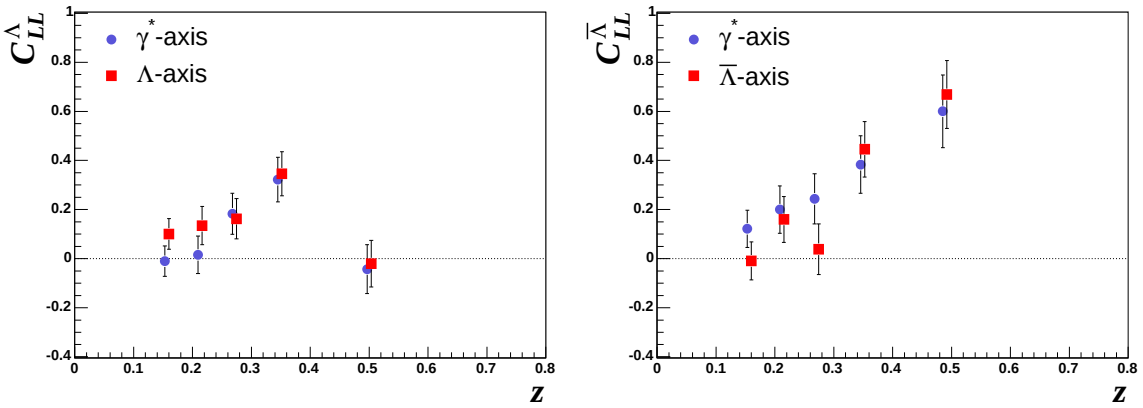

Figure 5.43: Dependence of the spin transfer Λ (left) and $\overline{\Lambda}$ (right) on the choice of the quantization axis in the reference frame. The data samples are compared in the kinematic variable z. In both plots the square points are shifted horizontally with respect to the measured value.

5.7 Kinematic Dependences

The statistics of the experimental data set allows to study the dependence of the spin transfer on several kinematic variables. The spin transfer was therefore extracted for five different bins for each kinematic variable, without an additional constraint on the other variables. The bin positions and widths were optimized for each V^0 sample to have approximately the same number of events per bin. The extraction of the polarization for these subsamples was performed in analogy to the extraction for the full samples described in the previous section. To determine the overall results for each kinematic variable, the results of the spin transfer for each year have been weighted by their statistical errors. The respective numerical values of the spin transfer and mean values of the kinematic variables with the corresponding bins are listed in Appendix C.

5.7.1 Dependence of C_{LL} on Inclusive Variables

The theoretical expectation of the spin transfer in DIS indicates a dependence on the inclusive kinematic variables, and one may naïvely expect that Q^2 and x_{Bj} have some influence on the spin transfer. The resulting spin transfers for the 2002-2004 data sample are plotted versus Q^2 and x_{Bj} in Fig. 5.44. The upper two plots show the Q^2 and x_{Bj} dependencies of the spin transfer for Λ and $\overline{\Lambda}$. In the lower two plots, the dependencies of the spin transfer for the K^0 are shown, which again is taken as an estimate for the systematic uncertainty in the same kinematic region.

A significant positive spin transfer for $\overline{\Lambda}$ is observed in the overall region of Q^2 and x_{Bj}, whereas the Λ has zero value of spin transfer in both variables. The spin transfer of Λ and $\overline{\Lambda}$ are independent on Q^2 and x_{Bj}. Moreover, the spin transfer values do not show any tendency to increase with higher Q^2 and x_{Bj}, where the flavor distribution is expected to be different than in lower x_{Bj} regions. The difference between spin transfer for Λ and $\overline{\Lambda}$ is about 25%, which is compatible with the result of the overall data. The negligible spin transfer values of K^0 extracted in the same kinematic bins indicate that the analysis method used in this analysis is valid in all kinematic regions.

In addition to the kinematic variables Q^2 and x_{Bj}, the spin transfer may also depend on the properties of the virtual photon, in particular on the relative energy transfer y and invariant mass of the final state hadrons W^2. The dependences of spin transfer on y and W^2 are illustrated together in Fig. 5.45. Since $D(y)$ is correlated with y, the low depolarization factor $D(y)$ leads to an increase in the statistical error of the spin transfer with decreasing y. Due to the large errors in the low and intermediate y and W^2 regions, the dependencies of the spin transfer of Λ and $\overline{\Lambda}$ on y and W^2 are less clear than those of Q^2 and x_{Bj}. The spin transfer of Λ are found to be compatible with zero and independent on y and W^2. For the case of the $\overline{\Lambda}$,

the averaged spin transfer is about 30%. Again, the spin transfer does not show a significant dependence on y and W^2.

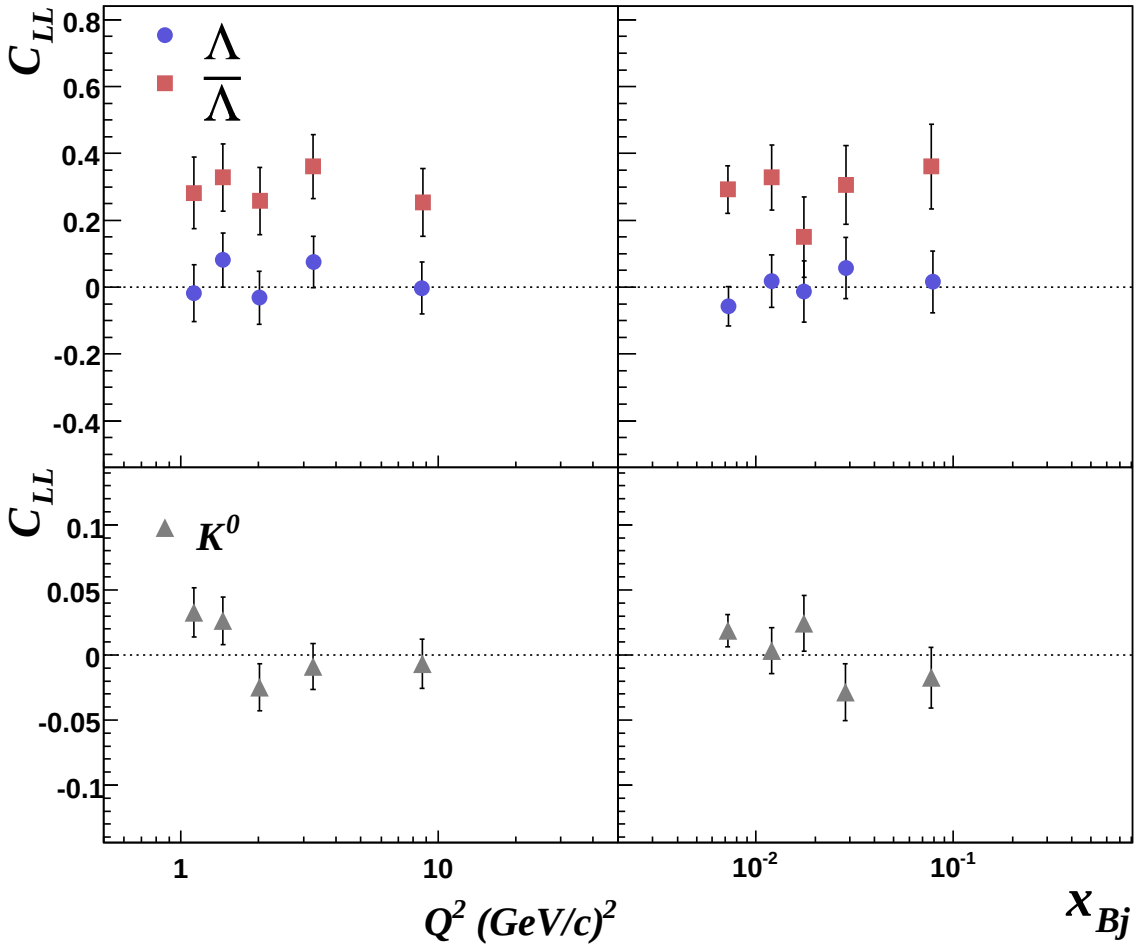

Figure 5.44: Dependence of the spin transfer on the inclusive kinematic variables Q^2 and x_{Bj} The blue circles denote the Λ spin transfers and the red squares represent the one for $\overline{\Lambda}$. In the lower plot the K^0 spin transfers are plotted with grey triangles. The errors shown in this figure are statistical only.

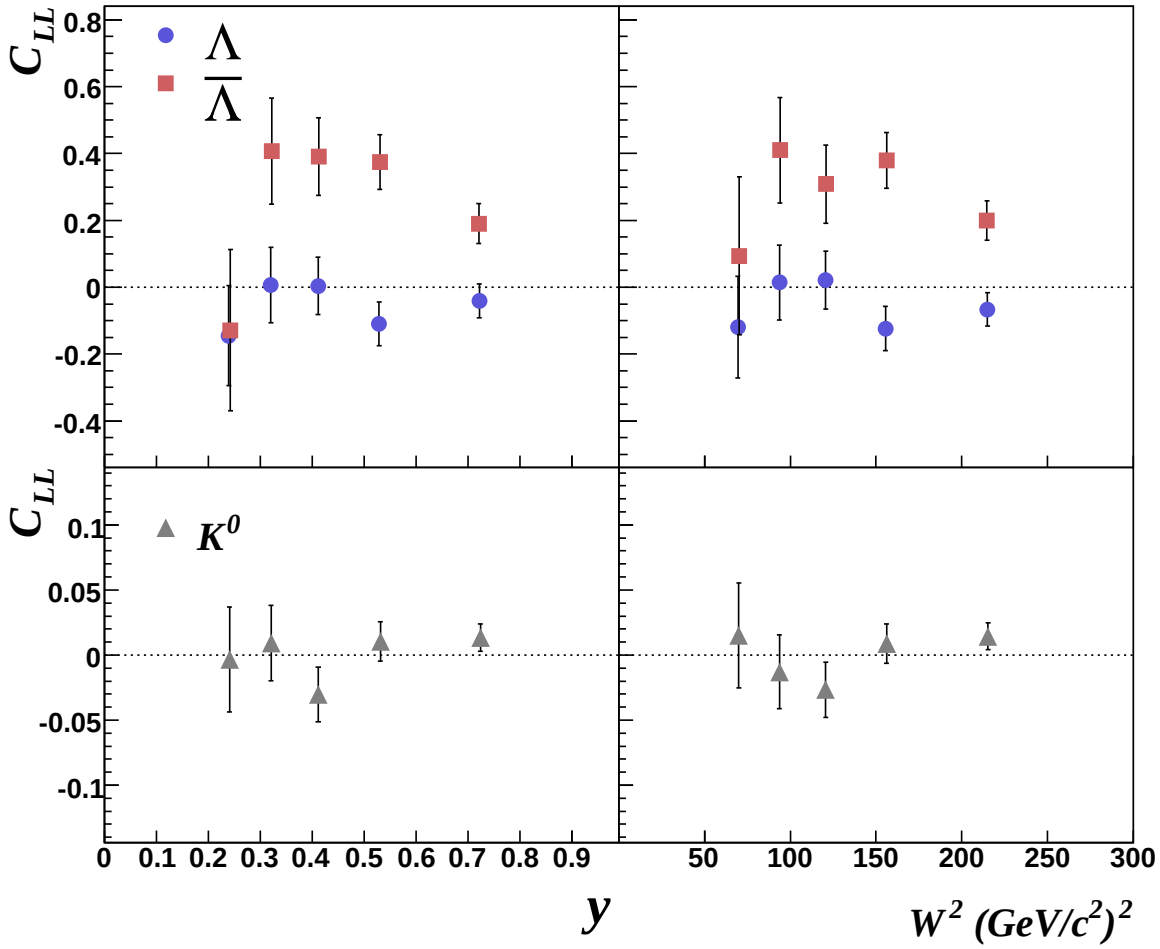

Figure 5.45: Dependence of the spin transfer on the inclusive kinematic variables *y* and W^2. The errors shown in this figures are statistical only.

5.7.2 Dependence of C_{LL} on Semi-Inclusive Variables

The results for the semi-inclusive variables p_T, x_F and z are shown together in Fig. 5.46. The spin transfer of Λ and $\overline{\Lambda}$ are found to be independent of p_T, and a larger positive spin transfer is found for $\overline{\Lambda}$ as compared to the one of Λ. In contrast to the inclusive variables, the spin transfer of Λ and $\overline{\Lambda}$ show a clear dependence on x_F and z. The spin transfer of $\overline{\Lambda}$ rises strongly with increasing x_F and z. The magnitude of the spin transfer seems to be lowest near $x_F \approx 0$, where the influence of the target fragmentation is strongest. The spin transfer of $\overline{\Lambda}$ reaches values of around +60% in the highest x_F and z bin. The x_F and z dependence of Λ is less dominant. There seems to be only a slight trend in the intermediate x_F region between 0.05 and 0.35, and it seems to vanish in the largest x_F and z bin. This is rather unexpected from a theoretical point of view since most models predict roughly the same magnitude and trend of spin transfer for Λ and $\overline{\Lambda}$ at high x_F and z. The maximum difference in spin transfer between Λ and $\overline{\Lambda}$ is about 60% in the last bin. The spin transfer of K^0 does not show any dependence on x_F and z, which is of cause expected. Since the present data cover a x_F range from 0.05 to 0.5, the target fragmentation region is not accessible. Since x_F is strongly correlated with z, it is not surprising that the results are more or less identical.

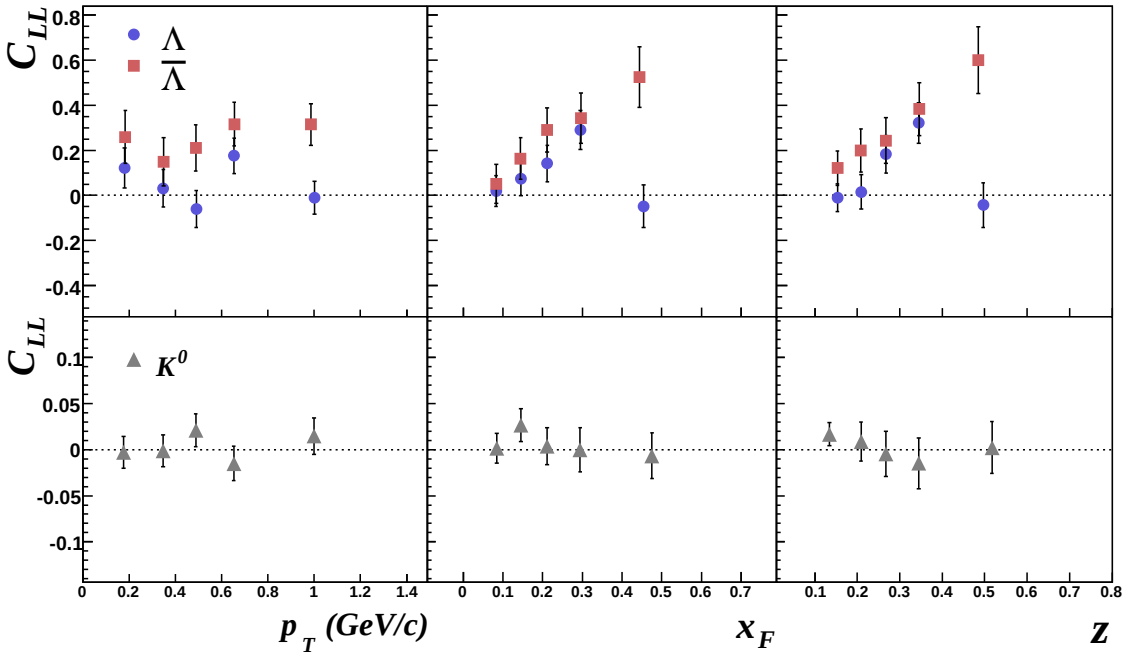

Figure 5.46: Dependence of the spin transfer on the semi-inclusive variable p_T, x_F, and z. The errors shown here are statistical only.

Chapter 6

Interpretation and Discussion

The longitudinal spin transfer of Λ hyperons has previously been measured by various experiments. In order to illustrate the level of agreement on dependences of kinematic variables, a comparison is provided with other DIS experiments. However, the measurements of spin transfer cannot be directly compared with each other due to the different reaction. Hence, only the results in the current fragmentation region can be compared with the results of this analysis. Some theoretical predictions for the spin transfer and the polarization of Λ and $\overline{\Lambda}$ will also be addressed in this Section. Additional information about the quark flavors and contributions of heavier hyperons are provided to interpret the results for spin transfers from the Monte Carlo.

6.1 Comparison with other Experiments and Theory

6.1.1 x and y Dependence of Spin Transfer

In Fig. 6.1 and 6.2 the spin transfer of Λ and $\overline{\Lambda}$ are shown with theoretical predictions of Quark-Diquark models by J. Ellis et al. [134] (see Section 3.3.1) as functions of x and y. These predictions have been calculated with the GRV98LO parton distribution function in the QPM approach. The results for Λ could be used to distinguish between Model A and B for the Quark-Diquark model, because the shape of the two models are significantly different in the different x and y regions. The more realistic Model B compared to the Model A describes the measured data on the spin transfer for Λ, adequately. On the other hand, the predictions of the spin transfer for $\overline{\Lambda}$ are almost constant in x as well as y, but neither Model A nor Model B describe the data. The prediction of the Quark-Diquark model seems to be incorrected for $\overline{\Lambda}$, since the measured spin transfer are larger than the predicted value by a factor of about three. In Fig. 6.2 the dependence of the spin transfer on y is shown together with the result obtained by the NOMAD experiment. If a negligible contribution from antiquarks is assumed, the quantity $-P_x^{\Lambda}$ of NOMAD experiment can be compared to C_{LL}^{Λ} of this analysis (see Section 3.4). The spin transfer has been found to be independent on y, which agrees

with the smallness of the antiquark contributions with respect to the quark contributions. The result from the NOMAD experiment is also in good agreement with this analysis.

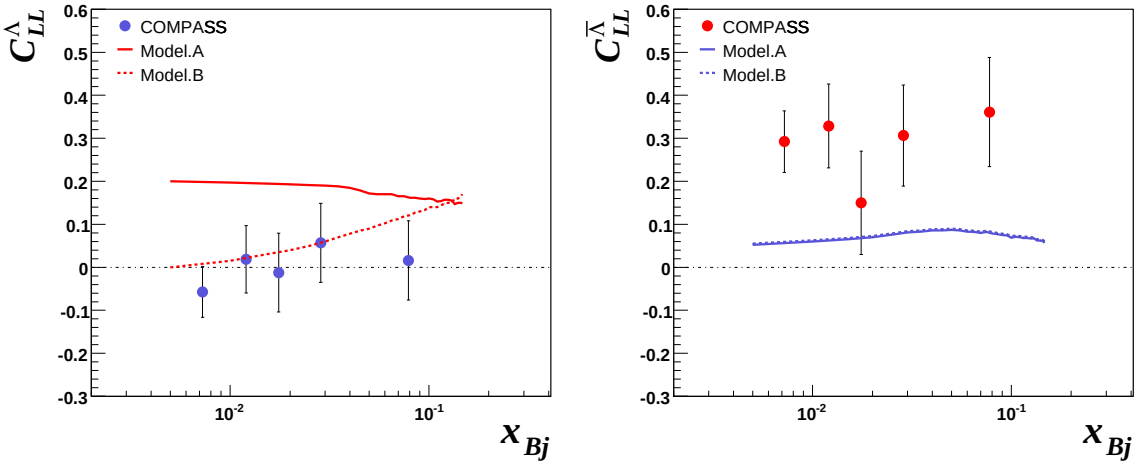

Figure 6.1: Dependence of the spin transfer C_{LL}^{Λ} (left) and $C_{LL}^{\overline{\Lambda}}$ (right) on x: The Quark-Diquark model prediction by J. Ellis et al. [134] are shown together with the COMPASS results in the Model A (solid curve) and Model B (dotted curve) using QPM and GRV98LO. The errors are statistical only.

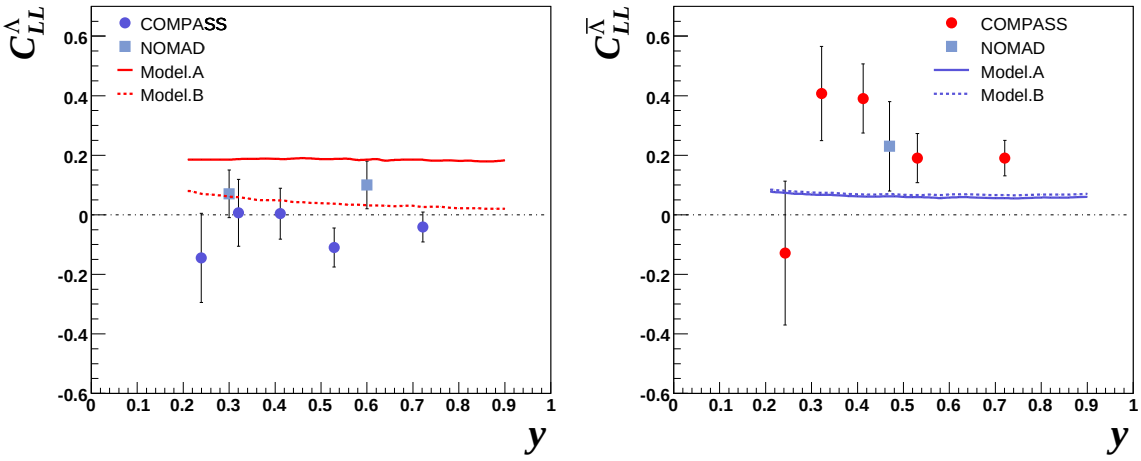

Figure 6.2: Dependence of the spin transfer C_{LL}^{Λ} (left) and $C_{LL}^{\overline{\Lambda}}$ (right) on y: The NOMAD results are represented by light blue squares. The predictions are the Quark-Diquark Model A and B. The errors are statistical only.

6.1.2 z Dependence of Spin Transfer

Most models predict a strong z and x_F dependence of the spin transfer, therefore the dependence on z and x_F for the spin transfer is a crucial test of these models. The z dependence of the spin transfer for Λ obtained by COMPASS and HERMES is shown in Fig.6.3. Taking into account the slightly different kinematics, the results of both experiments are comparable within the statistical error for the full region of z. Not only the magnitude of the spin transfer are the same, but also the behavior is similar. The spin transfer of Λ decreases with increasing z. Although the spin transfer measured by HERMES are extended to higher values of z up to 0.65, which could not measured at COMPASS, the results display no evidence of a strong dependence on z.

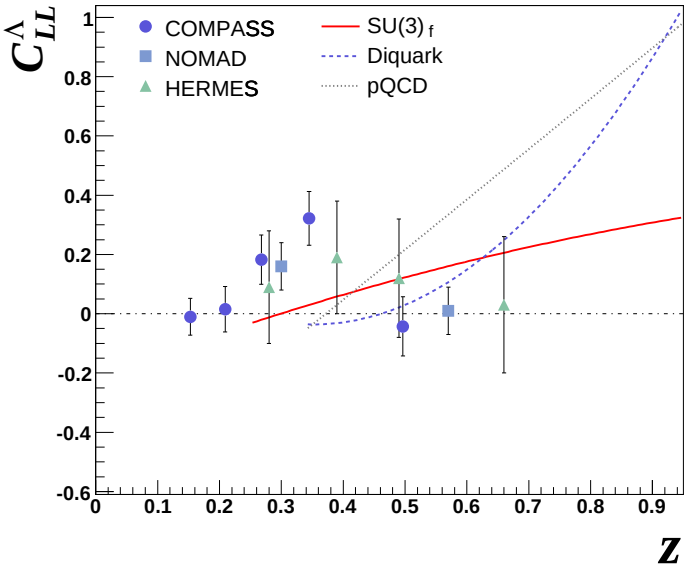

Figure 6.3: Dependence of the spin transfer C_{LL}^{Λ} on z in the current fragmentation region: COMPASS data are represented by blue circles. The NOMAD and HERMES measurements are represented by lightblue squares and lightgreen triangles, respectively. The predictions of the spin transfer come from pQCD (dotted curve) [144], Quark-Diquark (dashed curve) [144] and SU(3) [146] (solid curve) based model. The plotted uncertainties are statistical only.

The model prediction given in Fig.6.3 show the dependence of the spin transfer on z by B. Ma et al., which is introduced in Section 3.3.1. It has been suggested that the spin transfer of Λ are sensitive to the polarized quark and their flavor in the nucleon. In contrast, the fragmentation functions are taken as an input factor. Due to the absence of data, the authors calculated the ratio u_Λ / s_Λ and $\Delta q_\Lambda / q_\Lambda$ for Λ with a parametrization of polarized quark distributions at large x, where the Gribov-Lipatov relation is applicable (see Section 3.2.3).

A perfectly positive polarized s quark is assumed and u and d quarks are expected to have a weakly positive polarization inside the Λ. Using the three different approaches, it was found that u_Λ / s_Λ is 0 in the Quark-Diquark model, 0.5 in the pQCD model and 0.25 in the SU(3) approach [146]. The available data from HERMES and COMPASS are inconsistent with the predictions from Quark-Diquark and pQCD based model within the presented errors. Concerning SU(3) approach a conclusion cannot be made. However, Λ was assumed to be produced directly from the polarized struck quark, i.e., the contribution from heavier hyperon decays was not included in these model.

6.1.3 x_F Dependence of Spin Transfer

In the top of Fig. 6.4 the results of the spin transfer are plotted with data obtained by the E665 experiment and the HERMES experiment as well as the NOMAD experiment as a function of x_F. There is a reasonable agreement between the COMPASS and other experiments excepts for the E665 experiment. The statistical accuracy of the E665 experiment is strongly limited, so that this trend can neither be excluded nor verified in the comparison with another experiments. The spin transfer of Λ measured by the HERMES experiment seems to be consistent with zero, and the results show no clear dependence of the spin transfer on x_F within the statistical error. HERMES pointed out that the Λ production is dominated by scattering off u quarks in their Monte Carlo study. The observation of a small value of C_{LL}^{Λ} seems to indicate the dominance of u quarks in the Λ production since the polarization of u quark in the Λ hyperon is expected to be small.

In the bottom of Fig. 6.4, the grey curves are the predictions of the spin transfer with the QPM and SU(3) symmetry based model by D. Ashery and H. Lipkin, which show a pronounced increase of the spin transfer at high x_F. In addition, the predictions of the Quark-Diquark models by J. Ellis et al. are shown as red curves. The Quark-Diquark model B predicts the x_F dependence of the spin transfer by three different approaches; the first approach use the QPM for the baryon spin structure with GRV98LO parton distribution functions, the second one use the QPM with the CETQ parametrization, and the last approach was made in the BJ based model with GRV98LO. The predictions of the Ashery-Lipkin models show a gradual increase than the Quark-Diquark models in the intermediate region of x_F. Unfortunately experimental accuracy is still not enough to distinguish which model is more adequate for describing all results. Furthermore, the covered range of x_F of the present data does not allow to confirm the behavior in the higher x_F region, where the models predict different tendencies.

Fig. 6.5 shows the dependence of the spin transfer of $\overline{\Lambda}$ on x_F with the NOMAD and the E665 measurements as well as the theoretical predictions. The result of spin transfer measured by the NOMAD experiment and the E665 measurement seem to be positive in the current fragmentation. Even though the statistical accuracy of all measurements for the $\overline{\Lambda}$ are more limited than for the Λ, a weak trend is showing toward positive values of the spin transfer with

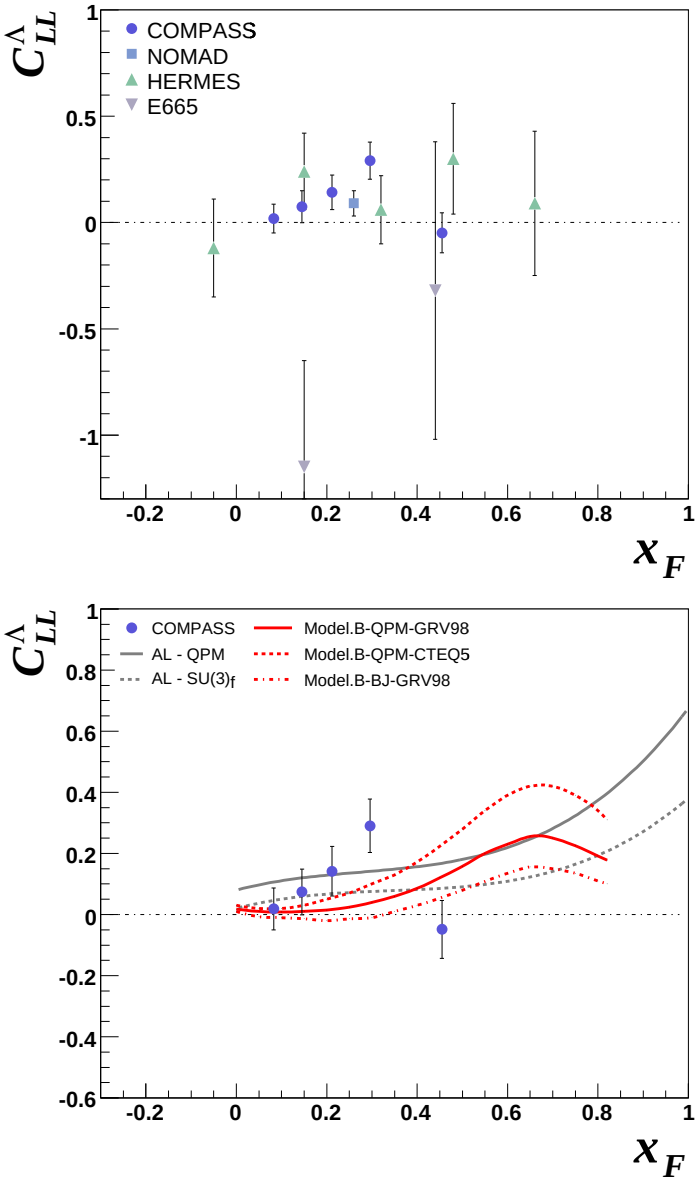

Figure 6.4: Top : Dependence of the spin transfer C_{LL}^{Λ} on x_F. The COMPASS measurements are represented by blue circles. The HERMES and E665 measurements are represented by lightgreen triangles and hellgrey squares, respectively. Errors of all measurements are statistical only. Bottom : The theoretical predictions of C_{LL}^{Λ} are shown with the COMPASS results. The grey curves are the predictions of QPM and SU(3) based model by D. Ashrey and H. Lipkin [123], and three different approaches of Quark-Diquark models by J. Ellis et al. [134] are shown as the red curves.

increasing x_F. The statistics and thus the precision of the results is significantly improved by the COMPASS measurement.

The two grey curves correspond to the Ashery-Lipkin models as already shown in Fig. 6.4. It was assumed that the prediction of the spin transfer of $\overline{\Lambda}$ is exactly the same as the one of Λ. The three different predictions of the Quark-Diquark models by J. Ellis et al. are shown with blue curves. The experimental results are in good agreement with the Quark-Diquark model by using the CTEQ parametrization and the QPM approach. The model prediction for $\overline{\Lambda}$ are consistent with the data predicting essentially an increase of the spin transfer up to $x_F = 0.7$. However, the experimental data increase more rapidly than the model predictions in the intermediate region of x_F.

The different trend of spin transfer between Λ and $\overline{\Lambda}$ might be interpreted as a change in the dominant reaction mechanism for the hadron production between target and current fragmentation regions. It was suggested that the spin transfer has a significant contribution from target fragmentation effects near $x_F \approx 0$. Fig. 6.6 shows the ratio of Λ over $\overline{\Lambda}$ in the kinematic variable x_F. It can be seen that the ratio increases clearly at high x_F. This indicates the change of production mechanism of Λ and $\overline{\Lambda}$. Based on this result, one can understand why the x_F

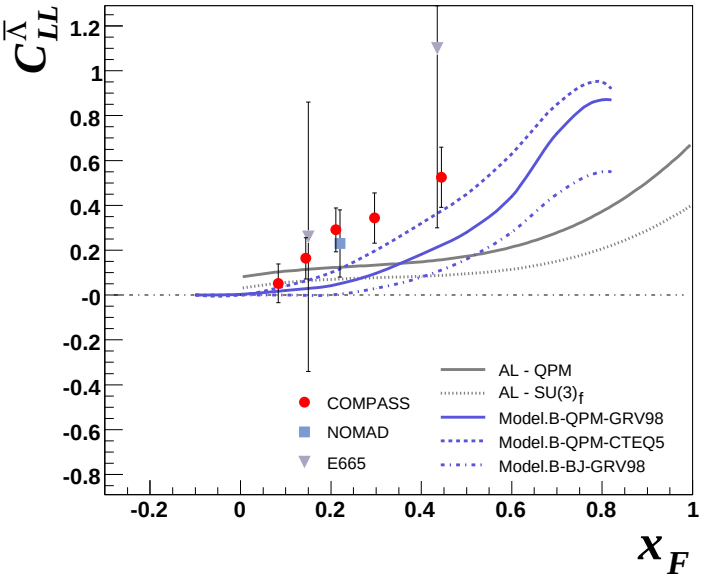

Figure 6.5: Dependence of the spin transfer of $\overline{\Lambda}$ C_{LL} on x_F: The COMPASS, NOMAD and E665 measurements of the spin transfer for $\overline{\Lambda}$ are represented by the circles, square and triangles, respectively. The grey solid and dotted curves are the corresponding predictions of the QPM and SU(3) symmetric based model by D. Ashery and H. Lipkin [123]. The Quark-Diquark model predictions by J. Ellis et al. [134] are shown as blue curves.

dependences of spin transfer for the Λ and $\overline{\Lambda}$ are significantly different at high x_F.

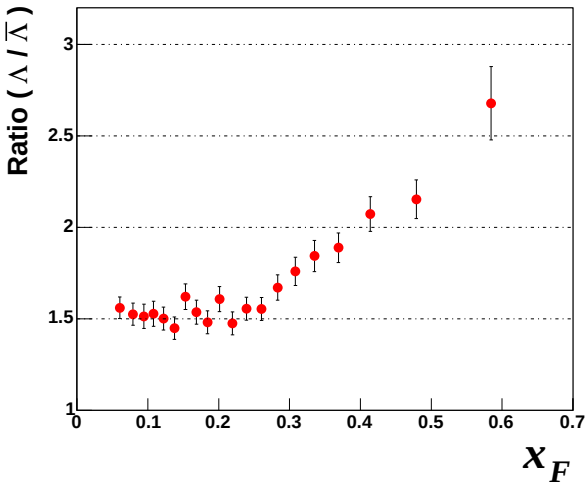

Figure 6.6: Production ratio of Λ over $\overline{\Lambda}$ as function of x_F in the 2004 data.

6.2 Information from the Monte Carlo

The Monte Carlo simulation with the LUND fragmentation model not only provides an acceptance correction of the spectrometer, but also allows to get an information about the hadron production processes. Most of the models assume that the produced Λ contains the struck quark and that the spin transfer of Λ hyperons depends on the flavor of the struck quark. The observed small spin transfer of Λ points to the dominance of scattering from u or d quark in the COMPASS kinematics since the u and d quarks are polarized very weakly in the SU(3) and QPM models. Information about quark flavor can be estimated using Monte Carlo. Fig. 6.7 shows contributions of different quark flavors to the Λ production. One can see clearly that the Λ production dominates by scattering off u quark in the DIS reaction.

Interesting information is also available due to the different production channels of the heavier hyperon. The Λ produced via Σ and Ξ decay may be polarized if their hyperon parents were produced with a polarization. Therefore to predict a spin transfer for Λ hyperons in a given kinematic domain one needs to know the relative yields of produced Λ in different channels and their polarization. Fig 6.7 shows the ratio of possible heavier hyperon sources in the Λ production, which is determined after final cuts applied in the Λ Monte Carlo sample. According to the estimate from the Monte Carlo with the LUND string model, the fraction of Λ produced directly via the string fragmentation is found to be only about 40%. A substantial part of Λs are produced from the heavier hyperon decays, most prominently from the decay of the Σ^0. It is about 20%. The result is consistent with the estimation of the HERMES

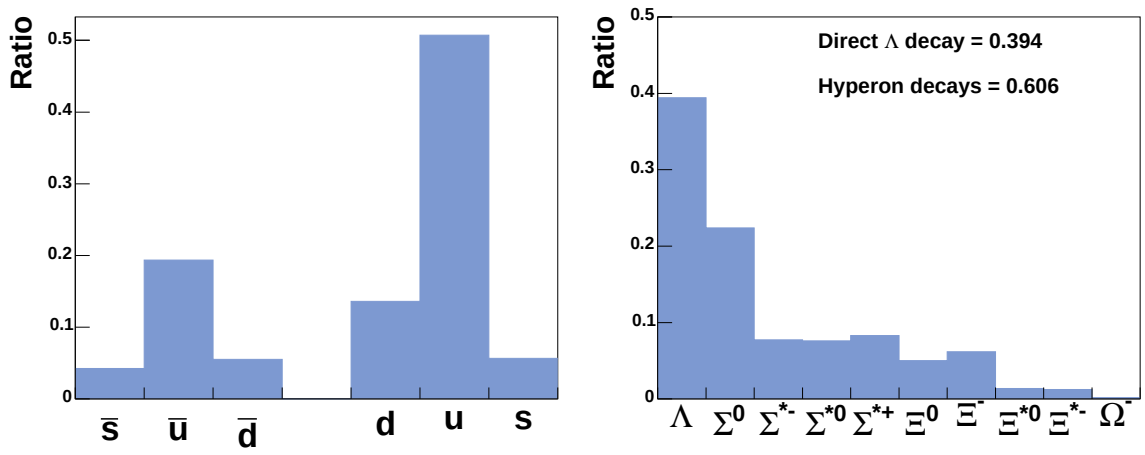

Figure 6.7: Left: Relative contributions of different quark flavors to the Λ production. Right: Relative contributions of different heavier hyperons to the Λ production.

experiment. Since the Σ^0 events was not distinguished in the Λ selection, they must be taken into account in the final results. The average polarization of the Λ produced in the $\Sigma^0 \to \Lambda\gamma$ decay is $P^\Lambda = -\frac{1}{3}P^{\Sigma^0}$ [237] resulting in Λ polarization (see Table 3.2). The polarizations of Σ^*, $\Xi^{0,-}$ and Ξ^* are estimated to be of the same size of the Λ polarization. Hence, the Λ polarization should be changed due to Σ^0 decay.

If one assumes that only the *u* quark is involved in Σ^0 decay process, a non-zero spin transfer is expected for this partial channel [123]. The *u* quark in the Σ^0 hyperon is assumed to be positively polarized (see Table 2.4). The measured Λ spin transfer can thus be corrected by

$$C_{LL}^{\Lambda}(\text{measured}) = R_\Lambda \cdot C_{LL}^{\Lambda}(\text{direct}\,\Lambda) + R_{\Sigma^0} \cdot C_{LL}^{\Lambda}(\Sigma^0 \to \Lambda) \tag{6.1}$$

$$0.03 = 0.8 \cdot \frac{\Delta D_u^\Lambda}{D_u^\Lambda} - 0.2 \cdot \frac{1}{3}\frac{\Delta D_u^{\Sigma^0}}{D_u^{\Sigma^0}}, \tag{6.2}$$

where R_Λ and R_{Σ^0} are the relative rates of the direct Λ and Σ^0 decay, respectively. The contributions of other heavier hyperons are still contained in the R_Λ, because polarizations of those decays are assumed to be the same. Using the constrain of the $D_u^{\Sigma^0} > |\Delta D_u^{\Sigma^0}|$ one obtains

$$0.038 < \frac{\Delta D_u^\Lambda}{D_u^\Lambda}(\text{direct}) < 0.120. \tag{6.3}$$

The correction for the Σ^0 is positive and the real spin transfer is expected to be higher than the result actually obtained in this analysis.

Chapter 7

Summary and Outlook

This thesis presents a study on the spin transfer of Λ and $\overline{\Lambda}$ via a measurement of the longitudinal Λ and $\overline{\Lambda}$ polarizations in the deep inelastic scattering process. The analysis is based on the data taken by the COMPASS experiment at CERN during the years 2002, 2003 and 2004 using a longitudinally polarized μ^+ beam of 160 GeV scattering off a ^{6}LiD target. The longitudinal Λ and $\overline{\Lambda}$ polarizations were measured in the kinematic region $Q^2 > 1$ (GeV/c)^2. These events contain a fraction of DIS events that directly probe the spin transfer from a polarized quark fragmenting into a Λ hyperon. The selected events are 79,000 Λ and 49,000 $\overline{\Lambda}$.

A Monte Carlo simulation is used to correct the acceptance of the COMPASS spectrometer. To obtain reasonable agreement between data and Monte Carlo several LEPTO parameters have been adjusted. The modified LEPTO provides the acceptance correction needed to extract the spin transfer of Λ and $\overline{\Lambda}$. From the acceptance corrected angular distribution of the decay proton, the spin transfers C_{LL}^{Λ} and $C_{LL}^{\overline{\Lambda}}$ are determined.

The results for the spin transfer of Λ hyperons measured in the current fragmentation region $x_F > 0$ are

$$\begin{aligned} C_{LL}^{\Lambda} &= +0.030 \pm 0.031(\text{stat}) \pm 0.010(\text{sys}) \qquad \text{at} < x_F >= 0.24, \\ C_{LL}^{\overline{\Lambda}} &= +0.232 \pm 0.039(\text{stat}) \pm 0.022(\text{sys}) \qquad \text{at} < x_F >= 0.22. \end{aligned}$$

The data show a significantly positive spin transfer for the $\overline{\Lambda}$ while the spin transfer for the Λ is compatible with zero within the present statistical accuracy. As an estimate of the systematic uncertainties the spin transfer of K^0 was measured. The value was consistent with zero. A value of $C_{LL}^{K^0} = +0.005 \pm 0.007(\text{stat.}) \pm 0.002(\text{sys.})$ was observed at $< x_F >$ = 0.24. C_{LL}^{Λ} and $C_{LL}^{\overline{\Lambda}}$ are similar to previous measurements by the NOMAD, E665 and HERMES collaborations, but of much improved statistics.

A measurement of the dependence on the kinematic variable Q^2, x_{Bj}, y, W^2, p_T, z and x_F of C_{LL}^{Λ} and $C_{LL}^{\overline{\Lambda}}$ in the current fragmentation region are also made. The measured C_{LL}^{Λ} and $C_{LL}^{\overline{\Lambda}}$ are independent on the inclusive kinematic variables Q^2, x_{Bj}, y, and W^2 as well as transverse momentum p_T. For the Λ, no clear dependence of C_{LL}^{Λ} on z and x_F are observed, which is quite astonishing, since so far the spin transfer of Λ hyperons are predicted to increase with increasing z and x_F. In contrast, the spin transfer of $\overline{\Lambda}$ shows a significant dependence on z and x_F, reaching a maximum value of up to 60% at high $< z >$ = 0.44 and vanishing $C_{LL}^{\overline{\Lambda}}$ near the target fragmentation region. At present the COMPASS result constitutes the most precise data on the spin transfer of $\overline{\Lambda}$ in the current fragmentation region. By taking into account the production rates of Λ and $\overline{\Lambda}$ in the kinematic variable z, the observed tendencies can be interpreted in terms of a different contribution of target fragmentation for both Λ and $\overline{\Lambda}$ at high z. There are several model predictions about the spin transfer of Λ hyperons. But any conclusive decision between the models has to wait for improved statistics on both Λ and $\overline{\Lambda}$. The result in the present data agrees with the data from measurements done by the NOMAD and HERMES experiments.

At COMPASS, additional measurement of the sideways (P_z) and transverse (P_y) Λ and $\overline{\Lambda}$ polarization are possible to achieve a more detailed understanding of Λ and $\overline{\Lambda}$ production in the present data. Since the data which has been taken in 2006, increases the statistics by about 50%, a more accurate determination of the spin transfer will be possible. The statistical error of the spin transfer for the Λ will decrease to 0.025 and for the $\overline{\Lambda}$ to 0.030. Furthermore, the kinematic domain of x_F can be extended to the high current fragmentation region as well as to the target fragmentation region. With enhanced statistic, it will become interesting to study the spin correlations for Λ and $\overline{\Lambda}$ in reactions with associated $\overline{s}$ and s quark production like $\mu^+ N \rightarrow \mu^{+'} \Lambda K^+ (\overline{\Lambda} K^-) X$ or $\mu^+ N \rightarrow \mu^{+'} \Lambda \overline{\Lambda} X$. The polarization measurements of coherently produced $\Lambda\overline{\Lambda}$ pairs can provide important information about the state of $s\overline{s}$ pairs in the nucleon. Future results of the spin transfer of Λ and $\overline{\Lambda}$ are also expected to have smaller systematic uncertainties. The main improvement will be achieved by more thorough Monte Carlo studies.

Appendix A

Comparison of Data with Monte Carlo

A.1 Comparison between Data and Monte Carlo in 2002

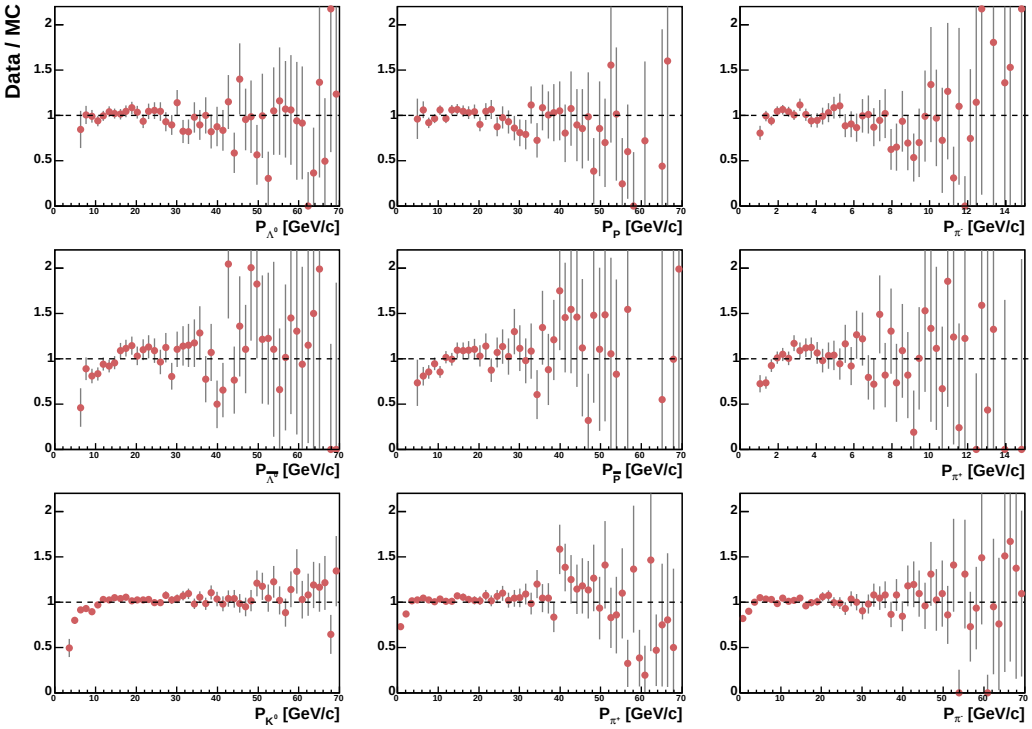

Figure A.1: Comparison of 2002 data with Monte Carlo for the momentum distributions of reconstructed particles in V^0 events. The histograms represent the Monte Carlo samples and the points show the data samples. The distributions are normalized to the total number of entries. The means of distributions are also given.

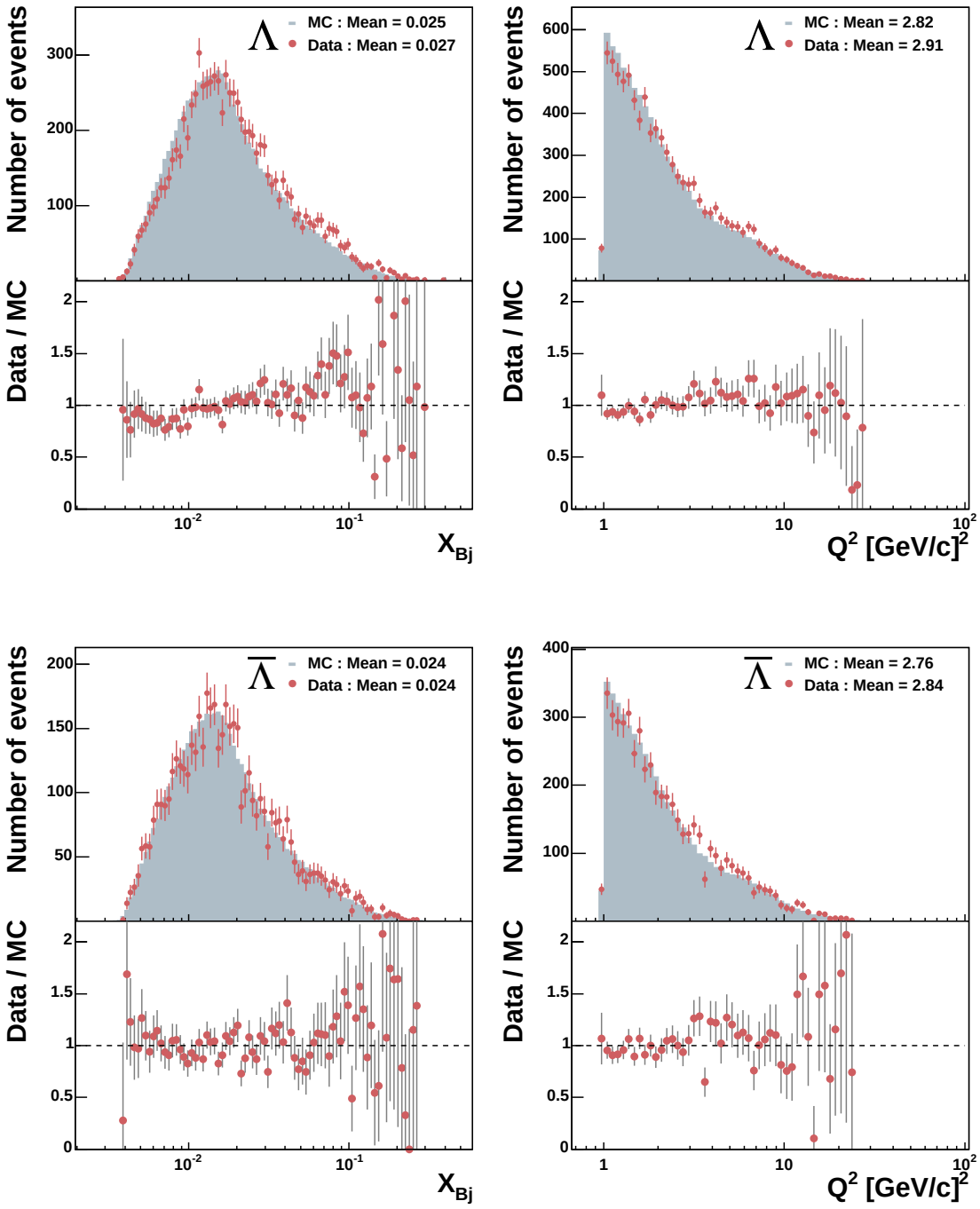

Figure A.2: Comparison of 2002 data with Monte Carlo for the inclusive kinematic variables x_{Bj} and Q^2 for Λ and $\overline{\Lambda}$ event. The histograms represent the Monte Carlo samples and the points show the data samples. The distributions are normalized to the total number of entries. The means of distributions are also given.

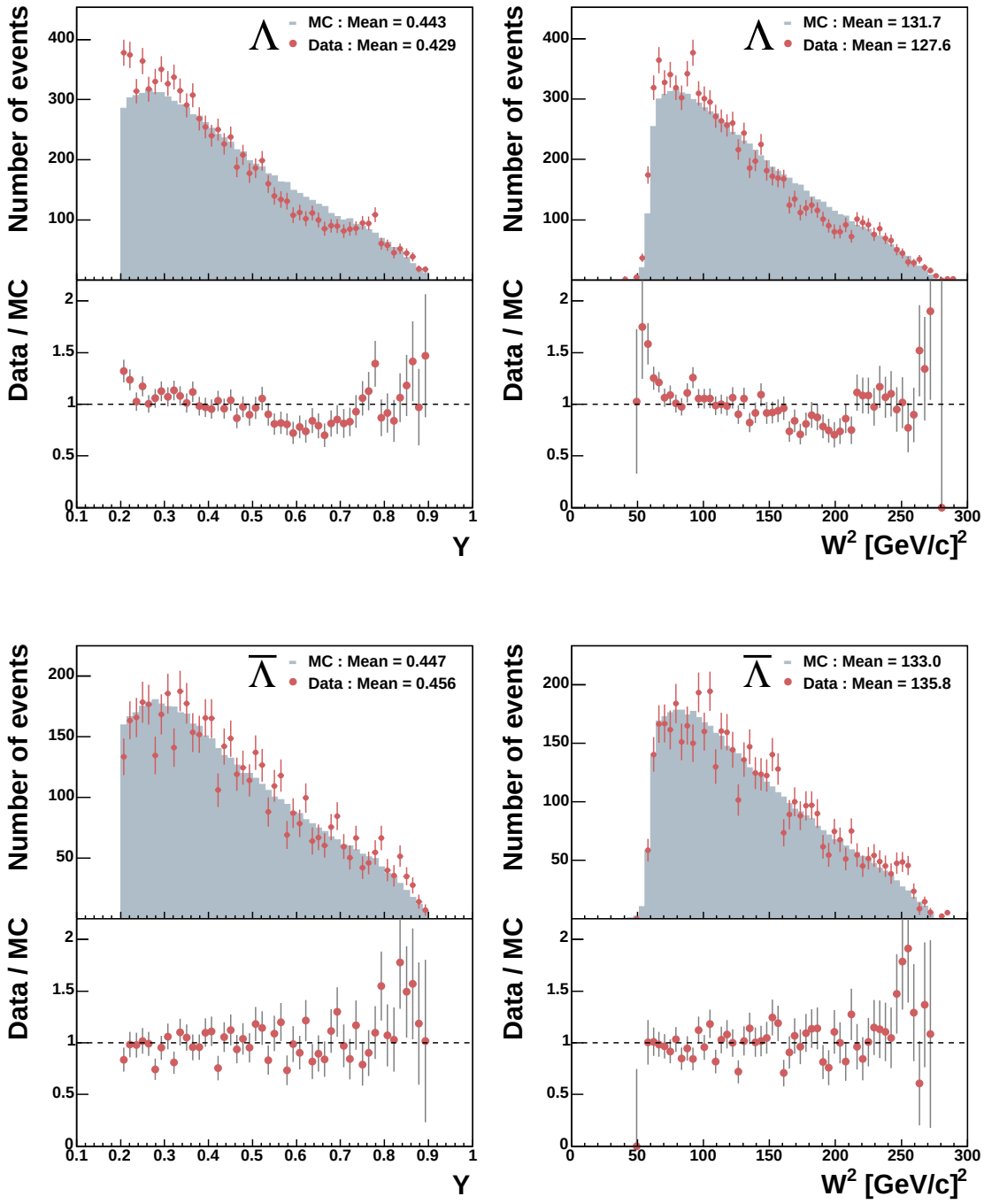

Figure A.3: Comparison of 2002 data with Monte Carlo for the inclusive kinematic variables y and W^2 for Λ and $\overline{\Lambda}$ event. The histograms represent the Monte Carlo samples and the points show the data samples. The distributions are normalized to the total number of entries. The means of distributions are also given.

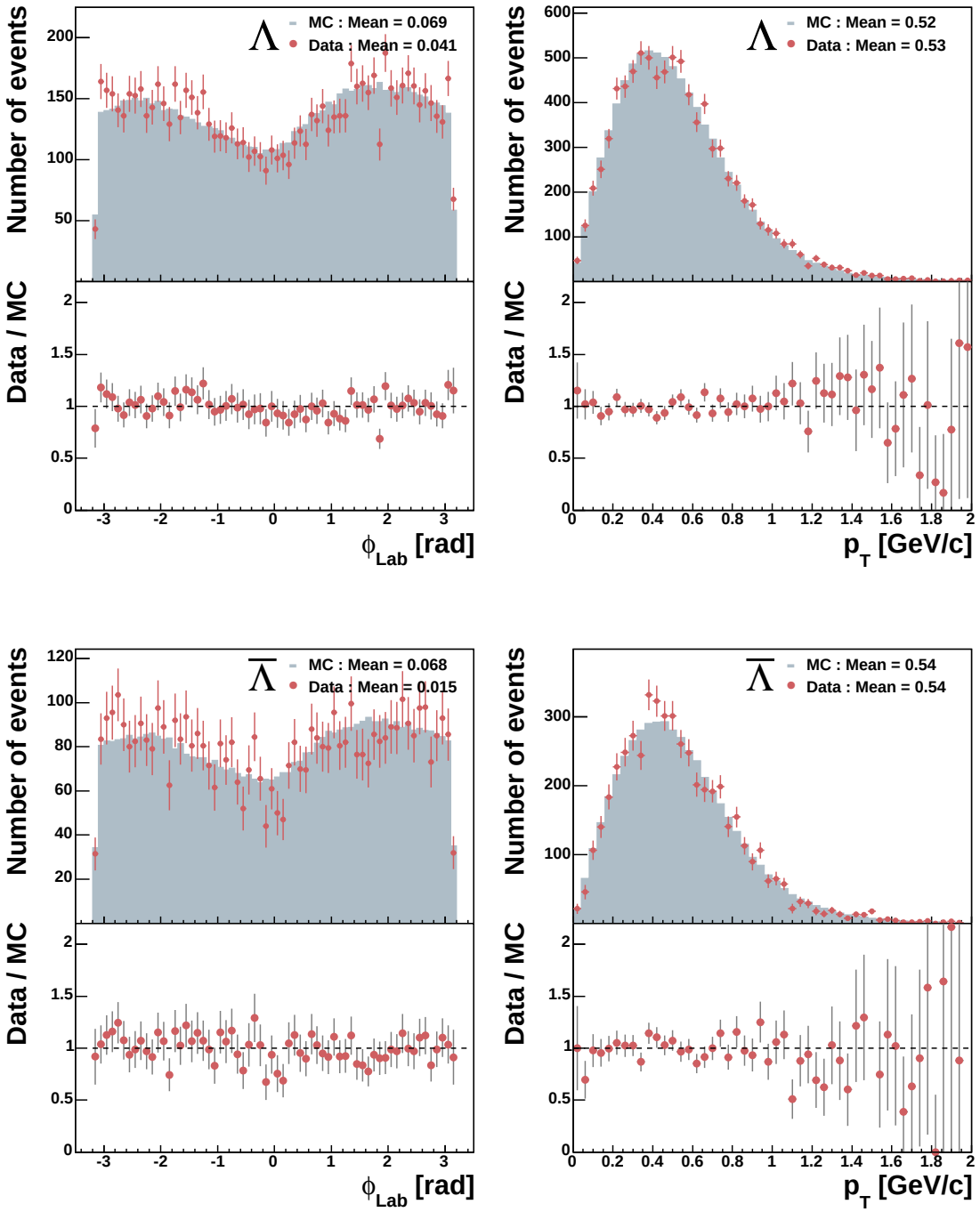

Figure A.4: Comparison of 2002 data with Monte Carlo for the semi-inclusive kinematic variables ϕ and p_T for Λ and $\overline{\Lambda}$ event. The histograms represent the Monte Carlo samples and the points show the data samples. The distributions are normalized to the total number of entries. The means of distributions are also given.

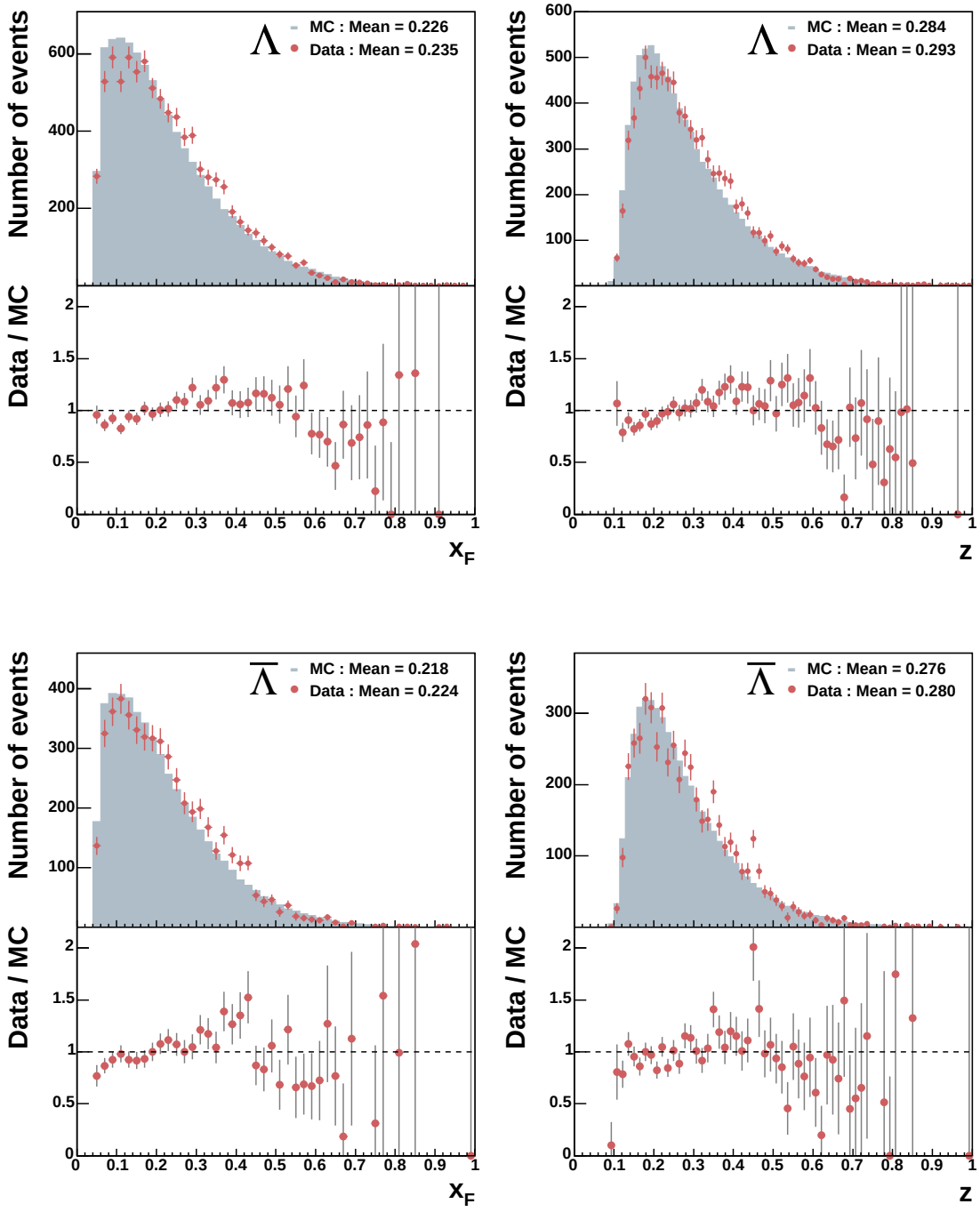

Figure A.5: Comparison of 2002 data with Monte Carlo for the semi-inclusive kinematic variables x_F and z for Λ and $\overline{\Lambda}$ event. The histograms represent the Monte Carlo samples and the points show the data samples. The distributions are normalized to the total number of entries. The means of distributions are also given.

A.2 Comparison between Data and Monte Carlo in 2003

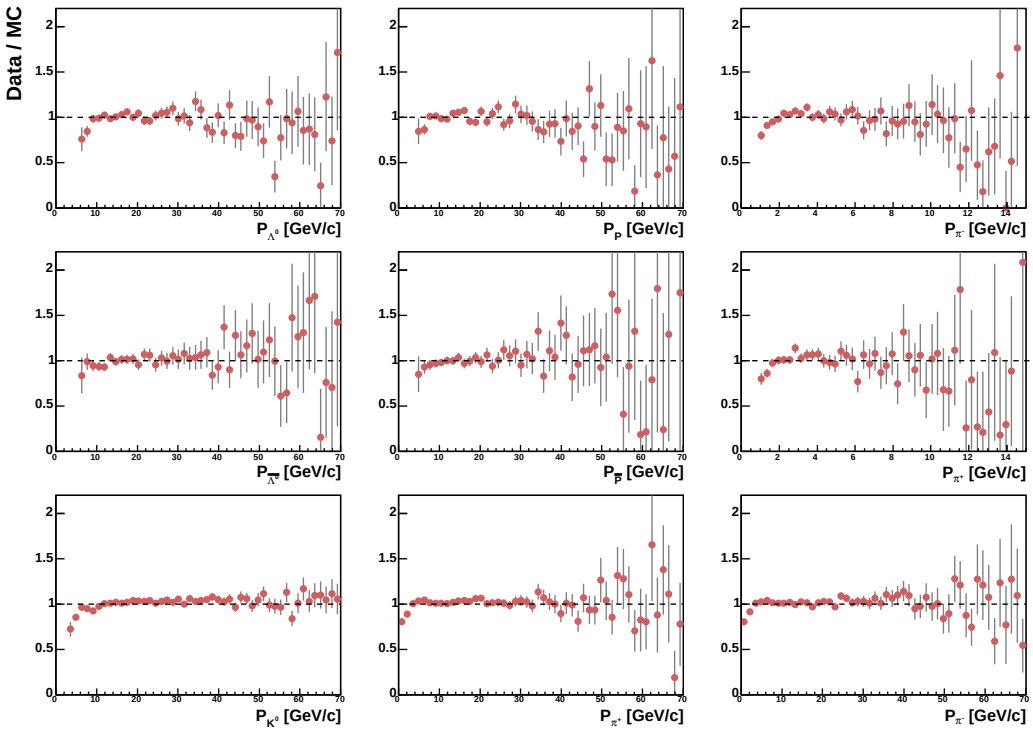

Figure A.6: Comparison of 2003 data with Monte Carlo for the momentum distributions of reconstructed particles in V^0 events. The histograms represent the Monte Carlo samples and the points show the data samples. The distributions are normalized to the total number of entries. The means of distributions are also given.

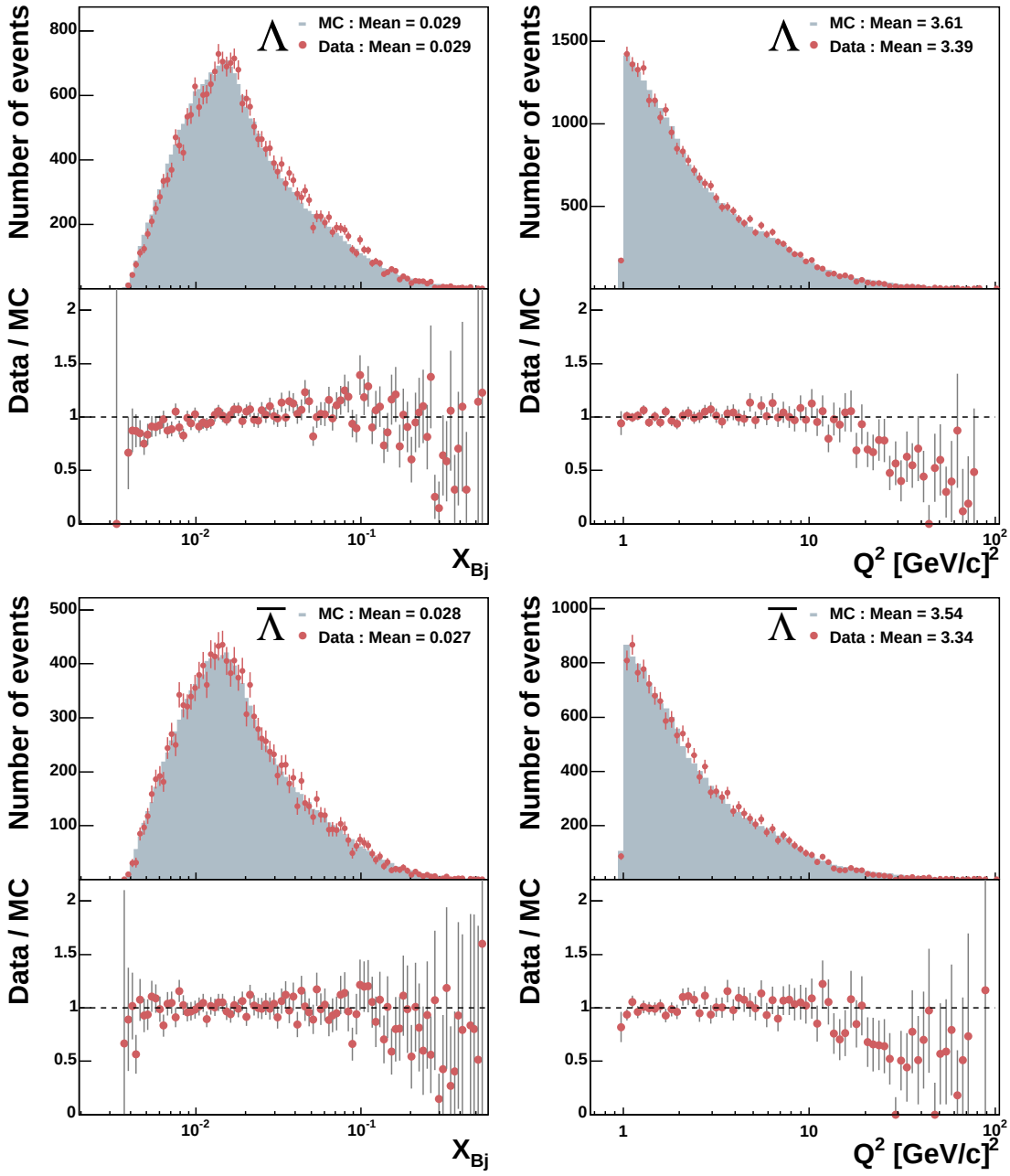

Figure A.7: Comparison of 2003 data with Monte Carlo for the inclusive kinematic variables x_{Bj} and Q^2 for Λ and $\overline{\Lambda}$ event. The histograms represent the Monte Carlo samples and the points show the data samples. The distributions are normalized to the total number of entries. The means of distributions are also given.

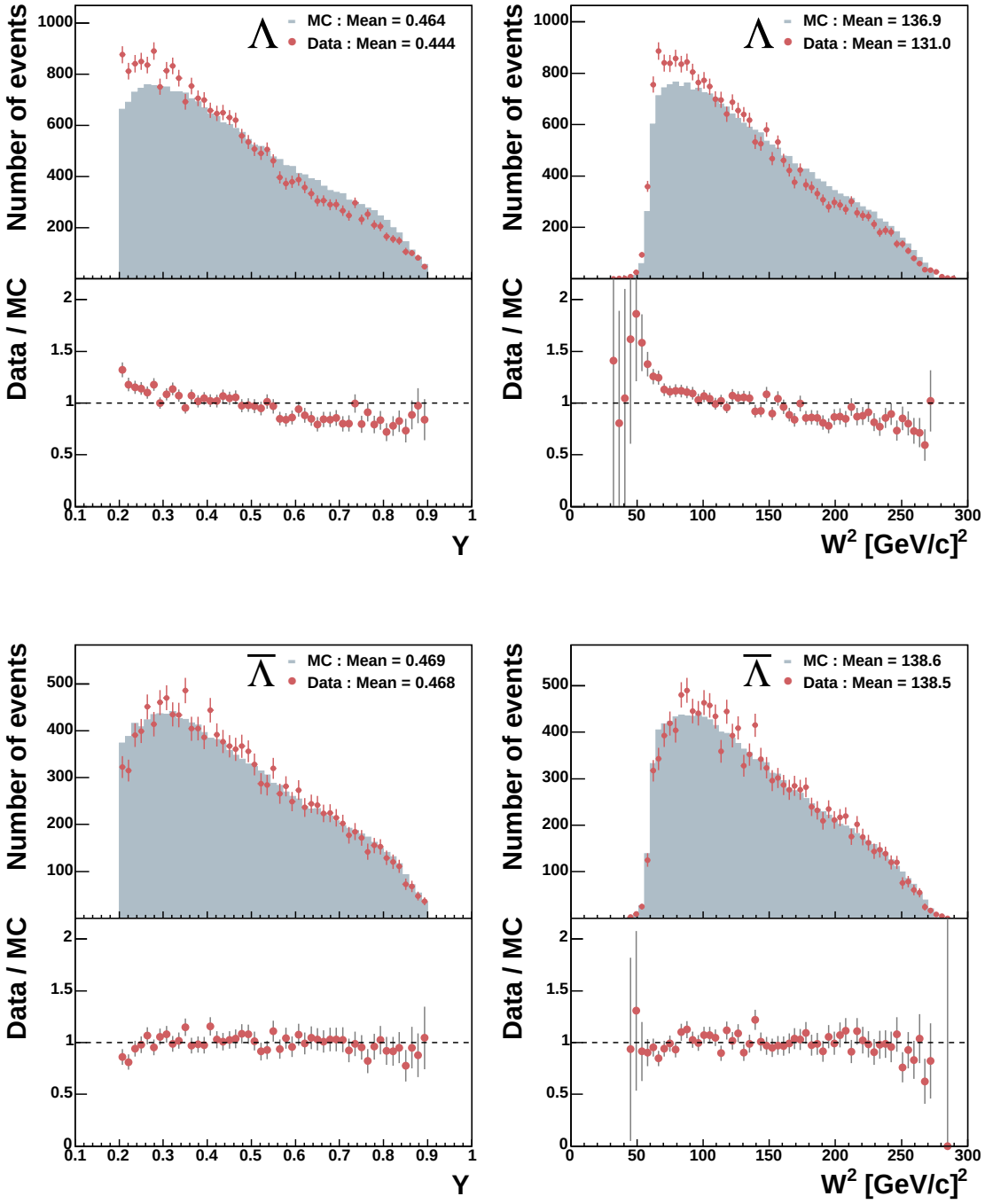

Figure A.8: Comparison of 2003 data with Monte Carlo for the inclusive kinematic variables y and W^2 for Λ and $\overline{\Lambda}$ event. The histograms represent the Monte Carlo samples and the points show the data samples. The distributions are normalized to the total number of entries. The means of distributions are also given.

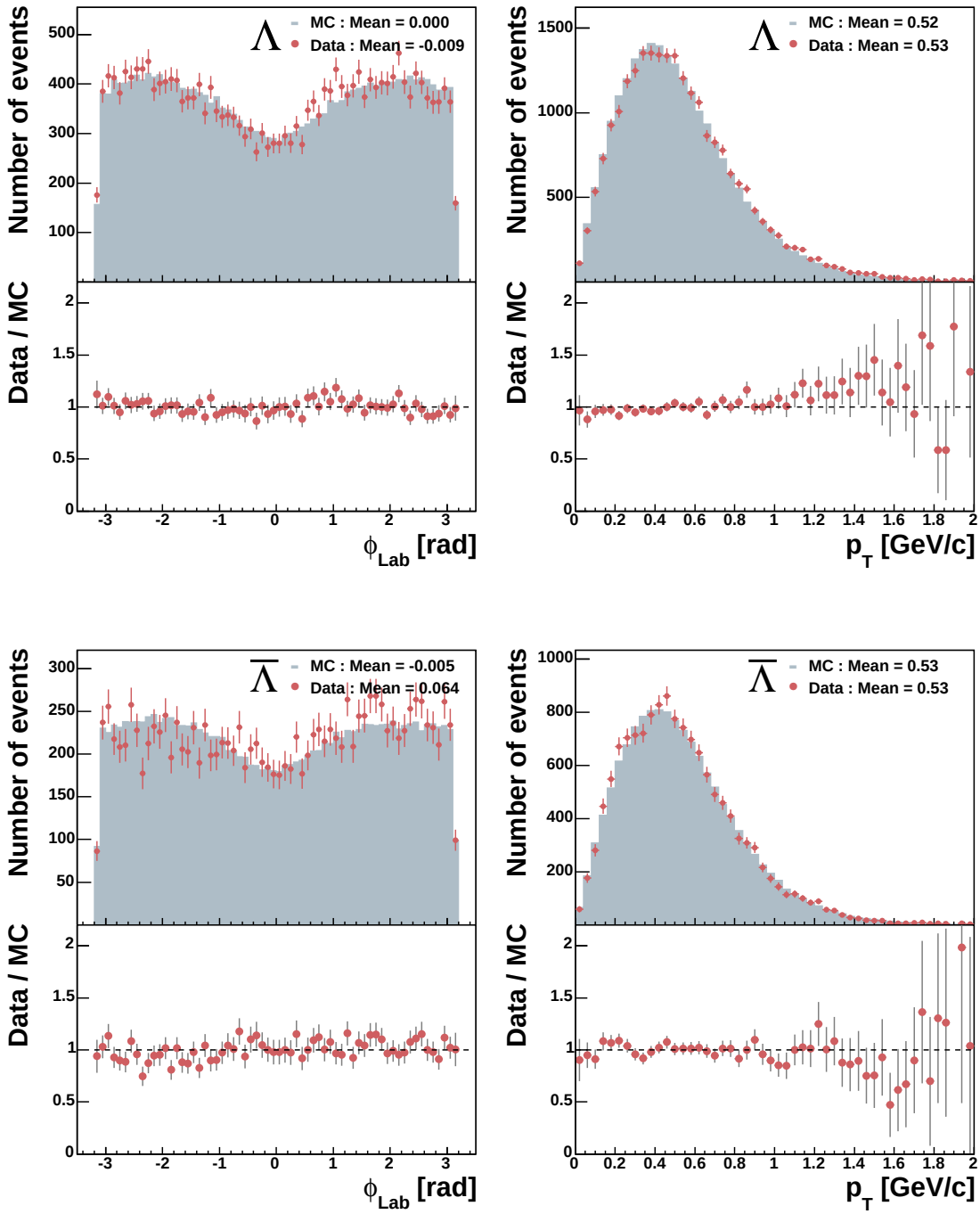

Figure A.9: Comparison of 2003 data with Monte Carlo for the semi-inclusive kinematic variables ϕ and p_T for Λ and $\overline{\Lambda}$ event. The histograms represent the Monte Carlo samples and the points show the data samples. The distributions are normalized to the total number of entries. The means of distributions are also given.

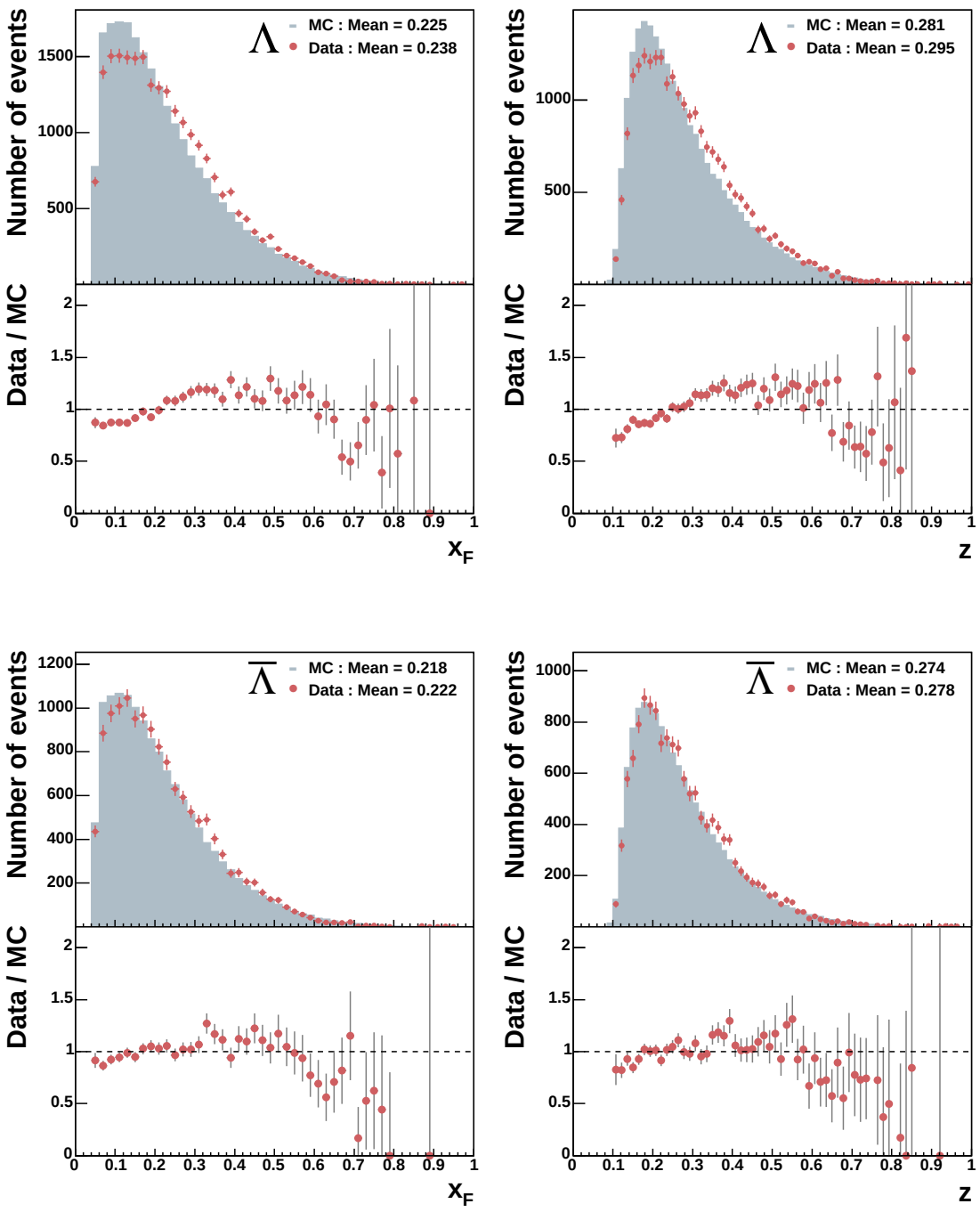

Figure A.10: Comparison of 2003 data with Monte Carlo for the semi-inclusive kinematic variables x_F and z for Λ and $\overline{\Lambda}$ event. The histograms represent the Monte Carlo samples and the points show the data samples. The distributions are normalized to the total number of entries. The means of distributions are also given.

Appendix B

Tables of Systematic Studies

The following tables detail the results of the Λ and $\overline{\Lambda}$ polarizations in the systematic studies, as presented in the Section 5.6.

Table B.1: Dependence of polarization on the different binnings or errors of cosθ

Parameter	Λ	$\overline{\Lambda}$	K^0
2002			
10 cosθ bins	$+\ 0.031 \pm 0.035$	$-\ 0.167 \pm 0.049$	$+\ 0.003 \pm 0.008$
4 cosθ bins	$+\ 0.025 \pm 0.036$	$-\ 0.160 \pm 0.050$	$+\ 0.005 \pm 0.008$
Δ cosθ = $1/\sqrt{12}$	$+\ 0.036 \pm 0.035$	$-\ 0.170 \pm 0.052$	$+\ 0.004 \pm 0.008$
2003			
10 cosθ bins	$-\ 0.018 \pm 0.022$	$-\ 0.096 \pm 0.031$	$-\ 0.002 \pm 0.005$
4 cosθ bins	$-\ 0.019 \pm 0.023$	$-\ 0.087 \pm 0.031$	$-\ 0.001 \pm 0.005$
Δ cosθ = $1/\sqrt{12}$	$-\ 0.019 \pm 0.022$	$-\ 0.093 \pm 0.033$	$-\ 0.003 \pm 0.005$
2004			
10 cosθ bins	$-\ 0.017 \pm 0.016$	$-\ 0.092 \pm 0.023$	$-\ 0.002 \pm 0.004$
4 cosθ bins	$-\ 0.023 \pm 0.017$	$-\ 0.097 \pm 0.022$	$-\ 0.003 \pm 0.004$
Δ cosθ = $1/\sqrt{12}$	$-\ 0.019 \pm 0.016$	$-\ 0.094 \pm 0.024$	$-\ 0.003 \pm 0.004$

Table B.2: Dependence of polarization on the various data taking periods

Parameter	Λ	$\overline{\Lambda}$	K^0
P1C, P2A	$+ 0.091 \pm 0.058$	$- 0.156 \pm 0.079$	$+ 0.005 \pm 0.013$
P2D, P2E	$- 0.052 \pm 0.059$	$- 0.177 \pm 0.080$	$- 0.003 \pm 0.013$
P1F, P2G	$+ 0.084 \pm 0.072$	$- 0.151 \pm 0.101$	$+ 0.015 \pm 0.015$
P1A, P1B	$+ 0.036 \pm 0.057$	$- 0.117 \pm 0.078$	$+ 0.008 \pm 0.012$
P1C, P1D	$- 0.071 \pm 0.050$	$- 0.120 \pm 0.070$	$- 0.005 \pm 0.011$
P1E, P1F	$- 0.025 \pm 0.041$	$- 0.040 \pm 0.057$	$- 0.002 \pm 0.009$
P1I, P1J	$+ 0.000 \pm 0.037$	$- 0.112 \pm 0.051$	$- 0.007 \pm 0.008$
W22	$- 0.057 \pm 0.046$	$- 0.163 \pm 0.062$	$- 0.004 \pm 0.010$
W23, W26	$+ 0.007 \pm 0.044$	$- 0.150 \pm 0.060$	$- 0.018 \pm 0.009$
W27, W28	$+ 0.042 \pm 0.052$	$- 0.128 \pm 0.072$	$+ 0.013 \pm 0.011$
W29, W30	$+ 0.054 \pm 0.047$	$- 0.076 \pm 0.064$	$- 0.022 \pm 0.010$
W31, W32	$- 0.081 \pm 0.041$	$- 0.060 \pm 0.053$	$+ 0.002 \pm 0.009$
W37, W38	$- 0.017 \pm 0.032$	$+ 0.005 \pm 0.044$	$+ 0.005 \pm 0.007$
W39, W40	$- 0.028 \pm 0.046$	$- 0.170 \pm 0.064$	$+ 0.002 \pm 0.010$
Mean	$- 0.010 \pm 0.012$	$- 0.100 \pm 0.017$	$- 0.002 \pm 0.003$

Table B.3: Dependence of polarization on the various V^0 momentum directions

Parameter	Λ	$\overline{\Lambda}$	K^0
2002 Left, Up	$+ 0.030 \pm 0.068$	$- 0.152 \pm 0.096$	$- 0.014 \pm 0.015$
2002 Left, Down	$+ 0.097 \pm 0.075$	$- 0.292 \pm 0.097$	$+ 0.006 \pm 0.017$
2002 Right, Up	$+ 0.000 \pm 0.068$	$- 0.182 \pm 0.095$	$- 0.001 \pm 0.015$
2002 Right, Down	$+ 0.031 \pm 0.077$	$- 0.120 \pm 0.109$	$+ 0.033 \pm 0.017$
2003 Left, Up	$- 0.053 \pm 0.043$	$- 0.149 \pm 0.058$	$- 0.007 \pm 0.010$
2003 Left, Down	$+ 0.001 \pm 0.047$	$- 0.083 \pm 0.062$	$+ 0.016 \pm 0.011$
2003 Right, Up	$- 0.065 \pm 0.043$	$- 0.113 \pm 0.062$	$- 0.003 \pm 0.010$
2003 Right, Down	$+ 0.069 \pm 0.048$	$- 0.063 \pm 0.067$	$- 0.020 \pm 0.011$
2004 1/8 sector	$- 0.079 \pm 0.045$	$- 0.091 \pm 0.060$	$- 0.013 \pm 0.011$
2004 2/8 sector	$+ 0.006 \pm 0.045$	$- 0.185 \pm 0.062$	$- 0.012 \pm 0.011$
2004 3/8 sector	$- 0.013 \pm 0.049$	$- 0.077 \pm 0.065$	$- 0.004 \pm 0.012$
2004 4/8 sector	$+ 0.088 \pm 0.052$	$- 0.090 \pm 0.067$	$+ 0.016 \pm 0.013$
2004 5/8 sector	$+ 0.020 \pm 0.052$	$- 0.006 \pm 0.065$	$+ 0.031 \pm 0.013$
2004 6/8 sector	$- 0.032 \pm 0.046$	$- 0.077 \pm 0.060$	$+ 0.013 \pm 0.012$
2004 7/8 sector	$+ 0.012 \pm 0.045$	$- 0.180 \pm 0.061$	$- 0.017 \pm 0.011$
2004 8/8 sector	$- 0.060 \pm 0.046$	$- 0.134 \pm 0.061$	$- 0.019 \pm 0.011$
Momentum	$- 0.007 \pm 0.013$	$- 0.116 \pm 0.017$	$- 0.002 \pm 0.003$

Table B.4: Dependence of polarization on the different triggers

Parameter	Λ	$\overline{\Lambda}$	K^0
2002 IT & LT	-0.088 ± 0.086	-0.339 ± 0.117	-0.001 ± 0.020
2002 MCT	$+0.064 \pm 0.079$	-0.029 ± 0.109	$+0.004 \pm 0.017$
2002 incOT	$+0.092 \pm 0.058$	-0.184 ± 0.079	-0.005 ± 0.013
2002 incMT	$+0.002 \pm 0.073$	-0.175 ± 0.103	$+0.027 \pm 0.016$
2003 IT & LT	$+0.119 \pm 0.061$	-0.314 ± 0.084	$+0.007 \pm 0.015$
2003 MCT	-0.012 ± 0.060	-0.108 ± 0.080	-0.005 ± 0.014
2003 incOT	$+0.066 \pm 0.052$	-0.229 ± 0.073	-0.007 ± 0.012
2003 Calo	-0.015 ± 0.050	-0.078 ± 0.062	$+0.013 \pm 0.011$
2003 incMT	$+0.025 \pm 0.042$	-0.044 ± 0.060	-0.016 ± 0.010
2004 IT & LT	-0.053 ± 0.071	-0.065 ± 0.095	-0.006 ± 0.018
2004 MCT	-0.098 ± 0.081	-0.039 ± 0.120	-0.028 ± 0.022
2004 incOT	-0.115 ± 0.066	-0.281 ± 0.092	-0.008 ± 0.017
2003 Calo	$+0.032 \pm 0.023$	-0.089 ± 0.030	-0.003 ± 0.006
2004 incMT	-0.040 ± 0.030	-0.086 ± 0.042	$+0.004 \pm 0.008$
Trigger mean	$+0.008 \pm 0.013$	-0.117 ± 0.017	-0.001 ± 0.003

Table B.5: Dependence of polarization on the different target polarizations

Parameter	Λ	$\overline{\Lambda}$	K^0
2002 upstream (+ pol)	$+0.114 \pm 0.090$	-0.204 ± 0.120	-0.004 ± 0.022
2002 upstream ($-$ pol)	-0.066 ± 0.090	-0.045 ± 0.121	-0.014 ± 0.021
2002 downstream (+ pol)	$+0.019 \pm 0.060$	-0.301 ± 0.082	$+0.014 \pm 0.012$
2002 downstream ($-$ pol)	$+0.064 \pm 0.062$	-0.083 ± 0.090	$+0.002 \pm 0.013$
2003 upstream (+ pol)	$+0.072 \pm 0.053$	-0.203 ± 0.075	$+0.004 \pm 0.013$
2003 upstream ($-$ pol)	-0.046 ± 0.057	-0.085 ± 0.076	-0.008 ± 0.014
2003 downstream (+ pol)	-0.031 ± 0.040	-0.079 ± 0.054	-0.011 ± 0.008
2003 downstream ($-$ pol)	-0.025 ± 0.038	-0.070 ± 0.053	$+0.005 \pm 0.008$
2004 upstream (+ pol)	-0.021 ± 0.040	-0.070 ± 0.052	-0.005 ± 0.011
2004 upstream ($-$ pol)	-0.024 ± 0.039	-0.160 ± 0.054	$+0.008 \pm 0.011$
2004 downstream (+ pol)	-0.037 ± 0.028	-0.062 ± 0.039	-0.002 ± 0.006
2004 downstream ($-$ pol)	$+0.014 \pm 0.029$	-0.102 ± 0.038	-0.006 ± 0.006
Target Polarization Mean	-0.009 ± 0.012	-0.104 ± 0.017	-0.002 ± 0.003

Table B.6: Dependence of polarization on the different target positions

Parameter	Λ	$\overline{\Lambda}$	K^0
2002 upstream1	-0.021 ± 0.100	-0.132 ± 0.133	$+0.007 \pm 0.025$
2002 upstream2	$+0.053 \pm 0.083$	-0.139 ± 0.106	-0.014 ± 0.020
2002 downstream1	$+0.047 \pm 0.066$	-0.285 ± 0.092	$+0.017 \pm 0.015$
2002 downstream2	$+0.041 \pm 0.058$	-0.158 ± 0.082	$+0.003 \pm 0.012$
2003 upstream1	$+0.003 \pm 0.060$	-0.103 ± 0.087	-0.002 ± 0.017
2003 upstream2	$+0.025 \pm 0.050$	-0.161 ± 0.068	-0.001 ± 0.013
2003 downstream1	-0.020 ± 0.042	-0.148 ± 0.057	-0.007 ± 0.010
2003 downstream2	-0.031 ± 0.037	-0.030 ± 0.050	-0.000 ± 0.008
2004 upstream1	$+0.001 \pm 0.044$	-0.157 ± 0.060	-0.007 ± 0.013
2004 upstream2	-0.036 ± 0.037	-0.097 ± 0.050	$+0.008 \pm 0.011$
2004 downstream1	$+0.001 \pm 0.031$	-0.076 ± 0.041	-0.006 ± 0.008
2004 downstream2	-0.018 ± 0.027	-0.083 ± 0.037	-0.002 ± 0.006
Target Up & Down Mean	-0.007 ± 0.012	-0.107 ± 0.017	-0.001 ± 0.003
2002 Quadrant 1	-0.092 ± 0.078	-0.040 ± 0.112	-0.006 ± 0.018
2002 Quadrant 2	$+0.047 \pm 0.090$	-0.358 ± 0.114	$+0.023 \pm 0.019$
2002 Quadrant 3	$+0.039 \pm 0.062$	-0.201 ± 0.085	$+0.003 \pm 0.014$
2002 Quadrant 4	$+0.095 \pm 0.067$	-0.155 ± 0.092	$+0.000 \pm 0.015$
2003 Quadrant 1	$+0.018 \pm 0.047$	-0.088 ± 0.064	-0.009 ± 0.011
2003 Quadrant 2	-0.009 ± 0.043	-0.081 ± 0.058	-0.016 ± 0.010
2003 Quadrant 3	-0.055 ± 0.049	-0.192 ± 0.064	$+0.010 \pm 0.011$
2003 Quadrant 4	$+0.005 \pm 0.043$	-0.058 ± 0.060	$+0.006 \pm 0.010$
2004 Quadrant 1	-0.029 ± 0.036	-0.068 ± 0.049	-0.004 ± 0.009
2004 Quadrant 2	-0.029 ± 0.030	-0.138 ± 0.039	-0.003 ± 0.008
2004 Quadrant 3	-0.012 ± 0.038	-0.107 ± 0.050	-0.010 ± 0.009
2004 Quadrant 4	$+0.004 \pm 0.032$	-0.054 ± 0.044	$+0.002 \pm 0.008$
Target Quadrant Mean	-0.009 ± 0.013	-0.108 ± 0.017	-0.002 ± 0.003

Appendix C

Tables of Kinematic Dependences

The following tables detail the results of the Λ and $\overline{\Lambda}$ polarizations and spin transfers in various kinematic bins, as presented in the Section 5.7. The χ^2/ndf and the respective average mean values of additional kinematic variables are weighted from the results of three different years and listed in each columns.

Table C.1: Dependence of polarization and spin transfer on Q^2

Range	P_x	C_{LL}	χ^2 / ndf	Q^2 GeV/c^2	x_{Bj}	y	$D(y)$	W^2 (GeV/c^2)^2	p GeV/c	p_T GeV/c	x_F	z
Λ												
$1.000 < Q^2 \leq 1.264$	0.009 ± 0.028	-0.018 ± 0.084	0.59	1.13	0.0099	0.44	0.44	132.5	18.8	0.55	0.23	0.29
$1.264 < Q^2 \leq 1.685$	-0.027 ± 0.028	0.081 ± 0.082	0.48	1.45	0.0128	0.44	0.45	133.2	19.0	0.54	0.23	0.29
$1.685 < Q^2 \leq 2.451$	0.005 ± 0.028	-0.032 ± 0.080	0.75	2.02	0.0176	0.45	0.47	132.9	19.2	0.54	0.24	0.29
$2.451 < Q^2 \leq 4.495$	-0.027 ± 0.028	0.076 ± 0.077	1.16	3.28	0.0285	0.45	0.48	131.9	19.4	0.53	0.24	0.29
$4.495 < Q^2$	0.000 ± 0.029	-0.003 ± 0.078	1.43	8.55	0.0763	0.42	0.46	117.8	19.3	0.50	0.25	0.31
$\overline{\Lambda}$												
$1.000 < Q^2 \leq 1.264$	-0.099 ± 0.038	0.282 ± 0.107	0.78	1.12	0.0093	0.47	0.48	141.2	19.1	0.55	0.22	0.27
$1.264 < Q^2 \leq 1.685$	-0.115 ± 0.036	0.328 ± 0.101	0.63	1.45	0.0121	0.47	0.48	139.6	19.5	0.54	0.22	0.28
$1.685 < Q^2 \leq 2.451$	-0.097 ± 0.037	0.258 ± 0.101	0.89	2.03	0.0167	0.47	0.49	140.0	19.7	0.55	0.22	0.28
$2.451 < Q^2 \leq 4.495$	-0.137 ± 0.037	0.361 ± 0.096	1.09	3.27	0.0268	0.47	0.50	138.4	19.8	0.52	0.23	0.28
$4.495 < Q^2$	-0.101 ± 0.040	0.253 ± 0.102	0.60	8.54	0.0713	0.45	0.50	127.1	19.2	0.49	0.22	0.28
K^0												
$1.000 < Q^2 \leq 1.264$	-0.012 ± 0.007	0.033 ± 0.019	0.85	1.12	0.0096	0.46	0.46	137.8	17.9	0.49	0.24	0.27
$1.264 < Q^2 \leq 1.685$	-0.010 ± 0.007	0.026 ± 0.018	0.59	1.46	0.0124	0.46	0.47	137.6	18.0	0.49	0.24	0.27
$1.685 < Q^2 \leq 2.451$	0.009 ± 0.007	-0.025 ± 0.018	0.65	2.02	0.0170	0.46	0.49	138.3	18.0	0.48	0.24	0.27
$2.451 < Q^2 \leq 4.495$	0.004 ± 0.007	-0.009 ± 0.018	1.01	3.26	0.0273	0.46	0.50	136.9	18.0	0.48	0.24	0.26
$4.495 < Q^2$	0.003 ± 0.007	-0.007 ± 0.019	1.21	8.65	0.0730	0.44	0.48	123.9	17.8	0.48	0.25	0.27

Table C.2: Dependence of polarization and spin transfer on x_{Bj}

Range	P_x	C_{LL}	χ^2 / ndf	Q^2 GeV/c^2	x_{Bj}	y	$D(y)$	W^2 (GeV/c^2)^2	p GeV/c	p_T GeV/c	x_F	z
Λ												
$0.0000 < x_{Bj} \leq 0.0097$	0.029 ± 0.029	-0.057 ± 0.059	1.06	1.33	0.0073	0.62	0.65	187.7	22.8	0.58	0.19	0.23
$0.0097 < x_{Bj} \leq 0.0145$	-0.009 ± 0.028	0.019 ± 0.078	1.29	1.65	0.0120	0.46	0.47	137.2	19.5	0.55	0.22	0.28
$0.0145 < x_{Bj} \leq 0.0213$	0.004 ± 0.028	-0.012 ± 0.092	0.16	2.03	0.0175	0.39	0.40	114.9	18.0	0.53	0.25	0.31
$0.0213 < x_{Bj} \leq 0.0394$	-0.018 ± 0.027	0.057 ± 0.092	0.94	3.18	0.0286	0.37	0.39	109.0	17.8	0.51	0.26	0.32
$0.0394 < x_{Bj}$	-0.006 ± 0.028	0.016 ± 0.092	1.30	8.22	0.0785	0.35	0.38	98.0	17.5	0.49	0.27	0.33
$\overline{\Lambda}$												
$0.0000 < x_{Bj} \leq 0.0097$	-0.145 ± 0.036	0.292 ± 0.072	1.19	1.34	0.0073	0.63	0.66	189.8	23.4	0.58	0.19	0.24
$0.0097 < x_{Bj} \leq 0.0145$	-0.119 ± 0.036	0.328 ± 0.098	1.37	1.70	0.0121	0.47	0.49	140.8	19.7	0.55	0.22	0.27
$0.0145 < x_{Bj} \leq 0.0213$	-0.046 ± 0.038	0.150 ± 0.120	0.83	2.13	0.0176	0.40	0.42	120.4	17.7	0.52	0.23	0.29
$0.0213 < x_{Bj} \leq 0.0394$	-0.099 ± 0.038	0.306 ± 0.118	0.75	3.40	0.0287	0.40	0.42	116.4	18.1	0.52	0.24	0.30
$0.0394 < x_{Bj}$	-0.117 ± 0.041	0.361 ± 0.127	1.04	8.62	0.0770	0.37	0.40	103.2	17.1	0.47	0.24	0.30
K^0												
$0.0000 < x_{Bj} \leq 0.0097$	-0.010 ± 0.006	0.019 ± 0.013	0.38	1.34	0.0072	0.63	0.66	190.2	21.4	0.50	0.20	0.22
$0.0097 < x_{Bj} \leq 0.0145$	-0.002 ± 0.007	0.003 ± 0.018	0.71	1.69	0.0120	0.47	0.49	140.5	18.2	0.49	0.23	0.26
$0.0145 < x_{Bj} \leq 0.0213$	-0.007 ± 0.007	0.024 ± 0.021	0.83	2.09	0.0175	0.40	0.41	118.1	16.7	0.48	0.26	0.28
$0.0213 < x_{Bj} \leq 0.0394$	0.009 ± 0.007	-0.029 ± 0.022	0.58	3.26	0.0284	0.38	0.40	112.3	16.5	0.48	0.27	0.30
$0.0394 < x_{Bj}$	0.006 ± 0.007	-0.017 ± 0.023	0.74	8.35	0.0771	0.36	0.39	101.5	16.2	0.47	0.27	0.30

Table C.3: Dependence of polarization and spin transfer on y

Range	P_x	C_{LL}	χ^2 / ndf	Q^2 GeV/c^2	x_{Bj}	y	$D(y)$	W^2 (GeV/c^2)^2	p GeV/c	p_T GeV/c	x_F	z
Λ												
$0.200 < y \leq 0.280$	0.024 ± 0.026	-0.145 ± 0.150	0.67	3.04	0.0425	0.24	0.23	70.0	14.2	0.48	0.30	0.37
$0.280 < y \leq 0.363$	-0.003 ± 0.027	0.007 ± 0.113	0.74	3.36	0.0349	0.32	0.32	94.0	16.5	0.51	0.26	0.32
$0.363 < y \leq 0.464$	-0.001 ± 0.028	0.004 ± 0.086	0.84	3.33	0.0268	0.41	0.43	121.5	18.9	0.54	0.23	0.29
$0.464 < y \leq 0.607$	0.046 ± 0.028	-0.110 ± 0.065	0.39	3.37	0.0213	0.53	0.57	156.8	21.6	0.56	0.21	0.26
$0.607 < y \leq 0.900$	0.024 ± 0.030	-0.041 ± 0.050	0.39	3.01	0.0141	0.72	0.78	215.5	25.2	0.58	0.18	0.22
$\overline{\Lambda}$												
$0.200 < y \leq 0.280$	0.024 ± 0.043	-0.129 ± 0.241	0.77	2.90	0.0399	0.24	0.24	71.2	13.4	0.48	0.27	0.34
$0.280 < y \leq 0.363$	-0.101 ± 0.039	0.407 ± 0.158	1.05	3.21	0.0332	0.32	0.33	94.7	16.0	0.51	0.25	0.31
$0.363 < y \leq 0.464$	-0.122 ± 0.038	0.391 ± 0.116	0.49	3.24	0.0262	0.41	0.43	121.8	18.6	0.52	0.23	0.28
$0.464 < y \leq 0.607$	-0.160 ± 0.035	0.374 ± 0.082	0.94	3.42	0.0214	0.53	0.57	157.2	21.4	0.56	0.20	0.25
$0.607 < y \leq 0.900$	-0.114 ± 0.036	0.191 ± 0.060	0.22	3.02	0.0143	0.71	0.78	215.0	25.5	0.58	0.18	0.23
K^0												
$0.200 < y \leq 0.280$	0.001 ± 0.007	-0.003 ± 0.040	0.96	2.90	0.0403	0.24	0.23	70.5	13.4	0.46	0.32	0.35
$0.280 < y \leq 0.363$	-0.002 ± 0.007	0.009 ± 0.029	0.99	3.15	0.0328	0.32	0.32	94.4	15.3	0.47	0.27	0.30
$0.363 < y \leq 0.464$	0.009 ± 0.007	-0.030 ± 0.021	1.01	3.29	0.0266	0.41	0.43	121.6	17.3	0.48	0.24	0.26
$0.464 < y \leq 0.607$	-0.005 ± 0.006	0.010 ± 0.015	0.49	3.26	0.0205	0.53	0.57	157.6	19.8	0.49	0.21	0.23
$0.607 < y \leq 0.900$	-0.008 ± 0.006	0.014 ± 0.010	0.99	3.01	0.0141	0.72	0.78	216.1	23.0	0.51	0.19	0.21

Table C.4: Dependence of polarization and spin transfer on W^2

Range	P_x	C_{LL}	χ^2 / ndf	Q^2 GeV/c^2	x_{Bj}	y	$D(y)$	W^2 (GeV/c^2)^2	p GeV/c	p_T GeV/c	x_F	z
Λ												
$0.0 < W^2 \leq 81.6$	0.021 ± 0.027	-0.119 ± 0.152	0.31	3.54	0.0478	0.24	0.24	69.4	14.3	0.48	0.30	0.37
$81.6 < W^2 \leq 106.2$	-0.005 ± 0.027	0.014 ± 0.112	0.91	3.34	0.0335	0.32	0.32	93.5	16.5	0.51	0.26	0.32
$106.2 < W^2 \leq 136.2$	-0.007 ± 0.028	0.021 ± 0.086	0.87	3.35	0.0264	0.41	0.43	120.7	18.9	0.54	0.23	0.29
$136.2 < W^2 \leq 178.7$	0.051 ± 0.028	-0.124 ± 0.066	0.35	3.20	0.0199	0.52	0.56	155.4	21.4	0.56	0.21	0.26
$178.7 < W^2$	0.040 ± 0.030	-0.067 ± 0.050	0.39	2.68	0.0125	0.72	0.78	214.1	25.1	0.58	0.18	0.22
$\overline{\Lambda}$												
$0.0 < W^2 \leq 81.6$	-0.015 ± 0.043	0.094 ± 0.236	1.46	3.32	0.0445	0.24	0.24	70.5	13.3	0.48	0.27	0.35
$81.6 < W^2 \leq 106.2$	-0.101 ± 0.039	0.410 ± 0.158	1.24	3.40	0.0339	0.32	0.32	94.0	15.9	0.51	0.25	0.31
$106.2 < W^2 \leq 136.2$	-0.097 ± 0.038	0.309 ± 0.117	0.42	3.35	0.0264	0.41	0.43	120.5	18.5	0.52	0.23	0.28
$136.2 < W^2 \leq 178.7$	-0.161 ± 0.036	0.379 ± 0.083	0.60	3.22	0.0200	0.53	0.56	155.8	21.6	0.55	0.21	0.26
$178.7 < W^2$	-0.118 ± 0.035	0.199 ± 0.059	0.32	2.68	0.0125	0.72	0.78	212.0	25.3	0.58	0.18	0.22
K^0												
$0.0 < W^2 \leq 81.6$	-0.003 ± 0.007	0.015 ± 0.040	1.02	3.36	0.0453	0.24	0.24	69.9	13.4	0.46	0.32	0.35
$81.6 < W^2 \leq 106.2$	0.003 ± 0.007	-0.013 ± 0.028	0.80	3.23	0.0325	0.32	0.32	93.7	15.3	0.47	0.27	0.30
$106.2 < W^2 \leq 136.2$	0.008 ± 0.007	-0.027 ± 0.021	1.22	3.25	0.0257	0.41	0.43	120.6	17.2	0.48	0.24	0.26
$136.2 < W^2 \leq 178.7$	-0.004 ± 0.007	0.009 ± 0.015	0.57	3.16	0.0196	0.53	0.56	156.1	19.7	0.49	0.21	0.23
$178.7 < W^2$	-0.009 ± 0.006	0.014 ± 0.010	0.86	2.72	0.0126	0.72	0.78	215.2	23.0	0.51	0.19	0.21

Table C.5: Dependence of polarization and spin transfer on p_T

Range	P_x	C_{LL}	χ^2 / ndf	Q^2 GeV/c^2	x_{Bj}	y	$D(y)$	W^2 (GeV/c^2)^2	p GeV/c	p_T GeV/c	x_F	z
Λ												
$0.000 < p_T \leq 0.275$	-0.043 ± 0.030	0.122 ± 0.090	0.63	3.47	0.0317	0.42	0.44	123.2	17.7	0.18	0.23	0.29
$0.275 < p_T \leq 0.418$	-0.011 ± 0.029	0.031 ± 0.083	0.52	3.38	0.0304	0.43	0.45	126.8	18.2	0.35	0.23	0.29
$0.418 < p_T \leq 0.564$	0.023 ± 0.028	-0.060 ± 0.082	1.88	3.21	0.0283	0.43	0.45	127.5	18.5	0.49	0.23	0.29
$0.564 < p_T \leq 0.759$	-0.065 ± 0.028	0.176 ± 0.078	0.64	3.14	0.0270	0.44	0.47	131.6	19.4	0.65	0.24	0.29
$0.759 < p_T$	0.004 ± 0.027	-0.010 ± 0.072	0.83	2.93	0.0239	0.47	0.50	140.4	21.9	1.00	0.24	0.31
$\overline{\Lambda}$												
$0.000 < p_T \leq 0.275$	-0.091 ± 0.042	0.260 ± 0.118	0.76	3.57	0.0306	0.44	0.47	130.6	18.2	0.19	0.22	0.27
$0.275 < p_T \leq 0.418$	-0.053 ± 0.039	0.149 ± 0.106	0.21	3.21	0.0272	0.45	0.48	133.7	18.2	0.35	0.22	0.27
$0.418 < p_T \leq 0.564$	-0.079 ± 0.038	0.211 ± 0.102	1.01	3.09	0.0251	0.46	0.49	137.0	18.7	0.49	0.22	0.27
$0.564 < p_T \leq 0.759$	-0.117 ± 0.037	0.316 ± 0.097	0.95	3.07	0.0249	0.47	0.49	138.8	19.6	0.66	0.22	0.28
$0.759 < p_T$	-0.124 ± 0.037	0.315 ± 0.093	0.21	2.93	0.0223	0.50	0.53	147.5	22.6	0.98	0.24	0.30
K^0												
$0.000 < p_T \leq 0.275$	0.001 ± 0.006	-0.003 ± 0.017	1.26	3.18	0.0274	0.44	0.47	131.7	15.8	0.18	0.23	0.24
$0.275 < p_T \leq 0.418$	0.000 ± 0.006	-0.001 ± 0.017	1.05	3.14	0.0266	0.45	0.48	133.8	16.5	0.35	0.23	0.25
$0.418 < p_T \leq 0.564$	-0.008 ± 0.007	0.021 ± 0.018	0.97	3.10	0.0261	0.46	0.48	135.6	17.6	0.49	0.24	0.26
$0.564 < p_T \leq 0.759$	0.006 ± 0.007	-0.015 ± 0.019	0.62	3.09	0.0257	0.46	0.48	136.6	19.2	0.65	0.26	0.28
$0.759 < p_T$	-0.005 ± 0.008	0.015 ± 0.020	0.65	3.11	0.0250	0.48	0.50	141.6	22.8	1.00	0.29	0.33

Table C.6: Dependence of polarization and spin transfer on x_F

Range	P_x	C_{LL}	χ^2 / ndf	Q^2 GeV/c^2	x_{Bj}	y	$D(y)$	W^2 (GeV/c^2)^2	p GeV/c	p_T GeV/c	x_F	z
Λ												
$0.050 < x_F \leq 0.114$	-0.007 ± 0.029	0.018 ± 0.068	1.58	3.02	0.0221	0.52	0.55	155.3	12.6	0.53	0.08	0.16
$0.114 < x_F \leq 0.176$	-0.028 ± 0.029	0.074 ± 0.075	0.46	3.16	0.0252	0.47	0.50	140.0	15.3	0.53	0.15	0.21
$0.176 < x_F \leq 0.249$	-0.051 ± 0.028	0.142 ± 0.081	0.76	3.23	0.0281	0.43	0.46	128.6	18.2	0.53	0.21	0.27
$0.249 < x_F \leq 0.349$	-0.094 ± 0.028	0.291 ± 0.087	1.09	3.33	0.0318	0.40	0.41	117.1	21.5	0.53	0.30	0.34
$0.349 < x_F \leq 1.000$	0.014 ± 0.028	-0.048 ± 0.095	1.19	3.40	0.0343	0.37	0.38	107.9	28.4	0.55	0.45	0.50
$\overline{\Lambda}$												
$0.050 < x_F \leq 0.114$	-0.018 ± 0.037	0.052 ± 0.086	0.68	3.14	0.0225	0.53	0.57	157.8	12.8	0.52	0.08	0.16
$0.114 < x_F \leq 0.176$	-0.063 ± 0.037	0.164 ± 0.092	0.61	3.22	0.0248	0.49	0.52	145.5	15.7	0.52	0.14	0.21
$0.176 < x_F \leq 0.249$	-0.108 ± 0.036	0.291 ± 0.098	0.50	3.07	0.0259	0.45	0.47	133.4	18.7	0.53	0.21	0.27
$0.249 < x_F \leq 0.349$	-0.115 ± 0.037	0.343 ± 0.112	0.77	3.22	0.0287	0.42	0.44	124.7	22.8	0.54	0.30	0.34
$0.349 < x_F \leq 1.000$	-0.169 ± 0.043	0.526 ± 0.134	0.61	3.24	0.0293	0.41	0.43	120.2	30.7	0.56	0.40	0.48
K^0												
$0.050 < x_F \leq 0.114$	-0.000 ± 0.007	0.002 ± 0.016	0.66	3.10	0.0208	0.56	0.59	165.6	9.9	0.43	0.08	0.11
$0.114 < x_F \leq 0.176$	-0.010 ± 0.007	0.027 ± 0.018	0.77	3.13	0.0242	0.49	0.52	145.0	13.1	0.45	0.15	0.17
$0.176 < x_F \leq 0.249$	-0.001 ± 0.007	0.004 ± 0.020	0.20	3.15	0.0268	0.45	0.47	132.1	16.5	0.47	0.21	0.23
$0.249 < x_F \leq 0.349$	0.000 ± 0.008	-0.000 ± 0.024	0.32	3.16	0.0289	0.41	0.43	122.4	20.7	0.50	0.29	0.31
$0.349 < x_F \leq 1.000$	0.002 ± 0.007	-0.007 ± 0.025	1.05	3.09	0.0304	0.38	0.40	113.4	29.3	0.55	0.48	0.49

Table C.7: Dependence of polarization and spin transfer on z

Range	P_x	C_{LL}	χ^2 / ndf	Q^2 GeV/c^2	x_{Bj}	y	$D(y)$	W^2 (GeV/c^2)^2	p GeV/c	p_T GeV/c	x_F	z
Λ												
$0.000 < z \leq 0.183$	0.005 ± 0.029	-0.010 ± 0.062	1.22	2.95	0.0188	0.57	0.61	171.7	13.9	0.49	0.09	0.15
$0.183 < z \leq 0.237$	-0.007 ± 0.028	0.015 ± 0.076	0.55	3.21	0.0252	0.47	0.49	138.6	15.6	0.52	0.14	0.21
$0.237 < z \leq 0.302$	-0.063 ± 0.028	0.183 ± 0.083	0.51	3.23	0.0289	0.42	0.44	123.1	17.8	0.54	0.21	0.27
$0.302 < z \leq 0.395$	-0.100 ± 0.028	0.322 ± 0.091	1.29	3.32	0.0325	0.38	0.40	113.0	21.1	0.54	0.29	0.35
$0.395 < z \leq 1.000$	0.012 ± 0.027	-0.043 ± 0.099	1.29	3.43	0.0360	0.35	0.36	102.9	27.4	0.57	0.45	0.49
$\overline{\Lambda}$												
$0.000 < z \leq 0.183$	-0.056 ± 0.037	0.121 ± 0.076	0.86	3.01	0.0187	0.59	0.63	174.6	14.2	0.49	0.09	0.15
$0.183 < z \leq 0.237$	-0.073 ± 0.037	0.200 ± 0.096	0.54	3.32	0.0259	0.48	0.50	140.8	15.8	0.52	0.14	0.21
$0.237 < z \leq 0.302$	-0.088 ± 0.036	0.243 ± 0.102	1.15	3.06	0.0264	0.44	0.46	129.1	18.6	0.54	0.21	0.27
$0.302 < z \leq 0.395$	-0.122 ± 0.037	0.383 ± 0.117	1.30	3.27	0.0303	0.40	0.42	119.2	22.4	0.55	0.30	0.35
$0.395 < z \leq 1.000$	-0.181 ± 0.045	0.600 ± 0.148	0.37	3.22	0.0305	0.39	0.40	114.5	29.6	0.58	0.44	0.44
K^0												
$0.000 < z \leq 0.183$	-0.007 ± 0.005	0.017 ± 0.013	1.01	3.10	0.0215	0.54	0.57	160.4	11.4	0.41	0.11	0.13
$0.183 < z \leq 0.237$	-0.003 ± 0.008	0.009 ± 0.021	0.28	3.14	0.0260	0.46	0.48	135.2	15.2	0.47	0.19	0.21
$0.237 < z \leq 0.302$	0.002 ± 0.008	-0.005 ± 0.025	0.36	3.15	0.0280	0.42	0.44	125.7	18.2	0.50	0.25	0.27
$0.302 < z \leq 0.395$	0.005 ± 0.009	-0.015 ± 0.027	0.36	3.18	0.0299	0.40	0.42	118.2	22.1	0.53	0.32	0.34
$0.395 < z \leq 1.000$	-0.001 ± 0.008	0.002 ± 0.028	1.06	3.10	0.0311	0.38	0.39	110.8	30.0	0.58	0.50	0.52

Bibliography

[1] E. Rutherford, The Scattering of α and β Particles by Matter and the Structure of the Atom, Phil. Mag. 21 (1911) 669

[2] H. W. Kendall, Deep inelastic scattering: Experiments on the proton and the observation of scaling, Rev. Mod. Phys. 63 (1991) 597

[3] R. P. Feynman, Very high-energy collisions of hadrons, Phys. Rev. Lett. 23 (1969) 1415

[4] M. M. Gellmann, A schematic model of baryons and mesons, Phys. Lett. 8 (1964) 214

[5] G. Zweig, An SU(3) Model for Strong Interaction Symmetry and its Breaking II, CERN-8419-TH-412 (1964)

[6] J. Ashman et al. [The European Muon Collaboration], A measurement of the spin asymmetry and determination of the structure function g_1 in deep inelastic muon-proton scattering, Phys. Lett. B 206 (1988) 364

[7] D. Adams et al. [Spin Muon Collaboration], Spin structure of the proton from polarized inclusive deep-inelastic muon-proton scattering, Phys. Rev. D 56 (1997) 5330

[8] R. L. Jaffe and Aneesh Manohar, The g_1 problem: Deep inelastic electron scattering and the spin of the proton, Nucl. Phys. B 337 (1990) 509

[9] G. Baum et al. [COMPASS Collaboration], COMPASS proposal, CERN-SPSLC-96-14(1996)

[10] W. Bartel et al., Electroproduction of pions near the Δ(1236) isobar and the form factor G_M^* (q^2) of the (γNΔ)-vertex, Phys. Lett. B28 (1968) 148

[11] E. D. Bloom et al., High energy inelastic $e-p$ scattering at 6° and 10°, Phys. Rev. Lett. 23 (1969) 930

[12] M. Anselmino, A. Efremov and E. Leader, The theory and phenomenology of polarized deep inelastic scattering, Phys. Rept. 261 (1995) 124

[13] F. Halzen and A. D. Martin, Quarks and Leptons: Introduction Course in Modern Particle Physics, Wiley (1983)

[14] Particle Data Group, Review of particle physics, Phys. Lett. B 592 (2004)

[15] W. Greiner and A. Schäfer, Quantum Chromodynamics, Springer (1995)

[16] J. D. Bjorken and E. A. Paschos, Inelastic Electron-Proton and γ-Proton Scattering and the Structure of the Nucleon, Phys. Rev. 185 (1969) 1975

[17] C. G. Callan and D. J. Gross, High-energy electroproduction and the constitution of the electric current, Phys. Rev. Lett. 22 (1969) 156

[18] C. Adloff et al. [H1 Collaboration], Deep-inelastic inclusive ep scattering at low x and a determination of α_s, Eur. Phys. J. C 21 (2001) 33

[19] S. Chekanov et al. [ZEUS Collaboration], Measurement of the neutral current cross section and F_2 structure function for deep inelastic e^+p scattering at HERA, Eur. Phys. J. C 21 (2001) 443

[20] A. C. Benvenuti et al. [BCDMS Collaboration], A High Statistics Measurement of the Proton Structure Functions $F_2(x,Q^2)$ and R from Deep Inelastic Muon Scattering at High Q^2, Phys. Lett. B 223 (1989) 485

[21] A. C. Benvenuti et al. [BCDMS Collaboration], A High Statistics Measurement of the Deuteron Structure Functions $F_2(x,Q^2)$ and R from Deep Inelastic Muon Scattering at High Q^2, Phys. Lett. B 237 (1990) 592

[22] M. R. Adams et al. [Fermilab E665 Collaboration], Proton and deuteron structure functions in muon scattering at 470 GeV, Phys. Rev. D 54 (1996) 3006

[23] M. Arneodo et al. [The New Muon Collaboration], Measurement of the proton and deuteron structure functions, F_2^p and F_2^d, and of the ratio σ_L/σ_T, Nucl. Phys. B 483 (1997) 3

[24] L. W. Whitlow et al. [SLAC Collaboration], Precise Measurements of the Proton and Deuteron Structure Functions from a Global Analysis of the SLAC Deep Inelastic Electron Scattering Cross Sections, Phys. Lett. B 282 (1992) 475

[25] T. Pussieux and R. Windmolders, A collection of formulas for spin dependent deep inelastic scattering, Note SMC-93/16 (1996)

[26] P. L. Anthony et al. [E142 Collaboration], Deep inelastic scattering of polarized electrons by polarized ^{3}He and the study of the neutron spin structure, Phys. Rev. D 54 (1996) 6620

[27] K. Ackerstaff et al. [HERMES Collaboration], Measurement of the neutron spin structure function g_1^n with a polarized ^{3}He internal target, Phys. Lett. B 404 (1997) 383

[28] K. Abe et al. [E154 Collaboration], Precision Determination of the Neutron Spin structure Function g_1^n, Phys. Rev. Lett 79 (1997) 26

[29] X. Zheng et al. [Jefferson Lab Hall A Collaboration], Precision measurement of the neutron spin asymmetries and spin-dependent structure functions in the valence quark region, Phys. Rev. C 70 (2004) 065207

[30] G. Baum et al. [E130 Collaboration], New Measurement of Deep-Inelastic $e-p$ Asymmetries, Phys. Rev. Lett 51 (1983) 1135

[31] K. Abe et al. [E143 Collaboration], Measurement of the proton and deuteron spin structure functions g_1 and g_2, Phys. Rev. D 58 (1998) 112003

[32] P. L. Anthony et al. [E155 Collaboration], Measurement of the Q^2-dependence of the proton and neutron spin structure function g_1^p and g_1^n, Phys. Lett. B 493 (2000) 19

[33] J. Ashman et al. [The European Muon Collaboration], An investigation of the spin structure of the proton in deep inelastic scattering of polarized muons on polarised protons, Nucl. Phys. B 328 (1989) 1

[34] B. Adeva et al. [Spin Muon Collaboration], Spin asymmetries A_1 and structure functions g_1 of the proton and the deuteron from polarized high energy muon scattering, Phys. Rev. D 58 (1998) 112001

[35] A. Airapetian et al. [HERMES Collaboration], Measurement of the proton spin structure function g_1^p with a pure hydrogen target, Phys. lett. B 442 (1998) 484

[36] M. Hirai, S. Kumano, and N. Saito [Asymmetry Analysis Collaboration], Determination of polarized parton distribution functions with recent data on polarization asymmetries, Phys. Rev. D 74 (2006) 014015

[37] A. Airapetian et al. [HERMES Collaboration], Precise determination of the spin structure function g_1 of the proton, deuteron, and neutron, Phys. Rev. D 75 (2007) 012007

[38] B. Adeva et al. [Spin Muon Collaboration], Spin asymmetries A_1 of the proton and the deuteron in the low x and low Q^2 region from polarized high energy muon scattering, Phys. Rev. D 60 (1999) 072004

[39] P. L. Anthony et al. [E155 Collaboration], Measurement of the Deuteron Spin Structure Function $g_1^d(x)$ for 1 (GeV/c)^2 < Q^2 < 40 (GeV/c)^2, Phys. Lett. B 463 (1999) 339

[40] E. S. Ageev et al. [COMPASS Collaboration], Measurement of the Spin Structure of the Deuteron in the DIS Region, Phys. Lett. B 612 (2005) 154

[41] R. L. Jaffe, The context of high energy QCD spin physics at the RIKEN Symposium, arXiv:hep-ph/9603422 (1996)

[42] R. L. Jaffe and X. Ji, Studies of the transverse spin-dependent structure function $g_2(x,Q^2)$, Phys. Rev. D 43 (1991) 724

[43] P. L. Anthony et al. [E155 Collaboration], Measurement of the proton and deuteron spin structure functions g_2 and asymmetry A_2, Phys. Lett. B 458 (1999) 529

[44] K. Abe et al. [E154 Collaboration], Measurement of the Neutron Spin Structure Function g_2^n and Asymmetry A_2^n, Phys. Lett. B 404 (1997) 377

[45] S. P. Parker, Nuclear and particle physics source book, MaGraw-Hill Book Company (1987)

[46] G. Altarelli, Partons in Quantum Chromodynamics, Phys. Rep. 81 (1982) 1

[47] E. B. Zijlstra and W. L. van Neerven, Order-α_s^2 correction to the polarized structure function $g_1(x,Q^2)$, Nucl. Phys. B 417 (1994) 61

[48] R. Mertig and W. L. van Neerven, The calculation of the two-loop spin splitting functions $P_{ij}^{(1)}(x)$, Z. Phys. C 70 (1996) 637

[49] W. Vogelsang, Rederivation of the spin-dependent next-to-leading order splitting functions, Phys. Rev. D 54 (1996) 2023

[50] B. Lampe and E. Reya, Spin Physics and Polarized Structure Functions, Phys. Rept. 332 (2002) 1-163.

[51] Y. L. Dokshitzer, Calculation of the Structure Functions for Deep Inelastic Scattering and e^+ e^- Annihilation by Perturbation Theory in Quantum Chromodynamics, Sov. Phys. JETP 46, (1977) 641

[52] V. N. Gribov and L. N. Lipatov, Deep inelastic *ep* scattering in perturbation theory, Sov. J. Nucl. Phys. 15,(1972) 438

[53] G. Altarelli and G. Parisi, Asymptotic freedom in parton language, Nucl. Phys. B 126 (1977) 298

[54] R. D. Ball, S. Forte, and G. Ridolfi, Next-to-leading order determination of the singlet axial charge and the polarized gluon content of the nucleon, Phys. Lett. B 378 (1996) 255

[55] G. Altarelli, R. D. Ball, S. Forte, and G. Ridolfi, Determination of the Bjorken sum and strong coupling from polarized structure functions, Nucl. Phys. B 496 (1997) 337

[56] M. C. Vetterli, Spin Structure of the nucleon, Lectures at the 13th Lake Louise Winter Institute, arXiv:hep-ph/9812420 (1998)

[57] G. K. Mallot, The spin Structure of the Nucleon from the SMC Experiments, Habilitation thesis (1996)

[58] S. A. Larin, The next-to-leading QCD approximation to the Ellis-Jaffe sum rule, Phys. Lett. B 334 (1994) 192

[59] J. Kodaira et al., Quantum-chromodynamic effects in polarized electroproduction, Phys. Rev. D 20 (1979) 627

[60] A. L. Kataev and V. V. Starshenko, Estimations of the higher-order QCD corrections to $R(s), R_\tau$ and deep inelastic scattering sum rules, Mod. Phys. Lett. A 10 (1995) 235

[61] Y. Goto et al. [Asymmetry Analysis Collaboration], Polarized parton distribution functions in the nucleon, Phys. Rev. D 62 (2000) 034017

[62] V. Yu. Alexakhin et al. [COMPASS Collaboration], The Deuteron Spin-dependent Structure Function g_1^d and its First Moment, CERN-PH-EP/2006-029

[63] W. A. Bardeen et al., Deep-inelastic scattering beyond the leading order in asymptotically free gauge theories, Phys. Rev. D 18 (1978) 3998

[64] S. Adler and W. A. Bardeen, Absence of Higher-Order Correction in the Anomalous Axial-Vector Divergence Equation, Phys. Rev. 182 (1969) 1517

[65] R. D. Carlitz, J. C. Collins and A. H. Mueller, The Role of the Axial Anomaly in Measuring Spin-Dependence Parton Distribution, Phys. Lett. B 214 (1988) 229

[66] E. Leader, A. V. Sidorov and D. B. Stamenov, Scheme Dependence in Polarized Deep Inelastic Scattering, Phys. Lett. B 445 (1998) 232

[67] G. Altarelli and G. G. Ross, The anomalous gluon contribution to polarized leptoproduction, Phys. Lett. B 212 (1988) 391

[68] A. V. Efremov and O. V. Teryaev, Spin structure of the nucleon and triangle anomaly, JINR-E2-88-287 (1988)

[69] D. Müller and O. V. Teryaev, Nonlocal generalization of the axial anomaly and x dependence of the anomalous gluon contribution, Phys. Rev. D 56 (1997) 2607

[70] E. Leader, A. V. Sidorov and D. B. Stamenov, Polarized parton densities in the nucleon, Phys. Rev. D 58 (1998) 114028

[71] D. L. Adams et al. [FNAL E581/704 Collaboration], Measurement of the double-spin asymmetry A_{LL} for inclusive multi-γ pair production with 200 GeV/c polarized proton beam and polarized proton target, Phys. Lett. B 336 (1994) 269

[72] E. S. Ageev et al. [COMPASS Collaboration], Gluon polarization in the nucleon from quasi-real photoproduction of high p_T hadron pairs, Phys. Lett. B 633 (2006) 25

[73] M. J. Alguard et al., Deep Inelastic Scattering of Polarized Electrons by Polarized Protons, Phys. Rev. Lett. 37 (1976) 1261

[74] M. J. Alguard et al., Deep Inelastic $e-p$ Asymmetry Measurements and Comparison with the Bjorken Sum Rule and Models of Proton Spin Structure, Phys. Rev. Lett. 41 (1978) 70

[75] J. D. Bjorken, Applications of the Chiral $U(6)\otimes U(6)$ Algebra of Current Densities, Phys. Rev. 148 (1966) 1467

[76] J. D. Bjorken, Asymptotic Sum Rules at Infinite Momentum, Phys. Rev. 179 (1969) 1547

[77] J. D. Bjorken, Inelastic Scattering of Polarized Leptons from Polarized Nucleons, Phys. Rev. D (1970) 1376

[78] A. Airapetian et al. [HERMES Collaboration], Quark helicity distributions in the nucleon for up, down, and strange quarks from semi-inclusive deep-inelastic scattering, Phys. Rev. D 71 (2005) 012003

[79] A. Kotzinian, Polarized SIDIS: comment on purity method for extraction of polarized quark distributions, Phys. Lett. B 552 (2003) 172

[80] E. Leader and D. B. Stamenov, Can the polarization of the strange quarks in the proton be positive?, Phys. Rev. D 67 (2003) 037503

[81] Howard Georgi, Weak Interactions and Modern Particle Theory, The Benjamin/Cummings Publishing Company (1984)

[82] M. J. Savage and J. Walden, SU(3) breaking in neutral current axial matrix elements and the spin content of the nucleon, Phys. Rev. D 55 (1997) 5376

[83] W. Greiner and B. Mueller, Quantum mechanics, Symmetries, Springer, 1994

[84] F. E. Close and R. G. Roberts, Consistent Analysis of the Spin Content of the Nucleon, Phys. Lett. B 316 (1993) 165

[85] L. Chun-xiu and L. Zuo-tang, Spin structure and longitudinal polarization of a hyperon in e^+e^- annihilation at high energies, Phys. Rev. D 62 (2000) 094001

[86] D. H. Perkins, Introduction to High Energy Physics, Addison wesley (1983)

[87] B. E. Bonner et al., Spin-parameter measurements in Λ and K_S production, Phys. Rev. D 38 (1988) 729

[88] J. Lach, Hyperons: Insights into Baryon Structures, FERMILAB-Conf-91/200

[89] J. Lach, Hyperon Polarization: An Experimental Overview, FERMILAB-Conf-92/378

[90] J. W. Cronin et al., Measurement of the decay parameters of the Λ particle, Phys. Rev. 129 (1963) 1795

[91] O. E. Overseth and R. F. Roth, Time reversal invariance in Λ decay, Phys. Rev. Lett. 19 (1967) 391

[92] W. E. Cleland et al., A measurement of the β-parameter in the charged nonleptonic decay of the Λ hyperon, Nucl. Phys. B 40 (1972) 221

[93] P. Astbury et al., Measurement of the differential cross section and the spin correlation parameters *P*, *A*, and *R* in the backward peak of $\pi^- p \to K^0\Lambda$ at 5 GeV/c Nucl. Phys. B 99 (1975) 30

[94] P. M. Dauber et al., Productuion and Decay of Cascade Hyperons, Phys. Rev. 179 (1969) 1262

[95] A. Lesnik et al., Observation of a Difference between Polarization and Analyzing Power in Λ^0 Production, Phys. Rev. Lett. 35 (1975) 770

[96] G. Bunce et al., Λ^0 Hyperon Polarization in Inclusive Production by 300-GeV Protons on Beryllium, Phys. Rev. Lett. 36 (1976) 1113

[97] M. Wiesmann, A first measurement of the transverse polarization of Λ^0 Hyperons from quasi-real photo-production, PhD Thesis, Technishe Univerität München (2004)

[98] K. Abe et al., Inclusive Λ^0 polarization in proton-nucleus collision at 12 GeV, Phys. Rev. D 34 (1986) 1950

[99] A. M. Smith et al. [R608 Collaboration], Λ^0 polarization in proton-proton interaction from $\sqrt{s}$ = 31 to 62 GeV, Phys. Lett. B 185 (1987) 209

[100] S. J. Brodsky, G. P. Lepage, Helicity selection rules and tests of gluon spin in exclusive quantum-chromodynamic processes, Phys. Rev. D 24 (1981) 2848

[101] P. M. Ho et al., Production Polarization and Magnetic Moment of $\overline{\Xi}^+$ Antihyperons Produced by 800-GeV/*c* Protons, Phys. Rev. Lett. 65 (1990) 1713

[102] A. Morelos et al. [E761 Collaboration], Polarization of Σ^+ and $\overline{\Sigma}^-$ Hyperons Produced by 800-GeV/c protons, Phys. Rev. Lett. 71 (1993) 2172

[103] J. Soffer, Is the riddle of the hyperon polarization solved? In Batavia 1999, Hyperon physics (Hyperon99), arXiv:hep-ph/9911373 (1999)

[104] T. A. DeGrand and H. I. Miettinen, Models for polarization asymmetry in inclusive hadron production, Phys. Rev. D 24 (1981) 2419

[105] A. Bravar, Experimental overview of spin effects in hadronic interactions at high energies, 13th Symposium on High Energy Spin Physics [SPIN98] Proceeding (1998)

[106] V. V. Abramov, Universal scaling behaviour of the transverse polarization for inclusively produced hyperons in hadron-hadron collisions, arXiv:hep-ph/0111128 (2001)

[107] M. Anselmino, D. Boer, U. D'Alesio, and F. Murgia, Λ polarization from unpolarized quark fragmentation, Phys. Rev. D 63 (2001) 054029

[108] D. Hui and L. Zou-tang, Hyperon polarization in different inclusive production processes in unpolarized high energy hadron-hadron collisions, Phys. Rev. D 70 (2004) 014019

[109] M. Anselmino, D. Boer, U. D'Alesio, and F. Murgia, Transverse Λ polarization in semi-inclusive deep inelastic scattering, Phys. Rev. D 65 (2002) 114014

[110] F. Baldracchini et al., Fortschritte der Physik 30 (1981) 505

[111] I. I. Y. Bigi, Some Quantitative Estimates about Final State Polarization in Deep Inelastic Lepton-Nucleon Scattering, MPI-PAE/PTH 19/77 (1977)

[112] X. Artru and M. Mekhfi, Transversely polarized parton densities, their evolution and their measurement, Z. Phys. C 45 (1990) 669

[113] J. J. Aubert et al. [The European Muon Collaboration], Measurement of the Q^2, x and W^2 dependence of single hadron production in deep inelastic muon scattering, Phys. Lett. B 114 (1982) 373

[114] G. Gustafson and J. Häkkinen, Λ-polarization in e^+e^--annihilation at the Z^0-pole, Phys. Lett. B 303 (1993) 350

[115] C. Boros, L. Zuo-tang, Spin content of Λ and its longitudinal polarization in e^+e^- annihilation at high energies, Phys. Rev. D 57 (1998) 4491

[116] V. Barone, A. Drago, and B. Ma, Connection between distribution and fragmentation functions, Phys. Rev. C 62 (2000) 062201

[117] B. Ma, I. Schmidt, J. Soffer, J. Yang, Phenomenological relation between distribution and fragmentation functions, Phys. Lett. B 547 (2002) 245

[118] V. N. Gribov and L. N. Lipatov, Deep inelastic electron scattering in perturbation theory, Phys. Lett. B 37 (1971) 78

[119] P. J. Mulder and R. D. Tangerman, The complete tree-level result up to order $1/Q$ for the polarized deep-inelastic leptoproduction, Nucl. Phys. B 461 (1996) 197

[120] R. L. Jaffe, Polarized Λ's in the current fragmentation region, Phys. Rev. D 54 (1996) 6581

[121] A. Kotzinian, A. Bravar, D. von Harrach, Λ and $\overline{\Lambda}$ polarization in lepton induced processes, Eur. Phys. J. C 2 (1998) 329

[122] M. Burkardt and R. L. Jaffe, Polarized $q \to \Lambda$ Fragmentation Functions from $e^+e^- \to \Lambda + X$, Phys. Rev. Lett. 70 (1993) 2537

[123] D. Ashery, H. J. Lipkin, Expected polarization of Λ particles produced in deep inelastic polarized lepton scattering, Phys. Lett. B (1999) 263

[124] A. Airapetian et al. [HERMES Collaboration], Longitudinal Spin Transfer to the Λ hyperon in Semi-Inclusive Deep-Inelastic Scattering, arXiv:hep-ex/0607004, (2006)

[125] M. Göckeler et al., A lattice study of the spin structure of the Λ hyperon, Phys. Lett. B 545 (2002) 112

[126] A. O. Bazarko et al., [CCFR Collaboration], Determination of the strange quark content of the nucleon from a next-to-leading-order QCD analysis of neutrino charm production, Z. Phys. C 65 (1995) 189

[127] M. Burkardt and B. J. Warr, Chiral symmetry and the charge asymmetry of the $s\bar{s}$ distribution in the proton, Phys. Rev. D 45 (1992) 958

[128] S. J. Brodsky, B. Ma, The quark-antiquark asymmetry of the nucleon sea, Phys. Lett. B 381 (1996) 317

[129] V. Barone et al., A new global analysis of deep inelastic scattering data, Eur. Phys. J. C 12 (2000) 243

[130] F. Olness et al., Neutrino dimuon production and the strangeness asymmetry of the nucleon, Eur. Phys. J. C 40 (2005) 145

[131] M. Anselmino et al., Parton densities and fragmentation functions from polarized Λ production in semi-inclusive DIS, Phys. Lett. B 509 (2001) 246

[132] B. Ma, I. Schmidt, J. Soffer, J. Yang, The quark-antiquark asymmetry of the nucleon sea from Λ and $\overline{\Lambda}$ fragmentation, Phys. Lett. B 488 (2000) 254

[133] J. Ellis, A. Kotzinian, D. V. Naumov, Intrinsic polarized strangeness and Λ^0 polarization in deep-inelastic production, Eur. Phys. J. C 25 (2002) 603

[134] J. Ellis, A. Kotzinian, D. V. Naumov and M. G. Sapozhnikov, Longitudinal polarization of Λ and $\overline{\Lambda}$ hyperons in lepton-nucleon deep inelatic scattering, CERN-PH-TH/2007-008

[135] T. Sjöstrand, The LUND Monte Carlo for JET fragmentation and e^+e^- physics - JETSET version 6.2 Comp. Phys. Comm 39 (1986) 347

[136] T. Sjöstrand, The LUND Monte Carlo for JET fragmentation and e^+e^- physics - JETSET version 6.3 - An update Comp. Phys. Comm 39 (1987) 367

[137] M. Glück, E. Reya, A. Vogt, Dynamical Parton Distributions Revisited, Eur. Phys. J C5 (1998) 461

[138] D. De Florian, M. Stratmann, W. Vogelsang, QCD analysis of unpolarized and polarized Λ-baryon production in leading and next-to-leading order, Phys. Rev. D 57 (1998) 5811

[139] M. Anselmino, M. Boglione, F. Murgia, Λ and $\overline{\Lambda}$ polarization in polarized DIS, Phys. Lett. B 481 (2000) 253

[140] D. Hui, Z. Jian, and L. Zuo-tang, Spin transfer and polarization of antihyperons in lepton induced reactions, Phys. Rev. D 72 (2005) 033006

[141] A. A. Anselm, M. Ryskin, Simple model for spin-crisis, Z. Phys. C 68 (1995) 297

[142] M. Nzar, P. Hoodbhoy, Quark fragmentation functions in a diquark model for proton and Λ hyperon production, Phys. Rev. D 51 (1995) 32

[143] C. Boros, J. T. Londergan, A. W. Thomas, Structure and production of lambda baryons, Phys. Rev. D 61 (1999) 014007

[144] B. Ma, I. Schmidt, J. Yang, Flavor and spin structure of Λ-baryon at large x, Phys. Lett. B 477 (2000) 107

[145] B. Ma, I. Schmidt, J. Soffer, and J. Yang, Λ, $\overline{\Lambda}$ polarization and spin transfer in lepton deep-inelastic scattering, Eur. Phys. C 16 (2000) 657

[146] B. Ma, I. Schmidt, J. Soffer, and J. Yang, Quark distributions of octet baryons from SU(3) symmetry, Phys. Rev. D 65 (2002) 034004

[147] J. Ellis, D. Kharzeev, A. Kotzinian, The proton spin puzzle and Λ polarization in deep-inelastic scattering, Z. Phys. C 69 (1996) 467

[148] J. Ellis, M. Karliner, D. E. Kharzeev, M. G. Sapozhnikov, Abundant ϕ-meson production in $\overline{p}p$ annihilation at rest and strangeness in the nucleon, Phys. Lett. B 353 (1995) 319

[149] A. Bertin et al. [OBELIX Collaboration], New data on OZI rule violation in $\overline{p}p$ annihilation at rest, Phys. Lett. B 388 (1996) 450

[150] J. Ellis, M. Karliner, D. E. Kharzeev, M. G. Sapozhnikov, Hadronic probes of the polarized intrinsic strangeness of the nucleon, Nucl. Phys. A 673 (2000) 256

[151] M. Alberg, J. Ellis, D. E. Kharzeev, The proton spin puzzle and depolarization in $\overline{p}p \to \overline{\Lambda}\Lambda$, Phys. Lett. B 356 (1995) 113

[152] H. Fischer et al. [PS185 Collaboration] Measurement of the $\overline{p}p \to \overline{\Lambda}\Lambda$ and $\overline{p}p \to \overline{\Sigma}^0\Lambda+$ c.c. reactions at 1.7626 and 1.771 GeV/c, Phys. Rev. C 54 (1996) 2381

[153] D. S. Carman et al. [CLAS Collaboration], First Measurement of Transferred Polarization in the Exclusive $\vec{e}p \to e'K^+\vec{\Lambda}$ Reaction, Phys. Rev. Lett. 90 (2003) 131804

[154] M. L. Mangano et al, Physics at the front-end of a neutrino factory: a quantitative appraisal, arXiv:hep-ph/0105155 (2001)

[155] W. Melnitchouk, A. W. Thomas, Meson cloud of the nucleon in polarized semi-inclusive deep inelastic scattering, A. Phys. A 353 (1995) 311

[156] M. Arneodo et al. [EMC Collaboration], Quark and diquark fragmentation into neutral strange particles as observed in muon-proton interactions at 280 GeV, CERN-EP/84-71, (June 1984)

[157] G. T. Jones et al. [Birmingham-Bonn-CERN-Imperial College-München (MPI)-Oxford Collaboration], Polarization of Λ Hyperons Produced Inclusively in νp and $\overline{\nu}p$ Charged Current Interaction, Z. Phys. C 28 (1985) 23

[158] S. Willocq et al. [WA59 Collaboration], Neutral strange particle production in antineutrino-neon charged current interactions, Z. Phys. C 53 (1992) 207

[159] D. DeProspo et al. [E632 Collaboration], Neutral strange particle production in neutrino and antineutrino charged-current interactions on neon, Phys. Rev. D 50 (1994) 6691

[160] P. Astier et al. [NOMAD Collaboration], Measurement of the Λ polarization in ν_μ charged current interactions in the NOMAD experiment, Nucl. Phys. B 588 (2000) 3

[161] M. R. Adams et al. [E665 Collaboration], Λ and $\overline{\Lambda}$ polarization from deep inelastic muon scattering, Eur. Phys. J. C 17 (2000) 263

[162] A. Ackerstaff et al. [OPAL Collaboration], Polarization and forward-backward asymmetry of Λ baryons in hadronic Z^0 decays, Eur. Phys. J. C 2 (1998) 49

[163] D. Buskulic et al. [ALEPH Collaboration], Measurement of Λ polarization from Z decays, Phys. Lett. B 374 (1996) 319

[164] P. Astier et al. [NOMAD Collaboration], Measurement of the $\overline{\Lambda}$ polarization in ν_μ charged current interactions in the NOMAD experiment, Nucl. Phys. B 605 (2001) 3

[165] COMPASS web page, http://wwwcompass.cern.ch/compass/

[166] P. Abbon et al., The COMPASS experiment at CERN, CERN-PH-EP/2007-001, Preprint submitted to Nucl. Instru. Meth. A

[167] H. W. Atherton et al., Precise measurement of particle production by 400 GeV protons on beryllium targets, CERN Yellow Report 80-07 (1987)

[168] T. Schmidt, A Common Readout Driver for the COMPASS Experiment, PhD Thesis, Univerität Freiburg (2001)

[169] N. Doble et al., The upgraded muon beam at the SPS, Nucl. Instru. Meth. A 343 (1994) 351

[170] M. von Hodenberg, First measurement of the gluon polarisation in the nucleon using *D* mesons at COMPASS, PhD Thesis, Univerität Freiburg (2006)

[171] D. Adams et al., [SMC Collaboration] Measurement of the SMC muon beam polarisation using the asymmetry in the elastic scattering off polarised electrons, Nucl. Instru. Meth. A 443 (2000) 1

[172] J. Ball et al., First results of the large COMPASS ^{6}LiD polarized target, Nucl. Instru. Meth. A 498 (2003) 101

[173] K. Kondo, The polarization measurement and the feature investigation of the COMPASS ^{6}LiD target, PhD Thesis, Nagoya University (2003)

[174] N. Takabayashi, Polarized target for the measurement of the gluon contribution to the nucleon spin in the COMPASS experiment PhD Thesis, Nagoya University (2002)

[175] K. Kondo et al., Polarization measurement in the COMPASS polarized target, Nucl. Instru. Meth. A 526 (2004) 70

[176] H. Angerer et al., Present status of silicon detectors in COMPASS, Nucl. Instru. Meth. A 512 (2003) 229

[177] I. Daito et al., Time resolution of multi-cladding scintillating fiber hodoscope, Nucl. Instru. Meth. A 433 (1999) 587

[178] J. Bisplinghoff et al., A scintillating fibre hodoscope for high rate applications, Nucl. Instru. Meth. A 490 (2002) 101

[179] C. Bernet et al., The 40 $\times$ 40 cm^2 gaseous microstrip detector Micromegas for the high-luminosity COMPASS experiment at CERN. Nucl. Instru. Meth. A 536 (2005) 61

[180] C. Altunbas et al., Construction, test commissioning of the triple-gem tracking detector for compass, Nucl. Instru. Meth. A 490 (2002) 177

[181] S. Panebianco, Performances of Drift Cahmbers and MicroMegas in 2003, COMPASS Collaboration Meeting, Lissabon (October 2003)

[182] V. N. Bychkov, et al., The large size straw drift chambers of the COMPASS experiment, Nucl. Instru. Meth. A 556 (2006) 66

[183] A. Amoroso et al., The front-end electronics for the COMPASS MWPCs, Nucl. Instru. Meth. A 518 (2004) 495

[184] M. Leberig, W45 Calibration and Resolution, COMPASS Analysis Meeting, CERN, Geneva (May 2004)

[185] E. Albrecht, et al., Status and characterisation of COMPASS RICH-1, Nucl. Instru. Meth. A 553 (2005) 215

[186] E. Iarocci, et al., Plastic streamer tubes and their applications in high energy physics, Nucl. Instru. Meth. 217 (1983) 30

[187] O. Gavrishchuk et al., Calorimeter for Hadron Detection in the Energy-Range 10 - 100 GeV, Tech. Rep. JINR D13-2004-186, Dubna (2004)

[188] N. V. Vlasov et al., A Calorimeter for detecting hadrons with energies of 10 - 100 GeV, Instruments and Experimental Techniques 49 (2006) 41

[189] A. V. Dolgopolov, et al., Results of a beam test of the combined lead glass and PWO cells detector for the COMPASS electromagnetic calorimeter, Nucl. Instru. Meth. A 420 (1999) 20

[190] A. Airapetian et al., The COMPASS trigger system for muon scattering, Nucl. Instru. Meth. A 550 (2005) 217

[191] B. Grube, A trigger control system for COMPASS and a measurement of the Transverse Polarisation of Λ and Ξ Hyperons from Quasi-Real Photo Production, PhD Thesis, Technishe Univerität München (2006)

[192] M. Leberig, Das COMPASS Triggersystem zur Messung von Δ G, PhD Thesis, Univerität Mainz (2002)

[193] H. Fischer, et al., The DAQ of the COMPASS Experiment, IEEE Trans. Nucl. Sci. 49 (2002) 443

[194] L. Schmitt, et al., The DAQ of the COMPASS Experiment, IEEE Trans. Nucl. Sci. 51 (2004) 439

[195] J. C. Santiard, et al., A low noise analog signal processor for read-out of gaseous detectors, presented at the 6th Pisa Meeting on Advanced Detectors, La Biodola, Isola d'Elba, Italy (1994)

[196] M. J. French, et al., Design and results from the APV25, a deep sub-micron CMS front-end chip for the CMS tracker, Nucl. Instru. Meth. A 466 (2001) 359

[197] H. Fischer, et al., Implementation of the dead-time free F1 TDC in the COMPASS detector readout, Nucl. Instru. Meth. A 461 (2001) 507

[198] A. Grüenemaier, Eine universelle Ausleseschnittstelle für das COMPASS Experiment, PhD Thesis, Univerität Freiburg (2002)

[199] H. C. vam der Bij, et al., S-Link, a Data Link Interface Specification for the LHC Era, IEEE Trans. Nucl. Sci. 44 (1997) 398

[200] CASTOR - CERN Advanced STORage system web page, http://castor.web.cern.ch/castor/

[201] ALICE DAQ and ECS user's guide, ALICE-INT-2005-015 v.1

[202] W. Kastaun, Erste Untersuchungen zur Hadron-Produktion am COMPASS Experiment, Diploma Thesis, Universität Freiburg (2002)

[203] R. Brun, et al., ROOT - An object oriented data analysis framework, Nucl. Instru. Meth. A 389 (1997) 81, http://roor.cern.ch

[204] COMPASS Electronic Log Book, http://wwwcompass2.cern.ch/runLogbook/dirphp/

[205] B. Gobbo, et al., CORAL web page, http://coral.web.cern.ch/coral/

[206] Y. Bedfer, et al., COMPASS's track reconstruction algorithm, COMPASS Note 2004-1

[207] K. Kurek, et al., An algorithm for track reconstruction in the large angle spectrometer in the COMPASS experiment, Nucl. Instru. Meth. A 485 (2002) 720

[208] R. Frühwirth, Application of Kalman filtering to track and vertex fitting, Nucl. Instru. Meth. A 262 (1987) 444

[209] E. J. Wolin and L. L. Ho, Covariance matrices for tracking fitting with the Kalman filter, Nucl. Instru. Meth. A 329 (1993) 493

[210] A. Korznev, et al., Vertex reconstruction in the COMPASS spectrometer. Part I. Monte Carlo studies, COMPASS Note 2001-17

[211] S. Gerassimov, PHAST - PHysics Analysis Software Tools web page, http://ges.home.cern.ch/ges/phast/index.html

[212] GridKa - Grid Computing Centre Karlsruhe web page, http://gridka.fzk.de

[213] J. Zhao et al., DST and mDST production web page, http://na58dst1.home.cern.ch/na58dst1/dstprod.html

[214] F. H. Heinsius, Definition of beam track, scattered muon and vertex, http://wwwcompass.cern.ch/compass/software/offline/reconstruction/tracks.html

[215] S. Koblitz and A. Korzenev, Data Quality web page, http://wwwcompass.cern.ch/compass/software/offline/input/stab/index.html

[216] S. Hedicke and C. Bernet, Measurement of high p_T asymmetries on 2002 data, COMPASS Note 2004-7

[217] A. Korzenev, Univerität Mainz, Private Communication (June 2007)

[218] R. J. Barlow, Statistics: A Guide to the use of Statistical Methods in the Physical Sciences, J. Wiley & Sons (1989)

[219] V. Alexakhin et al., Results on Λ and $\overline{\Lambda}$ polarization from the 2002 data, COMPASS Note 2005-04.

[220] R. Armenteros and J. Podolanski, Analysis of V-events, Philos. Mag. 45 (1954) 13

[221] E. Byckling and K. Kajantie, Particle Kinematics, J. Wiley & Sons (1972)

[222] G. Ingelman, et al., LEPTO 6.5 - A Monte Carl Generator for Deep Inelastic Lepton-Nucleon Scattering, DESY 96-057, ISSN 0418-9833

[223] V. Alexakhin, COMGEANT web page, http://valexakh.web.cern.ch/valexakh/wwwcomg/index.html

[224] GEANT - Detector Description and Simulation Tool, GERN Program Library Writeup W5013, CERN

[225] I. Akushevich, et al., RADGEN 1.0 - Monte Carlo Generator for Radiative Events in DIS on Polarized and unPolarized targets, arXiv:hep-ph/9906408v1 (1999)

[226] PDFLIB: Proton, Pion and Photon Parton Density Functions, User's Manual, CERN COmputer Program Library entry W5051

[227] M. Glučk, E. Reya, A. Vogt, Dynamical parton distributions of the proton and small-x physics, Z. Phys C 67 (1995) 433

[228] H. L. Lai et al., Global QCD analysis and the CTEQ parton distributions, Phys. Rev. D 51 (1995) 4763

[229] H. L. Lai et al., Global QCD Analysis of Parton Structure of the Nucleon: CTEQ5 Parton Distributions, Eur. Phys. J C12 (2002) 375

[230] B. A. Kniehl, G. Kramer, B, Potter, Testing the Universality of Fragmentation Functions, Nucl. Phys. B 597 (2001) 337

[231] B. Anderesson, G. Gustafson, T. Sjostrand, Baryon Production in Jet Fragmentation and Υ-Decay, Phys. Scripta. 32 (1985) 574

[232] T. Sjostrand, et al., PYTHIA 5.7 and JETSET 7.4: Physics and manual, arXiv:hep-ph/9508391 (1995)

[233] V. Alexahkin, Monte Carlo studies for HCAL threshold, COMPASS Analysis Meeting, CERN (July 2005).

[234] V. Alexahkin, News on Lambda analysis, COMPASS Analysis Meeting, CERN (June 2004).

[235] E. S. Ageev et al. [COMPASS Collaboration], A new measurement of the Collins and Sivers asymmetries on a transversely polarized deuteron target, CERN-PH-EP/2006-031

[236] P. R. Bevington, Data reduction and error analysis for the physical sciences, McGraw-Hill Co. (1969)

[237] R. Gatto, Relations between the Hyperon Polarizations in Associated Production, Phys. Rev. 10 (1957) 610

List of Figures

List of Tables

Acknowledgements

First and foremost I would like to thank my supervisor, Prof. Dr. Kay Königsmann, for his consistent support and for his devoted guidance throughout my research. He was always patient for explaining to me the importance of clarity, preciseness and simplicity in physics, never disrespecting. It has been truly a great privilege to be his student.

I have a special debt to Prof. Dr. Horst Fischer, who the first showed me the basic of experiments, for his warm and encouraging attitude. His kindness and encouragement have elevated my spirit many times during my Ph.D. in Freiburg. I am most impressed with his pride and enthusiasm for physics. I would like to thank Prof. Dr. Fritz-Herbert Heinsius. As an adviser, he was always willing to discuss current status and difficulties and to offer advice on the path forward. I have enjoyed very interesting and insightful discussions with him. I would also like to express my appreciation to Dr. Jürgen Franz who read and corrected my thesis carefully and helped me when I got a lot of problems.

The direction of my Ph.D. work has been strongly influenced by the members of the Freiburg group. I would like to thank all former and current members, Prof. Dr. Hans Schmitt, Dr. Eric Weise, Dr. Thomas Schmidt, Dr. Andreas Grünemaier, Dr. Sonja Hedicke, Dr. Martin von Hodenberg, Wolfgang Kastaun, Dr. Falcone Karstens, Dr. Hugo Pereira da Costa, Chiara Spáno, Anna Danasino, Inga Ludwig, Sebastian Trippel, Dominik Setter, Dr. Andreas Mutter, Florain Hermann, Anselm Vossen, Roland Hagemann, Jasmin Kiefer, Konrad Wenzl, Jochen Barwind, Sebastian Schopferer, Gisela Mössner, Khalil Rehmani, and Rainer Fastner. The help and support from these peoples has been in large part responsible for my successes. Notably, Dr. Christian Schill, Dr. Frank Nerling, Heiner Wollny, Wolfgang Käfer, and Julia Vogel have provided me invaluable help, far and beyond their duty while completing my Ph.D. work. I am deeply grateful to all members in Freiburg for their kindness and the creation of wonderful working environment.

The work appearing in this dissertation was done with the members of the COMPASS collaboration at CERN. Mikhail Sapozhnikov at Dubna was always willing to listen to my frequently wrong ideas. His knowledge was useful to me much about how my research should be done. I am specially thankful to Vadim Alexakhin at Dubna. He taught me how to handle the Monte Carlo simulation through direct communication with his great experience. I thank to Andrea Ferrero, Boris Grube, Nikolai Vlasov, Vladimir Rapatsky and Aram Kotzinian for lending me their considerable intellects. Jiawei Zhao was also always willing to help me with coding the scripts I needed. I am thankful for the opportunity to participate in an exciting and interesting research group.

I suppose this is also a wonderful opportunity to express my parents how grateful I am. Above all, they gave me the gift of freedom to choose my path in life. They never imposed themselves on me, never told me what to study or where to live. They were happy and proud of my decisions even when those did not meet their expectations or hopes. I would not have been able to reach this point and to pursue my dreams without them. I give them my deepest thanks for all the love, support and encouragement that they have given me over the years. I would also like to thank Donghwa's parents for their endless encouragement, and for allowing me to marry with my fiancee so that I could married in this summer. They are the kindest and most caring people I know.

Finally, I am indebted to my wife, Donghwa Kang, for being on my mind. She has been a source of tremendous encouragement throughout my master and Ph.D. works. She came with me to Freiburg away from her family six years ago. She has been around to celebrate when our life was going well, as well as to commiserate when it was not. She has expanded my horizons on life and become the touchstone of my being. I love her with all of my heart, and am so thankful that she decided to marry with me during difficult times.

The time of Universität Freiburg will always be missing.